

# **Distinct Element Modeling of the Shimizu Tunnel No.3 in Japan**

By  
Sotirios Vardakos

Thesis submitted to the Faculty of the Virginia Polytechnic Institute and State University in partial fulfillment of the requirements for the degree of

Master of Science  
In  
Geotechnical Engineering

Dr. Marte S. Gutierrez, Chair

Dr. Matthew Mauldon

Dr. Erik Westman

December, 2003

Blacksburg, Virginia

Keywords: tunneling, sequential excavation, distinct element, convergence-confinement.

Copyright: Sotirios Vardakos

# Distinct Element Modeling of the Shimizu Tunnel No.3 in Japan

By

Sotirios Vardakos

## ABSTRACT

In the present research a highway twin tunnel project completed in Japan in 1998 is used as a case study to verify results of numerical analyses with measurement data. Each of the tunnels had approximately 1.1 km of length. For this project a wide geometry of approximately 18.0 m was selected by the designers to facilitate three lanes per tunnel. A sequential tunneling technique known in Japan as the “TBM pilot and enlargement method” was used along with NATM principles. The tunnel was used as a reference project, involving performance testing and extensive monitoring in order to verify and standardize support requirements for other tunnels excavated under similar geologic conditions in the Tomei II expressway.

The tunnel was excavated in a region consisting mainly of soft sedimentary rocks, such as locally weathered sandstone, underlain by interbedded sandstone and mudstone. Due to observed non symmetric deformations and loads in the tunnel, the distinct element and the convergence-confinement methods were used during the numerical simulations.

A parametric analysis was performed initially in a pseudo-continuum approach to study the behavior of the wide tunnel geometry under various conditions. The effects of rock mass elastic modulus, in situ  $K_0$  ratio and boundary conditions are discussed.

More complex parametric studies were performed in a stochastically generated model by using joint spatial data from geotechnical investigations. The Barton-Bandis constitutive law was assumed for the behavior of the joints. The sensitivity of the ground “characteristic curves” was examined by statistical variation of the joint shear strength parameters. A final simulation using the code UDEC and the convergence-confinement method yields interesting results which are comparable to the monitored data.

## GRANT INFORMATION

This project and the studies of the author leading to the  
Master of Science Degree  
were performed under  
Governmental Sponsorship by the U.S Department of State via the  
Fulbright Foundation for the year  
2002-2003.

## Acknowledgements

The present research project and thesis benefited from supervision and supportive guidance of Dr. Marte Gutierrez at the Department of Civil and Environmental Engineering at Virginia Polytechnic Institute and State University. The author also wishes to express gratitude towards Dr. Matthew Mauldon from the Department of Civil and Environmental Engineering and to Dr. Erik Westman from the Department of Mining and Minerals Engineering for their support during the progress of the research.

During the execution of this research a very important and time consuming stage was the translation of available documents and reports in Japanese. Special thanks should be given to colleagues who helped in the initial translation but also for their support during continuous updating of the translation as the research proceeded:

Dr. Seungcheol Baek

Ms. Atsuko Kotake

Mr. Soonkie Nam

Mr. Ming Zhang

The author also feels to acknowledge and express gratitude towards Ms. Noriko Seki from the Japan Tunnelling Association for assisting in selecting and providing reports from JTA.

# CONTENTS

CHAPTER 1 : Introduction .....	1
1.1 Scope of work .....	1
1.2 Historical background.....	3
1.3 Tunneling in Japan.....	6
1.4 The Tomei - Meishin Expressway .....	10
CHAPTER 2 : The Shimizu tunnel No.3.....	13
2.1 Tunnel location .....	13
CHAPTER 3 : Geotechnical data .....	16
3.1 Field Investigations.....	16
3.2 Rock mass classification.....	21
3.2.1 General.....	21
3.2.2 Q rock mass classification system .....	21
3.2.2.a Q system classification from seismic surveys at Shimizu tunnel No.3.....	26
3.2.2.b Q system classification from core logging at Shimizu tunnel No.3 .....	29
3.2.3 Japanese rock mass classification system.....	35
3.2.3.a Japanese rock mass classification at Shimizu tunnel No.3 .....	38
3.3 Joint set data.....	40
3.4 Laboratory tests.....	40
3.5 Shear strength of discontinuities.....	44
3.5.1 Failure criteria.....	44
3.5.2 Rock joint parameters for Shimizu tunnel No.3 .....	48
CHAPTER 4 : Tunneling methods .....	49
4.1 Modern tunneling techniques.....	49

4.2 The New Austrian Tunneling Method .....	50
4.3 The Norwegian Method of Tunneling .....	58
4.4 Tunneling method used at Shimizu tunnel No.3.....	63
4.5 Tunnel support system .....	69
 CHAPTER 5 : Tunnel analysis and design.....	 76
5.1 General.....	76
5.2 Available analytical methods.....	76
5.2.1 Analytical solutions .....	77
5.2.2 Methods that account for three dimensional effects .....	81
5.2.2.a The Convergence-Confinement Method.....	81
5.2.2.b The equivalent modulus method.....	86
5.2.3 The Finite Element Method .....	89
5.2.4 The Finite Difference Method .....	91
5.2.5 The Boundary Element Method.....	92
5.2.6 The Distinct Element Method.....	93
5.2.7 Discontinuous Deformation Analysis (DDA).....	94
5.2.8 Previous numerical simulations for the Shimizu tunnel No.3 .....	94
 CHAPTER 6 : Numerical analyses using the Distinct Element Method.....	 96
6.1 Modeling parameters .....	96
6.2 Main features of the DEM formulation .....	97
6.3 Application of the Barton-Bandis model in UDEC .....	101
6.3.1 Normal behavior .....	101
6.3.2 Shear behavior .....	107
6.4 Numerical modeling for the Shimizu tunnel No.3.....	113
6.5 Simple continuum model analysis .....	120
6.5.1 Effects of the elastic modulus .....	121
6.5.2 Effects of the $K_0$ stress ratio in simple models .....	152

6.6 Monitoring data from the Shimizu tunnel No.3 site .....	172
6.7 Single tunnel jointed model analyses.....	180
6.7.1 General.....	180
6.7.2 Advantages and disadvantages of the method .....	183
6.7.3 Analysis results from initial jointed model.....	184
6.7.4 DEM constructed characteristic curves for the initial jointed model .....	188
6.7.5 Discussion of results for initial DEM analysis .....	202
 CHAPTER 7 : Parametric analysis for characteristic curves .....	 207
7.1 General procedure.....	207
7.2 Vertically relocated tunnel models .....	207
7.2.1 Downward relocation of the tunnel.....	207
7.2.2 Upward relocation of the tunnel .....	211
7.3 Influence of the Joint Roughness Coefficient (JRC <sub>o</sub> ).....	213
7.4 Influence of the Joint Wall Compressive Strength (JCS <sub>o</sub> ).....	216
7.5 Influence of the residual friction angle $\phi_r$ in the model behavior .....	219
 CHAPTER 8 : Back-analyzed models.....	 222
8.1 General considerations.....	222
8.2 Ground characteristic curves for back analysis .....	224
8.2.1 Single tunnel jointed model with E=3800 MPa.....	224
8.2.2 Jointed model including localized refinement.....	228
8.2.3 Refined jointed model with E=4300 MPa block elastic modulus .....	231
8.3 Final analysis with the distinct element and convergence-confinement methods	234
 CHAPTER 9 : Summary and conclusions.....	 253
 REFERENCES: .....	 258

APPENDIX.....	264
A.1 Main input file in UDEC.....	265
A.2 Controlled relaxation analysis input files.....	291
A.2.1 Relaxation subroutine for pilot tunnel .....	291
A.2.2 Relaxation subroutine for top heading.....	296
A.3 Complete input file for controlled relaxation.....	299
VITA.....	305



## LIST OF FIGURES

Figure 1.1: Marc I. Brunel (1820) and his pioneering iron tunneling shield (From Brunel Engine House, Rotherhithe, United Kingdom, 2003).....	4
Figure 1.2: Greathead’s shield (1880), that was used in the Tower Subway of London....	4
Figure 1.3 a,b: The Hoosac Tunnel in Boston, Massachusetts. ....	5
Figure 1.4: Investment trends in Japan since 1985. (From R.Craig, World Tunnelling Magazine). ....	9
Figure 1.5: The Shinkansen Railway network in Japan and view of the Tokaido Shinkansen (From Japan Railway Company.).....	9
Figure 1.6: Modern Tunnel boring machine industry in Japan (From Japan Tunnelling Association). ....	9
Figure 1.7: Comparison between the Tomei I and Tomei II highway sections (From Y.Ishihara, 2002). ....	11
Figure 1.8: The Old and New Tomei II expressways, linking Tokyo to Kobe (Y.Ishihara, 2002). ....	11
Figure 1.9: The Standard type of cross section used in Shimizu tunnel No.3. (From Japan Tunnelling Association, 1998). ....	11
Figure 2.1: Map of Southeast Japan and location of Shimizu city (2003).....	15
Figure 2.2: Present status of highway infrastructure development between Tokyo and Kyoto (From JHPC, 2002). ....	15
Figure 3.1: a and b: Longitudinal geologic cross sections of West Sector and $V_p$ velocity measurements, c: cross section at 912+67.5 (From Japan Highways, 1995). ....	17
Figure 3.2: West and Central sector borehole locations. Top: BH-2, BV2-1- Bottom: BH-1, BV2-2 (From Japan Highways, 1995). ....	18
Figure 3.3: Geologic Cross section at borehole location BV2-1 of central sector STA 915+25, viewing to east (From Japan Highways, 1995). ....	19
Figure 3.4: Geological cross sections of central and east sectors, top section: location of BV-4, BV-2, BH-2 (east), bottom: location of BV-3, BV-1, BH-1 (east) (From Japan Highways, 1995). ....	20
Figure 3.5: The Q index support estimates. ....	25
Figure 3.6: Example of rock core sampling for western sector (From NGI, 1995). ....	33
Figure 3.7: Rock mass ratings for Q and RMR systems in horizontal borehole BH1 (dotted line indicates most probable rock mass quality at the $Walt_2$ formation).....	34
Figure 3.8: Worksite plan of Shimizu No.3 twin tunnels on Tomei II Expressway, Japan. Rock mass quality grading and support system (After Japan Highways, 1998).....	39
Figure 3.9: Stereonet for primary joint sets in Wadajima Sandstone (NGI, 1995). ....	42
Figure 3.10: Typical shear stress-shear displacement plots for direct shear tests at rock joints under different loading conditions. ....	44
Figure 3.11: Patton’s “saw tooth” model of discontinuities. ....	45
Figure 3.12: Bilinear shear strength model (after Patton, 1966).....	46
Figure 4.1: Peck’s idealization for effect of support rigidity on pressure distribution. ....	53
Figure 4.2: Top Hat connections (From Barla, 1999).....	56
Figure 4.3: Müller’s idealization for problematic cases of top heading excavations. ....	56
Figure 4.4: Visualization of the pilot tunnel ahead of the top heading (Ishihara,2001). ..	64

Figure 4.5: The sequential stages in the “TBM pilot and enlargement method”.....	64
Figure 4.6 a, b, c: Sequential stages for the Shimizu tunnel No.3.....	65
Figure 4.7 a,b: The triple shield TBM used at the Shimizu site. ....	67
Figure 4.8: Geometry and rock bolt locations for the Shimizu tunnel No.3.....	71
Figure 4.9: Typical results from tested shotcrete uniaxial compressive strength. ....	71
Figure 4.10 a,b: Breakthrough of the “Suruga” TBM. ....	73
Figure 4.11: TBM pilot tunnel with pre-reinforcement and top heading excavation at Shimizu site. The destroyed plastic cables after blasting can be still seen. (note: illustrated dates are incorrect).....	74
Figure 4.12: Drilling equipment used in Shimizu tunnel No.3.....	74
Figure 4.13: Pilot tunnel with pre-reinforcement and primary support of shotcrete and H100 beams. Top heading with completed primary support up to the face (courtesy: Japan Tunnelling Association).....	75
Figure 4.14: Pre-reinforcement from pilot tunnel.....	75
Figure 5.1: Typical curves of loss factor $\lambda$ versus normalized distance from the face for different values of the $N_s$ ratio, produced by AFTES. The most reliable method to generate such curves is a full three dimensional numerical analysis (after Kavvadas, 2000). ....	85
Figure 5.2: The Convergence-Confinement method (After Panet, 1986).....	87
Figure 5.3: The Equivalent modulus method (after Laabmayer and Swoboda, 1978). ....	88
Figure 6.1: The computational cycle used by UDEC (Itasca,2000). ....	99
Figure 6.2: Detail of a distinct element model in UDEC. Blocks are being divided into finite difference zones for elastoplastic analysis. ....	100
Figure 6.3: Corner rounding length definition used by UDEC (After Itasca,2000). ....	100
Figure 6.4: Normal closure under cyclic normal loading of the joint (case 1, after Bandis et al., 1985) .....	106
Figure 6.5: Normal closure under cyclic normal loading of the joint (case 2, after Bandis et al., 1985) .....	106
Figure 6.6: a: Non linear Barton-Bandis failure envelope, b: dilation vs. shear displacement, c,d: JCS and JRC versus joint length, e & f: shear strength versus horizontal displacement (case 1).....	110
Figure 6.7: a: Non linear Barton-Bandis failure envelope, b: dilation versus shear displacement, c, d: JCS and JRC versus joint length, e & f: shear strength versus horizontal displacement (case 2).....	112
Figure 6.8: Method followed for numerical simulations with UDEC for the Shimizu tunnel No.3.....	114
Figure 6.9: Artificial blocking for simple tunnel models in UDEC. ....	117
Figure 6.10: Finite Difference zoning in continuum models. Close to the tunnel the finite difference zone length becomes small to increase plastic flow precision. ....	117
Figure 6.11: Excavation stages during numerical simulation.....	118
Figure 6.12: UDEC fracture network for single tunnel jointed model. ....	119
Figure 6.13: Refined finite difference zoning around tunnel region. ....	119
Figure 6.14: Simplified model used for continuum parametric analyses, by using prescribed lateral pressure boundary conditions.....	123
Figure 6.15: Stresses close to TBM opening in continuum model. ....	123

Figure 6.16: (a): E=4000 MPa model, TBM roof convergence vs. cycle time, (b): Springline convergence, (c): Unbalanced force plot.....	124
Figure 6.17: E=4000 MPa model, (a): Pilot tunnel total displacements, (b): Vertical displacements shaded contours, (c): Horizontal displacements shaded contours...	125
Figure 6.18: Definition of the strength over stress ratio as a means of estimating proximity to failure in UDEC. ....	127
Figure 6.19: E=4000 MPa model, (a):principal stress tensors, (b): mobilization of shear strength, (c): color coded deviator stresses.....	128
Figure 6.20: E=4000 MPa model, (a): Top heading excavation roof convergence, (b): Unbalanced force plot.....	130
Figure 6.21: E=4000 MPa model, (a): Total displacements around top heading, (b): Vertical displacement shaded contour plot, (c): Horizontal displacements shaded contour plot.....	131
Figure 6.22: E=4000 MPa model, (a): Redistribution of stresses around top heading tunnel, (b): Strength/stress plot, (c): Deviatoric stresses. ....	132
Figure 6.23: E=4000 MPa model, (a): Crownline convergence, (b): Left wall convergence (shoulder), (c) unbalanced forces plot. ....	134
Figure 6.24: E=4000 MPa model, (a): Total displacements around final unsupported tunnel, (b): Shaded contours of vertical displacements, (c): Shaded contours of horizontal displacements.....	135
Figure 6.25: E=4000 MPa model, (a): Principal stresses around full excavation, (b): Strength/stress plot, (c): Deviatoric stresses. ....	136
Figure 6.26: E=12000 MPa (a) Pilot tunnel roof convergence, (b): Tunnel springline convergence, (c): unbalanced force plot at end of solution. ....	138
Figure 6.27: E=12000 MPa. (a): Total displacements around TBM opening, (b): Shaded contour plot of vertical displacements, (c): Shaded contour plot of horizontal displacements.....	139
Figure 6.28: E=12000 MPa model, (a): Principal stresses around TBM opening, (b): Mobilization of shear strength around TBM tunnel, (c): Deviatoric stresses around pilot tunnel. ....	141
Figure 6.29: E=12000 MPa. (a): Crownline convergence, (b): Unbalanced forces at end of solution. ....	143
Figure 6.30: E=12000 MPa. (a): Total displacements around top heading stage, (b): Shaded contours of vertical displacements, (c): Shaded contours of horizontal displacements.....	144
Figure 6.31: E=12000 MPa. (a)Principal stresses around top heading, (b): Strength mobilization plot, (c): Deviatoric stresses. ....	145
Figure 6.32: E=12000 MPa. (a): Crownline convergence vs. cycling, (b): Shoulder convergence, (c): Unbalanced force plot. ....	146
Figure 6.33: E=12000. (a): Bench excavation stage total displacements, (b):Shaded contours of vertical displacements, (c): Shaded contours of horizontal displacements.....	147
Figure 6.34: E=12000 MPa. (a)= Principal stresses around final excavation, (b):Mobilization ofshear strength, (c): Deviatoric stresses.....	148
Figure 6.35: Plots of predicted deformation of continuum models, using UDEC for elastic moduli in the range from 2000 - 12000 MPa.....	151

Figure 6.36: Elastic modulus and unconfined compressive strength from various soft rock types in Japan. (After Kikuchi et al., 1984) .....	153
Figure 6.37: Correlations between the intact rock elastic modulus and the uniaxial compressive strength in the Wss sandstone of the Shimizu tunnel No.3 site. ....	153
Figure 6.38 a,b: Non linear strength envelopes in $\sigma_1, \sigma_3$ space and $\sigma, \tau$ space using the Hoek-Brown criterion. ....	155
Figure 6.39: $K_0=0.5$ , (a): Stress redistribution, (b): Total displacements, (c): Shaded contours for vertical displacements, (d): Shaded contours for horizontal displacements. $K_0=1.2$ , (e): Stress redistribution, (f): Total displacements, (g): Shaded contours for vertical displacements, (h): Shaded contours for horizontal displacements. ....	163
Figure 6.40: TBM pilot tunnel- $K_0=0.5$ , (a): Deviatoric stresses, (b): Strength/stress ratio. $K_0=1.2$ , (c): Deviatoric stresses, (d): Strength/stress ratio. ....	164
Figure 6.41: Top Heading- $K_0=0.5$ , (a): Total displacements, (b): Stress redistribution, (c): Shaded contours for vertical displacements, (d): Shaded contours for horizontal displacements. $K_0=1.2$ , (e): Stress redistribution, (f): Total displacements, (g): Shaded contours for vertical displacements, (h): Shaded contours for horizontal displacements. ....	165
Figure 6.42: $K_0=0.5$ , (a): Deviatoric stresses, (b): mobilization of shear strength. $K_0=1.2$ , (c): Deviatoric stresses, (d): Mobilization of shear strength. ....	166
Figure 6.43: $K_0=0.5$ , (a): Stress redistribution, (b): Total displacements, (c): Shaded contours for vertical displacements, (d): Shaded contours for horizontal displacements. $K_0=1.2$ , (e): Stress redistribution, (f): Total displacements, (g): Shaded contours for vertical displacements, (h): Shaded contours for horizontal displacements. ....	167
Figure 6.44: $K_0=0.5$ , (a): Deviatoric stresses around tunnel at bench stage, (b): Mobilization of shear strength and overstressing of shoulder area. $K_0=1.2$ , (c): Deviatoric stresses around tunnel at bench stage, (d): More uniform mobilization of shear strength for $K_0=1.2$ case and more stable tunnel. ....	168
Figure 6.45: Simplified model for parametric analysis, using a zero lateral strain boundary condition. ....	169
Figure 6.46: Plots of deformation versus $K_0$ ratio for $E=2000$ MPa for continuum parametric analyses. ....	170
Figure 6.47: Plots of deformation versus $K_0$ ratio for $E=5000$ MPa for continuum parametric analyses. ....	171
Figure 6.48: Shimizu tunnel No.3 section geometry and locations of reflex targets for three dimensional geodetical surveying. ....	174
Figure 6.49: Measurement locations at STA913+65 section. R=measurement anchors, E=extensometers. ....	174
Figure 6.50: Monitoring data from 3D surveying in tunnels at chainage 913+65. Vertical deformation versus time at locations C,D,H. The advance of the top heading from the chainage 913+65 is also presented (After Japan Highways,1998). ....	175
Figure 6.51: Length closure versus time at for D1,D2 and D3 reference distances. The advance of the top heading from the chainage 913+65 is also presented (After Japan Highways, 1998). ....	175

Figure 6.52: Monitoring data from 3D surveying in tunnels at chainage 913+65. Vertical deformation versus time at locations C,D,H. The advance of the top heading from the chainage 914+10 is also presented (After Japan Highways,1998). .....	176
Figure 6.53: Length closure versus time at for D1,D2 and D3 reference distances. The advance of the top heading from the chainage 914+10 is also presented (After Japan Highways, 1998). .....	176
Figure 6.54 a-j: Results from extensometer and measurement anchor locations around top heading at 913+65 chainage. ....	178
Figure 6.55 : Locations of primary lining stress measurement elements for chainage: a) STA 913+65 and b) STA 914+10.....	179
Figure 6.56: Final deformation results from dynamic (left column) and controlled relaxation analysis (right column) for pilot opening in jointed mass. The dynamic solution reveals slightly higher deformations. a & d) Total displacement plots, b & e) shaded contours of vertical displacements, c & f) shaded contours of horizontal displacements.....	186
Figure 6.57: Strength / stress results from (a) dynamic and (b) controlled relaxation analysis, for pilot tunnel in jointed mass. In both cases no plastic yielding occurs in the rock mass.....	187
Figure 6.58: Characteristic curves in jointed model using $E=5000$ MPa, for $D=5.0$ pilot opening using controlled deformation in UDEC. ....	190
Figure 6.59: Characteristic curves in jointed model using $E=5000$ MPa, for top heading using controlled deformation in UDEC. At a loss factor of $\lambda=0.9$ unstable rock blocks start detaching from the surrounding rock mass.....	190
Figure 6.60: Approximate characteristic curves in jointed model using $E=5000$ MPa for points located at the crown (C) and at 2.0, 3.4 and 6.0 m above the crown. ....	191
Figure 6.61: Schematic representation of the convergence-confinement principle used in the initial UDEC analysis. Curve $\epsilon_b$ is calculated for the boundary of the excavation. Curve $\epsilon_m$ is calculated for an internal point in the rock mass close to the boundary but stable enough so that large displacements do not occur. Both curves are associated simultaneously by the exactly known loss (relaxation) factor $\lambda$ which is used to “drive the analysis”.....	194
Figure 6.62: Schematic representation of ground-support interaction used in UDEC. ..	195
Figure 6.63: Deformation versus cycling time at 6.0 m above the crown of the top heading and tracking of the cycling time for the corresponding loss factor. ....	197
Figure 6.64: Equivalent steel beam for shotcrete-steel beam lining used for support (lengths in meters).....	200
Figure 6.65: Shaded contours of vertical displacements after installation of support in top heading, assuming a block elastic modulus of $E=5000$ MPa. ....	203
Figure 6.66: Deformations along directions of extensometer locations in top heading. ....	203
Figure 6.67: Strength/stress plot for supported top heading excavation. It is shown that there is a region of distressed blocks above the tunnel as well as at the temporary floor level. Stress concentration around the edges tends to cause initialization of plastic yielding at these points. ....	204
Figure 6.68: Shear displacements around supported top heading, using $E=5000$ MPa..	204
Figure 6.69: Comparison between original geometry and deformed block geometry after excavation in jointed model.....	206

Figure 6.70: Axial forces on composite beam structure for jointed model by using E=5000 MPa. ....	206
Figure 7.1: Characteristic curves in jointed model using E=5000 MPa with upward shifted bedding.....	210
Figure 7.2: Characteristic curves in jointed model using E=5000 MPa with upward shifted bedding.....	210
Figure 7.3: Characteristic curves in jointed model using E=5000 MPa with downward shifted bedding.....	211
Figure 7.4: Characteristic curves in jointed model using E=5000 MPa with downward shifted bedding.....	212
Figure 7.5: Characteristic curves for pilot tunnel in jointed model using E=5000 MPa with low JRC parameter.....	214
Figure 7.6: Characteristic curves for top heading in jointed model using E=5000 MPa with low JRC parameter.....	214
Figure 7.7: Characteristic curves for pilot tunnel in jointed model using E=5000 MPa with increased JRC parameter. ....	215
Figure 7.8: Characteristic curves for top heading excavation in jointed model using E=5000 MPa with increased JRC parameter. ....	215
Figure 7.9: Characteristic curves for pilot tunnel in jointed model using E=5000 MPa with low JCS parameter. ....	217
Figure 7.10: Characteristic curves for top heading excavation in jointed model using E=5000 MPa with low JCS parameter.....	217
Figure 7.11: Characteristic curves for pilot tunnel in jointed model using E=5000 MPa with high JCS parameter.....	218
Figure 7.12: Characteristic curves for top heading excavation of tunnel in jointed model, using E=5000 MPa with high JCS parameter. ....	218
Figure 7.13: Characteristic curves for pilot tunnel in jointed model using E=5000 MPa and assuming reduced residual friction angle $\phi_r$ . ....	220
Figure 7.14: Characteristic curves for top heading stage in jointed model using E=5000 MPa and assuming reduced residual friction angle $\phi_r$ . ....	220
Figure 7.15: Characteristic curves for pilot tunnel in jointed model using E=5000 MPa and assuming increased residual friction angle $\phi_r$ . ....	221
Figure 7.16: Characteristic curves for top heading stage in jointed model using E=5000 MPa and assuming increased residual friction angle $\phi_r$ . ....	221
Figure 8.1: Maximum total displacements in unsupported top heading at 100% relaxation, by using E=3800 MPa.....	225
Figure 8.2: Comparison between initial and deformed fracture network (x20) at 100% relaxation of top heading in E=3800 MPa bedded sandstone.....	226
Figure 8.3: Convergence curves of pilot tunnel, using E=3800 MPa.....	226
Figure 8.4: Convergence curves of top heading roof, assuming E=3800 MPa. ....	227
Figure 8.5: Convergence curves at 2.0, 3.4 and 6.0 m above the crown of top heading stage, by using E=3800 MPa. ....	227
Figure 8.6: Total displacements for top heading excavation stage at 100% relaxation of locally refined jointed model assuming E=5000 MPa.....	229
Figure 8.7: Comparison of initial and deformed fracture network (x60) at 100% relaxation of top heading in E=5000 MPa closely bedded sandstone. ....	229

Figure 8.8: Convergence curves for top heading stage in locally refined jointed model. Point D located at the left of the crown exhibits more deformation in contrast to point H to the right, due to the effects of bedding induced anisotropy. This behavior is also recorded by onsite measurements from extensometers. ....	230
Figure 8.9: Convergence curves for top heading stage at three locations above the crown, for locally refined model.....	230
Figure 8.10: Total displacements for top heading excavation stage at 100% relaxation of locally refined jointed model, using $E_{block}=4300$ MPa. ....	232
Figure 8.11: Comparison of initial and deformed fracture network (x60) at 100% relaxation of top heading in closely bedded sandstone assuming $E_{block}=4300$ MPa. ....	232
Figure 8.12: Characteristic curves for the top heading excavation in rock mass of $E=4300$ MPa.....	233
Figure 8.13: Approximate characteristic curves at the locations of 2.0, 3.4 and 6.0 m above the tunnel crown. ....	233
Figure 8.14 : Characteristic curves for top heading excavation assuming $E_{block}=3000$ MPa.....	235
Figure 8.15: Results for pilot tunnel in 3000 MPa jointed model, a) Total displacements b) contours of vertical displacements, c) Contour plots of horizontal displacements. ....	237
Figure 8.16: Shaded contours of vertical displacements after ground-support equilibrium for jointed model assuming $E=3000$ MPa. ....	238
Figure 8.17: Predicted displacements along extensometer locations.....	238
Figure 8.18: Comparison between original and deformed block assemblage (x60) at the end of top heading excavation and support for jointed model assuming $E=3000$ MPa. ....	239
Figure 8.19: Distribution of axial forces on composite beam element and rock bolts axial forces (MN/m) for top heading. ....	239
Figure 8.20: Distribution of bending moments on composite beam element simulating the primary lining (MN.m/m). ....	240
Figure 8.21: Mobilized shear strength around the tunnel at the end of top heading excavation stage and support. ....	240
Figure 8.22: Shear displacements at the end of the top heading and support.....	241
Figure 8.23: Schematic representation of measurement location and components of pre-convergence due to already completed excavation activity from the pilot opening and the proximity of the top heading. ....	241
Figure 8.24: Total displacement vectors at the end of construction. ....	248
Figure 8.25: Shaded contours of vertical displacements at the end of construction. ....	248
Figure 8.26: Shaded contours of horizontal displacements at the end of construction... ..	249
Figure 8.27: Comparison between initial and deformed block geometry after completion of excavation and support. ....	249
Figure 8.28: Vertical displacements (m) of composite beam element at the end of construction.....	250
Figure 8.29: Horizontal displacements developed at the composite beam after bench excavation and support. ....	250
Figure 8.30: Axial loads in primary lining and rock bolts at the end of construction. ...	251

Figure 8.31: Moment distribution on primary lining and invert at the end of construction.	251
Figure 8.32: Deviator stresses around tunnel at the end of ground-support equilibrium.	252
Figure 8.33: Shaded contours of strength/stress ratio around tunnel after final support and equilibrium. Only local failure should be expected at the elephant foot level of the tunnel.	252

## LIST OF TABLES

Table 1.1: Tunnel projects in Japan (After Lotschberg, 2003; Sofianos, 2000)	6
Table 1.2: Design data of the Tomei I and Tomei II highways.	12
Table 3.1: Parametric ratings for the Q – rock mass quality index (Barton, 1974).	24
Table 3.2: Equivalent support ratio (ESR) values for the Q system.	25
Table 3.3: Representative values of compressive and transverse velocities for various rock types (After Dobrin,1976)	26
Table 3.4: Rock mass classification estimates by Barton et. al (1995)	29
Table 3.5: Logging results from the Western sector.	30
Table 3.6: Photo interpretation results for Western Sector.	30
Table 3.7: Photo interpretation results for Central Sector.	30
Table 3.8: Photo interpretation results for Eastern Sector.	31
Table 3.9: Overall rock mass classification per section.	31
Table 3.10 a,b: The Japan Highways rock mass classification system.	36
Table 3.11: Discontinuity orientation data for sandstone at the Shimizu tunnel No.3.	40
Table 3.12: Strength measurements in soft Shimizu site rocks.	43
Table 3.13: Measured strength parameters for Wadajima Sandstone (NGI).	48
Table 4.1: Construction timetable for Shimizu tunnel No.3.	66
Table 4.2: Tunnel boring machine data for the “Suruga No.1” triple shield.	67
Table 4.3: Support system utilized in Shimizu tunnel No.3.	70
Table 6.1: Example values for joint shear strength comparisons using the Barton-Bandis model (After Bandis, 1985)	103
Table 6.2 : Example of joint closure under normal loading JRC=5, JCS=100 MPa, $\sigma_c=150$ MPa.	104
Table 6.3: Example of joint closure under normal loading JRC=15, JCS=100 MPa, $\sigma_c=150$ MPa.	105
Table 6.4: Example of Barton-Bandis shear behavior model (case 1).	109
Table 6.5: Example for Barton-Bandis model (case 2).	111
Table 6.6: Results for pilot opening deformations with no support from different methods.	122
Table 6.7: Simplified elastoplastic analysis using a spreadsheet calculation for pilot tunnel, assuming $E=4000$ MPa. (After Kavvadas, 2001)	126



Table 6.8: Simplified elastic analysis assuming the same initial stresses generated by UDEC during model consolidation. The stresses after model consolidation may be yield to a slightly different $K_0$ ratio than the prescribed value. ....	126
Table 6.9: Tunnel deformations predicted by UDEC for top heading stage and by using an elastic modulus of $E=4000$ MPa. ....	129
Table 6.10: Tunnel deformations predicted by UDEC for bench excavation stage assuming an elastic modulus of $E=4000$ MPa. ....	133
Table 6.11: Tunnel deformations predicted by different methods for pilot stage and by using an elastic modulus of $E=12000$ MPa. ....	137
Table 6.12: Simplified elastoplastic analysis using a spreadsheet calculation for pilot tunnel, assuming $E=12000$ MPa. (After Kavvadas,2001) ....	140
Table 6.13: Simplified elastic analysis assuming the same initial stresses generated by UDEC during model consolidation and an elastic modulus of $E=12000$ MPa. ....	140
Table 6.14: Tunnel deformations predicted by UDEC for top heading stage and by using an elastic modulus of $E=12000$ MPa. ....	142
Table 6.15: Tunnel deformations predicted by UDEC for bench stage assuming an elastic modulus of $E=12000$ MPa. ....	143
Table 6.16: Cumulative results for unsupported tunnel using continuum models using	150
Table 6.17: Correlation table between RMR, Q and Japan Highways' rock mass classification systems. ....	154
Table 6.18: Estimated average elastic modulus using Hoek-Brown parameters. ....	155
Table 6.19: Results of continuum parametric analysis for different $K_0$ values and elastic moduli. ....	158
Table 6.20: Comparison of predicted deformations by UDEC for the unsupported pilot opening for two extreme values of $K_0$ , assuming $E=2000$ MPa. ....	159
Table 6.21: Comparison of predicted deformations by UDEC for the unsupported top heading stage for two extreme values of $K_0$ , assuming $E=2000$ MPa. ....	160
Table 6.22: Continuum analysis results for cases of $K_0=0.5$ and $K_0=1.2$ , assuming $E=5000$ MPa. ....	161
Table 6.23: Continuum analysis results for cases of $K_0=0.5$ and $K_0=1.2$ , assuming $E=5000$ MPa. ....	161
Table 6.24: Continuum analysis results for bench excavation stage, assuming $E=5000$ MPa. ....	162
Table 6.25: Mean values of joint strengths according to Barton and Gutierrez (1995)..	180
Table 6.26: Comparison of predicted deformations for pilot tunnel using UDEC and simple elastoplastic analyses. ....	185
Table 6.27: Calculation of rock bolt input parameters in UDEC (After Lorig, 1985). ..	199
Table 6.28: Comparison between predicted results for top heading using UDEC and measurement data. $E=5000$ MPa jointed model. ....	201
Table 7.1: Statistical processing of stochastically generated sandstone bedding spacing in UDEC. ....	208
Table 7.2: Parameter values used in UDEC to examine the influence of the Joint Roughness Coefficient ( $JRC_0$ ) on the convergence curves. ....	213
Table 7.3: Parameter values used in UDEC to examine the influence of the Joint Compressive Strength ( $JCS_0$ ) on the convergence curves. ....	216

Table 8.1: Comparison between UDEC and simplified elastoplastic analysis for pilot tunnel.....	225
Table 8.2 : Comparison table between results from convergence curves for $\lambda=0.5$ and from dynamic UDEC solution during excavation, at two time points.....	235
Table 8.3: Comparison table between results from convergence curves for $\lambda=0.65$ and from dynamic UDEC solution during excavation. ....	236
Table 8.4: Comparison between predicted results for top heading using UDEC and measurement data.....	247

## CHAPTER 1 : Introduction

### 1.1 Scope of work

Stability analysis of underground engineering works has been a challenging and difficult subject in geomechanics. From the early rock load theories by Terzaghi (1946) and Protodiakonov (1970) to the three dimensional numerical analysis methods available today there has always been an effort by engineers and researchers to investigate the behavior of excavations in ground either soft soils or rock masses under various conditions.

The last two decades great advancements were made in continuum based numerical approaches and their contribution has been exceptional in tunneling. Two of the limitations in using a two dimensional continuum element approach are the three dimensional effects observed during tunneling in any kind of ground type, and the fact that some ground types may not be correctly simulated by a continuous physical mass. The truth is that three dimensional effects do need to be considered in some logical way, while at the same time the ground itself could be a discontinuous rock mass, whose behavior can be influenced by the kinematic response of the assembling rock units. Research for the first issue was addressed by Panet (1986) and the convergence-confinement method, while the second was mainly addressed by the development of two numerical approaches, the Distinct Element Method (Cundall and Hart, 1988) and the Discontinuous Deformation Analysis (Shi, 1988). The convergence confinement method has proved so far to be a very good design tool when coupled with two dimensional continuum based numerical codes.

The present research focuses in the application of the Distinct Element method in the case of a sequentially excavated tunnel project in Japan. The scope of the research is twofold. Due to the statistical but natural variation of some parameters involving the shear strength of inherent discontinuities in a rock mass, a parametric study is performed to examine the sensitivity of the ground “characteristic curves” (Pacher, 1964) on these parameters. Since the application of a controlled relaxation analysis can be the only

means of addressing the important issue of support installation delays, the sensitivity of the “characteristic” curves on different parameters can aid the designer and user of the distinct element method to better understand the discontinuous model behavior and enhance engineering judgment.

The final part of the research examines the combined application of the convergence-confinement method along with the use of a two dimensional distinct element code and the validity is investigated by comparisons with measurements at the Shimizu Tunnel No.3 in Japan. The methodical application of the above principles in design of underground engineering works, proves to apply well even when a discontinuous rock mass is simulated. In order to apply these principles in back analysis it is paramount that an effective monitoring system has been applied and detailed data are recorded within the excavation. It also necessitates that a well planned geological investigation program has been performed with investigations mainly concentrated in rock mass characterization.

## 1.2 Historical background

It is a well known fact that in every society and at all times man has tried to improve his life, his surrounding and progress the civilization. In the modern world this attempt is highly reflected in the infrastructure works that take place everywhere. Perhaps this type of work is the one contributing most in the contact between people and whole countries in the means of commuting or financial and commerce interacting.

One of the most challenging fields in infrastructure works today is underground construction and especially tunneling applications. From the ancient times man has turned to deep earth when the first miners in Swaziland at 40000 BC tried to exploit the wealth of the underground (Sofianos, 2000). Since that time and before the Roman Era many civilizations have tried to excavate underground areas not only for mining purposes but also for water supply and public commuting. Ancient Greece, Egypt and Middle East were regions of such activities. During the Roman Era advancements were made and larger tunnels for mining, water ducts and transportation were excavated. As the time passed, the need for the use of underground space and the necessity of tunnels rapidly increased.

At the same time the technical skills of engineers of the time were continuously advancing. One of the pioneer works in tunneling during the nineteenth century was performed in 1820 by Marc Isambard Brunel, a French engineer who migrated initially to America. His first application of a primary iron made shield to excavate a 360 m tunnel under the river Thames in the London Clay, was considered a breakthrough despite the various failures and delays that had occurred. The tunnel was completed in 18 years (figure 1.1a, b, c). During the mid 1800s two significant achievements were made, the pneumatic assisted drilling rig and the circular shield, the last being ancestor of the modern shield machines. The compressed air drilling technology was patented by Jonathon Couch in Philadelphia. Later advancements on pneumatically assisted drilling were made by Germain Sommeiller (1857) who was the chief engineer for the first Alpine tunnel at Col de Frejus. The development of the shield was performed in Europe

by the British engineer J.H. Greathead (1880) who improved the technology of shield protected tunnel boring (figure 1.2)

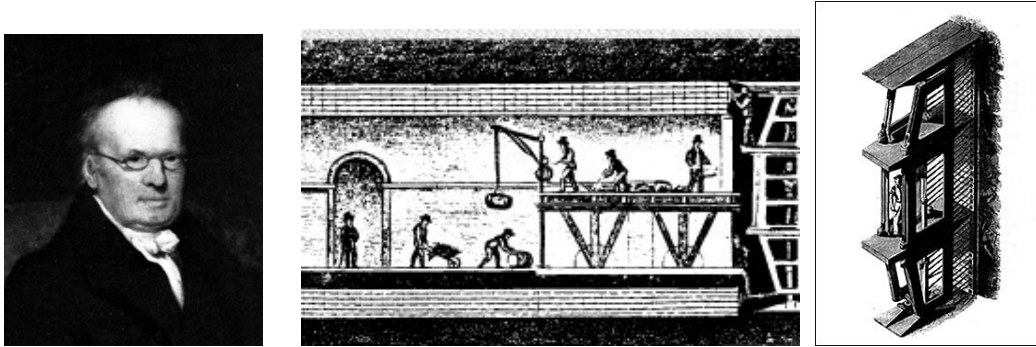


Figure 1.1: Marc I. Brunel (1820) and his pioneering iron tunneling shield (From Brunel Engine House, Rotherhithe, United Kingdom, 2003).

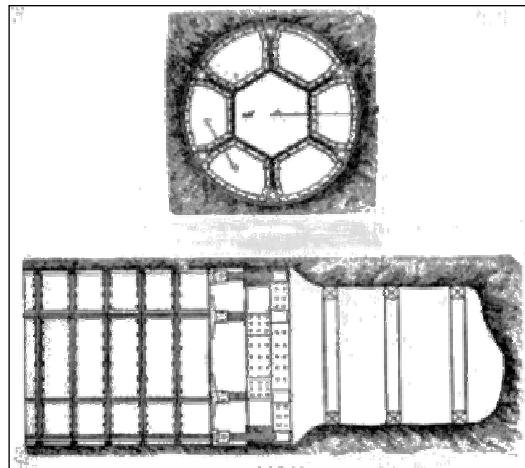


Figure 1.2: Greathead's shield (1880), that was used in the Tower Subway of London.

In the meantime in America, the Hoosac tunnel in Northwestern Massachusetts was considered as a benchmark tunneling project of the times. The tunnel was supposed to be 5.0 miles long and excavated through the Hoosac Mountain. The main challenge for this project was drilling through highly competent rock and simple mechanical excavation was practically impossible. According to White (1998), the contractor of the work at the time, Munn & Co. sought a new mechanized tunneling method. They adopted after some modifications, a machine design that can be considered as the ancestor of the modern tunnel boring machines. The machine was composed of wooden body parts, a

boiler to provide power and a rotating 24.0 ft front wheel that was equipped with cutting wheels. The machine was designed so that after a short advance it would stop, and miners would load the small boreholes with black powder. After the blasting round, the machine would restart the work. The machine was completed by a local mechanic J.Souther in Boston and references show that the machine was completed by March 1852. However, the first application of the Hoosac tunnel was unsuccessful and the machine did not respond well. Numerous mechanical difficulties were encountered and the project was abandoned for a few years. Later in 1856 the excavation of the Hoosac tunnel recommenced this time from a different portal, using sequential excavation and drill and blast techniques.

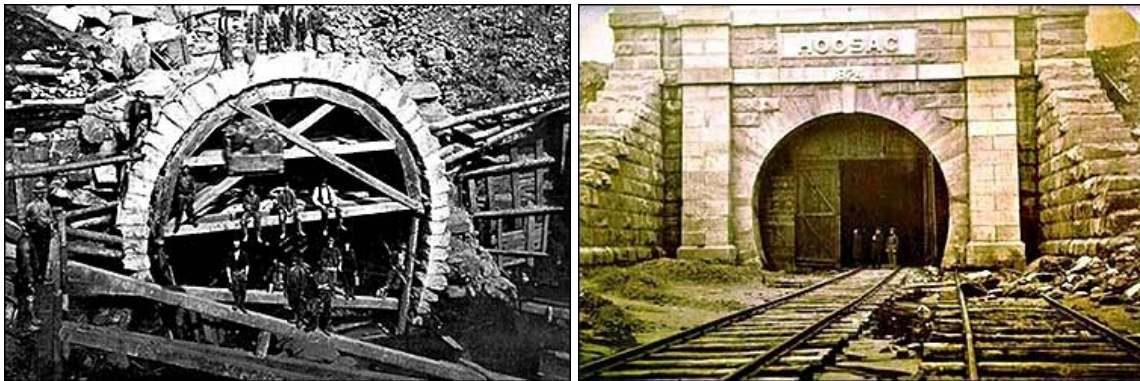


Figure 1.3 a, b: The Hoosac Tunnel in Boston, Massachusetts.

Since these times of pioneer engineering and under great difficulties the tunneling technology gradually forged into a great and challenging field of geotechnical engineering. The importance of these works in the infrastructure caused the acceleration of various methods, engineering trends and specialized equipment. Today tunneling involves more than ever principles of advanced geotechnical engineering and structural mechanics. Tunneling has caused to a great extent the development of modern geomechanics and underground design demands the knowledge of various parameters and factors that affect the behavior of the surrounding soil or rock mass. Even though initially tunneling was not founded on any sound theory and was considered more an art than science, nowadays advancements have been made both in mechanized and machine made tunneling and a great knowledge has been produced.

### 1.3 Tunneling in Japan

The present document is focused in Japan and will give an insight on modern Japanese Tunneling using sequential excavation approaches. Underground construction in Japan is a great challenge not only in urbanized areas but also in rural regions since soft ground generally predominates in Japan. Some of the tunnels that have been constructed in Japan are reproduced in Table (1.1)

Table 1.1: Tunnel projects in Japan (After Lotschberg, 2003; Sofianos, 2000)

Tunnel	Type	Year of Commencement	Length (km)	
Seikan	Railway	1988	53.850	subsea
Hakkoda	Railway	2009	26.455	Tohoku Shinkansen
Iwate	Railway		25.810	Tohoku Shinkansen Extension
Iwate	Railway	2002	25.810	
Iiyama	Railway	2008	22.500	Hokuriku Shinkansen
Daishimizu	Railway	1982	22.221	Joetsu Shinkansen (Shimizu No.2)
Shinkanmon	Railway	1975	18.713	Sanyo Shinkansen (subsea)
Rokkou	Railway	1972	16.220	Sanyo Shinkansen
Haruna	Railway	1982	15.350	Joetsu Shinkansen
Gorigamine	Railway	1997	15.175	Hokuriku Shinkansen
Nakayama	Railway	1982	14.857	Joetsu Shinkansen
Hokuriku	Railway	1962	13.870	Hokuriku Line
Shinshimizu	Railway	1967	13.500	Joetsu Line
Aki	Railway	1975	13.030	Sanyo Shinkansen
Kitakushu	Railway	1975	11.747	Sanyo Shinkansen
Kubiki	Railway	1970	11.200	
Kan Etsu	Road	1985 north	11.010	
Kan Etsu		1991 south	10.926	
Hida	Road	started 1997	10.700	Tokai-Hokuriku Expressway
Ikuta	Railway		10.314	
Shioyama			10.000	
Tagami		2000	7.000	Kyushu Shinkansen
Tagami			5.242	Kyushu Prefecture



Hakkoda Daini	Railway	started 2000	4.3	Honsu -Shinkansen
Shibisan	Railway		3.394	Kyushu Prefecture
Arimakita	Twin Road	2003	1.845	Hanshin Expressway Tomei- Meishin
Shizuoka Shimizu	Road	2003	1.18	Expressway Tomei- Meishin
No.3	Road	1999	1.12	Expressway

These are only few of the past and current tunneling activities in Japan. Construction is highly active in the Tokyo as well as in areas like Yokohama for the Metro system. According to Craig (2000), the activity of Japan in the underground excavation business is reflected by the investment trends. Statistics show that tunneling investment in Japan was doubled from 1985 to 1995. This twofold increase was followed by a decrease due to sustainable infrastructure restraints generated by the Japanese government which reduced construction budget by 10.7% for 2002. Since then a small increase was noted mainly due to the start of a new project. The New Tomei – Meishin Expressway attracted investment due to its importance in the foreseeable economic growth of the Southern Japan. Linking Tokyo with Kobe this high profile project substituted the onset of a new infrastructure challenge. Figure 1.4 from World Tunnelling (2002) shows investment trends for works by Japanese contracting companies in Japan and overseas from 1985 to 2001. Even though in most 4-5 year contracts the annual investment is not the same, starting usually from a 20–30%, a rough approximation is made by assuming an average construction time of 4 years. Craig (2002) estimates an annual figure of 8-10 billion USD. Ishihara (2002) gives data for 10,000 road and railway tunnels nowadays in Japan having a total length about 3,900 km. Taking into account other underground openings for utilities the figures rise to 11,000 km. The idea of self funded works or otherwise known as Private Financial Initiative is thought to be a promising idea for the expansion and continuity of large scale infrastructure works in Japan (Ishihara, 2002). Yet this private penetration into the public domain is not employed in Japan. It has been successfully applied and is still applied in the European Union where in fact the Union itself demands the provision of such funding.

With data available from JTA (2000) 50 % of the whole tunnel projects in Japan are excavated in mountainous regions while the rest are executed with other methods such as cut and cover, shield machines, etc.

One of the most important large scale projects in Japan is the Shinkansen high speed railway network. Started in 1959 with the construction of the Tokaido Shinkansen, the project caught national attention for its success while it traveled at a speed of 200 km/h. After that, gradual expansion of the network was accomplished and great tunneling works had to be made. Today the Shinkansen network is composed of three lines: The “Tokaido” Shinkansen linking Tokyo to Osaka, the “Sanyo” linking Kansai to Kyushu and the “Joetsu” serving the distance Tokyo-Niigata. Two new additions to the network were made with the development of the Tohoku and Nagato lines. According to the Japanese Railways the Shinkansen, otherwise known as the “Bullet Train” is the busiest intercity carrier internationally and serves more than a million people per day during peak seasons. Today their speed reaches 300 km/h and future plans are made for speeds in excess of 550 km/h. The development of this project along Japan necessitated the construction of many railway tunnels due to the needs for a straight alignment, in order to achieve high speeds safely. This becomes apparent in the data in Table 1.1.

It is seen that Japan has been highly active, despite economic shortcomings, in underground construction and gained worldwide respect for its innovative solutions. Additionally, the tunneling industry in Japan started looking with great attention the potential of tunnel boring machines to achieve economic, productive and safe tunneling. Today many Japanese firms have manufactured highly advanced Tunnel Boring Machines amongst which Kawasaki Heavy Industries, Hitachi and Mitsubishi, and exotic machines have been presented to the tunneling industry. Examples of these machines are shown in figure 1.6.

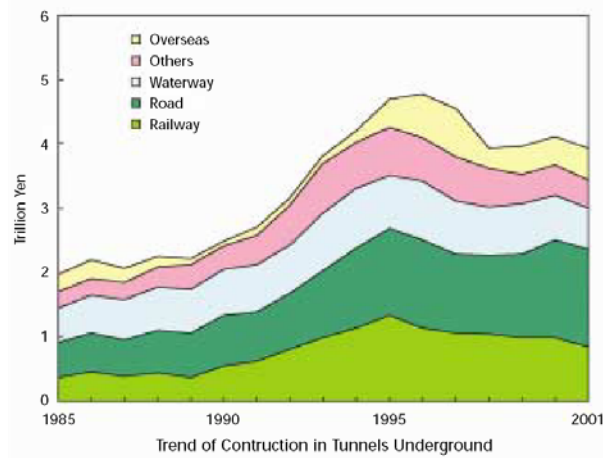


Figure 1.4: Investment trends in Japan since 1985. (From R.Craig, World Tunnelling Magazine).



Figure 1.5: The Shinkansen Railway network in Japan and view of the Tokaido Shinkansen (From Japan Railway Company.)

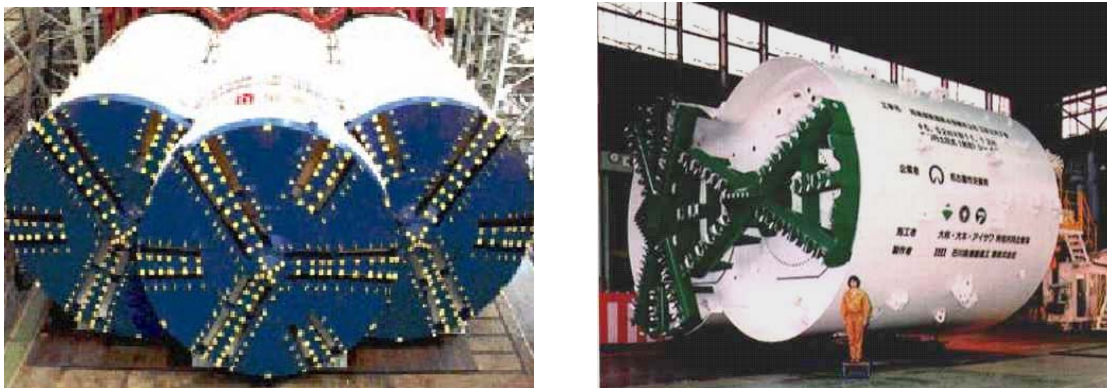


Figure 1.6: Modern Tunnel boring machine industry in Japan (From Japan Tunnelling Association).

## 1.4 The Tomei - Meishin Expressway

According to the Japan Tunnelling Association, the Tomei - Meishin Expressway is the largest future transportation infrastructure program planned for Japan. The whole expressway is 502 km long and links Tokyo with the city of Nagoya (328 km) and Nagoya to Kobe (174 km) (figure 1.8). The project is planned to be delivered for opening by 2009. The new expressway includes 167 tunnels that have a total length of 224 km. According to Craig (2000) tunnels substitute 25% of the new route in contrast to the existing Tomei Highway that includes only 2.6% of length in tunnels. The project is divided and controlled by four bureaus of the Japan Highways: The Tokyo construction bureau, the Shizuoka, the Chubu and the Kansai regional offices. The complete project is estimated to cost around 10 (ten) trillion Japanese Yen. The tunnel section is of an unusually large span having a height of about 12.0 m and a width of about 18.0 m. According to JTA this geometry was preferred in order to provide a safe but also psychologically comfortable travel through the tunnel, which is designed for speeds in the order of 140 km/h. The main difference of the New Tomei II highway is the provision for 3 lanes per carriageway each having a width of 3.75 m and a shoulder of 3.25 m. The existing Tomei Highway is a two lane road with a width of 3.6m per lane and a hard shoulder of 3.0 m (figures 1.7, 1.9). The design details are represented in Table 1.2.

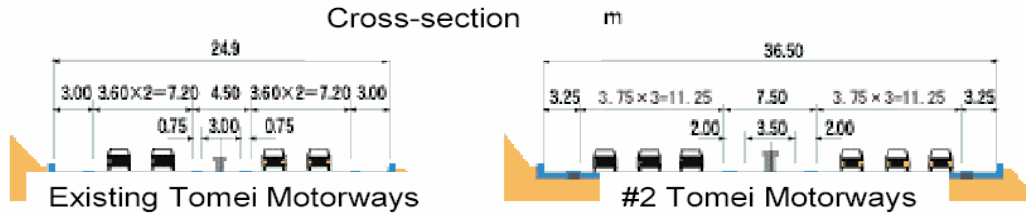


Figure 1.7: Comparison between the Tomei I and Tomei II highway sections (From Y.Ishihara, 2002).



Figure 1.8: The Old and New Tomei II expressways, linking Tokyo to Kobe (Y.Ishihara, 2002).

### Standard Cross Section

(mm)

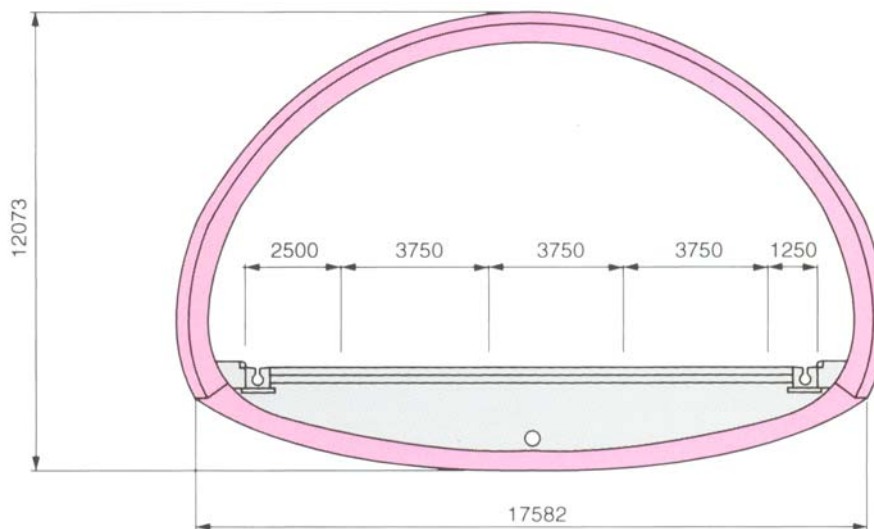


Figure 1.9: The Standard type of cross section used in Shimizu tunnel No.3. (From Japan Tunnelling Association, 1998).

Table 1.2: Design data of the Tomei I and Tomei II highways.

Carriageway Detail at grade and viaducts	Existing Tomei Highway	Tomei II Expressway
Number of lanes	2 carriageways with 2 lanes	2 carriageways with 3 lanes
Width of lanes	3.60 m	3.75 m
Hard Shoulder	3.00 m	3.25 m
Central Reserve	4.50 m	7.50 m
Marginal Strip	0.75 m	2.00 m
Total Width of two carriageways	24.90 m	36.50 m
Tunnels		
Total Width of carriageway	9.0 m	15.0 m
Inspection gallery (left side)	0.75 m	0.75 m
Inspection gallery (right side)	0.75 m	0.75 m
Total Width	11.5 m	18.0 m
Total Height of Excavation	9.5 m	12.4 m
Excavated Cross Section	80 m <sup>2</sup>	190 m <sup>2</sup>
Completed Tunnel Section	68 m <sup>2</sup>	170 m <sup>2</sup>

## CHAPTER 2 : The Shimizu tunnel No.3

### 2.1 Tunnel location

One of the most important tunnels for the New Tomei Expressway is the Shimizu tunnel No.3 located in the area of the city Shimizu in the Shizuoka Prefecture (figure 2.1). Shizuoka city is roughly only 1 hour away from Tokyo and 1 and 2 hours away from Nagoya and Osaka, respectively by the Shinkansen (Shizuoka Prefecture Commerce and Labor Planning Department, 1996). The city of Shimizu is the fourth largest in Shizuoka prefecture having a population of about 230,000 people and it is located 175 km Southwest of Tokyo. This tunnel was chosen by the owner of the Tomei II project, the Japan Highway Public Corporation (JHPC) as a research tunnel. Tunneling through the mountainous region would be made in an experimental way so that the behavior of the ground would be better understood and recorded. In addition different support systems would be employed and tested in terms of material performance and strength. The use of different support methods would help to standardize support systems along a large group of large section tunnels of the Tomei – Meishin Expressway and establish safe and adequate support solutions for different ground conditions. JHPC's goal was to execute close investigation and verification of the possible conditions that would be encountered during tunneling.

Tender documents for the project were prepared from the early 1995. The winning contractor for the project was a joint venture of companies Taisei, Obayashi and Mitsui. Two of the main concerns were the safe construction and retention of unusually large section tunnels and the need to achieve high advance rates. Uncertainties and field verification problems had to be dealt in a way that would satisfy efficiency but also adaptivity to various conditions.

For the relatively long tunnels in soft sedimentary rocks, a type of sequential excavation method was employed, known in Japan as the “TBM Pilot and Enlargement Excavation Method” in addition to the simpler sequential approaches with a top heading

and a bench stage or the side drift sequential designs using NATM. At the Shimizu tunnel No.3, TBM operation started from an offset position at 45 degrees of the western portal at chainage 911+73 and at 912+60 the TBM aligned to the main tunnel axis. The tunnel heading to Shizuoka from Tokyo had a length of 1114 m. At chainage 920+20 close to the eastern portal, the TBM started a U-turn of 30.0 m radius and was realigned to excavate the second tunnel of a 1119 m length.





Figure 2.1: Map of Southeast Japan and location of Shimizu city (2003).

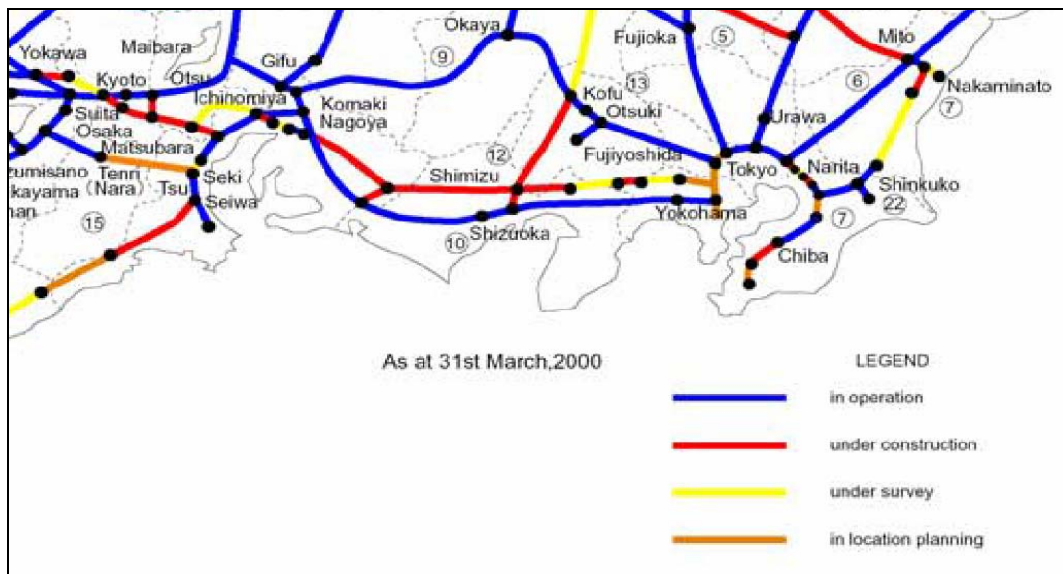


Figure 2.2: Present status of highway infrastructure development between Tokyo and Kyoto (From JHPC, 2002).

## CHAPTER 3 : Geotechnical data

### 3.1 Field Investigations

Geotechnical data are based on investigations performed by the Norwegian Geotechnical Institute (Barton & Gutierrez, 1995) including inspection of drill cores, field logging and mapping as well as index testing of selected sampling. In accordance to the technical report dated 29 August 1995 and submitted by the Norwegian Geotechnical Institute to the Fuji Research Corporation, the ground through which the tunnel would be bored is composed of soft sedimentary rock formations. Geological investigations showed the existence of five rock formations. The main rock formation is the weathered soft Tertiary “Wadajima” Sandstone of the late Miocene and Pliocene, which was recognized as member of the “Hamaishidake” Geological Group. This formation designated as Wss, was found to vary in quality along the tunnel direction based on downhole seismic measurements (compressive wave velocity  $V_p$ ) as well as extensive borehole logging. The Wss formation compose most of the ground through which the tunnel would be excavated. It is underlain by interbedded Mudstone –Sandstone designated as  $W_{alt1}$  and  $W_{alt2}$ . Mainly in the eastern sector highly weathered, nearly soil like materials are present, and they are designated as  $W_1$  and  $W_2$ . The geological data are shown in longitudinal and transverse sections in figures 3.1-3.4.

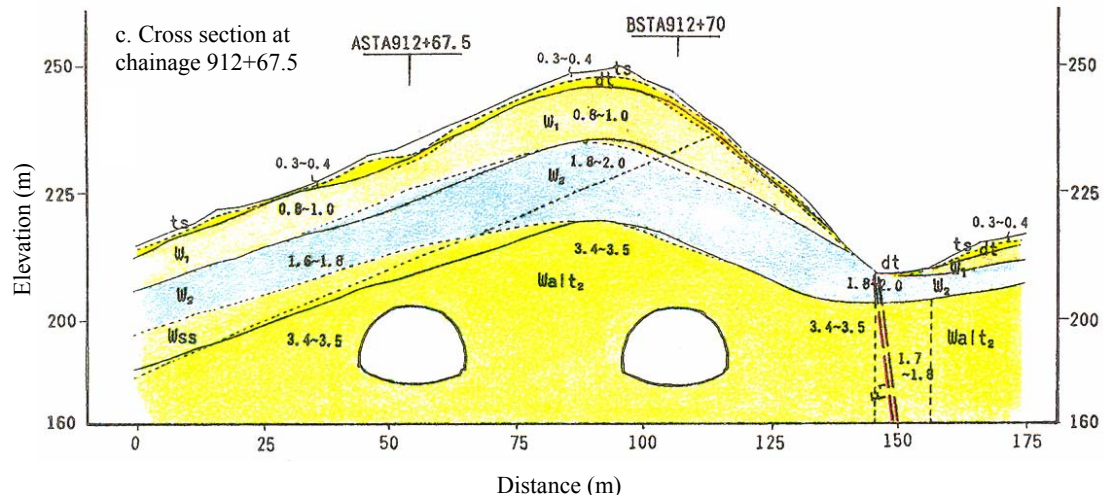
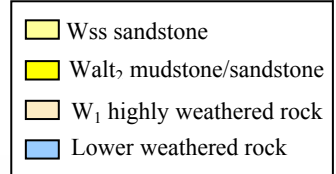
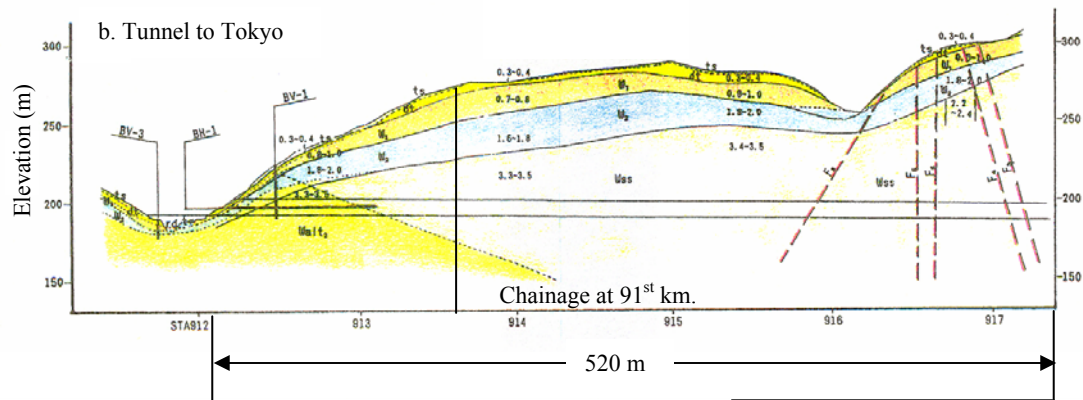
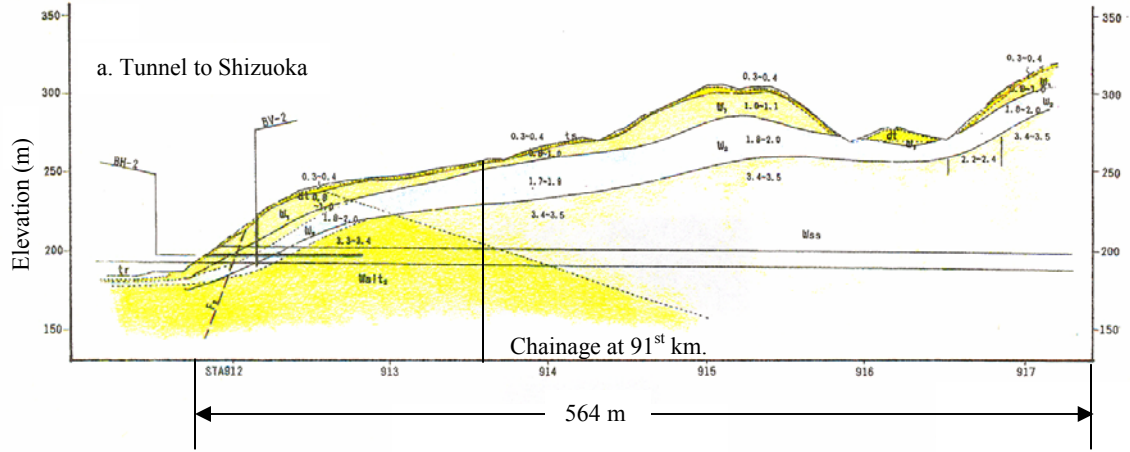


Figure 3.1: a and b: Longitudinal geologic cross sections of West Sector and  $V_p$  velocity measurements, c: cross section at 912+67.5 (From Japan Highways, 1995).

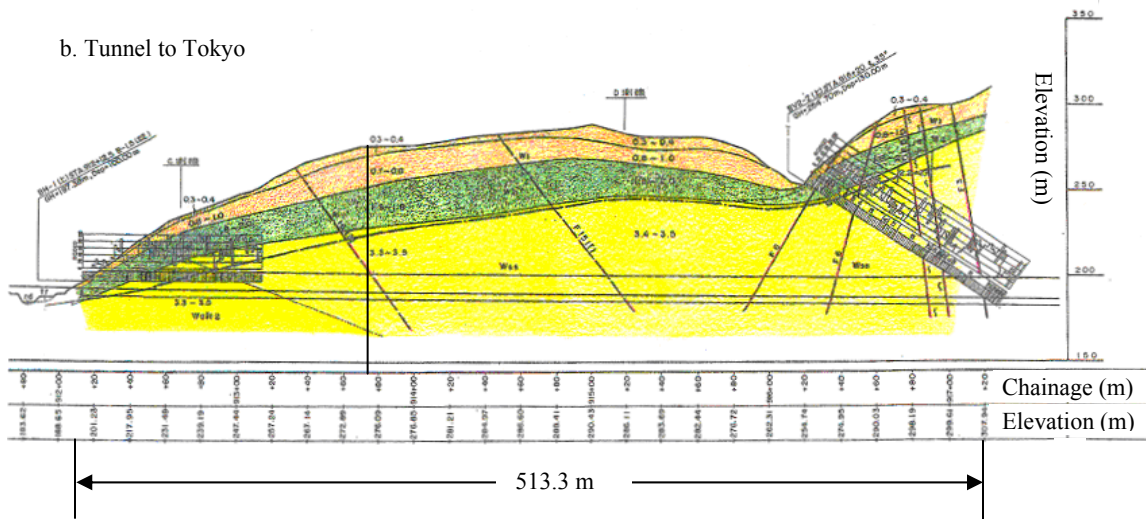
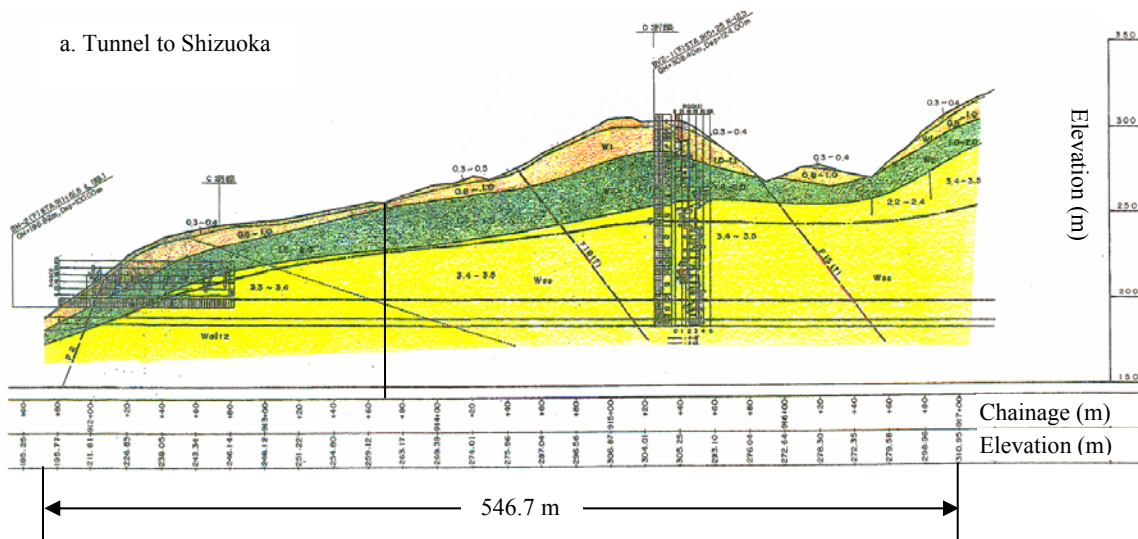


Figure 3.2: West and Central sector borehole locations. Top: BH-2, BV2-1- Bottom: BH-1, BV2-2 (From Japan Highways, 1995).



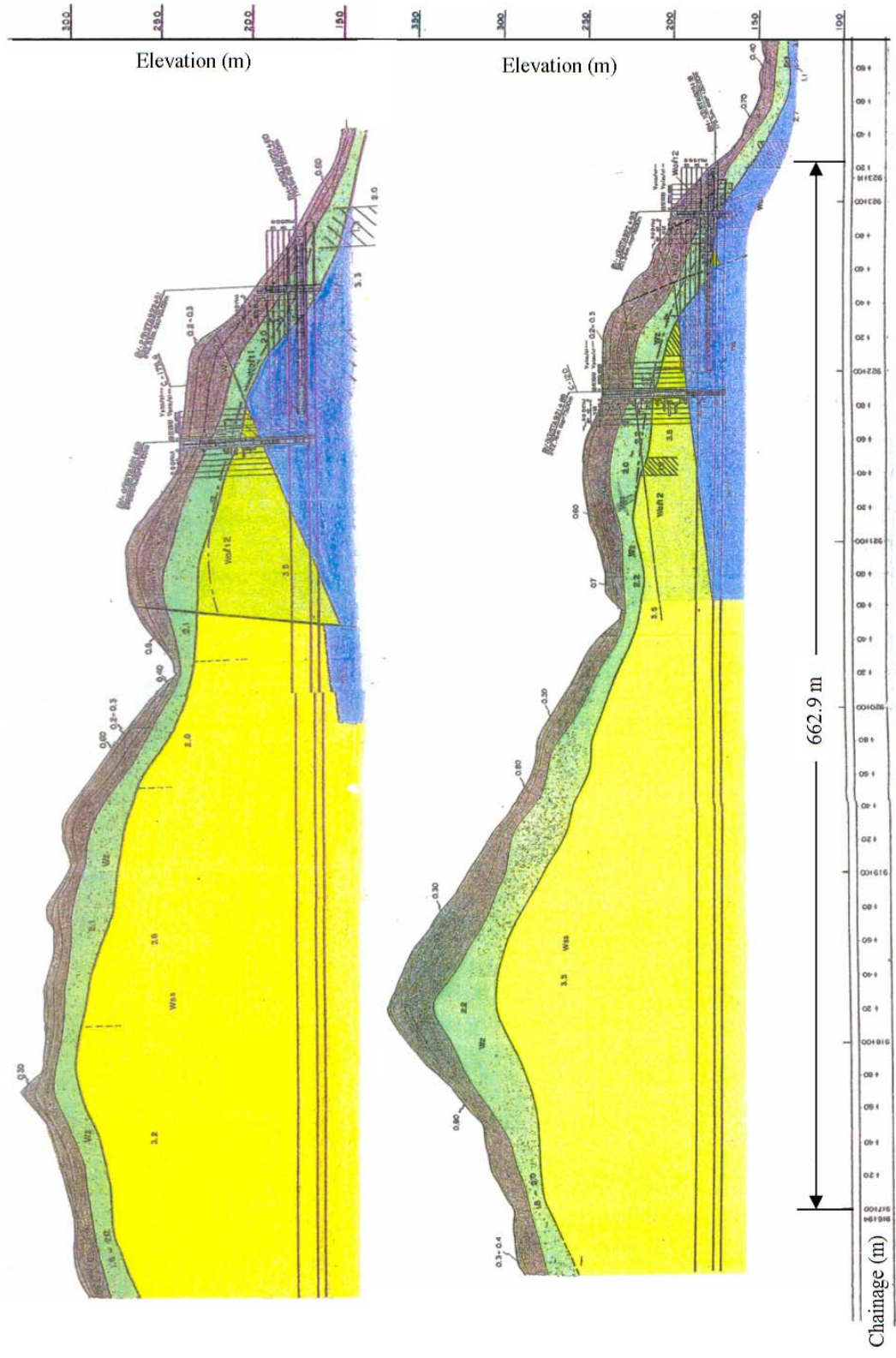


Figure 3.4: Geological cross sections of central and east sectors, top section: location of BV-4, BV-2, BH-2 (east), bottom: location of BV-3, BV-1, BH-1 (east) (From Japan Highways. 1995).

## 3.2 Rock mass classification

### 3.2.1 General

Rock masses are rarely continuous or isotropic in properties. In most cases, the existence of various inherent imperfections such as joints, beddings and weathering require attention from the tunnel designers and engineers. In deep underground projects in rock masses, a dedicated sampling and mapping program should be followed in order to record and evaluate joint orientation and other spatial or geological data. Several rock mass classification systems have been presented so far in the area of geomechanics: Rock Load classification (Terzaghi, 1946), Stand up time (Lauffer, 1958), NATM (Rabcewicz-Pacher, 1964; John, 1974), the RQD (Deere et. al, 1967) , Franklin, 1971, RMR (Bieniawski, 1974), Q tunneling index (Barton, 1974), GSI (Hoek, 1995; Hoek & Marinos, 2000), RMi (Palmstrøm, 1995). The most frequently applied systems nowadays are the RMR and Q index classifications. A detailed Q index rock mass characterization is given by Barton & Gutierrez (1995) for the Shimizu tunnel No.3 based on field observations, logging and geophysical data interpretation. In addition to these systems it is also important to acknowledge that other rock mass classification systems have been developed by various Japanese authorities that control infrastructure projects in Japan. One of these systems is the Japan Highway Public Corporation's Rock Mass Classification. Basic principles behind this classification scheme will be given in subsequent paragraphs.

### 3.2.2 Q rock mass classification system

Classification using the Q system is based on core logging but also field mapping results that are quantified and represented statistically. Initially introduced in 1974, the Q system received gradual refinements and verifications, the last being in 1994. According to the Q system the rock mass quality is designated by the index Q which is a function of the form:

$$Q = \frac{RQD}{J_n} \cdot \frac{J_r}{J_a} \cdot \frac{J_w}{SRF} \quad \text{Equation 3.1}$$

Q index varies from 0.001 for exceptionally poor rock masses to 1000 for exceptionally good qualities. The parameters involved in the Q system are given as follows:

<p>RQD = rock quality designation</p> <p><math>J_n</math> = number of joint sets includes 9 possible values 0.5 – 20 <math>J_n</math> is inversely proportional to the joint frequency.</p>	}	$\frac{RQD}{J_n}$ is a measure of block size
<p><math>J_r</math> = joint roughness number has 7 possible values 0.5 – 4</p> <p><math>J_a</math> = joint alteration number 15 values which range from 0.75 – 20</p>	}	$\frac{J_r}{J_a}$ is a measure of interblock shear strength
<p><math>J_w</math> = joint water seepage or pressure has 6 values which range from 0.05 – 1.0</p> <p>SRF = stress reduction factor to account for specific stress conditions ranges from 0.5 – 20</p>	}	$\frac{J_w}{SRF}$ is a measure of the active stresses

Details for the quantification of the above parameters are given in Table 3.1. The second step in the application of the Q index system is the quantitative estimation of a type of support to be used depending on the ground conditions. Figure 3.5 presents the latest development by Barton (1994) for a correlation between Q index and suggested support system. On the horizontal axis the Q rating is given in logarithmic scale. On the left vertical axis a ratio expressing the geometry of the excavation is included. This ratio is:

$$\frac{\text{Span or height of excavation}(m)}{ESR} \quad \text{Equation 3.2}$$



ESR is the Excavation Support Ratio which according to Barton and Grimstad can be regarded as a means to provide and include a desired margin of safety in the support estimates and depends on the type and importance of the structure. For most civil engineering works ESR is usually 1.0 while values of less than one may lead to conservative designs and high costs.

With respect to the Q system it is interesting that Loset (1992) also notes that for tunnels where  $4 < Q < 30$  (poor to medium good conditions) and where blasting methods are used, then damage will result to the surrounding rock mass which unavoidably will lower the Q rating. Specifically for tunnels in rock excavated with an initial pilot TBM opening and with subsequent enlargement, Loset (1992) suggests that Q index estimates from the pilot are recorded by an added increment of Q in the range 3-30 in relation to a drill and blast bored tunnel. Loset (1992) also reports that for the case of a Norwegian tunnel, changes in the estimates of support requirements based on these two methods can be in the order of 64% to 77%. Barton and Grimstad (1993) also complement the Q rating with an empirical correlation to past cases, as a tool to estimate the pressure acting upon the opening:

$$P_{roof} = \frac{2\sqrt{J_n} \cdot Q^{-1/3}}{3J_r}, \quad (MPa) \quad \text{Equation 3.3}$$

With respect to the above relation, Barton (1993) notes that the pressure is independent of the tunnel size and is only related to the type of the rock mass.

Table 3.1: Parametric ratings for the Q – rock mass quality index (Barton, 1974).

1. Rock Quality Designation		RQD	
A	Very poor	0 - 25	
B	Poor	25 - 50	
C	Fair	50 - 75	
D	Good	75 - 90	
E	Excellent	90 - 100	
Note: i) Where RQD is reported or measured as $\leq 10$ (including 0), a nominal value of 10 is used to evaluate Q. ii) RQD intervals of 5, i.e., 100, 95, 90, etc., are sufficiently accurate.			

2. Joint Set Number		$J_n$	
A	Massive, no or few joints	0.5 - 1.0	
B	One joint set	2	
C	One joint set plus random joints	3	
D	Two joint sets	4	
E	Two joint sets plus random joints	6	
F	Three joint sets	9	
G	Three joint sets plus random joints	12	
H	Four or more joint sets, random, heavily jointed, "sugar cube", etc.	15	
J	Crushed rock, earthlike	20	
Note: i) For intersections, use $(3.0 \times J_n)$ ii) For portals, use $2.0 \times J_n$			

3. Joint Roughness Number		$J_r$	
<b>a) Rock-wall contact, and b) rock-wall contact before 10 cm shear</b>			
A	Discontinuous joints	4	
B	Rough or irregular, undulating	3	
C	Smooth, undulating	2	
D	Slickensided, undulating	1.5	
E	Rough or irregular, planar	1.5	
F	Smooth, planar	1.0	
G	Slickensided, planar	0.5	
Note: i) Descriptions refer to small scale features and intermediate scale features, in that order.			
<b>c) No rock-wall contact when sheared</b>			
H	Zone containing clay minerals thick enough to prevent rock-wall contact	1.0	
J	Sandy, gravelly or crushed zone thick enough to prevent rock-wall contact	1.0	
Note: i) Add 1.0 if the mean spacing of the relevant joint set is greater than 3m. ii) $J_r = 0.5$ can be used for planar slickensided joints having lineations, provided the lineations are oriented for minimum strength.			

4. Joint Alteration Number		$\Phi_r$ approx.		$J_a$	
<b>a) Rock-wall contact (no mineral fillings, only coatings)</b>					
A	Tightly healed, hard, non-softening, impermeable filling, i.e., quartz or epidote			0.75	
B	Unaltered joint walls, surface staining only	25-35°		1.0	
C	Slightly altered joint walls. Non-softening mineral coatings, sandy particles, clay-free disintegrated rock, etc.	25-30°		2.0	
D	Silty- or sandy-clay coatings, small clay fraction (non-softening)	20-25°		3.0	
E	Softening or low friction clay mineral coatings, i.e., kaolinite or mica. Also chlorite, talc, gypsum, graphite, etc., and small quantities of swelling clays.	8-16°		4.0	
<b>b) Rock-wall contact before 10 cm shear (thin mineral fillings)</b>					
F	Sandy particles, clay-free disintegrated rock, etc.	25-30°		4.0	
G	Strongly over-consolidated non-softening clay mineral fillings (continuous, but < 5mm thickness)	16-24°		6.0	
H	Medium or low over-consolidation, softening, clay mineral fillings (continuous, but < 5mm thickness)	12-16°		8.0	
J	Swelling-clay fillings, i.e., montmorillonite (continuous, but < 5mm thickness). Value of $J_a$ depends on percent of swelling clay-size particles, and access to water, etc.	6-12°		8-12	
<b>c) No rock-wall contact when sheared (thick mineral fillings)</b>					
KLM	Zones or bands of disintegrated or crushed rock and clay (see G, H, J for description of clay condition)	6-24°		6, 8, or 8-12	
N	Zones or bands of silty- or sandy-clay, small clay fraction (non-softening)	-		5.0	
OPR	Thick, continuous zones or bands of clay (see G, H, J for description of clay condition)	6-24°		10, 13, or 13-20	

5. Joint Water Reduction Factor		approx water pres. (kg/cm <sup>2</sup> )		$J_w$	
A	Dry excavations or minor inflow, i.e., < 5 l/min locally	< 1		1.0	
B	Medium inflow or pressure, occasional outwash of joint fillings	1-2.5		0.66	
C	Large inflow or high pressure in competent rock with unfilled joints	2.5-10		0.5	
D	Large inflow or high pressure, considerable outwash of joint fillings	2.5-10		0.33	
E	Exceptionally high inflow or water pressure at blasting, decaying with time	> 10		0.2-0.1	
F	Exceptionally high inflow or water pressure continuing without noticeable decay	> 10		0.1-0.05	
Note: i) Factors C to F are crude estimates. Increase $J_w$ if drainage measures are installed. ii) Special problems caused by ice formation are not considered.					

6. Stress Reduction Factor		SRF			
<b>a) Weakness zones intersecting excavation, which may cause loosening of rock mass when tunnel is excavated</b>					
A	Multiple occurrences of weakness zones containing clay or chemically disintegrated rock, very loose surrounding rock (any depth)	10			
B	Single weakness zones containing clay or chemically disintegrated rock (depth of excavation $\leq 50m$ )	5			
C	Single weakness zones containing clay or chemically disintegrated rock (depth of excavation > 50m)	2.5			
D	Multiple shear zones in competent rock (clay-free), loose surrounding rock (any depth)	7.5			
E	Single shear zones in competent rock (clay-free) (depth of excavation $\leq 50m$ )	5.0			
F	Single shear zones in competent rock (clay-free) (depth of excavation > 50m)	2.5			
G	Loose, open joints, heavily jointed or "sugar cube", etc. (any depth)	5.0			
Note: i) Reduce these values of SRF by 25-50% if the relevant shear zones only influence but do not intersect the excavation.					
<b>b) Competent rock, rock stress problems</b>					
H	Low stress, near surface, open joints	$\sigma_c / \sigma_1$	$\sigma_2 / \sigma_3$	SRF	
J	Medium stress, favourable stress condition	> 200	< 0.01	2.5	
K	High stress, favourable to stability, may be unfavourable for wall stability.	200-10	0.01-0.3	1	
L	Moderate slabbing after > 1 hour in massive rock	10-5	0.3-0.4	0.5-2	
M	Slabbing and rock burst after a few minutes in massive rock	5-3	0.5-0.65	5-50	
N	Heavy rock burst (strain-burst) and immediate dynamic deformations in massive rock	3-2	0.65-1	50-200	
Note: ii) For strongly anisotropic virgin stress field (if measured): when $5 \leq \sigma_1 / \sigma_3 \leq 10$ , reduce $\sigma_c$ to $0.75\sigma_c$ . When $\sigma_1 / \sigma_3 > 10$ , reduce $\sigma_c$ to $0.5\sigma_c$ , where $\sigma_c$ = unconfined compression strength, $\sigma_1$ and $\sigma_3$ are the major and minor principal stresses, and $\sigma_\theta$ = maximum tangential stress (estimated from elastic theory). iii) Few case records available where depth of crown below surface is less than span width. Suggest SRF increase from 2.5 to 5 for such cases (see H).					
<b>c) Squeezing rock: plastic flow of incompetent rock under the influence of high rock pressure</b>					
O	Mild squeezing rock pressure	$\sigma_\theta / \sigma_c$	SRF		
P	Heavy squeezing rock pressure	1-5	5-10		
Note: iv) Cases of squeezing rock may occur for depth $H > 350 Q^{1/3}$ (Singh et al., 1992). Rock mass compression strength can be estimated from $q = 0.7 \gamma Q^{1/3}$ (MPa) where $\gamma$ = rock density in $kN/m^3$ (Singh, 1993).					
<b>d) Swelling rock: chemical swelling activity depending on presence of water</b>					
R	Mild swelling rock pressure	5-10			
S	Heavy swelling rock pressure	10-15			

Note: $J_r$ and $J_a$ classification is applied to the joint set or discontinuity that is least favourable for stability both from the point of view of orientation and shear resistance, $\tau$ (where $\tau = \sigma_n \tan^1(J_r / J_a)$ ). Choose the most likely feature to allow failure to initiate.					
$Q = \frac{RQD}{J_n} \times \frac{J_r}{J_a} \times \frac{J_w}{SRF}$					

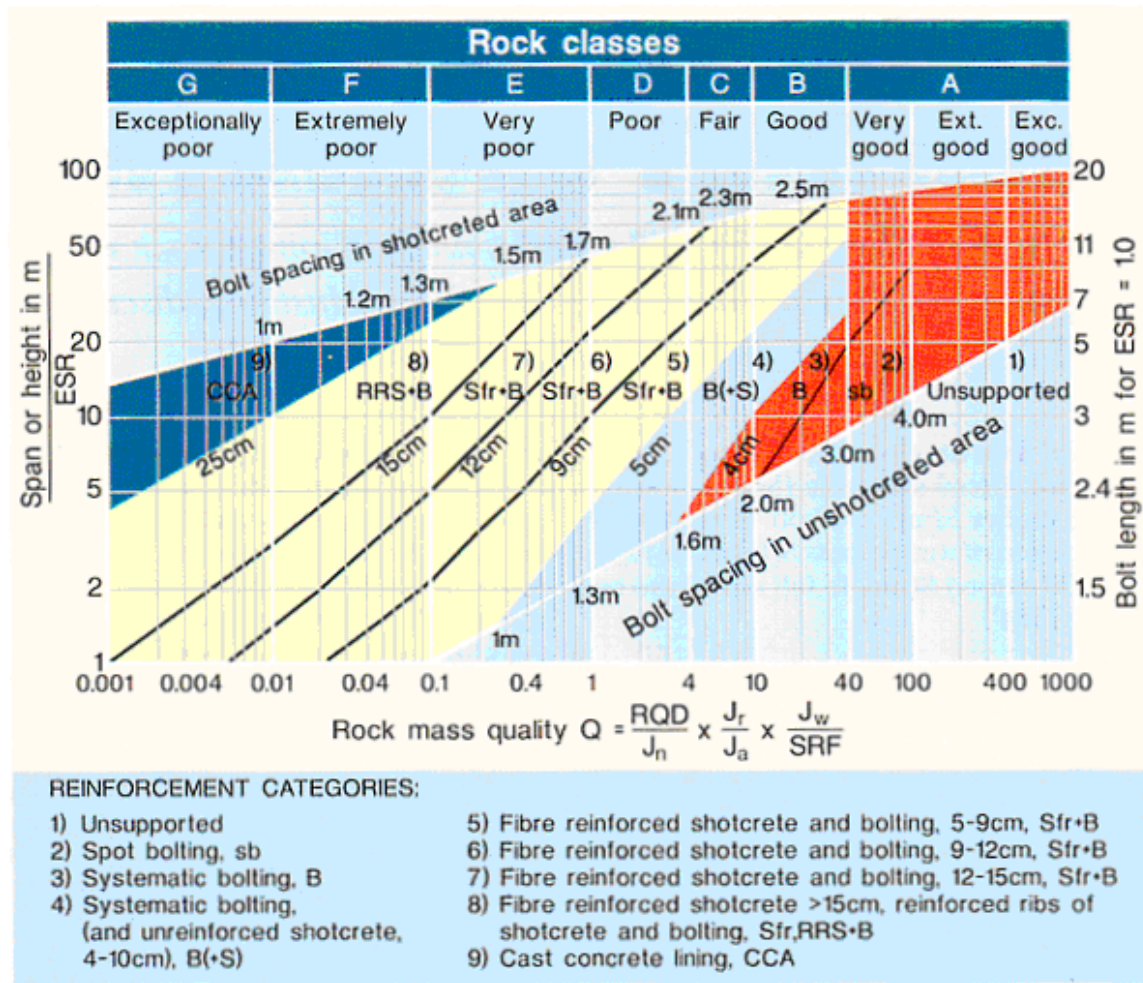


Figure 3.5: The Q index support estimates.

Table 3.2: Equivalent support ratio (ESR) values for the Q system.

	Type of Excavation	ESR
A	Temporary mine openings	2-5
B	Permanent mine openings, water tunnels for hydropower (exclude high pressure penstocks), pilot tunnels, drifts and headings for large openings, surge chambers	1.6-2.0
C	Storage Caverns, water treatment plants, minor road and railway tunnels, access tunnel	1.2-1.3
D	Power stations, major road and railway tunnels, civil defense chambers, portals, intersections	0.9-1.1
E	Underground nuclear power stations, railway stations, sports and public facilities, factories, major pipeline tunnels.	0.5-0.8

### 3.2.2.a Q system classification from seismic surveys at Shimizu tunnel No.3

Before a more detailed description of the results from the geophysical investigation, it is appropriate to point out some principles behind the seismic surveying methods and interpretation of results.

In mechanical wave propagation there are two distinct kinds of waves, waves that propagate through the mass of a medium and thus are called bulk or body waves and waveforms that progress on a physical discontinuity separating media. In the mass of a medium such as rock masses there can be developed waves that cause oscillation of material particles in the direction of wave propagation which are the longitudinal or Primary waves and waves causing particle movement perpendicular to the direction of the propagation and are called transverse or Secondary waves, with a lower transmission velocity (practically 50%) of the compressive velocity  $V_p$ . These two phenomena have been found to be associated and correlated with mechanical properties of the host mass such as the elastic modulus  $E$ . The following Table 3.3 proposed by Dobrin (1976) includes typical values of compressive and shear wave velocity ranges for different rock masses, that may be used as a typical comparison with measured velocities from the Shimizu tunnel No.3.

Table 3.3: Representative values of compressive and transverse velocities for various rock types (After Dobrin,1976).

Rock Type	Compressive $V_p$ (m/s)	Transverse $V_s$ (m/s)
Granite	5000 - 6000	2500 - 3300
Granodiorite	4780	3100
Diorite	5780	3060
Gabbro	6450	3420
Basalt	5400 - 6400	2700 - 3500
Dunite	6800 - 8640	3500 - 4400
Gneiss	3500 - 7500	-
Marble	3700 - 7000	-
Sandstone	1400 - 4300	-
Limestone	5900 - 6100	2800 - 3100
Anhydrite	4100	-
Shale	2100 - 3400	-

In the past years the field application of geophysical methods and equipment, including cross hole, down hole, seismic refraction and reflection measurements and the advancement in result processing methods that yield in tomography representations, has proved to be a promising and good tool in geotechnical assessments. Seismic refraction technology has become a popular method aiding in the geotechnical exploration of mostly hard media as rock masses. It is based on the principle of measuring the time that a refracted waveform takes to arrive at a sensor location after it has been artificially generated at a “shot” location by a sort of impact mechanism. A series of sensors installed at various distances from the source will detect the incoming wave signal. Usually closer sensors detect first arriving waves from nearby subsurface spatial geologic anomalies. Further located sensors detect refracted waves that travel through different subsurface layers. Usually the arrangement of this method uses surface installed equipment (wave source and detectors - recorders) while in cross hole measurements the generation of the wave and the detecting from sensors takes place in parallel boreholes. In the later case the aim is the measurement of the P or S wave velocity of the rock mass by recorded data. Both of these velocities (primarily the P wave velocity) can be used in rock mass quality assessments.

In Japan the use of down hole sonic measurements is widely popular and seismic data are included as primary parameters in Japanese classification systems. Advancements and worldwide application of such methods have made feasible the development of correlations between the P wave velocity and the Q index (Barton et al., 1994). Barton has presented the following correlation between these two magnitudes for non porous rock formations:

$$V_p = 1000 \cdot \log Q + 3500 \text{ (m/sec)} \quad \text{Equation 3.4}$$

Useful correlations between  $V_p$  and other rock quality parameters (RQD, discontinuity frequency) have also been presented (Sjorgen et al., 1979). Figures 3.1 and 3.2 present longitudinal and transverse sections of the Western sector where horizontal boreholes BH-1 (to Tokyo) and BH-2 (to Nagoya) were performed. Geological sections of figure

3.2 present the vertical boring BV2-1 and the inclined by  $35^{\circ}$  borehole BV2-2, of the central sector.

According to NGI (1995), downhole seismic measurements in BV2-1 give  $V_p=3.4-3.5$  km/sec for the Wss sandstone. From figure 3.2 which shows the west sector, it is apparent that the tunnel overburden ground is locally maximum at about 90 m. Barton et al. (1995) notes the existence of a fault zone east of the tunnels that expands sub-parallel to the tunnel headings which might implicate the stability of the tunnels.

Towards the central section where the overburden increases to more than 180.0 m the rock quality of the rock mass is expected to be of better quality and tunneling thru that region should be probably easier. The maximum overburden of the Shimizu tunnel No.3 occurs at the chainage of 918+20 m approximately and the overburden is about 190 m thick. Geophysical measurements reveal for the weathered sandstone (Wss)  $V_p= 3.4-3.5$  km/sec while locally velocities at as low as 2.8 km/sec have been recorded.

The Eastern Sector of the tunnel is of very poor quality rock masses  $W_1$  and  $W_2$  while mudstone formations  $W_{alt1}$  and  $W_{alt2}$  are somewhat better. In the regions of low overburden, especially less than 30.0 m the quality of the ground is vastly decreased. Geophysical measurements showed that:

$W_1$  unit  $V_p=1.3 -1.4$  km/sec

$W_2$  unit  $V_p=1.8-2.2$  km/sec

According to NGI (1995) the Wss sandstone unit would compose a 80-85% of the bored rock mass. It includes moderate to wide spacing of bedding planes. The same intensity stands for the mudstone. Local sandstone discontinuities had clay coatings or infilling and reduced expected shear strength. For areas of pronounced faulting action, disturbance of the rock unit Wss caused reduction in the wave velocities to 1.7-1.8 km/sec.

### 3.2.2.b Q system classification from core logging at Shimizu tunnel No.3

In their geological investigation Barton and Gutierrez (1995) performed core logging for a total of four selected drill cores from the Shimizu site. The core samples were obtained from the central sector borings, BV2-1, BV2-2, and the western sector BH1 and BH2 horizontal borings. The aim of the logging was to determine Q index parameters as well as discontinuity shear strength parameters. Analysis showed that for the vertical boring BV2-1 in the central sector, Q varies from 0.3-18 with a weighted mean value of  $Q_{BV2-1}=2.6$ . Sampling from the inclined borehole BV2-2 yielded a range of  $Q=0.04-2$  and a mean value  $Q_{BV2-2}=0.5$  due to the intersection with several faults. Combination of the results provides a weighted mean  $Q=0.8$  and a typical range of 0.04-3.0 for the investigated length of the tunnel.

Barton et al. (1995) gives the following information from the combined borehole data for the Shimizu tunnel No.3:

Table 3.4: Rock mass classification estimates by Barton et. al (1995).

Parameter	Value	Description
RQD	57.2	Fair quality (Deer et al.)
$J_n$	9.8	Three joint sets or more
$J_r$	1.4	Rough, planar or slickensided, undulating joints.
$J_a$	2.9	Silty, sandy clayey coatings
$J_w$	0.61	Medium water inflow
SRF	2.3	Minor stress effects

$$Q_{mean} = \frac{57.2}{9.8} \cdot \frac{1.4}{2.9} \cdot \frac{0.61}{2.3} = 0.78$$

Logging results from the western portal borings are included cumulatively in the following Table 3.5 along with previous Q indexes.

From core logging (Walt<sub>2</sub>)  $Q_{core} = \frac{74.8}{8.9} \cdot \frac{1.5}{3.0} \cdot \frac{0.62}{1.3} = 2.0$

From field logging (Walt<sub>2</sub>)  $Q_{field} = \frac{48.5}{10.6} \cdot \frac{1.9}{2.2} \cdot \frac{0.58}{1.0} = 2.3$

Table 3.5: Logging results from the Western sector.

Logged Depth (m)	Borehole	Rock unit	Q mean	Q typical range
70-125	BV2-1	Wss	2.6	0.3-1.8
50-130	BV2-2	Wss	0.5	0.04-2
	Combined		0.8	0.04-3
50-100	BH-1	Walt <sub>2</sub>	2.0	0.2-4.4
75-100	BH-2	Walt <sub>2</sub> -Wss		
W portal and BV2-2 site		Walt <sub>1+2</sub>	2.3	0.2-13

Extensive core photo analysis was also conducted by NGI and interpretation in terms of Q index was performed. Tables 3.6, 3.7 and 3.8 give the results of the analysis.

Table 3.6: Photo interpretation results for Western Sector.

Rock Unit	Length logged (m)	Number of boreholes	Q (mean)	Q (typ.range)
W <sub>1</sub>	75	4	0.07	0.008-1.4
W <sub>2</sub>	40	4	1.3	0.3-2.6
Walt <sub>2</sub>	141	3	4.0	0.8-33
Wss	10	1	3.9	1.7-11

Table 3.7: Photo interpretation results for Central Sector.

Rock Unit	Length logged (m)	Number of boreholes	Q (mean)	Q (typ.range)
W <sub>1</sub>	22	1	0.02	0.01-0.05
W <sub>2</sub>	35	2	0.4	0.01-5.9
Wss	197	2	2.1	0.01-22



Table 3.8: Photo interpretation results for Eastern Sector.

Rock Unit	Length logged (m)	Number of boreholes	Q (mean)	Q (typ.range)
W <sub>1</sub>	89	6	0.009	0.004-0.1
W <sub>2</sub>	112	4	0.02	0.008-0.2
Walt <sub>1</sub>	184	6	0.03	0.008-4.3
Walt <sub>2</sub>	31	2	0.09	0.01-0.08
Wss	20	2	0.07	0.008-0.8

The following Table is represented here from NGI , and includes a complete rock mass classification for each sector.

Table 3.9: Overall rock mass classification per section.

Rock unit		Q (weighted mean values at designated tunnel sectors)					
		Western		Central		Eastern	
W1		0.01,0.08 0.02,0.19	0.07	0.02	0.02	0.007,0.02,0.008 0.009,0.009	0.009
W2		0.5,1.4 1.5,1.3	1.3	0.4,0.3	0.4	0.02,0.3,0.02 0.03	0.02
Walt1		-	-	-	-	0.03,0.02,4.5 0.6,0.04,0.02	0.03
Walt2		5.4,2.8,3.0	4.0	-	-	0.06,0.01	0.09
Wss		3.9	3.9	3.1,1.7	2.1	0.008,0.3	0.07
Core Logging	Walt2	2.0	2.0	-	-	-	-
	Wss	-	-	2.6,0.5	0.8	-	-

Figure 3.7 presents representative core logging analysis from horizontal boring BH-1 (figure 3.6) at the Western portal from JHPC site data. Three plots are shown depicting the variation of RQD, Q and RMR rating over length of boring. It becomes immediately apparent the improvement of quality of the rock mass as the penetration depth increases, while at the greater depths Q index concentrates in the range 1-10 for the Walt<sub>2</sub> rock. Independent RMR rating is in the range 55-63 for the deeper section. In the third graph

the following correlation between RMR and Q rating is also plotted giving a good approximation (Barton, 1995):

$$RMR = 15 \cdot \log Q + 50, \quad \text{Equation 3.5}$$

This relationship was found by Barton (1995) to give correlation between Q and RMR than the original correlation proposed by Bieniawski (1976), which is given as:

$$RMR = 9 \cdot \log Q + 44, \quad \text{Equation 3.6}$$

From the above, most of the rock mass in which the tunnel will be excavated, ranges in quality from extremely poor to poor close to the portals and locally fair in some cases. From the above information, it becomes obvious that the tunneling process would be expected to be locally difficult due to the poor quality rock and the support requirements are expected to be relatively high.

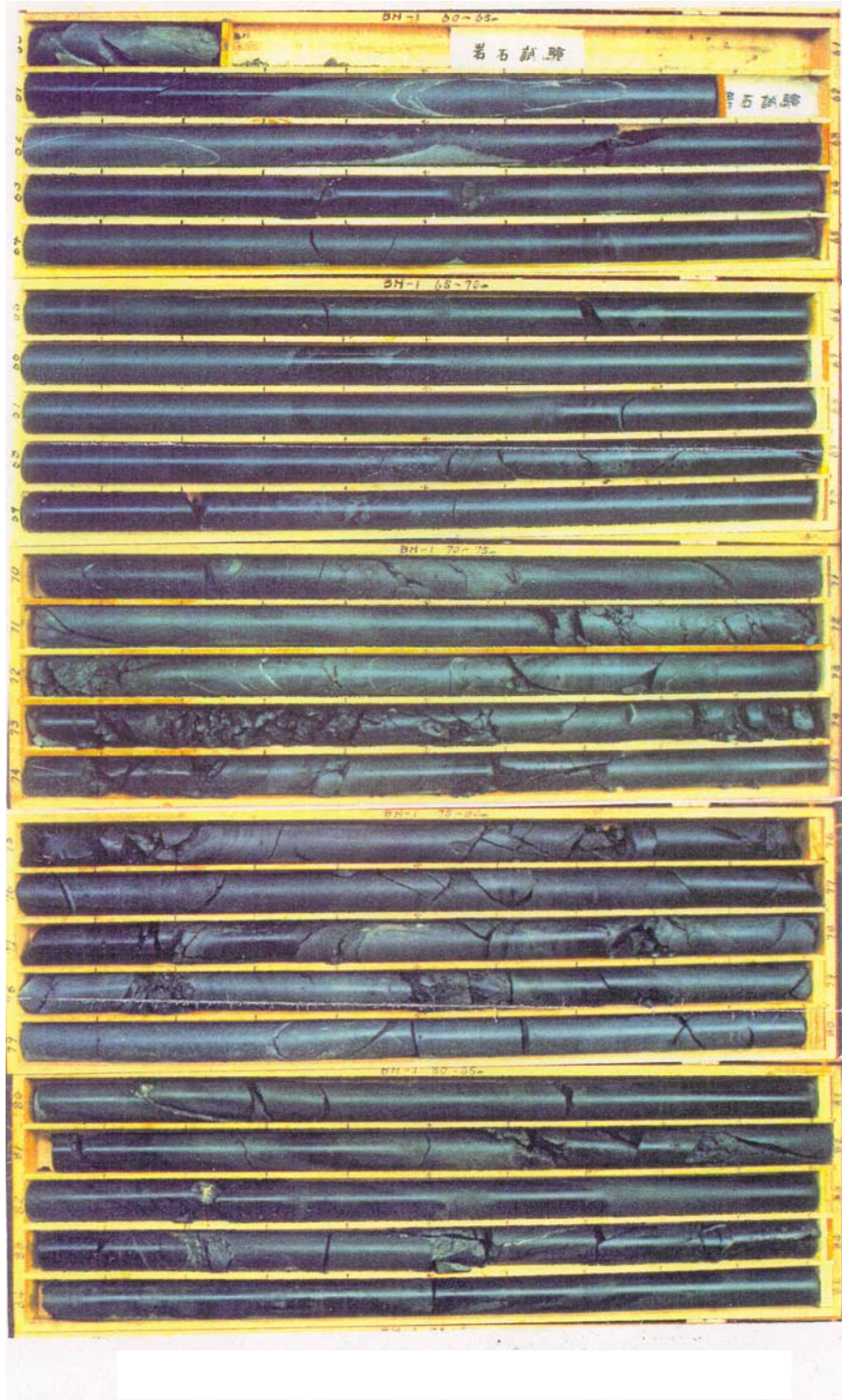


Figure 3.6: Example of rock core sampling for western sector (From NGI, 1995).

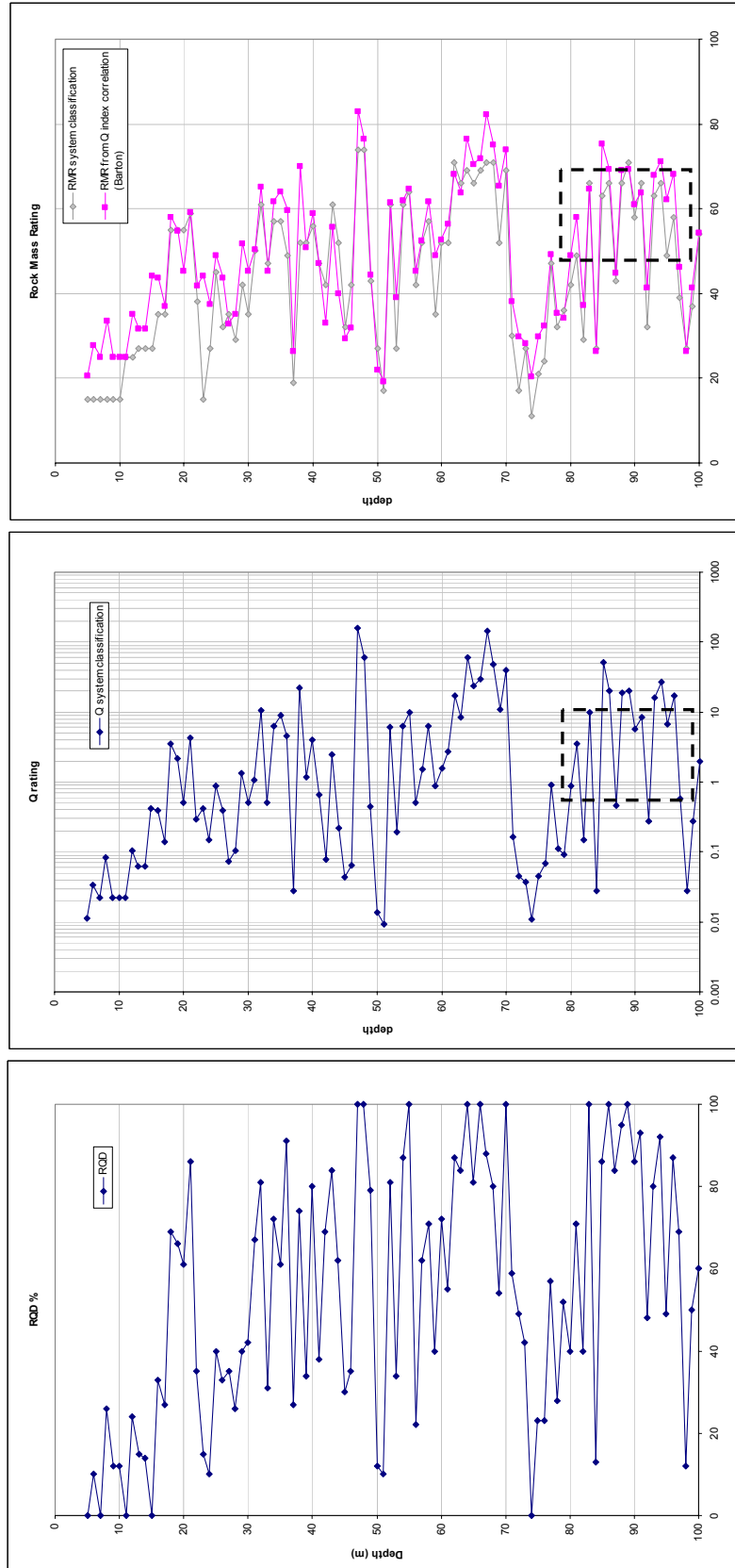


Figure 3.7: Rock mass ratings for Q and RMR systems in horizontal borehole BH1 (dotted line indicates most probable rock mass quality at the Walt<sub>2</sub> formation).

### 3.2.3 Japanese rock mass classification system

Several Japanese public organizations, such as the JHPC, the Public Works Research Institute (PWRI), the Central Research Institute of Electric Power Industry (CRIEPI), have established their own rock mass classification systems in order to better characterize frequently occurring rock types in Japanese constructions. These classification systems are based and are suitable for the geology of Japan. They are based on extensive work, verification and gradual refinement of data from experience in Japanese construction. According to the Japan Society of Engineering Geology an additional fact is that these classification systems also are founded on independent criteria imposed by the specific authorities. One of the commonly applied systems is briefly described in the present work, which is the classification system by JHPC for tunneling that was used by geotechnical companies and contractors at the Shimizu tunnel No.3 site.

The JHPC distinguishes five primary rock mass qualities A to E, shown in Tables 3.10 a,b. Classification is based on the selection of appropriate criteria based on six independent standards and one standard based on the petrological composition of the geologic unit. The six standards used are:

1. Seismic compressive wave velocities : 1.0 – 6.0 km/sec

$$\text{The well known strength/stress ratio: } GN = \frac{\sigma_c}{\gamma \cdot H}, \quad \text{Equation 3.7}$$

where  $\sigma_c$  is the uniaxial compressive strength of the ground,  $\gamma$  the unit weight of the rock mass and H the overburden thickness of the tunnel.

2. Boring core rate characterization and RQD% measurement.
3. Standard from field ground investigation (recognition of alterations, hardness and jointing estimation).
4. Standard based on observation (hammer blows, discontinuity spacing measurement).
5. Post construction ground condition verification. The system also provides for some rough convergence range estimates.

Table 3.10 a,b: The Japan Highways rock mass classification system.

Standards for Rock Mass Classification									
Rock Mass Grade	Petrological Classification	(1) Standard by Seismic Waves Velocity (Vp, km/sec)					(2) Gw	(3) Standard by Boring Core Sample	
		1.0	2.0	3.0	4.0	5.0		6.0	condition of core sample
A	a							Core recovery rate is more than about 90% with complete column shape, having length of more than about 20cm. without containing small pieces.	more than 90
	b								
	c								
	d <sub>1</sub>								
B	a						Core recovery rate is more than about 70% and the core shows large block or short column or bar shape. Core having length may be about 10 to 20cm. but in rare case, 5cm or so.	90 ~ 70	
	b								
	c								
	d <sub>1</sub>								
C	I	a						Core recovery rate is roughly 40 to 70% containing many cracks, and the core also cracks easily to a mass less than 5cm.	70 ~ 10
		b							
		c							
		d <sub>1</sub>							
		d <sub>2</sub>							
	II	a						Restore of original shape is difficult or impossible.	
		b							
		c							
		d <sub>1</sub>							
		d <sub>2</sub>							
D	I	a						Core recovery rate reduces down to less than 40%, the core may be composed of small pieces or may be a rubble sand state or clay state.	about less than 10
		b							
		c							
		d <sub>1</sub>							
		d <sub>2</sub>							
	II	a							
		b							
		c							
		d <sub>1</sub>							
		d <sub>2</sub>							
E	a						less than 1	—	
	b								
	c								
	d <sub>1</sub>								
	d <sub>2</sub>								
	e								

1. Petrological classification  
a: Metamorphite: (phyllite, graphite, schist, silicic graphite schist, quartzschist, greenschist, gneiss, serpentine, hornfels, etc.) Plutonite: (gabbro, peridotite, etc.)  
b: Paleozoic strata and Mesozoic formation: (slate, sandstone and conglomerate, graywacke, limestone, quartzite, schalstein, etc.)  
c: Volcanic rock: (liparite, andesite, basalt, etc.)  
Dike rock: (quartz porphyry, granite, diabase, etc.)  
Plutonite: (granite, diorite, etc.)

2. The condition of boring core sample, RQD, and spacing of cracks applies petrological classification for a, b, c, d<sub>1</sub>.

a

Standards for Rock Mass Classification				
(4) Standard by geological condition (the result of ground investigation or the condition of excavated rock mass)	(5) Standard by Observation		(6) After excavated condition	
	Hitting with Hammer	Spacing of Cracks	Standard by stability of face	convergence
<ul style="list-style-type: none"> <li>The condition of rock is very hard and fresh, and consists of massive blocks without cracks, which continuous and stable over the large area.</li> <li>Rock mass is not inferior by water.</li> </ul>	<ul style="list-style-type: none"> <li>Hammer is bounded.</li> <li>The rock is cracked with fresh surface only when hit strongly.</li> </ul>	<ul style="list-style-type: none"> <li>100 ~</li> <li>more than 50cm</li> </ul>	<ul style="list-style-type: none"> <li>The condition of face stability is very good and not loose for a long time.</li> <li>Height of looseness, less than 1.6m</li> </ul>	<ul style="list-style-type: none"> <li>very</li> <li>small</li> </ul>
<ul style="list-style-type: none"> <li>The condition of rock is hard and fresh, and contains relatively less cracks.</li> <li>The condition of rock is relatively hard but shows somewhat altered property due to weathering.</li> <li>The condition of rock is hard but assumes a layer from having bedding or schistosity and tends to be cracked along the surface.</li> <li>Rock mass is not inferior by water.</li> </ul>	<ul style="list-style-type: none"> <li>The rock develops cracking or or cut relatively largely along the joint or crack when hit strongly.</li> </ul>	<ul style="list-style-type: none"> <li>70</li> <li>~</li> <li>30cm</li> </ul>	<ul style="list-style-type: none"> <li>Cutting face keeps stability and excavation without support has sectionally fall of rocks but generally stable.</li> <li>The sectionally loose zone must support.</li> <li>Height of looseness, 1.5 to 3.0m</li> </ul>	<ul style="list-style-type: none"> <li>very</li> <li>small</li> </ul>
<ul style="list-style-type: none"> <li>Altered property due to weathering, and the condition of rock is somewhat soft.</li> <li>The condition of rock is relatively hard but contains many small cracks thereby showing the appearance of small masses.</li> <li>Joint may contain clay despot.</li> <li>Bedding and schistosity are remarkable.</li> <li>Easy cleavage with thin layer.</li> <li>Narrow, small fault is contained.</li> <li>Rock mass is not inferior by water.</li> </ul>	<ul style="list-style-type: none"> <li>Crushed easily with hammer.</li> <li>Crushed into small pieces along the cracked face.</li> <li>Faces without containing cracks are hardly crushed.</li> </ul>	<ul style="list-style-type: none"> <li>about</li> <li>less than 50cm</li> </ul>	<ul style="list-style-type: none"> <li>Cutting face keeps stability.</li> <li>Excavation without support needs concrete shotcrete for crown area at once after blasting.</li> <li>Height of looseness, 2.0 to 4.0m</li> <li>Cutting face keeps stability.</li> <li>Excavation without support has fall of rock near crown area and which needs presupport.</li> <li>Height of looseness, 2.0 to 4.0m</li> </ul>	<ul style="list-style-type: none"> <li>less than</li> <li>50mm</li> </ul>
<ul style="list-style-type: none"> <li>Considerably weathered rock mass, partly showing soiled part containing some hard parts, is soft and fragile.</li> <li>Rock mass has many cracks and rock can be crushed easily from any part other than crack.</li> <li>Rock mass has crushed rock zone in which tendency toward clay, not much progressing, and contained some hard components in which clayey soil and fine pieces are being mixed.</li> <li>soils, taluses, etc.</li> <li>The case which the cutting face having fragile by water is D II grade.</li> </ul>	<ul style="list-style-type: none"> <li>Crushed easily if hit by hammer.</li> <li>Crushed easily by fingers.</li> <li>Crushed easily by a small hammer damage.</li> <li>The point of hammer sticks into rocks.</li> </ul>	<ul style="list-style-type: none"> <li>---</li> </ul>	<ul style="list-style-type: none"> <li>Cutting face and excavation without support have substantially fall of rocks, and the side wall has some squeezing.</li> <li>The ground needs presupport and landslide protection at a early stage.</li> <li>Plastic zone or height of looseness, 3.0 to 6.0m.</li> <li>Cutting face has substantially fall of rocks.</li> <li>At excavation without support, the side wall has squeezing.</li> <li>Plastic zone or height of looseness, 3.0 to 6.0m.</li> </ul>	<ul style="list-style-type: none"> <li>less than</li> <li>60mm</li> <li>less than</li> <li>200mm</li> </ul>
<ul style="list-style-type: none"> <li>Fault and crushed rock zone or taluses with a considerable width, on which considerable eccentric earth pressure is acting.</li> <li>Inferior by ground water is relatively, and to be weakness.</li> </ul>	<ul style="list-style-type: none"> <li>---</li> </ul>	<ul style="list-style-type: none"> <li>---</li> </ul>	<ul style="list-style-type: none"> <li>Cutting face has squeezing and in a striking case, cutting face collapse.</li> <li>Excavation without support has squeezing with circumference pressure.</li> <li>Plastic zone, more than 7.0m</li> </ul>	<ul style="list-style-type: none"> <li>less than</li> <li>400mm</li> </ul>

d: Tertiary formation and lower diluvium: ( mudstone, shale, siliceous shale, sandstone and psephite, limestone, tuff, breccia, agglomerate, etc. )  
But, the classification d<sub>1</sub> and d<sub>2</sub> is due to the compressive strength of fresh rock mass which point of out 200 kgf/cm<sup>2</sup>.  
d<sub>1</sub> :  $q_u \geq 200 \text{ kgf/cm}^2$   
d<sub>2</sub> :  $q_u < 200 \text{ kgf/cm}^2$   
e: Upper diluvium ( loam and clay, volcanic crushed formation, etc. )  
Alluvium ( talus, surface soil, etc. )  
3. G<sub>w</sub> =  $q_u / \gamma h$  q<sub>u</sub>: uniaxial compressive strength of ground,  $\gamma$ : unit weight of ground, h: depth of overburden

b

### 3.2.3.a Japanese rock mass classification at Shimizu tunnel No.3

Even though this system is not as quantitative as the RMR and Q index systems and does not provide for support type estimates, it is widely used in Japan and gives a ground type grading and associates this with some predicted behavior. Figure 3.8 (from JHPC) shows the variation of ground type along the length of the tunnels. All classes have been given qualities ranging from CI to very bad quality D type (it is assumed that D3 type is between DII and E and corresponds to practically soil conditions). Close to both of the portals, the ground is very poor (with measured velocities in the order of 1.0 - 2.0 km/sec) described by the system as considerably weathered rock mass, locally weathered into residual soil. Support needs are high and with a plastic zone around the opening between 3.0-6.0 m. Convergence estimates show values of less than 200 mm. Similar characteristics are shown for quality DI corresponding to highly fractured and altered rock and with estimated deformation in the order of 60 mm. Recommendation of pre-support measures is also given to ensure tunnel safety and stability.

Towards the western–central sector of the tunnels, improved rock quality is recorded with classes ranging from CI-CII to DI. Highest quality Class CI (subcategory “c” for sandstone Wss), corresponds to seismic velocities between 3.0–4.0 km/sec as reported before and with some alteration. This type of rock is described as somewhat soft and with a joint spacing less than 0.5 m. To avoid excessive loosening of the rock mass, the classification system suggests immediate support as close to the tunnel face as possible, with shotcrete application at least at the crown area. Deformations in this category are expected to be less than 50 mm. For category CIIc Wadajima sandstone the system predicts the need for presupport measures due to the enhanced possibility of rock fall and spalling. As will be seen later this technique was used in the tunnels during the pilot boring construction.



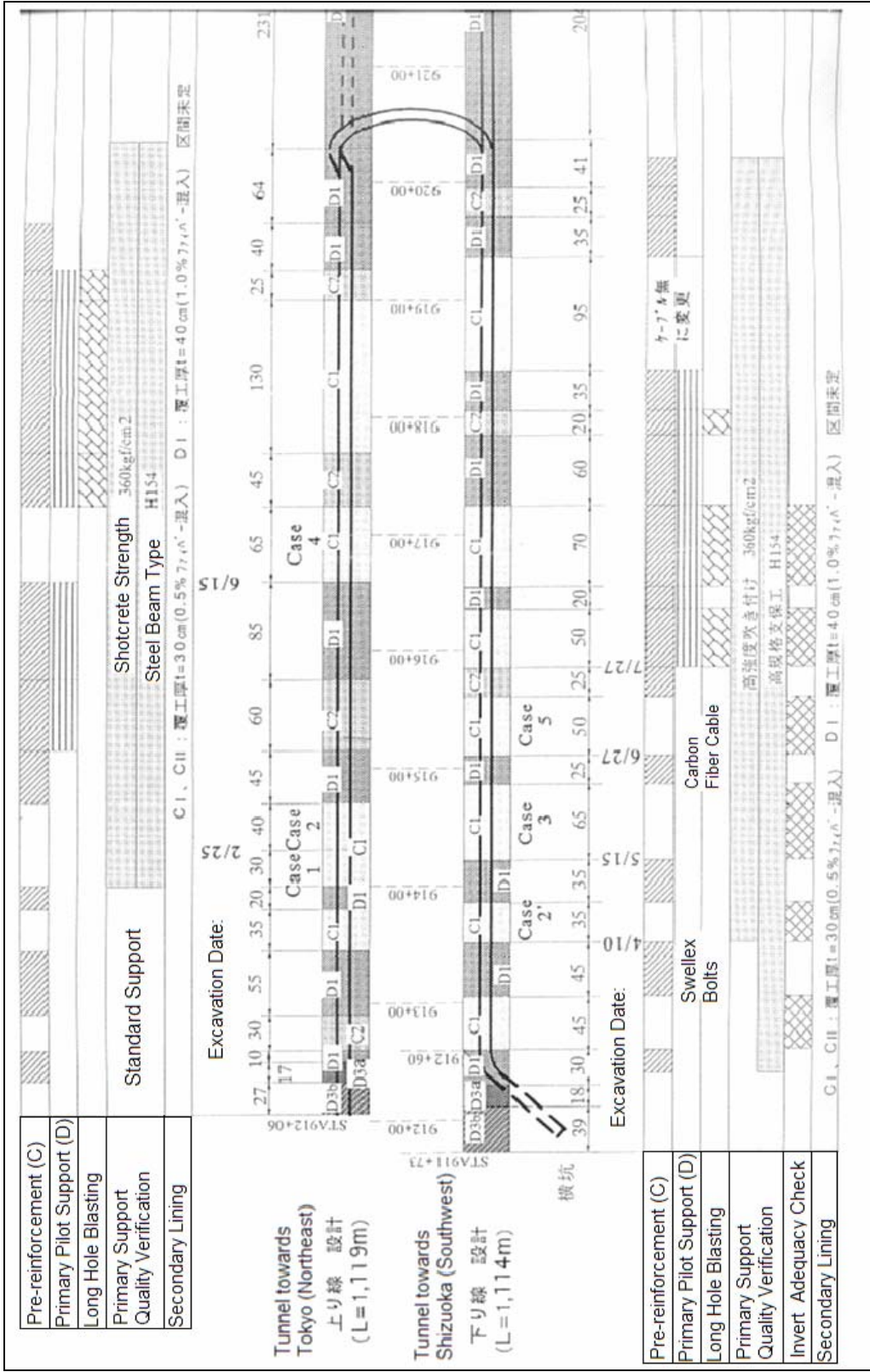


Figure 3.8: Worksite plan of Shimizu No.3 twin tunnels on Tomei II Expressway, Japan. Rock mass quality grading and support system (After Japan Highways,1998).

### 3.3 Joint set data

Available data from geotechnical investigations (Sanco Consultants, 1995) are represented in this section. According to the geotechnical investigations, three major discontinuity sets are recognized in the Wadajima sandstone. The first set J1 is formed by bedding plane joints and the second set J2 consists of cross joints at a random orientation. The third joint set J3 is also present which dips almost vertically. The three joint sets are shown by the hemispherical projection of figure 3.9 and represent most of the tunnel length, besides the areas close to the portals where more extensive fracturing and low quality rock masses were observed. The orientation data for the Wss are presented in Table 3.11:

Table 3.11: Discontinuity orientation data for sandstone at the Shimizu tunnel No.3.

Joint Set	Type	Dip	Dip Direction	Spacing (m)	Joint length (m)
J1	bedding	28	N50W	0.1-1.0 (0.3)	10-50 (25)
J2	cross	58	S54E	0.1-1.0 (0.3)	0.25-2.0 (1)
J3	cross joints	88	N18W	0.3-3.0	0.25-2.0 (1)

### 3.4 Laboratory tests.

Several Japanese geotechnical firms involved in the Tomei II project performed laboratory tests on rock specimens from the Shimizu tunnel No.3. These tests mainly included uniaxial compressive tests on samples selected from boreholes BV1, BV-2 (central sector), BV-3 (eastern sector) and BH-1, BH-2 (western sector). The results are shown in Table 3.12. Barton et al. (1995) reports compressive strengths in the range 60 to 90 MPa and elastic moduli between 8.5 to 20 GPa.

As far as the central sector is concerned, JHPC laboratory data from tested intact samples of BV2-1 and BV2-2 borings show P wave velocities (on Wss core) of  $V_p=3.5-4.5$  km/sec. In situ measured velocities have a range of 3.4-3.5 km/sec due to the natural jointing. Uniaxial compressive strengths for the intact Wss samples show some variance

in the range 20-78 MPa and elastic moduli in the range  $E=5.4-15$  GPa. Friction angles have been reported in the range  $37^{\circ}-53^{\circ}$  with a most probable value in the range of  $38^{\circ}-40^{\circ}$ . Finally, Table 3.12 shows a cohesion intercept for the intact rock in the range 1.9-6.8 MPa. The rock mass density is approximately  $25 \text{ g/cm}^3$ .

Besides core logging NGI conducted tilt, Schmidt hammer and joint index tests in order to evaluate strength properties of the discontinuities present in the rock masses. Tests were performed on selected core samples from borings BV2-2, BV2-1, BH-1. The results of the tests were used to assess the behavior of the joints under shearing.

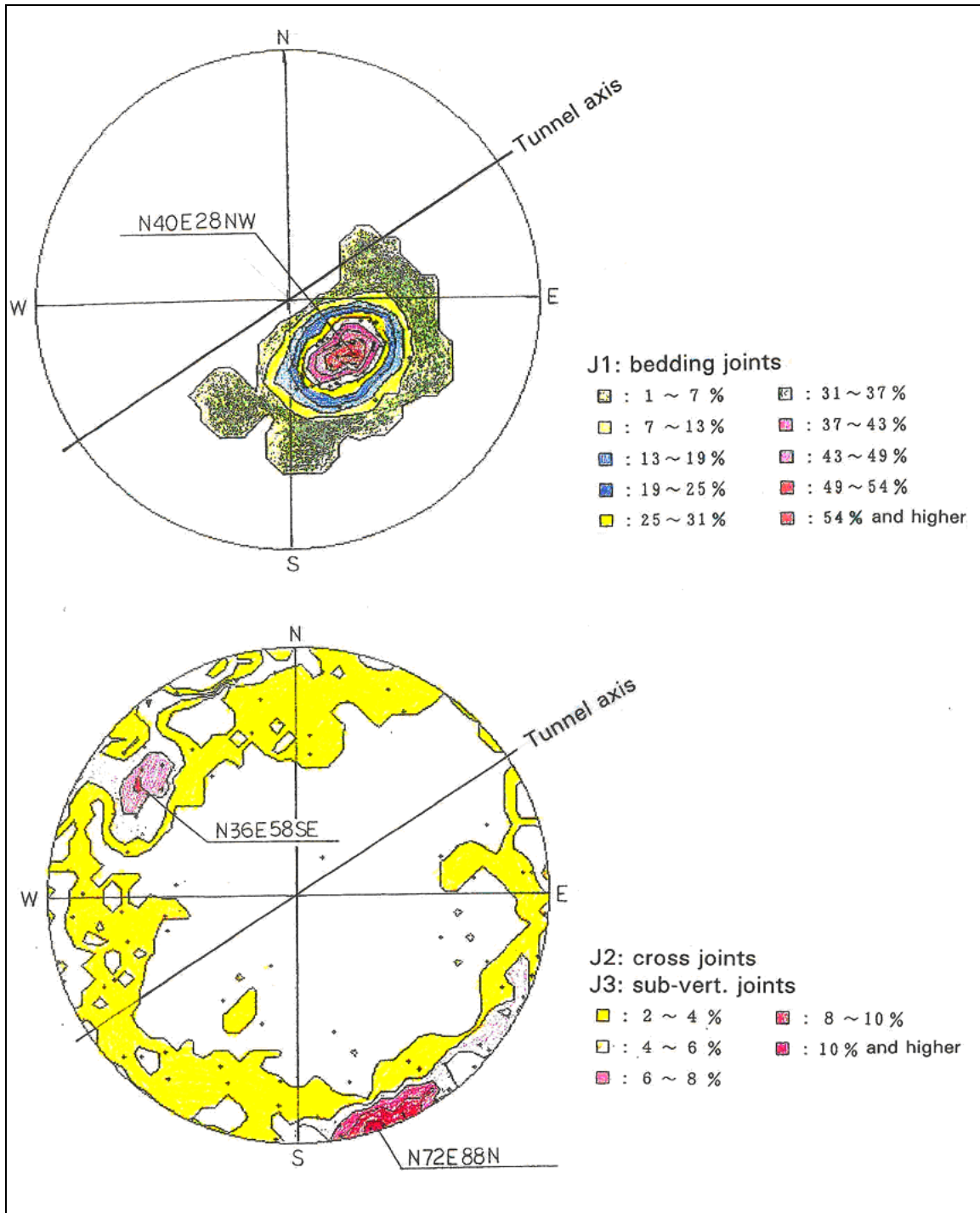


Figure 3.9: Stereonet for primary joint sets in Wadajima Sandstone (NGI, 1995).

Table 3.12: Strength measurements in soft Shimizu site rocks.

TEST #	Borehole No.:	Depth	Rock type	$\sigma_c$ (kgf/cm <sup>2</sup> )	$\sigma_c$ (MPa)	$\varepsilon_f$ %	$E_s$ (kgf/cm <sup>2</sup> )	$E_s$ (MPa)	$E_s/\sigma_c$	$E_d/E_s$
1	BV-1	8.55	alt w2	721	70.73	0.641	1.42E+05	13930.2	197	1.14
2	BV-1	27.3	alt rf	390	38.26	0.368	1.16E+05	11379.6	297	1.73
3	BV-1	32.75	alt rf	1059	103.89	0.608	2.04E+05	20012.4	193	0.96
4	BV-2	11.15	alt w1	952	93.39	0.844	1.34E+05	13145.4	141	1.14
5	BV-2	28.25	alt rf	533	52.29	0.879	8.50E+04	8338.5	159	1.86
6	BV-2	32.05	Ss rf	653	64.06	0.82	1.07E+05	10496.7	164	1.76
7	BV-3	5.75	Alt wl	812	79.66	1	1.20E+05	11772	148	
8	BV-3	8.55	Alt rf	710	69.65	0.574	1.48E+05	14518.8	208	
9	BH-1	30.75	Ss rf	860	84.37	0.58	1.70E+05	16677	198	1.42
10	BH-1	60.95	Ss-rf	742	72.79	0.565	1.53E+05	15009.3	206	1.59
11	BH-1	90.2	Md-rf	884	86.72	0.492	1.98E+05	19423.8	224	1.2
12	BH-2	29.55	SS w2	745	73.08	0.823	1.14E+05	11183.4	153	1.29
13	BH-2	61.2	Alt-rf	687	67.39	0.56	1.66E+05	16284.6	242	1.23
14	BH-2	88.7	Alt-rf	731	71.71	0.575	1.57E+05	15401.7	215	1.6
AVERAGE				750	73.57					

## 3.5 Shear strength of discontinuities

### 3.5.1 Failure criteria

Before further presentation of the analysis results, some aspects of the joint behavior may be discussed. Idealized behavior of a discontinuity can be seen at figure 3.10. These plots can be obtained by a direct shear test on a jointed specimen.

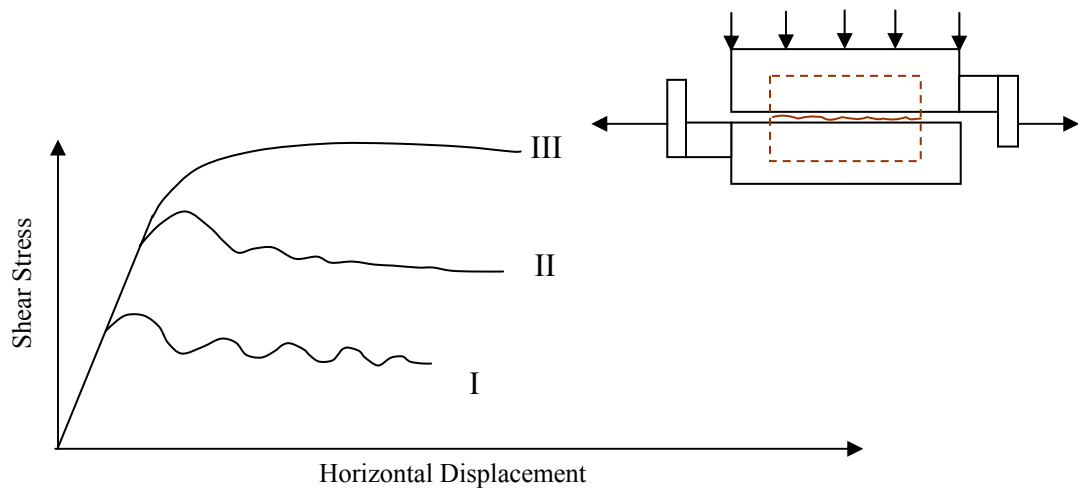


Figure 3.10: Typical shear stress-shear displacement plots for direct shear tests at rock joints under different loading conditions.

Under low normal stresses the stress-displacement graph of the test is like curve I. Under continued shear loading the shear stress increases until it reaches a maximum value that corresponds to slip on the top of the asperities and undulations of the joint. After the slip has occurred, the shear strength stabilizes to a steady state of slip which corresponds to the residual strength of the discontinuity feature. For this case no pronounced intact material failure occurs and only dilative response is observed. For a higher normal load the stress displacement plot should be similar to case ii. In such a case the advanced normal load necessitates the application of higher shear stress. During application of the load some localized failure occurs at the asperities of the joint surface. After the strength

reaches a peak value and can no longer increase, it stabilizes gradually to a constant residual level. At even higher level of normal compression, dilation is suppressed and behavior shifts from brittle like to more plastic. At this state failure of the asperities occurs fast and the load-displacement curve is expressed by plot III.

Pioneering work in the area of shear strength of discontinuities has been performed by Patton (1966) who assumed the “saw tooth” model for simulating the behavior of joints (figure 3.11).

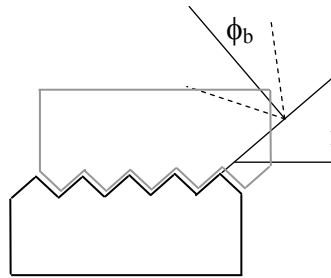


Figure 3.11: Patton’s “saw tooth” model of discontinuities.

According to Patton (1966) the shear strength of the discontinuity should be expressed by the relation:

$$\tau_{developed} = \sigma_n \cdot \tan(\phi_r + i) \quad \text{Equation 3.8}^1$$

where :

$\phi_r$  = residual friction angle (or basic friction angle, depending on state of discontinuity)

$i$  = the saw tooth angle from the horizontal

Patton recognized and tried to decouple two different properties of shear strength: a component due to residual or inherent mineral friction (microscopic frictional strength) and a component ( $i$ ) to account for dilation during shearing. According to Patton the above relation would only be valid for low stress ranges where failure of the asperities does not occur. For the case of higher loading, he supported the validity of the simple Coulomb criterion so that :

<sup>1</sup> This relation was first developed by Newland and Allely (1957) for coarse granular materials.(Data from Tsoutrelis,1985).

$$\tau_{developed} = c + \sigma_n \cdot \tan(\phi_o) \quad \text{Equation 3.9}$$

where:

$c$ ,  $\phi_o$  the shear strength parameters of the intact rock. His studies showed little difference between  $\phi_o$  and  $\phi_r$ . Combining the two stress ranges supported the idea of a bilinear model to predict the shear behavior of discontinuities. Following the work of Patton, Ladanyi and Archabault (1969) proposed several advancements in the shear behavior of fractures amongst which the idea of a non linear failure criterion.

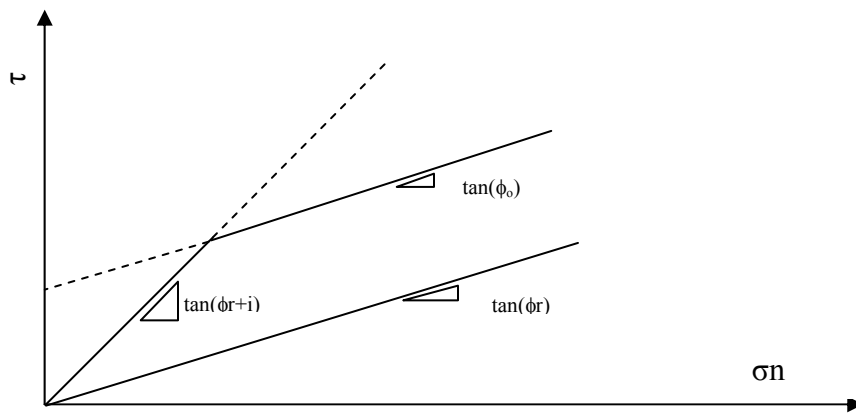


Figure 3.12: Bilinear shear strength model (after Patton, 1966).

An extensive research work on the behavior of jointed rock masses has been also conducted by Barton (1973), Barton and Bandis (1985). This work has yielded useful relations that express the shear and normal behavior of joints under different loading conditions. The key aspect of the analysis is the recognition, isolation and final quantification of parameters that control the frictional strength of the discontinuities. According to Barton and Bandis (1985) a constitutive equation that controls the strength of discontinuities is of the form:

$$\tau_{developed} = \sigma_n \cdot \tan\left(\phi_r + JRC \cdot \log\left(\frac{JCS}{\sigma_n}\right)\right) \quad \text{Equation 3.10}$$

where:



$\phi_r$  = residual friction angle (or the basic mineral angle)

JRC = Joint Roughness Coefficient is a coefficient controlling the joint wall roughness, takes values from 0 for very smooth joint surfaces to 20 for very rough surfaces.

JCS = the joint wall compressive strength. For fresh unweathered surfaces it is practically equal to the uniaxial compressive strength of the rock, while for weathered joints it can be reduced by a factor of 4 (Tsoutrelis, 1985).

Hence the relationship proposed by Barton includes a composite frictional strength that takes into account of:

1. basic frictional strength
2. the geometrical contribution to strength of a joint surface (associated to dilation)
3. strength produced by asperity failure (crushing of surface anomalies)
4. Stress dependent friction

The most important aspect the application of the above relation in rock mechanics problems is the estimation via measurements of parameters JRC and JCS.

According to results of analysis conducted by Barton and Choubey (1977), the joint roughness coefficient may be assumed to be independent of normal stress. Reference asperity profiles associated to a range of probable JRC values have been published by Barton and Choubey (1977). Laboratory guidelines to calculate JRC and JCS values have been proposed by Barton and Choubey (1977).

The parameters JRC and JCS were proved to be scale dependent and decrease in magnitude as the length of the discontinuity increases. Relationships to account for the scale effects were proposed by Barton and Bandis (1982).

$$JRC_n = JRC_o \cdot \left[ \frac{L_n}{L_o} \right]^{-0.02JRC_o} \quad \text{Equation 3.11}$$

$$JCS_n = JCS_o \cdot \left[ \frac{L_n}{L_o} \right]^{-0.03JRC_o} \quad \text{Equation 3.12}$$

where:

$JRC_n, JCS_n$  are the coefficients for a joint length of  $L_n$ .

$JRC_o, JCS_o$  are reference laboratory values of coefficients for a joint length of  $L_o$ .

### 3.5.2 Rock joint parameters for Shimizu tunnel No.3

Based on NGI's laboratory measurements the following parameters are given for the Wss rock:

Table 3.13: Measured strength parameters for Wadajima Sandstone (NGI).

Joint Set	Type	JRC 300 mm	JCS 300 mm	Amplitude	$\phi_r$	$\sigma_{ci}$
J1	bedding	2.6-5.3	26.8-49.3	0.1-0.5	30.7-	30-90
J2	cross	(3.9)	(37)	0.6-4.0	35.6	(50)
J3	cross joints			0.6-4.0	(30.3)	

Further insight on the Barton Bandis joint model will be described in subsequent chapters. Details regarding the behavior of the complete Barton-Bandis model will be discussed prior to its implementation in a numerical code that will be used for a detailed numerical analysis of the Shimizu tunnel No.3. The results from the laboratory analyses will be used along with other useful correlations as input to the computer program. Several parameters such as the elastic modulus, as well as the parameters JRC, JCS and  $\phi_r$  will be examined by a simpler model, in order to estimate their influence on the finer and larger model. The parametric analysis will be used to fine tune these parameters in order to gain better appreciation of the variables involved. The final model will be used in order to compare numerical results of the code with actual measurements in the tunnel at a specific chainage.

## CHAPTER 4 : Tunneling methods

### 4.1 Modern tunneling techniques

Since the development of the first tunneling approaches for large scale infrastructure tunneling in mid 1950's the tunneling industry has met great developments and improvements. The two great schools of simple or conventional mechanized tunneling and the automated fully mechanized methods by the use of tunnel boring equipment have noted significant progress in the last decades. In the simple mechanized approach the following methods were introduced in the past mainly in Europe (Sofianos, 2000).

1. The German "core" construction method (sequential).
2. The old Austrian method (sequential with bottom pilot opening).
3. The Belgian method (sequential with top heading and immediate final support).
4. The New Austrian Tunneling Method (NATM) (full face or sequential).
5. The Norwegian Method of Tunneling (Nordic – NMT, usually full face).
6. The old Italian construction method.
7. The Italian method (ADECO-RS, full face based on ground pre-improvement).

By the term simple or conventional mechanized tunneling methods all excavation methods that use drill and blast techniques and simple mechanical equipment (i.e., excavators, roadheader units, jumbos etc.) are included. Some principal conditions for the applicability of simple mechanized excavation methods are given by Mahtab and Grasso (1992):

- Strong, competent rock mass.
- Highly variable ground conditions.
- Variable dimensions as in caverns other than tunnels.
- Limited lengths of openings.

The second general tunneling method involves the use of full face mechanized tunneling via more sophisticated tunnel boring units. In this paper, features and

characteristics of only two of the most popular conventional methods will be discussed in relation with the method used in many Japanese works such as the Shimizu tunnel No.3. Therefore focus will be given on the New Austrian Tunneling Method (NATM) and the Norwegian Method of Tunneling (NMT).

## 4.2 The New Austrian Tunneling Method

The New Austrian tunneling method is considered among engineers as a rather semi-empirical approach in the design and construction of underground excavation coupled with extensive monitoring of deformation and stress development around a tunnel. This approach was introduced in Austria and other places between 1957 and 1965 (Schwaikheim tunnel in 1964) by the Austrian engineers Rabcewicz, Müller and Pacher. The term NATM is first given at a conference in Salzburg<sup>2</sup>, 1962. It was subsequently used by L. von Rabcewicz in a relevant technical publication<sup>3</sup>. The NATM is acknowledged more as a group of principles that should be considered and followed during tunneling and is not so much associated with an excavation pattern. Bieniawski (1989) makes an excellent review of the principles behind the New Austrian method and recognizes possible misconceptions. The NATM without being restricted to, often makes use of a ground type classification scheme gradually developed by case studies from European, Asian and South American countries. The system is usually presented in a Table format and proposes certain excavation stages and support requirements depending on the ground class. In general the New Austrian technique is based entirely on tunneling without any kind of full face support. Usual support measures employed by NATM are rockbolts, shotcrete with wire mesh or fiber reinforced and steel sets or lattice girders. In his review of the NATM philosophy Müller recognizes some 22 principles. Some of the most important recognized by Müller (1978) and also listed by Bieniawski (1989) are:

---

<sup>2</sup> The term NATM was presented by Dr. Rabcewicz during a lecture at the Thirteenth Geomechanics Colloquium in 1962 in Salzburg, Austria.

<sup>3</sup> Water Power magazine, 1964.

1. Design that takes into account mobilization of the surrounding rock mass. Therefore a great amount of support is given by the self capacity of the ground via the redistribution of stresses. Adequate primary support measures must be installed to avoid loosening of the rock mass. The measures (i.e., rock bolts, dowels) must have carefully chosen deformation features and be placed at a correct timing.
2. Primary support may also include shotcrete to prevent excessive loosening, preferably applied immediately after excavation. It is paramount that the shotcrete remains in immediate contact with the ground and shows compatible deformations.
3. The New Austrian Method as an observational technique involves optimization and verification of the design which is conducted in situ. It demands elaborate monitoring equipment and instrumentation from the early stages of the excavation. Monitoring equipment consists of extensometers, encapsulated pressure cells in shotcrete, pressuremeters, strains gauges etc., that can record the progress of deformation and pressure build ups and concentrations. Perhaps no other tunneling approach is more demanding and sensitive on monitoring. Data recording is to be used as a continuous verification for the adequacy of the support measures installed and may provide necessary information upon changes in the support design. Furthermore, the timing for the application of the support measures must be carefully considered. Too early placement leads to attraction and concentration of high structural loads that overstress the system and may lead to unwanted overdesigns. Too late support may prove to be useless since the rock mass might deform plastically beyond any rational limit and the tunnel opening may become unstable.
4. The lining system utilized (temporary and final) should be thin walled in order to avoid bending moment build ups and subsequent fracturing due to bending. The support used must be flexible and versatile to adapt to different ground conditions. The effect of relative support stiffness on tunnel deformation was investigated by Peck (1969). His research proved that in case of a tunnel

excavated under anisotropic stress conditions, a perfectly flexible tunnel support system will show deformations compatible with a uniform distribution of contact stresses. In contrast an infinitely rigid support responds to the anisotropic field and develops high bending moments (figure 4.1). After the primary support has been installed, dimensioning of any final support is based on the performance of the tunnel recorded by the monitoring system. Bieniawski (1989) notes that strengthening of the support is not achieved by increasing the thickness of the shotcrete but by increasing the number and geometrical components of elements like rock bolts and steel sets.

5. A necessary step especially in poor ground conditions where the NATM construction is deployed, is the quick structural closure of the invert so that a closed load bearing ring is formed and the tunnel support works as a tube.
6. Contracts for NATM tunnels must be flexible enough to allow for “design as you go” procedures including variation in the support systems installed, excavation pattern and or unprecedented difficult ground conditions.
7. NATM designs may account for an optional final (secondary) lining. According to Kavvadas (2000) this support is designed to handle the primary rock bolt load if the type of bolts is temporary and additionally any loads due to secondary rock deformations due to creep (i.e., evaporitic rocks). Furthermore, the final lining should handle a percentage of the shotcrete load in a way that the final shotcrete load ensures longevity by safety regulations for permanent works. Usually a cast in place concrete lining of 25-40 cm thickness is used. Einstein (1980) supports the overdimensioning in these cases since primary lining takes most of the support load. The design of the final lining is primarily dictated by an accepted residual deformation rate after full excavation and primary support works (i.e., 4-6 mm/month). It should also be designed to cope with unprecedented water pressure build ups, and against any dynamic loads that may arise e.g., from earthquakes.

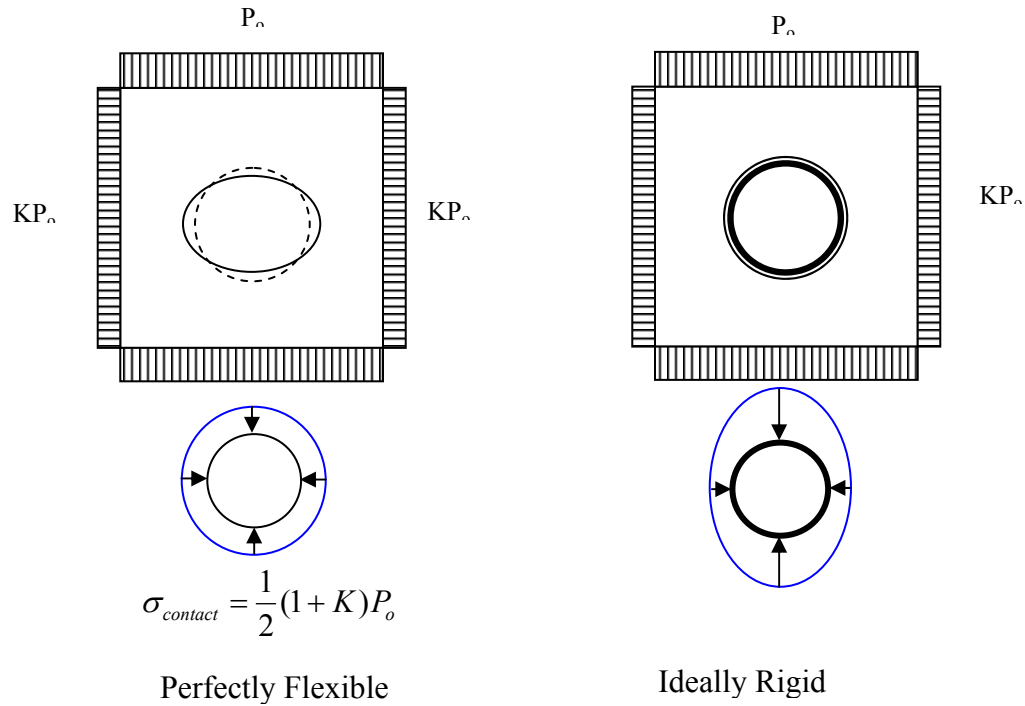


Figure 4.1: Peck's idealization for effect of support rigidity on pressure distribution.

Einstein and Schwartz (1980) reviewed the principles and characteristics of NATM and give some usual support systems employed by the method. Typically shotcrete with rock bolts and wire mesh is used, aided by steel beams in weak ground conditions. Sprayed concrete varies in thickness from 5-25 cm and grouted bolts prestressed or not are used as well, with lengths in the range 1.5-12.0 m and capacities in the range 147-245 MN. Wire mesh is reported to be of 3.12 kg/m<sup>2</sup> weight. When necessary high strength steel sets of 21 kg/m weight are also suggested and are formed in special U-type section. Typical spacing is in the range of 0.5-1.5 m and yield strength is in the order of 240-570 MPa. Today the most popular steel section is the I-type wide flanged section preformed to specific dimensions. The main advantage of the U (or top hat) sections is the ability of a special friction slip joint connection (figure 4.2) that permits the relative closure of the support (flexible) and relief the load buildups. A new method in today's controlled deformation tunneling has been applied in the Austrian tunnels Arlberg and Semmering, and includes the provision of slots in the shotcrete shell and the installation of sacrificial lining stress controllers, that are basically steel cylinders

which cushion the deformation of the shotcrete even in squeezing ground situations (Macht et al., 2003; Moritz et al., 1999). The use of lattice girders in the tunneling industry is also a great improvement in support systems since these elements are lighter, they can adapt to various conditions and enhance productivity. On the other hand more attention during installation steps is required as well as full encapsulation in shotcrete to ensure corrosion resistance.

One significant aspect behind the New Austrian tunneling method is the application of the ground reaction theory by Pacher (1964) in the dimensioning of the tunnel support system. This theory, even though it was established as a closed form type of solution for the problem of a circular tunnel in isotropically stressed elastoplastic rock, has been applied in various tunnels with success worldwide. Further developments by Sulem (1987), Panet (1995), Lunardi (1997) have improved the method which is now known as the Convergence-Confinement method and is frequently applied across Europe. Basic principles of the method will be discussed in subsequent chapter.

Due to confusion in NATM associated terminology, the last years there has been an effort to differentiate the NATM for hard rock tunneling and soft ground NATM (British ICE, 1996; Romero, 2002). In the later case soft ground requires all necessary actions to minimize ground disturbance and deformations, hence quick application of support measures. Sequential multiple stage excavation may be appropriate to ensure safer tunneling (i.e., side drift designs). For all cases, watertightness may be ensured by the use of a dedicated geomembrane. The main advantage of this approach is the adaptability in different ground conditions by variation of support measures, handling of different section geometries and utilization of relatively cheap mechanical equipment, including mainly drilling jumbos and trucks. This makes this method to be highly preferred in relatively small tunnels where more sophisticated equipment would be an expensive and less appropriate solution. On the other hand, precise and full utilization of this approach necessitates the design and installation of a monitoring system able to provide and record load (pressures) and deformations over time since this record will be used to verify the support system adequacy.



In his review, Müller (1978) notes and alerts for possible failures if attention during tunneling with the NATM is not provided. The main reasons for tunnel failures recorded in many countries including Austria are:

- Too thin and erroneously dimensioned lining without the use of steel sets and long anchors when necessary can lead to collapses.
- Sequential tunnel boring with long blast rounds may lead to excessive deformations and uncontrolled weakening and decomposition of the rock mass.
- Very long top heading driving (calotte stage). The “cantilevered” top heading in conjunction with incompatible displacements between the top heading and the bench stage can induce bending moments at the stage connection and crack the lining. This bending can be accelerated if the concentration of stresses below the top heading leads to localized failure at the foundation levels and settlement of the whole excavation.
- Perhaps the most important construction element in tunnels is the time for closing of the invert. Too long times or lack of it can lead to severe displacement problems. Specifically in soft ground tunneling this should be avoided and special investigation per case should be provided to estimate a maximum allowable invert closure delay.
- Allowance for excessive deformations to occur before support and subsequent failure of the mass.

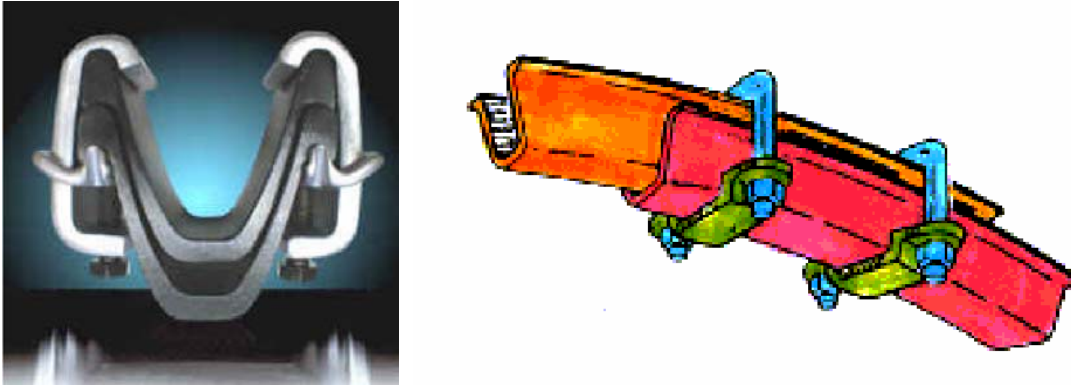


Figure 4.2: Top Hat connections (From Barla, 1999).

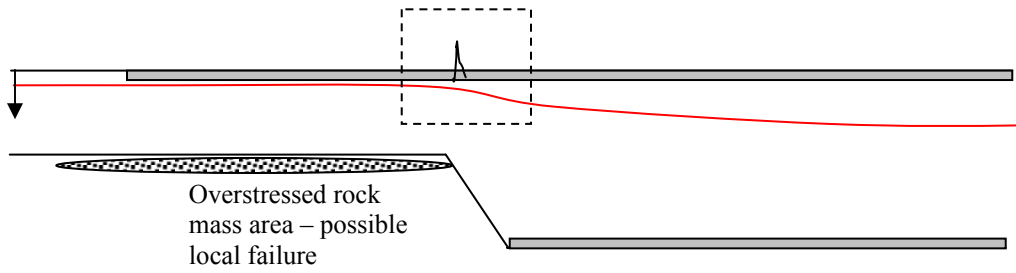


Figure 4.3: Müller's idealization for problematic cases of top heading excavations.

For more unfavorable conditions other temporary support measures can be provided (Sauer, 2000; Mahtab & Grasso, 1992):

- Sloping footrest for the face.
- Thin sprayed concrete on face.
- Temporary anchoring of the face with fiberglass elements .
- Forepoling and roof piping reinforcement works.
- Roof spilling.
- Thickening and or closer installation of steel beams.
- Increase in number of sequential excavation steps.
- Preconsolidation works with jet grouting and tube á manchette grouting.

The New Austrian tunneling method has been used worldwide with success in European countries including Austria, Germany, Greece, Great Britain, France, Portugal, Switzerland, Spain but also in Australia, United States, and Bolivia. A significant amount of tunnels has also been opened in Japan with the above principles until now. However the finally chosen tunneling methods in Japan were highly influenced by local technical and contractual traditions and were modified to account for specific geologic expectations based on previous works. The last years Japanese authorities have also shown interest for another tunneling approach developed in Norway and which is known as the Norwegian tunneling method.

### 4.3 The Norwegian Method of Tunneling

This approach was developed in Norway during the late 1970s, initially for the hard rock geologic environment of the country. Its development is practically parallel to the development of the Q index system (Barton, 1974), which estimates final support needs for a tunnel based on the rating (figure 3.5). The term “NMT” was first introduced by Barton in 1992. The Q system rock mass classification was described in chapter 3 and thus only major key issues of the NMT method will be added here.

NMT aims in the selection of an appropriate support system combination that will suffice for the long term support of the tunnel, and thus the logic of constructing a final lining can be avoided. The greatest target of the method is to eliminate the need for heavy support elements such as steel beams and secondary lining by utilizing high quality wet mix fiber reinforced shotcrete and high quality rock bolt elements designed with anticorrosion protection in mind.

The general trend of modern drill and blast Norwegian tunneling is a full face excavation using regular equipment like drilling jumbos, trucks and of course shotcrete mix-preparation and end-robotic units. The last years the NMT approach has also been associated with TBM tunneling in terms of support selection (Barton et al., 1994). The method has been gradually developed from many hydroelectric and other infrastructure tunneling and cavern projects in Norway and is considered as an economic alternative to the NATM approach. The advancements in the shotcrete technology in the country have made possible fast and precise application of high strength steel fiber sprayed concrete in many underground projects. In Norway mesh reinforced shotcrete was practically replaced by fiber reinforced shotcrete during the period from 1978 to 1984 where most advancements took place (Barton & Grimstad, 1994). According to the Norwegian Trade Council (1994), the key characteristics of the NMT philosophy are:

- Use of light and very flexible support, including shotcrete, rock bolts and shotcrete encapsulated ribs. For permanent applications high quality rock bolts, for example when ground water inflows are present, rust proof protected bolt designs are needed and incorporated in the system.
- Shotcrete quality is of paramount importance and its application should be executed by qualified personnel. Often after the application of the shotcrete a type of curing membrane can be applied to protect the shotcrete from shrinkage and cracking. Shotcrete quality control is described specifically by the tender documents of the work, and includes frequent on site examination and or testing (for each working section or shift). Mechanical characteristics of concern are compressive strength, thickness, density, fiber concentration, bond strength and ductility. By varying parameters such as the concrete strength and fiber geometrical properties a great range of support stiffnesses can be achieved, thus making a lining able to cope and follow a wide range of expected rock deformations.
- Primary support is usually the final support, and cast in place final lining is not included. The method assumes that a final concrete stiff lining does not offer appreciable advantage in stability characteristics but increases the cost of the structure significantly and completion times. Instead it is suggested that steel rebar reinforced shotcrete ribs can offer the support needed.
- The Norwegian method of tunneling necessitates the existence of a friendly and flexible contracting system to handle alterations in the design of the support system. Barton (1992) also suggests that the contractor of the work decides for temporary support while the Owner and owner consultant decide for the secondary lining requirements.

A description of the essential features of the NMT is directly given from Barton et al. (1992):

1. Areas of usual application:

- Jointed rock giving overbreak conditions. Harder end of uniaxial strength scale  $\sigma_c=3-300$  MPa.

- Clay bearing zones, stress slabbing.
  - $Q=0.001-10$  or more.
2. Usual methods of excavation:
- Drill and blast, hard rock, TBM , machine excavation in clay zones.
3. Temporary rock reinforcement and permanent tunnel support can be:
- Wet processed sprayed concrete (S), usually reinforced with fibers (otherwise designated as S(fr)).
  - Rock Bolts (B).
  - Steel reinforced ribs of shotcrete (RRS).
  - Cast Concrete lining (CCA).

The combinations of these supports can be:

- CCA
  - S(fr)+RRS+B
  - B+S(fr)
  - B+S
  - B
  - S(fr)
  - S
  - Spot bolting.
  - No support for stable tunnels in very competent rock masses.
4. Rock mass classification
- Use of Q system to predict rock quality and support requirements.
  - Continuous updating of quality index.
  - Monitoring is reserved for special cases.
5. NMT gives low production costs.
- Rapid advance rates.
  - Improved safety
  - Improved environment.

From the above many similarities with the New Austrian tunneling method are observed as in the support systems used and other contractual arrangements. However some major differences also exist. According to NMT, in cases of tunnels with overbreak, the application of steel sets or lattice girders is not appropriate due to the inability of such designs to follow and adapt well to irregular geometries. In contrast, it is advised to use shotcrete and rebar reinforced shotcrete ribs (RRS) for cases of clay zones, in weak or squeezing rock conditions.

It is also supported that the preparation, construction and installation of these elements is time consuming. In these cases some over consumption of concrete is inevitable and increases the total cost. NMT also explicitly rejects the use of steel mesh, supporting the development of electrolysis (galvanic corrosion) while the fiber reinforced shotcrete shell does not show this due to the discontinuity of the fibers. Another reason is the fact that installation of steel mesh prohibits correct application of shotcrete due to “shadow” effects created behind the wires and some rebound occurring during spraying on mesh.

A great difference is also located in the absence of a monitoring program as opposed to the variety of monitoring equipment used in the NATM. Barton (1994) suggests monitoring to be used for rock masses of  $Q < 0.01$  or in cases of large scale civil works (i.e., the Gjøvic underground Olympic Mountain Hall).

Finally, NMT is based on the assumption that the excavation is allowed to drain and no excess water pressures are let to develop behind the tunnel lining that would otherwise increase the total structural load. This further reduces the need for a secondary lining system and only requires provision for sufficient drain pipes (weep holes) in saturated grounds.

By utilizing the Q quality system the method is also able to cope with squeezing or overstressed rock mass conditions when encountered in underground engineering works, via the Stress Reduction Factor (SRF) parameter. Singh (1993) associates the

development of squeezing phenomena with overburden and rock mass quality conditions. According to his research the critical tunnel overburden for these condition to be developed is :

$$H \geq 350 \cdot Q^{1/3} \quad \text{Equation 4.1}$$

The “apparent” compressive strength of the rock mass then is:

$$q = 7 \cdot \gamma \cdot Q^{1/3} \quad \text{Equation 4.2}$$

Until today many tunnels have been constructed in Norway using NMT such as the Lærdal tunnel which was until recently the longest road tunnel internationally, the Oslo tunnel and the Freifjord tunnel (Norwegian Trade Council, 1994). So far the greatest doubt expressed from tunneling engineers in the world in the use of NMT, is the initial reliance of the approach on cases from the Norwegian geological environment and it has been believed that this method should be applied mainly in competent rock masses. However subsequent developments in the Q system (Barton & Grimstad, 1993) from about 1050 cases many of which concerned road tunnels, address these issues and promote the above philosophy as a cost efficient tunneling approach with high advance rates and ensured safety at the same time. Additionally a great difficulty for the application of this method in other countries may also be the acceptance of the validity of the suggested support systems as a primary and final lining from a geomechanics but also a contractual perspective.



#### 4.4 Tunneling method used at Shimizu tunnel No.3

In the Shimizu tunnel No. 3 a sequential type of excavation known as the “TBM pilot and enlargement method” was considered as the appropriate construction procedure. This method has been used successfully in the past in various projects worldwide and offers several advantages. As a design approach it is similar to the New Austrian tunneling method since in this particular case extensive monitoring was used in the tunnels to assist in validation and verification of the systems used. In this method a pilot tunnel is bored first at a designated elevation and within the tunnel cross section using a tunnel boring machine. In the Shimizu tunnel No.3 the TBM was chosen for high speed advance rates. After the circular tunnel has progressed at some extent subsequent gradual enlargement of the tunnel takes place in stages of a top heading, a bench and finally an invert. The steps of the excavation are shown in figures 4.5, 4.6.

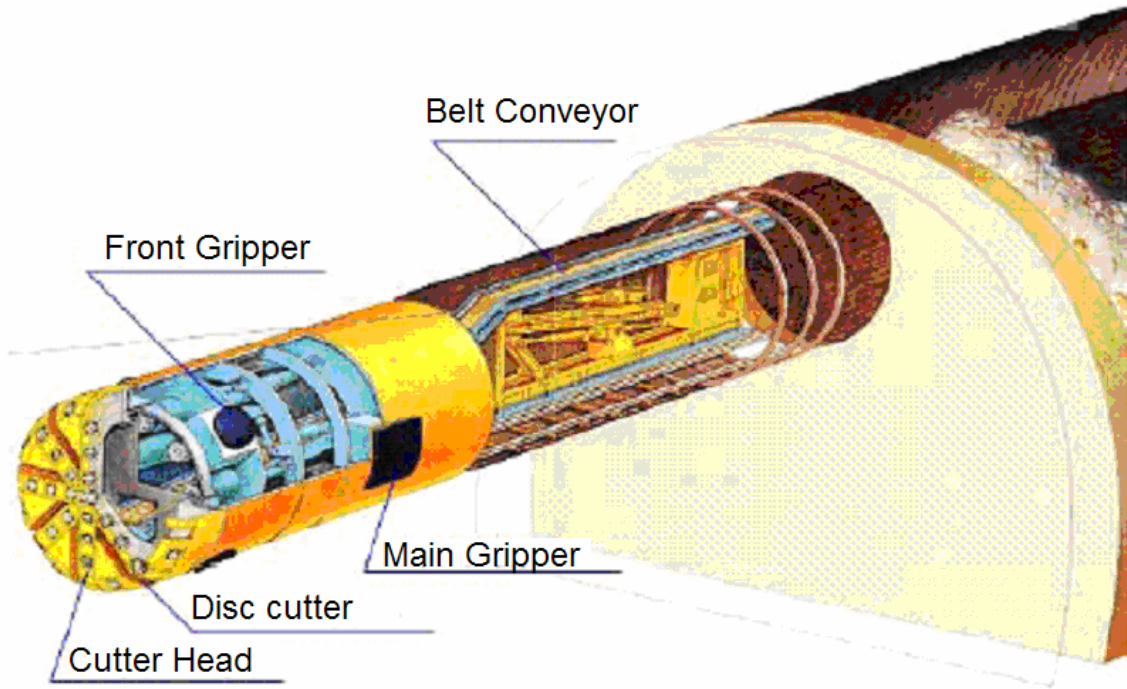


Figure 4.4: Visualization of the pilot tunnel ahead of the top heading (Ishihara,2001).

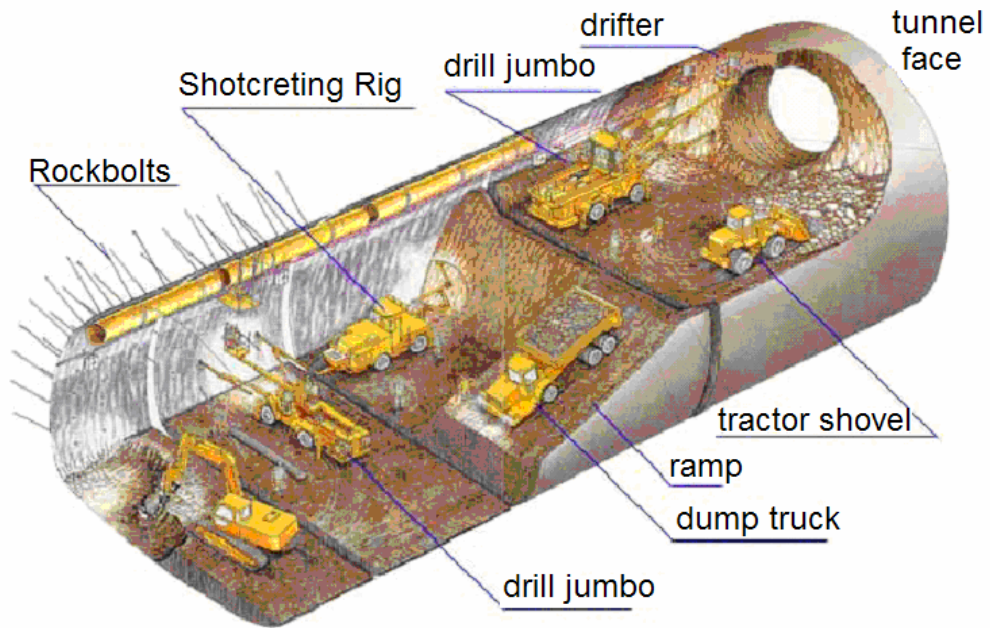
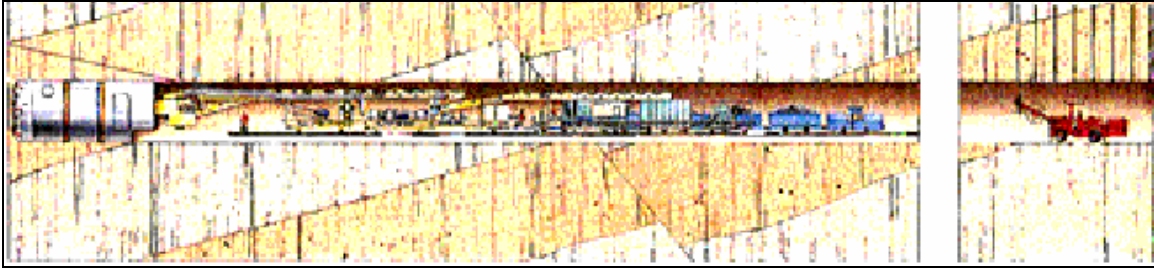


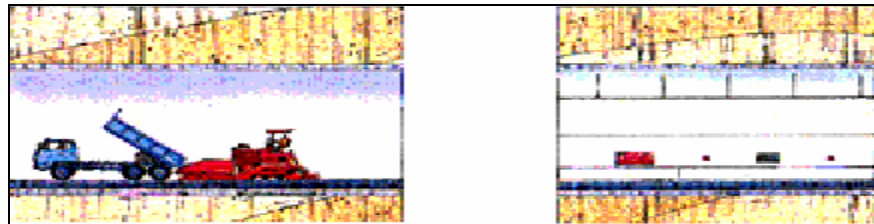
Figure 4.5: The sequential stages in the “TBM pilot and enlargement method”.



a: Pilot tunnel stage by D=5.0 m TBM. Pre-reinforcement using fiberglass or steel cable elements is performed by a separate drill rig.



b: Top heading excavation and support followed by bench excavation and support. A short invert stage is left to be excavated last. Finally a water proof geomembrane is installed and a “traveling shutter” (formwork shield) is used for final (secondary) support installation.



c: Pavement construction and utilities installation.

Figure 4.6 a, b, c: Sequential stages for the Shimizu tunnel No.3.

The following data are given by Ishihara (2001) and Miura (1998) with respect to project timing records for Shimizu tunnel No.3:

Table 4.1: Construction timetable for Shimizu tunnel No.3.

Time	Activity
October 1995	Construction work started
June 1996	TBM tunneling started (western portal)
May 1997	Breakthrough of pilot tunnels after completion of a U-turn.
September 1997	Main Construction (enlargement) work started.
October 1999	Completion of main tunnels.

The special features of this method are as follows (Miura, JHPC, 1998):

1. The geological condition of the ground can be evaluated in advance from the TBM pilot.
2. Ground stability is improved due to the effect of drainage into the pilot.
3. Advance reinforcement can be performed from the pilot in locations of unstable ground.
4. The pilot provides the effect of a free surface for blasting.
5. The TBM pilot can be used as a ventilation passage during the enlargement excavation.

Cases of sequential multiple stage construction, like the TBM and enlargement method, have been pointed out by many authorities and engineers. The US Army Core of Engineers (1997) notes that it may be advantageous in cases where:

- The cross section area of the tunnel to be excavated may not be handled by one drilling jumbo unit (i.e., three lane highway tunnels).
- Environmental protection reasons, such as limitations in the vibration levels may disallow the use of total explosive weight (per round).
- Ground conditions may be inappropriate for a full face excavation and stand up time may be limited to allow for installation of primary support.

In addition to these it is also well known that a carefully designed partial excavation causes less disturbance in the ground thus reducing the ground deformations, which is especially important for cases of urban tunneling.

The machine used in the Shimizu tunnel No.3 was a 5.0 m diameter shield rock TBM (named “Suruga No. 1”), which was considered as a rational choice for the ease of construction of the pilot and prereinforcement works. The TBM had two articulation mechanisms (shield joints that form a triple shield unit) which enable driving on a sharp curve. Similar TBM units were used in most Tomei II tunnels such as the Okabe 2.3 and 2.6 km long, twin tunnels. The specifications of the tunnel boring machine used in Shimizu tunnel No.3 are presented here (Ishihara, 2000):

Table 4.2: Tunnel boring machine data for the “Suruga No.1” triple shield.

Excavation Diameter	5.0 m
Length of TBM	11.2 m
Power	1,100 kW
Thrust (max)	7.84 MN (800 tn.)
Boring Stroke	1.5 m
Minimum turning radius	30.0 m
Muck handling capacity	250 m <sup>3</sup> /hr
Weight	300 tn machine
Follow on equipment	80 tn



Figure 4.7 a,b: The triple shield TBM used at the Shimizu site.

The geological environment of Shimizu tunnel No.3 mainly consisted of Neocene sandstone and mudstone (geology described in Chapter 3). According to the JTA, even though some time was spent during the U-turn movement, the TBM progressed almost according to plan. During the excavation of the first pilot heading to Tokyo some seepage was encountered in the rock and an abrupt inflow was also experienced with a flow rate of about 700 ltr/min, improvement was noticed during boring of the second opening and there was almost no seepage. The speed of excavation by the TBM improved after making the U-turn due to the effect of drainage.

Behind the TBM, light reinforcement is used to support the circular opening and if considered necessary, ground pre-improvement were carried out. In more unfavorable conditions the temporary lining is composed of light steel H section sets and shotcrete. Pre-improvement works usually include the insertion and grouting of fiberglass cable elements in the roof area of the pilot boring and less often steel cables (usual lengths in the order of 8-12 m). In certain cases subhorizontal spilling can also be included as a means of forepoling technique. The fiber glass elements are generally preferred for temporary works since they offer high tensile strength (comparable to steel tendons) but also minimal shear strength in such a way that their partial destruction during enlargement is easier.

After the advancement and support of the pilot tunnel, subsequent excavation for the top heading commenced. Craig (2000) reports that the average monthly advancement for the top heading was about 110 m. After the heading has progressed by some rounds (depending on the ground conditions, usually 2 or 3 rounds) rock bolts are installed systematically around the roof of the opening (more details on the installation of support will be discussed in following chapters). Following the rock bolts is the installation of H section steel sets at a specified spacing. In between the sets shotcrete is applied usually with mesh or without mesh or reinforced with fibers. In loose ground conditions the fastest possible support installation is needed to avoid excessive deformations and possible failures. The heading stage is then followed by the bench excavation and support of the tunnel walls by the same system. At the very end, a final shorter excavation of

the tunnel invert is performed and the support ring is closed with the use of shotcrete or cast in place reinforced concrete. In areas of high seepage a watertight membrane is used immediately after the shotcrete layer to seal the lining.

#### 4.5 Tunnel support system

As presented in figure 3.8, designs in the Shimizu tunnel No.3 specified the use of different support systems according to the ground category. For the majority of the tunnel the following system was used (data from Japan Highway Public Corporation, 1998):

##### 1. Primary pre-reinforcement support from pilot 5.0 tunnel.

Pre-reinforcement of the ground may be conducted from the pilot boring when it is deemed as necessary. Pre-improvement is mainly composed of cable elements installed at the roof in order to protect subsequent drill and blast excavation stages. Specifications suggest the following measures:

- Installation of circular steel beams H100 at a spacing of about 1.0 m.
- Application of thin layer of shotcrete to avoid ground loosening and protect pilot during TBM tail operations (muck removal, personnel traffic e.t.c).
- Installation of 8-12 m fiberglass cable elements in pilot tunnel (variable number of installed cables per section). Installation is completed by compact sized drill rig (jumbo).
- In selected locations of the western sector of the tunnel heading to Shizuoka, “Swellex” type bolts, or carbon fiber cables were installed for performance testing.

##### 2. Primary support during enlargement stages.

The support for the final enlargement stage is composed typically of steel beams, shotcrete and rock bolts and commences some distance behind the tunnel face after each blasting round. Figure 4.8 shows typical measurements in shotcrete strength on site

(Ishihara, 2000), while the complete primary support systems selected for the Shimizu tunnel No.3 were:

Table 4.3: Support system utilized in Shimizu tunnel No.3.

	Support std.	Sprayed concrete lining			Steel Arch	Rock bolts (x25)		
		$\sigma_c$	t	Type		$\tau_{ult}$	L	S
		MPa	cm			(MN)	(m)	(m)
CI Section	Standard Support	17.6	20	Normal	H200	0.176	6.0	1.2
Shotcrete & Steel arch Verification section	1	35.3	20	Normal	H150			
	2	35.3	15	Normal	H150			
	3	35.3	15-20	SFRC				
Rock bolt verification section	4	35.3	15-20	Normal	H150	0.304	6.0	2.0
	5	35.3	15-20	Normal	H150	0.176	4.0-6.0	1.0

Note:

- $\sigma_c$ =uniaxial compressive strength
- t=thickness
- L=length
- S=spacing
- 1 tn=0.0098 MN



### Rock Bolt Pattern - Shimizu No.3 Tunnels

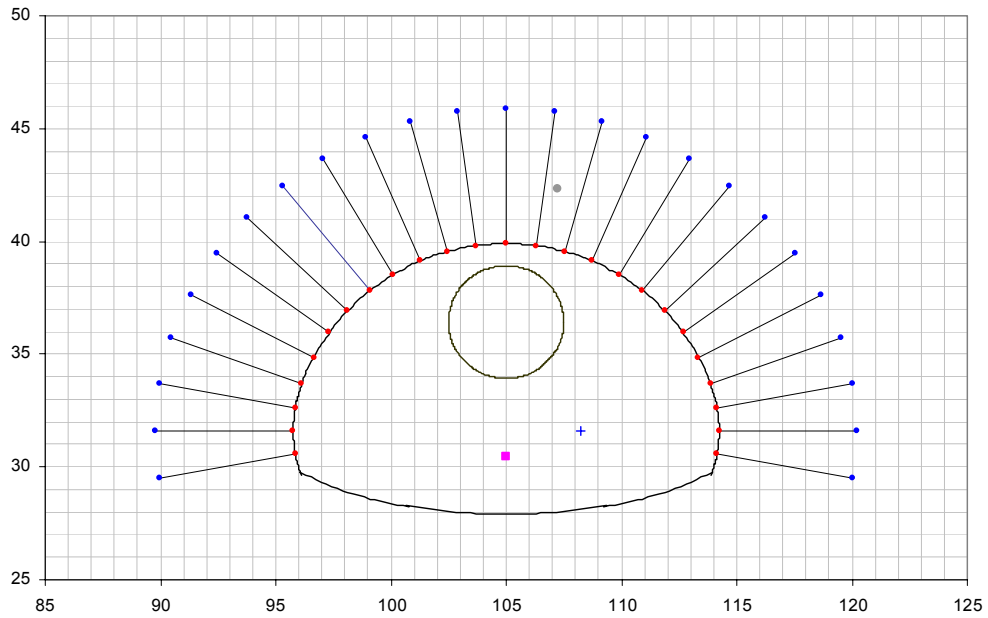


Figure 4.8: Geometry and rock bolt locations for the Shimizu tunnel No.3.

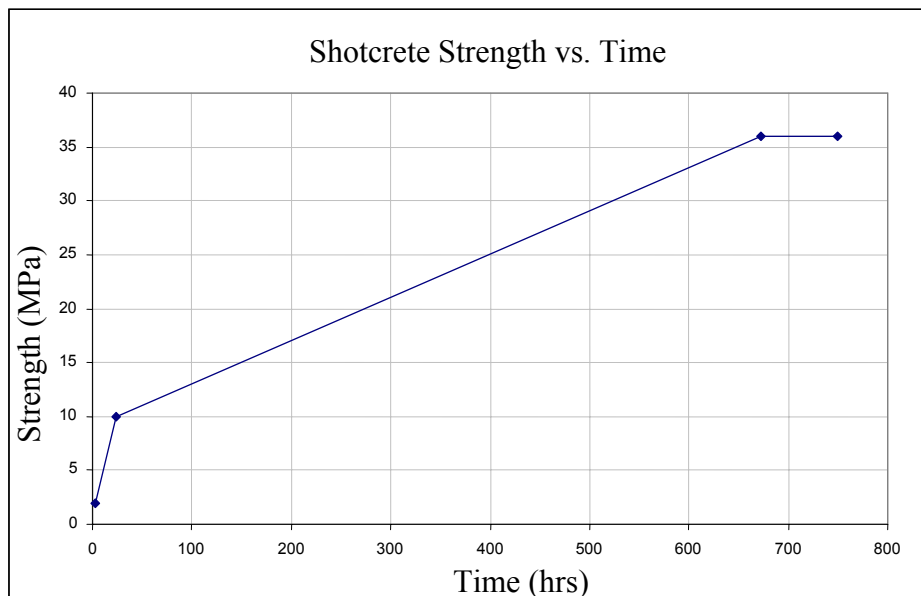


Figure 4.9: Typical results from tested shotcrete uniaxial compressive strength.

$$\sigma_{c \max} = 35.3 \text{ MPa (After, Y.Ishihara, 2001)}$$

### 3. Final (Secondary) lining.

A final cast-in-place concrete lining was also designed and installed. For the cases where rock mass classification was in the range CI-CII, the final lining had a thickness of  $t=30$  cm and included 0.5% per weight, of reinforcing fiber elements. For the cases of DI rock quality the thickness was  $t=40$  cm and fiber concentration was about 1.0% per weight.

These data will be used for numerical analyses that are presented in the following chapters. In figures 4.11, 4.13 and 4.14 the application of the TBM pilot method in the Shimizu tunnel is shown. Fiberglass elements are clearly shown as support in the pilot opening through the Wadajima Sandstone. From figures 4.11 and 4.13 the primary support system has been completed at the section right after the start of the pilot boring (some destroyed plastic elements are still depicted).



Figure 4.10 a,b: Breakthrough of the “Suruga” TBM.



Figure 4.11: TBM pilot tunnel with pre-reinforcement and top heading excavation at Shimizu site. The destroyed plastic cables after blasting can be still seen. (note: illustrated dates are incorrect).



Figure 4.12: Drilling equipment used in Shimizu tunnel No.3.



Figure 4.13: Pilot tunnel with pre-reinforcement and primary support of shotcrete and H100 beams. Top heading with completed primary support up to the face (courtesy: Japan Tunnelling Association).

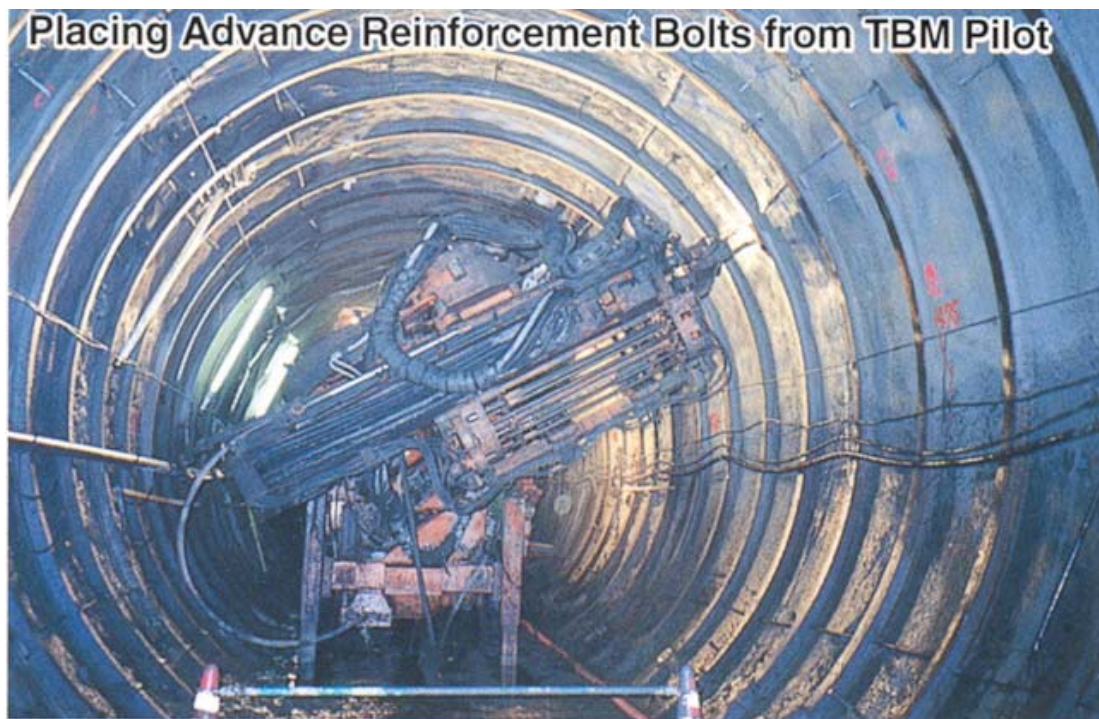


Figure 4.14: Pre-reinforcement from pilot tunnel.

## CHAPTER 5 : Tunnel analysis and design

### 5.1 General

One of the most important elements in design of underground excavations is analysis based on simple or more sophisticated methods. Analysis must be made taking into account realistic representation of the actual in situ conditions including geological and geotechnical parameters. These considerations most often have to deal with simplified identification of the key elements such as the geomechanical character of the ground, the type of the ground, the stress regime prevailing in the area of concern etc. in case precise details are not available. In addition the geometry of the excavation work plays a significant role in the stability performance at a given stress state. Hoek & Brown (1980), Palmstrøm (1995), Martin, Kaiser & McCreath (1997) point out the significance of the shape of the excavation in the stability of the opening. Mahtab and Grasso (1992) , Hoek (1996), Barton and Gutierrez (1995) also note the importance of selection of the appropriate method of analysis for a particular work which is inherently associated with estimates of stress-strain development on the vicinity of the underground project. Furthermore tunneling excavation is a complicated problem due to the interaction between the excavated ground and the support system used.

### 5.2 Available analytical methods

Often multiple step excavations apply more difficulties in the analysis and more elaborate approaches should be followed. Further implications arise when the excavated medium ceases to be a continuum media and is distinguished by fractures and jointing. The behavioral response of such system and its examination under the disturbance caused by an unloading factor is certainly a difficult issue demanding sophisticated means of analysis. The last decade with the quick development of electronic computers and the ability of cheap, fast and reliable processing, the application of advanced analytic tools has become increasingly popular. Einstein and Schwartz (1980) make an excellent review of the analytically based solutions for tunneling problems as they have been proposed by

various researchers. Currently the most popular available methods in the analysis of underground excavations are:

1. Simplified Elastoplastic Analysis.
2. The Convergence – Confinement Method.
3. Finite Element Method.
4. Finite Difference Method.
5. Boundary Element Method.
6. Distinct Element Method.
7. Discontinuous Deformation Analysis.

In the following, the present paper will present the basic principles behind each method and some commercially available computer codes are suggested. Of these methods focus will be given on the Convergence-Confinement Method (Panet, 1995) as well as the Distinct Element Method (Cundall, 1979) that are employed to analyze the tunnel deformations.

### 5.2.1 Analytical solutions

This type of analysis is an analytical method based on “closed-form” solutions for the problem of an isotropically stressed opening in a homogenous medium. This type of analysis has served and still serves many designers and engineers as a rough approximation for deformation and stress development estimates. A major use of this method is as a quick first parametric analysis (Mahtab & Grasso, 1992) for several parameters such as the elastic or strength properties that can aid in the better appreciation and examination of the case. The limitations of the method are also the assumptions behind it:

- The tunnel is circular having a radius  $R$ .
- Plane strain conditions apply to the problem.
- Medium is elastic and perfectly plastic (follows Mohr-Coulomb or the Hoek-Brown failure criteria).

For this type of problem there have been proposed solutions based on no post failure volumetric strain (purely non associated volumetric flow rule) as well as more complex solutions with a fully associated flow rule. There have also been solutions assuming isotropic stress field from Westergaard (1940), Salencon, (1969), Newmark et al. (1970), Hendron & Aiyer (1971) , Jaeger & Cook (1979) and solutions assuming a non hydrostatic field (Detournay, 1983). Furthermore elaborate research has also been focused on the mechanics of interaction between the surrounding ground and the support system by von Rabcewicz (1973) and Einstein & Schwartz (1979). For most cases of circular or near circular problems with a  $K_0$  stress ratio close to unity, a rough approximation can be made by assuming the average insitu stress as isotropic. The following symbols are used in the discussion of the available analytical solutions:

$\sigma_\theta$ = induced tangential stress

$\sigma_r$ = induced radial stress

$p_0$ = insitu isotropic stress

$\sigma_1, \sigma_3$  = insitu major and minor principle stresses.

$u_p$ = deformation in the yielded region

$u_e$ = deformation in the elastic region

$r_p$ = radius of yielded zone.

$\theta$ = angle of assumed point from the horizontal, counterclockwise.

$E$ = Elastic modulus of the material.

$\nu$ = Poisson's ratio

$G$ = Shear modulus.

Elastic Solution for Anisotropic Field:

For a point located at  $(r, \theta)$  polar coordinates and for a circular opening with a radius  $R$  in an infinite elastic region it is (Kirsch, 1898):

$$\frac{2\sigma_r}{\sigma_1 + \sigma_3} = 1 - \frac{R^2}{r^2} + \frac{\sigma_1 - \sigma_3}{\sigma_1 + \sigma_3} \cdot \left(1 - \frac{4R^2}{r^2} + \frac{3R^4}{r^4}\right) \cos(2\theta) \quad \text{Equation 5.1}$$

$$\frac{2\sigma_\theta}{\sigma_1 + \sigma_3} = 1 + \frac{R^2}{r^2} + \frac{\sigma_1 - \sigma_3}{\sigma_1 + \sigma_3} \cdot \left(1 + \frac{3R^4}{r^4}\right) \cos(2\theta) \quad \text{Equation 5.2}$$



$$\frac{2\tau_{r\theta}}{\sigma_1 + \sigma_3} = -\frac{\sigma_1 - \sigma_3}{\sigma_1 + \sigma_3} \cdot \left(1 - \frac{2R^2}{r^2} + \frac{3R^4}{r^4}\right) \sin(2\theta) \quad \text{Equation 5.3}$$

Elastoplastic Solution in Mohr Coulomb Medium with no dilation and Isotropic Field (Salencon, 1969):

The Coulomb criterion is satisfied when:

$$\sigma_\theta = \sigma_r \cdot K_p + 2c' \sqrt{K_p} = \sigma_r K_p + q \quad \text{Equation 5.4}$$

$$K_p = \frac{1 + \sin \phi'}{1 - \sin \phi'} = \tan^2(45 + \phi'/2) \quad \text{Equation 5.5}$$

In the Plastic zone stresses are calculated as follows:

$$\sigma_r = \left( p_i + \frac{2c' \sqrt{K_p}}{K_p - 1} \right) \cdot \left( \frac{r}{R} \right)^{K_p - 1} - \left( \frac{2c' \sqrt{K_p}}{K_p - 1} \right) \quad \text{Equation 5.6}$$

$$\sigma_\theta = \sigma_r \cdot K_p + 2c' \sqrt{K_p} = \sigma_r K_p + q \quad \text{Equation 5.7}$$

In the elastic range the stresses can be calculated from:

- If no plastic zone is formed then:

$$u = R(1 + \nu) \left( \frac{p_o - p_i}{E} \right) \left( \frac{R}{r} \right) \quad \text{Equation 5.8}$$

$$\sigma_r = p_o - (p_o - p_i) \cdot \left( \frac{R}{r} \right)^2 \quad \text{Equation 5.9}$$

$$\sigma_\theta = p_o + (p_o - p_i) \cdot \left( \frac{R}{r} \right)^2 \quad \text{Equation 5.10}$$

- If plastic zone is formed:

The radius of the plastic zone is calculated from:

$$\frac{r_{plastic}}{R} = \left( \frac{2}{K_p + 1} \cdot \frac{\frac{p_o}{2c'\sqrt{K_p}} + \frac{1}{K_p - 1}}{\frac{p_i}{2c'\sqrt{K_p}} + \frac{1}{K_p - 1}} \right)^{1/(K_p - 1)} \quad \text{Equation 5.11}$$

The stresses are:

Elastic range:

$$\sigma_r = p_o - \left[ \frac{r_p^2(1+\nu)}{K_p + 1} \cdot \frac{p_o(K_p - 1) + 2c'\sqrt{K_p}}{E} \right] - \frac{E(1-\nu)}{(1+\nu)(1-2\nu)} \cdot \left(1 - \frac{\nu}{1-\nu}\right) \cdot \frac{1}{r^2} \quad \text{Equation 5.12}$$

$$\sigma_\theta = p_o + \left[ \frac{r_p^2(1+\nu)}{K_p + 1} \cdot \frac{p_o(K_p - 1) + 2c'\sqrt{K_p}}{E} \right] - \frac{E(1-\nu)}{(1+\nu)(1-2\nu)} \cdot \left(1 - \frac{\nu}{1-\nu}\right) \cdot \frac{1}{r^2} \quad \text{Equation 5.13}$$

Plastic range: relations 5.6 & 5.7.

Deformations:

$$\text{Elastic range: Elastic Zone} \quad u = R(1+\nu) \left( \frac{p_o - p_i}{E} \right) \left( \frac{R}{r} \right) \quad \text{Equation 5.14}$$

$$\text{Plastic Zone} \quad u = r_p \left( \frac{1+\nu}{K_p + 1} \right) \frac{p_o(K_p - 1) + 2c'\sqrt{K_p}}{E} \quad \text{Equation 5.15}$$

$$\text{Plastic range:} \quad u = r - \sqrt{r^2 - u_p(2r_p - u_p)} \quad \text{Equation 5.16}$$

Therefore from the above relations and by making the necessary assumptions a radial stress vs. radial displacement plot can be constructed for a circular opening assuming gradual unloading from an initial  $p_o$  stress to zero internal pressure, simulating thus the excavation. This method formulates what is known as a characteristic curve for the ground mass and is the major component of the Convergence–Confinement method (Panet, 1995). The method will be described and used in the following. For subsequent

use a spreadsheet using Excel has been formulated to calculate stresses and deformations in a circular opening using the solution by Salencon (1969) for a Mohr–Coulomb material. A spreadsheet was also formed to calculate stresses and displacements of a tunnel in an elastic medium under anisotropic conditions. Specific calculations will be shown in the next chapter. The major shortcoming of the method is the limitation as far as the geometry is concerned and the assumption of a unique isotropic and homogenous ground. Several researchers have proposed improved solutions for circular openings assuming a separate set of residual shear strength parameters after failure, Jaeger & Cook (1979), Sofianos (2002), while others have also suggested the use of a reduced Elastic modulus and density after failure (Daemen & Fairhurst, 1970).

## 5.2.2 Methods that account for three dimensional effects

### 5.2.2.a The Convergence-Confinement Method

The idea of the ground response curve, or otherwise the “characteristic curve” of the ground mass was first presented by Pacher (1964) as a major design component behind the New Austrian tunneling method. The method was further improved by many researchers (Panet, 1995) and was proposed later by the French Tunneling and Underground Engineering Association (AFTES, 1984) for application in designs becoming a useful preliminary tool in the rational design of tunnels. Initially the ground is assumed to be naturally stressed at a hydrostatic  $p_0$  pressure and a tunnel of radius  $R$  is excavated. Assuming a point in the periphery of the opening as a reference point, some inward displacement (towards the tunnel axis) will be recorded as the tunnel face progresses towards the point of reference. This deformation can be simulated by the action of an equivalent pressure acting internally in the opening which can be expressed as a fraction of the initial in situ  $p_0$  stress. This is called the “equivalent support pressure” since it gives the same radial deformation or otherwise known as “pre-convergence”. At the same time, other phenomena such as the intrusion of the tunnel face in the excavation

take place, but are not considered in this approach.<sup>4</sup> From the initial pressure  $p_o$  the ground is gradually unloaded and for some time it behaves elastically (figure 5.2). After a point is reached, further unloading causes the mass to deform plastically and a failure zone is formed around the opening. The radius of the plastic zone can be estimated by classic elastoplastic analysis.

According to Panet (1995) convergence of the opening can be expressed as a function of several parameters including the distance of the assumed point from the tunnel face, the unsupported distance behind the face and the stiffness of the support system. The convergence – confinement method attempts to associate the convergence of the tunnel with the distance from the tunnel since if such a relation is known then any pre-convergence that has occurred before the support is installed and becomes effective, can be estimated. This is the mechanism exploited by the NATM philosophy and the fact that can lead to economic designs since timing of installation will determine the amount of picked up loads carried by the structural components of the support. The equivalent pressure  $p_i$  is expressed as a function of the insitu pressure by the use of the confinement loss factor  $\lambda$ :

$$p_i = (1 - \lambda)p_o \quad \text{Equation 5.17}$$

The parameter  $\lambda$  varies from 0 for initial conditions, to 1 for a full excavated tunnel and equilibrium conditions. Sakurai (1978) proposed the calculation of the parameter of the loss factor  $\lambda$  along the relative location of the examined section at distance  $x$  from the tunnel face, by the following expression:

$$\lambda(x) = \lambda_o + (1 - \lambda_o) \cdot (1 - e^{\frac{-x}{X}}) \quad \text{Equation 5.18}$$

where:

$$\lambda_o = \lambda(0) = 1/3$$

$X = \text{constant}$

---

<sup>4</sup> The latest Italian approach with the Convergence- Confinement method (Lunardi et al., 2003) takes into account the face intrusion in order to estimate support needs and preimprovement works of the ground ahead.

According to Panet (1995), the greatest challenge is the estimation of the loss factor  $\lambda_d$  at the time of the support system installation, for successful convergence predictions. Panet et al. (1982) and Sulem (1983) substituted the exponential with a factor of the following form in order to be used in an elastoplastic analysis:  $\frac{1}{(a + bx)^2}$ ,

Deffayet (1988), reports that the new model was verified at the Alpine tunnels in Frejus. The convergence equation may be expressed in the form:

$$f[(1 - \lambda)p_o, u] = 0 \quad \text{Equation 5.19}$$

At the time of installation of support at a distance  $d$  from the tunnel face, the radial displacement is:

$$u_d = u_o + a_d(u_\infty - u_o) \quad \text{Equation 5.20}$$

$$a_d = 1 - \left[ \frac{m \cdot R}{m \cdot R + \xi \cdot d} \right]^2 \quad \text{Equation 5.21}$$

The empirical expression of the deformation as a function of the distance from the face is:

$$u_R(x) = u_R(0) + [u_R(\infty) - u_R(0)] \cdot \left\{ 1 - \left[ \frac{m}{m + \xi(-x/R)} \right]^2 \right\} \quad \text{Equation 5.22}$$

$u_R(\infty)$  = final convergence of the tunnel at equilibrium

$u_R(0)$  = convergence at the tunnel face

$\xi = u_{Re}(\infty) / u_R(\infty)$  = ratio of infinite elastic displacement / infinite elastoplastic displacement.

For a homogenous, isotropic ground the infinite elastic displacement is given as:

$$u_{Re}(\infty) = \frac{p_o}{2G} R \quad \text{Equation 5.23}$$

where:

$m$  = an empirical factor

The factors  $m$  and  $\xi$  are a function of the overloading ratio:

$$N_s = \frac{2p_o}{\sigma_{c\ mass}} \quad \text{Equation 5.24}$$

Equivalently  $m$  and  $\xi$  are a function of the shear strength parameters  $c'$ ,  $\phi'$ . In the AFTES recommendations such values for different shear strength parameters ( $N_s$  ratio) are given. For the case of linearly elastic ground behavior, AFTES recommendations suggest the following relation to calculate the confinement loss factor:

$$\lambda_d = 1 - 0.75 \cdot \left[ \frac{0.75 \cdot R}{0.75 \cdot R + d} \right]^2 \quad \text{Equation 5.25}$$

where:

$d$ = distance between support system location and tunnel front.

With respect to the above relation and for  $d=0$ , Panet (1995) notes its dependence on the Poisson's ratio  $\nu$ . Specifically  $\lambda_{d=0}$  varies proportionally in the range 0.2-0.3 for  $0.2 < \nu < 0.5$ . For  $d/R > 0.25$  the relaxation factor becomes independent of the Poisson's ratio. The above relation for  $d=0$  (exactly at the tunnel front) predicts a loss factor of:  $\lambda_d = 1 - 0.75 = 0.25$  which means that some 25% of final deformation is likely to occur at the tunnel face. The ground mass remains in the elastic state if  $N_s \leq 0$ . Figure 5.1 shows the proposed "Panet" curves by AFTES, for use in two dimensional numerical analyses under the aforementioned assumptions. The curves present the variation of the confinement loss factor  $\lambda$  versus the distance from the tunnel front. The curves have been constructed for various values of the  $N_s$  ratio up to 4 ( $p_o = 2 \cdot \sigma_{cm}$ ) for heavily stresses rock masses, by the use of three dimensional finite element analyses, a method that will be described later.

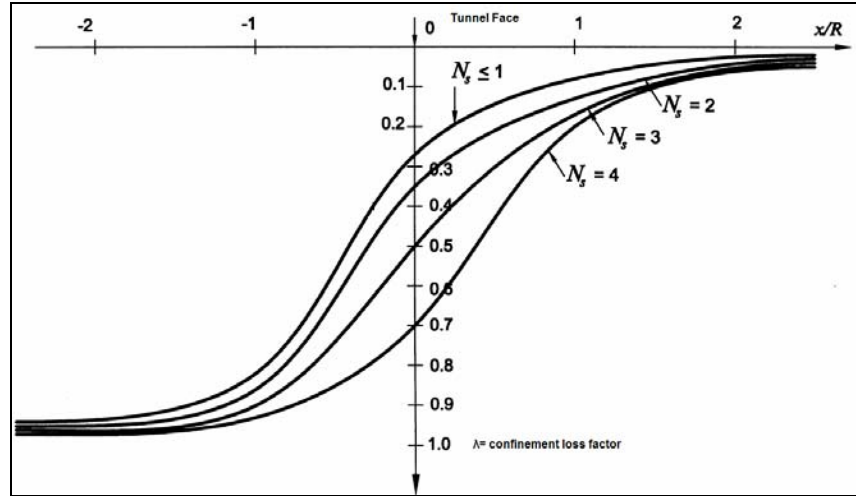


Figure 5.1: Typical curves of loss factor  $\lambda$  versus normalized distance from the face for different values of the  $N_s$  ratio, produced by AFTES. The most reliable method to generate such curves is a full three dimensional numerical analysis (after Kavvadas, 2000).

For an elastic – perfectly plastic ground the final radial displacement is calculated from the relation:

$$u_{final} = u_{\infty} = \frac{1}{\xi} \frac{p_o R}{2G} \quad \text{Equation 5.26}$$

where,

$G$  is the shear modulus of the mass.

Then:

$$a_d = 1 - \left[ \frac{0.75 \cdot R}{0.75 \cdot R + \xi d} \right]^2 \quad \text{Equation 5.27}$$

$$u_d = u_{\infty} \left[ 1 - 0.75 \cdot \left( \frac{0.75 \cdot R}{0.75 \cdot R + \xi \cdot d} \right)^2 \right] \quad \text{Equation 5.28}$$

After the construction of the ground characteristic curve, the method is useful in the calculation of the deformation before placement of the support. This is a powerful tool in cases where two dimensional numerical analysis is conducted (i.e., Finite Element modeling) to investigate stability. In such cases the most desired feature for a precision

made analysis is the ability to account for deformations in the ground before placement of the support system. In the analysis a second curve is also designed which expresses the load-deformation curve of the support system. At the point of intersection of the two curves, equilibrium is achieved between the support and the tunnel. No further deformation occurs past that point, assuming no creep effects in the rock mass. More explicit use and explanation of the method will be given in a later chapter, where coupling with a two dimensional numerical code will be made.

#### 5.2.2.b The equivalent modulus method

Another method for taking into account the effect of support installation delays during tunnel design, which is a similar approach to the convergence confinement method, was proposed by Swoboda & Laabmayr (1978). In their analysis the ground is assumed to be isotropically stressed. As the tunnel advances to a reference section, strains will start developing ahead of the tunnel face and gradual deformations will occur. In this method the excavation is simulated by a gradual factoring of the elastic modulus of the core of the tunnel until a value of  $E_{\text{core}}=0$  for complete deformation (figure 5.3).



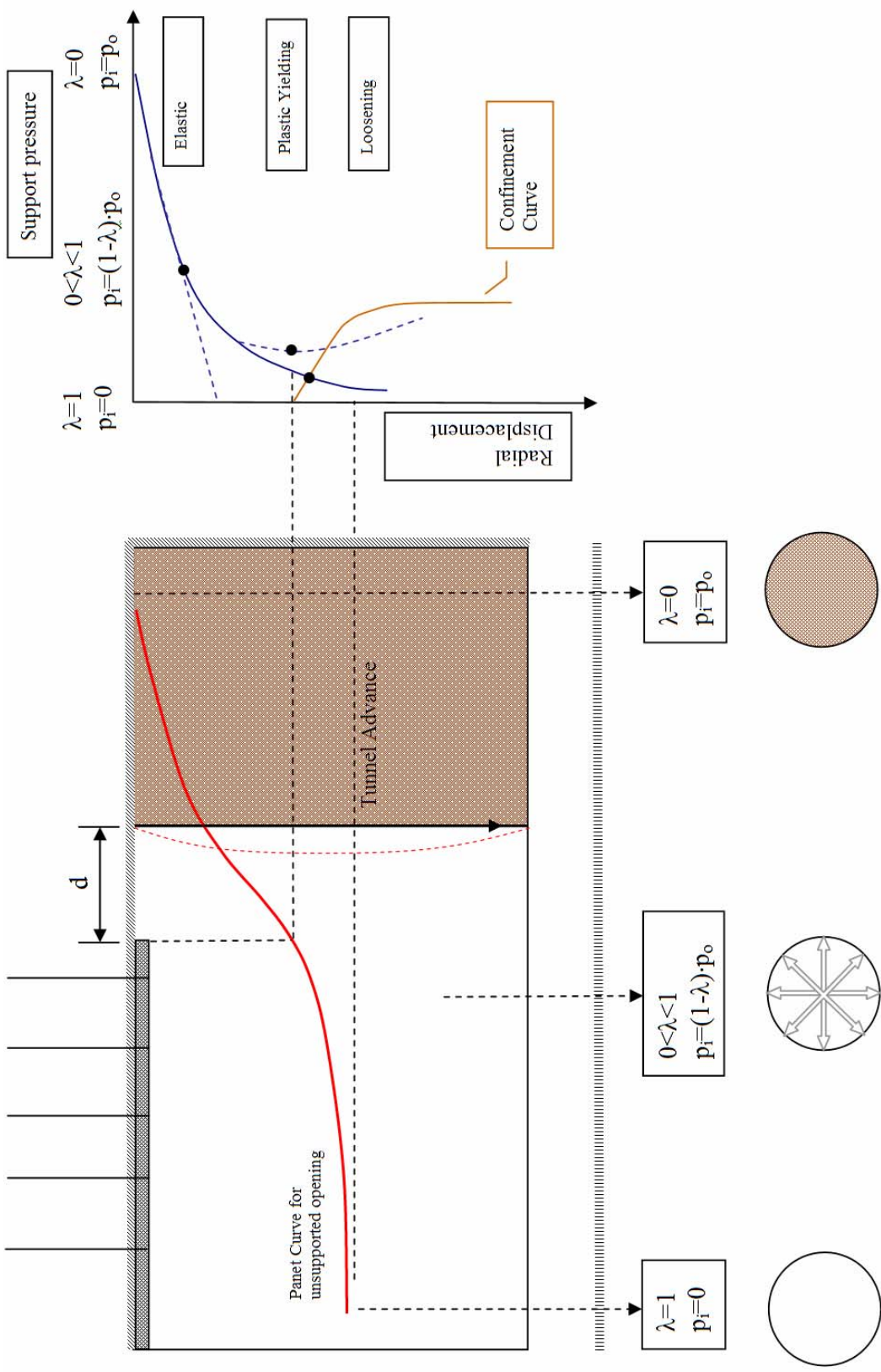


Figure 5.2: The Convergence-Confinement method (after Panet, 1986).

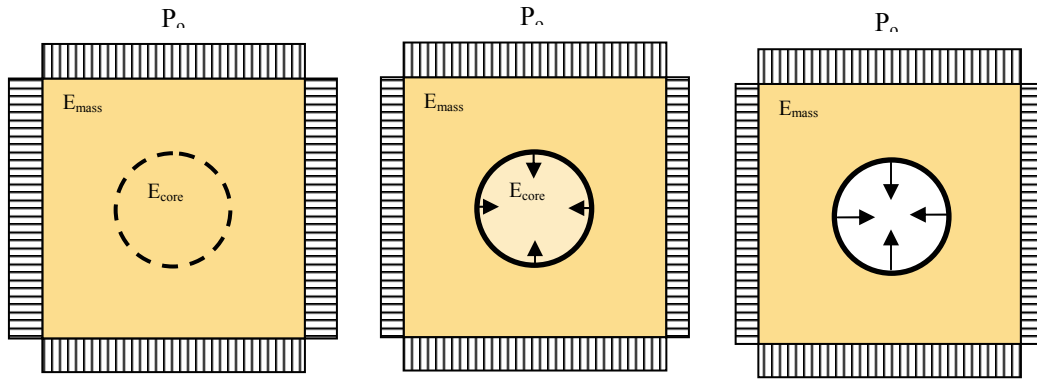


Figure 5.3: The Equivalent modulus method (after Laabmayer and Swoboda, 1978).

Therefore the new modulus for plane strain approximation is:

$$E'_{core} = (1 - \beta) \cdot E \quad \text{Equation 5.29}$$

Swoboda suggests  $\beta=0.5$  for a usual delay ratio. After the modulus reduction, support system is installed and the modulus is zeroed to simulate complete excavation. According to Einstein & Schwarz (1980) under isotropic loading the two methods are the same, while for anisotropic conditions the equivalent internal pressure of the Panet method needs to be anisotropic as well. For isotropic loading in elastic medium a connection between the two methods can be made (Kavvadas, 2000):

The convergence of an elastic disk under all around pressure  $p$  is:

$$u_R = \frac{(1 + \nu) \cdot (1 - 2\nu) \cdot R}{E} p \quad \text{Equation 5.30}$$

The elastic convergence of a circular opening under pressure  $p$  is:

$$u_R = \frac{(1 + \nu) \cdot R}{E} p \quad \text{Equation 5.31}$$

Assuming that the modulus reduction inside the tunnel causes pressure reduction from  $p_o$  to  $p_i$ , the deformations from both equations must be compatible.

The convergence of the disk (internal material) is:

$$u_{R_{\text{int}}} = - \left[ \frac{(1+\nu) \cdot (1-2\nu)R}{E_o} p_o - \frac{(1+\nu) \cdot (1-2\nu)R}{E} p_i \right] \quad \text{Equation 5.32}$$

The convergence of the tunnel under internal pressure  $p_i$  is:

$$u_R = \frac{(1+\nu)R}{E_o} p_o - \frac{(1+\nu)R}{E_o} p_i \quad \text{Equation 5.33}$$

For compatibility:

$$\frac{E}{E_o} = \frac{(1-2\nu) \cdot (1-\lambda)}{(1-2\nu) + \lambda} \quad \text{Equation 5.34}$$

Under isotropic loading Einstein & Schwarz (1980) describe a method to estimate and apply the reduced elastic modulus and arrive at the relation:

$$\beta = \frac{2 \cdot (1-\nu) \cdot (0.02 + 0.57(d/R))}{2(1-\nu) - 0.98 + 0.57(d/R)} \quad \text{Equation 5.35}$$

d= unsupported tunnel length.

### 5.2.3 The Finite Element Method

One of the most popular methods in the numerical analysis applied in engineering is the Finite Element Method. The late development of fast electronic computers has provided the designer-engineer with robust, quick and powerful tools especially in the challenging area of geomechanics. The Finite Element approach was first investigated by Turner et al. (1956) for use in structural analysis. The principal idea behind the method is the subdivision of a continuous material into smaller elementary units the behavior of which can be easily described and expressed by known mathematical relations. Thus the behavior of the whole can be simulated by a series of elements interacting with each other following some principles. Today's numerical codes offer a variety of elements for discretizing continuous systems and each element offers certain advantages and disadvantages. The most usual are the constant strain triangular element (CST) and the isoparametric quadrilateral element (Q4). Discussion of the formulation of Finite Element

method is beyond the scope of this paper and only some brief characteristics are given. The greatest advantage in the use of finite element modeling is the ability to closely represent the true conditions of the problem including gradual alterations in the model, such as the staged construction of a tunnel (excavation and support sequence).

The general steps in the formulation of a Finite Element model for a stress-strain problem are (after Gutierrez, 2001):

1. Discretization of model into elements connected at nodal points.
2. Recognition and expression of the physical quantities (i.e., displacements) using known functions and by applying appropriate interelementary nodal conditions, by following the principle of continuity of displacements and zero strain for rigid displacement of an element.
3. Assembly of all elementary stiffness matrices using appropriate stress-strain model and representation of a continuous system by assembly of a global stiffness matrix.
4. Assembly of the load vector table and insertion of appropriate boundary conditions.
5. Numerical solution of the system of equations
6. Back calculation of strains.
7. Final calculation of stresses.

Today there is a wealth of commercially available Finite Element computer programs specifically suited for geomechanics applications including tunneling. Most of the programs can handle two dimensional plane strain, plane stress or axisymmetric problems including highly sophisticated constitutive models. With the Finite Element method anisotropy, nonlinear behavior of ground, and staged construction can be accommodated rigorously. However, in elongated staged underground excavations the gradual unloading stress path for such cases is difficult to be simulated in two dimensions due to the existence of a third dimension influence especially in section areas close to the tunnel face. For these cases dedicated three dimensional analyses are theoretically more appropriate but generally demand higher computing effort and model set up time. The finite element method, however, is not a panacea and should always be applied with

engineering judgment. Clough (1980), Philip (1991) and Gutierrez (2001) identify the danger of tendency of modern users who are tempted by the power and features of new codes, to create so complex models that become impossible to control at the end. Some (but not all) popular commercially available finite element codes today for use in geomechanics analyses are:

- Abaqus (2D and 3D) (Hibbitt, Karlsson & Sorensen, 1978) – General FEM.
- BEFE (2D and 3D) (Boundary Element and Finite Element, Beer, 2001)
- Caesar LCPC (2D and 3D) (Laboratoire Central des Pontes et Chaussées)
- Diana (2D and 3D) (TNO Diana, 2003)- General FEM
- Phases 2 (2D) (Rocscience, 2001)
- Plaxis 8.0, and Plaxis Tunnel (2D and 3D) (Vermeer & De Brost, 1981)
- TALPA (2D) (Sofistik Aktiengesellschaft, 2003)

#### 5.2.4 The Finite Difference Method

This approach is similar to the Finite Element modeling but its formulation offers faster solution of the governing differential equations. According to Mahtab & Grasso (1992) its first application can be attributed to Runge (1908). Jaeger & Cook (1979) identify the difference between the FDM and the FEM in that the FEM establishes a precise solution to a differential approximation of the problem while the Finite Difference gives an approximate solution to approximate differential equations. Similar to the Finite Element method, the continuum medium is discretized into elements connected to grid points. All the terms involved in the partial differential equation are substituted by a difference formula, at all grid points, which may include the values of a shape function (i.e., deformation) at that and at adjacent grid points. By substituting the difference formulae into the PDE, a difference equation is obtained.<sup>5</sup>

One of the widely available Finite Difference software is the code FLAC2D (Fast Lagrangian Analysis of Continua), (Cundall, 1976) and FLAC3D (Cundall, 1983). Of the two methods, the FEM and the FDM, a significant issue often arises on whether or

---

<sup>5</sup> Data from [www.numerical methods.com](http://www.numerical methods.com)

not the formulation can sustain and solve large strain problems. For the most part codes that are based on small strain theory, i.e., the continuum is assumed not to deform appreciably from its initial geometry, upon which the formulation is based, may misbehave or even numerically collapse during the analysis. FLAC (Cundall, 1976) is a code that can cope with large strain problems.

### 5.2.5 The Boundary Element Method

The boundary element method (BEM) is another available tool for geomechanics applications. In this method a simplifying technique is used where only the boundary of the domain of interest (i.e., an underground excavation) requires discretisation into elements, thus providing attractive computational advantages over other methods. The surrounding rock mass is simulated as a infinite continuous medium and thus boundaries are not needed to be included in a model. The formulation of the BEM requires the governing partial differential equation to be reformulated as an integral equation (Crotty and Wardle, 1985). According to [www.numericalmethods.com](http://www.numericalmethods.com), the method is more often applied to problems of linear elasticity. A disadvantage of the method is that modeling of sequential excavations is extremely difficult numerically.

Gutierrez and Barton (1995) suggest the use of the Boundary Element method for rock excavation problems with a Q quality index in the range of  $Q=100$ . In the Boundary Element Method the solution to the continuum problem starts by the creation of an initial simple linearly elastic model, which forms an infinite domain where the excavation can take place, taking into account initial stresses ( $K_0$  ratio). All features such as zones of different materials, zones of different constitutive modeling (i.e., plasticity), discontinuities or other external factors (i.e., loads) can be simulation by superposition of separate “models” with independent boundary elements. The complete superposition of the models by application of necessary connecting relations, can yield to a solution of the problem (Mahtab & Grasso, 1992). There have been various computer codes for use in geomechanics many of which are intended for elastoplastic analyses such as the codes: Examine2D, 3D (Rocscience Inc., 2000) and Map3D (Mine Modelling Pty., 2003).

## 5.2.6 The Distinct Element Method

The Distinct Element Method was initially presented and developed by Cundall (1971) and was later implemented in the numerical code UDEC (Universal Distinct Element Code), (Cundall 1980; Cundall & Hart 1985) for static or dynamic analyses in rock mechanics problems. Later on research by Cundall (1983) yielded to the development of a three dimensional distinct element code 3DEC (Cundall 1988; Hart 1988). For rock mechanics problems, a key issue in analyses is the behavior of discontinuous masses, that include one or more joint sets or other discontinuity features. This behavior is difficult if not impossible to be included in a continuum formulation. Some numerical codes are able to implement certain features using interface finite elements or incorporate ubiquitous joint formulations. Despite this fact, the full simulation of the true mass is not achieved and often numerical difficulties may occur since these models may not be able to handle efficiently multiple discontinuities. (Itasca, 2000). According to the architects of the method the main aspects behind the formulation of the distinct element analysis are:

- Ability to calculate infinitesimal strains, rotational behavior of blocks including complete separation.
- Automatic recognition of new contacts between the blocks.

In this method, the domain is simulated by a group of “discrete” blocks and joints which are simulated as boundary conditions between the blocks, thus simulating explicitly a fractured rock mass behavior. The independent blocks can be rigid or deformable. For the later case the blocks are discretized into elements following a finite element or finite difference formulation. In the Distinct Element Method, the governing differential equations dictate the kinematics of the blocks in the assemblage. The numerical solution targets in converging to an acceptable displacement in order for grid forces to equilibriate. At that state out of balance forces are minimized. Therefore the individual blocks can interact following some behavioral model and deformation can also occur in the blocks thus the complete mass can be better modeled approximating the true

conditions. Barton and Gutierrez (1995) advice the use of the DEM method for rock mechanics problems of  $0.1 < Q < 100$ .

### 5.2.7 Discontinuous Deformation Analysis (DDA)

This is a similar approach to the DEM and the mass under numerical study is composed of an assemblage of discrete blocks that can be deformable. In this case the solution is based on minimization of the energy potential developed in the system with respect to deformations, rather than forces (Shi & Goodman 1984; Shi 1988). Lately this method was adapted for Windows computer environment (Sitar & McLaughlin, 1997). According to Sitar & McLaughlin (1997) contact detection logic is implemented in the code DDA similar to the DEM. Contact detection is performed in order to recognize the association between edges and corners between blocks. In this method interpenetration of blocks is avoided by a numerical iterative (algorithmic) procedure and thus the contacts are assumed to be rigid. The network of discontinuities, which are simulated by springs, creates and stores its own energy due to the above interpenetration canceling technique. The code tries to find the necessary compatible displacements of the blocks, so that this energy is minimized. The residual energy is then used to back calculate contact forces, element stresses etc. Like the DEM, DDA has been successful in simulating various geotechnical engineering problems such as rock slope stability, and underground excavations in fractured rock masses.

### 5.2.8 Previous numerical simulations for the Shimizu tunnel No.3

Numerical studies for the Shimizu tunnel No.3 were performed with three dimensional finite element modeling (Japan Highways, 1998) with simplified geometries during parametric analyses and initial tunnel method verification. Discontinuity features, which cause degradation of the rock mass behavior, were simulated by reduced shear strength and elastic parameters. Preliminary studies were also performed by the FUJI Research Group (1998) by use of two dimensional (Barton & Gutierrez, 1995) and three dimensional (Barton & Crysanthakis, 1995) distinct element analyses. In this study the commercially available code UDEC 3.1 (Itasca, 2000) is used to assess the tunnel



deformations. In the following chapter details of the distinct element code formulation are given along with the preliminary analysis set up.

## CHAPTER 6 : Numerical analyses using the Distinct Element Method

### 6.1 Modeling parameters

In the analysis for Shimizu tunnel No.3, the code UDEC-BB (Universal Distinct Element Code) ver. 3.1 was used to model and examine the rock mass behavior during the excavation stages. This code offers the advantage of simulating block interaction with individual joint behavior coupled with discrete behavior of the blocks. UDEC 3.1 is a two dimensional DEM code suited for plane strain problems such as tunnels, by assuming that the deformation of the mass perpendicular to the model is small enough. The discontinuity features are inherently assumed to strike perpendicular to the model section. This approach appears unrealistic in some cases. However, full representation using a full three dimensional distinct element analysis would demand excessive computing efforts and time, well beyond the scope of this analysis. Furthermore, joint orientation data presented in chapter 3, show that the major joint sets J1 (bedding) and J2 (cross joints) strike subparallel to the tunnel axis thus the assumption is considered to be rational. According to Itasca (2000), UDEC makes use of an explicit time stepping algorithmic process which allows for large deformation capabilities. Specific capabilities of UDEC include:

- Ability to simulate all stages of a staged construction (i.e., tunneling)
- Incorporation of non linear structural support elements including beam elements, rock bolts and cables.
- Allows for elastoplastic analysis of block material using the Coulomb and the Hoek-Brown failure criteria, including post failure dilative response.
- Allows simulation of the joint behavior using an appropriate constitutive model including the Coulomb slip and Barton-Bandis models.

Figure 6.1 shows the calculation cycle use in UDEC while figure 6.2 shows the discretization of distinct blocks into finite difference zones connected at gridpoints. The code uses constant strain elements (CST) which is the simplest triangular element formulation. The equivalent boundary condition expressing joint behavior is composed of

a normal elastic spring having a normal stiffness  $K_n$ , and an elastoplastic spring-slider with shear stiffness  $K_s$  and shear strength parameter  $\mu$  expressing the frictional resistance.

## 6.2 Main features of the DEM formulation

Perhaps the most important aspect behind the DEM, is the automatic contact recognition. This technique is responsible for the simulation of the fractured rock mass as correctly as possible, since during rock mass deformation shear displacements (slips) occur. First, the contact detection in UDEC uses edge to corner and corner to corner associated contacts. Specifically when using non deformable intact blocks contact points are automatically created at the corner points and meet the adjacent blocks either to the corner or to the edge. For the case of material deformability, point contacts are assumed exactly at the gridpoints of the discretization everywhere in the block (Itasca, 2000). To avoid cases of intact block “lockups” or contact overlaps and subsequent code misbehavior, a parameter expressing the corner rounding length can be prescribed in the analysis so as to deconvolve the assemblage system and relieve the rotational momentum of the blocks during deformations (figure 6.3).

Another significant issue for cases of full elastoplastic analysis is the ability of the code to perform plastic flow calculations based on the finite difference elements within intact blocks. According to Itasca (2000), during such an analysis there is a chance of overestimating the “collapse load” inside the triangular elements. This is a case occurring in many finite element computer codes and happens when a specific element in the mesh of a plane strain model becomes kinematically constrained mainly due to the plane strain formulation while this is of course an unnatural condition. This condition referred to as “mesh-locking” and results in a somewhat unconservative analysis. The code incorporates an automatic mesh generator that creates triangular and diagonally opposed elements in certain cases to better calculate plastic flow. For enhanced analysis in geometries where such meshing cannot be made, reduced zone length and finer element mesh should be constructed at least in the vicinity of the area where sudden changes will take place and most strains are likely to develop.

Additionally an important (optional) parameter used by UDEC in order to achieve fast convergence to an equilibrium solution, is the use of a damping factor in quasi-static or dynamic problems. For the case of static analysis UDEC makes use of mechanical velocity dependent damping. Itasca (2000) recognizes the following potential problems when it comes to the application of a damping factor:

- Application of damping includes the involvement of fictitious forces in the numerical system that may lead to erroneous results for elastoplastic analysis.
- Optimized block velocity dependent damping factors can only be calculated after a complete numerical evaluation of the eigenvalues of the matrix including the system of equations. Exact solution of this issue may need high computing effort.
- Nodal application of a constant damping factor for all the model may cause unjustified differences in yielding zone analysis in a model from location to location. According to Itasca this would need the application of a constantly varying damping factor in different areas.

UDEC incorporates automatic global viscous damping which absorbs kinetic energy depending on the rate of kinetic energy change, thus velocity. For this reason this method is also recognized as servo-controlled damping. A second more sophisticated damping technique can alternatively be used called “local damping”, which applies an adaptive discrete damping to all nodes.

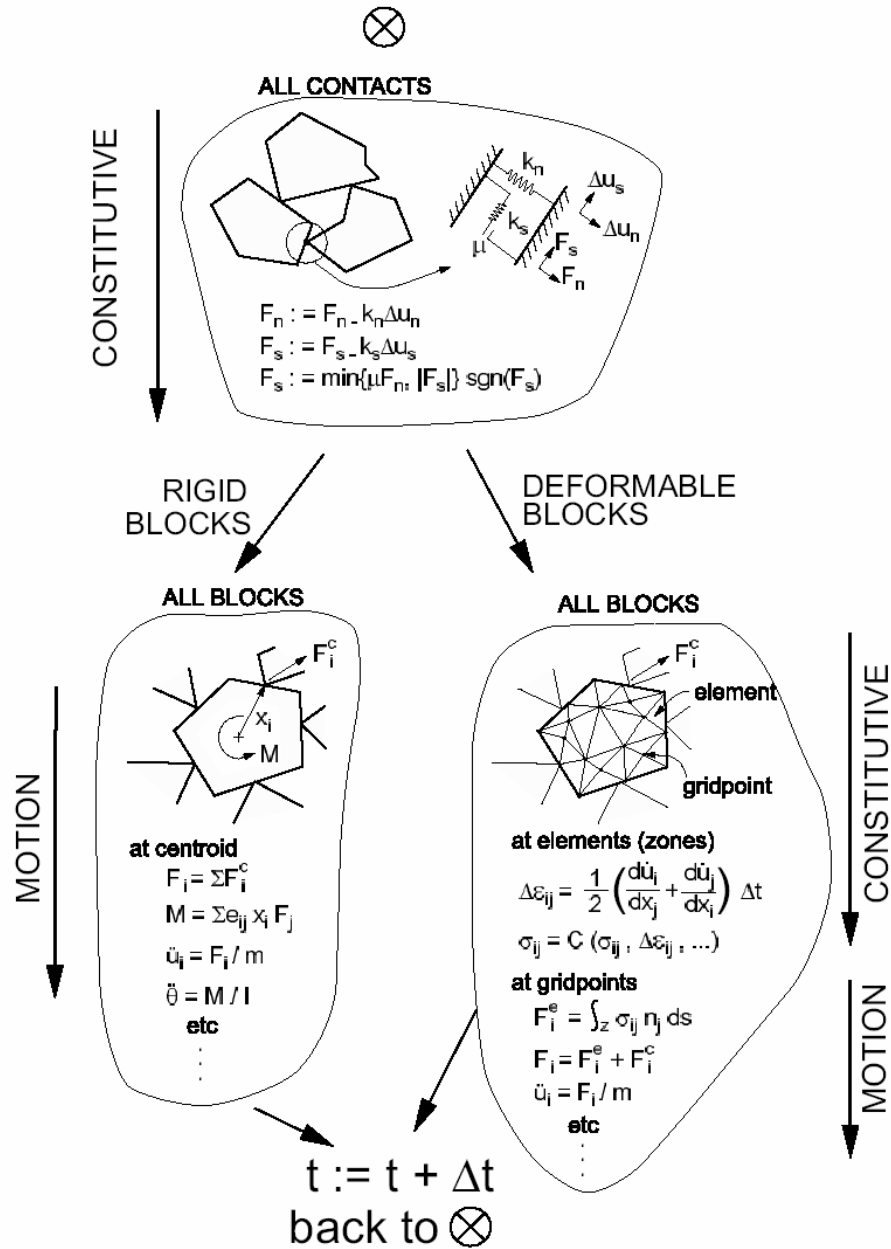


Figure 6.1: The computational cycle used by UDEC (Itasca,2000).

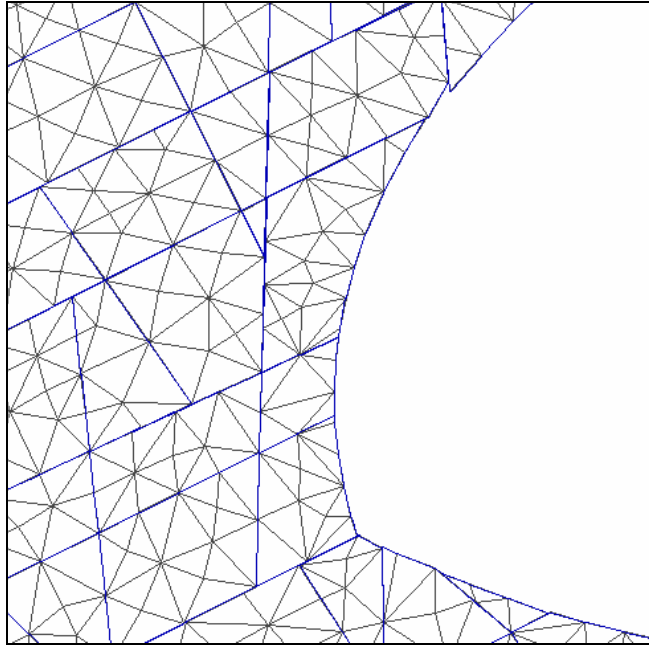


Figure 6.2: Detail of a distinct element model in UDEC. Blocks are being divided into finite difference zones for elastoplastic analysis.

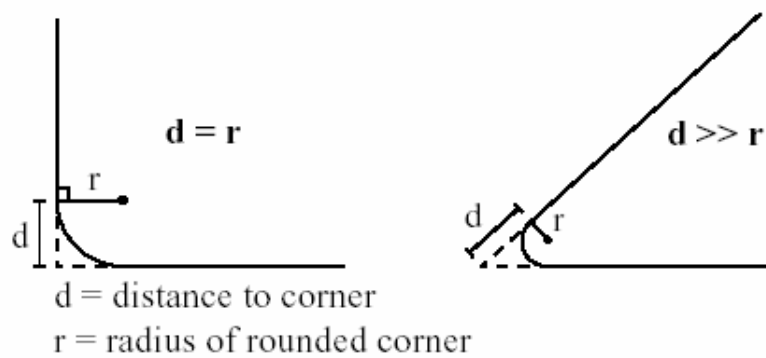


Figure 6.3: Corner rounding length definition used by UDEC (After Itasca,2000).

## 6.3 Application of the Barton-Bandis model in UDEC

In the analyses of Shimizu tunnel No.3, the Mohr-Coulomb constitutive model was assumed for the intact rock strength and the Barton- Bandis model was used to simulate joint behavior. Normal behavior of joints was thoroughly examined by Bandis (1980), Barton & Bandis (1983). Multiple direct shear tests were performed on various rock types such as slate, dolerite, limestone, siltstone and sandstone. Tests were conducted on similarly weathered intact rock samples and on specimens with matching and mismatching fractures, in order to calculate joint deformation.

### 6.3.1 Normal behavior

The model proposed by Bandis (1980) includes a hyperbolic normal stress-strain relation for normal loading and unloading based on the following empirical relations:

Initial joint aperture:

$$E_o \approx \frac{JRC}{5} \left( \frac{0.2\sigma_c}{JCS} - 0.1 \right) \quad \text{Equation 6.1}$$

$$\frac{\Delta V_j}{\sigma_n} = a - b \cdot \Delta V_j \quad \text{Equation 6.2}$$

where:

$\Delta V_j$  = joint closure

$\sigma_n$  = normal load

a,b = empirical constants expressing the hyperbola geometry.

$V_{\max} = a/b$  = maximum closure for a given loading cycle.

The empirical relations associating maximum deformation and initial stiffness, are given here:

$$V_m \cong A + B[JRC_o] + C \left[ \frac{JCS_o}{a_j} \right]^D \quad \text{Equation 6.3}$$

$$K_{n_{initial}} = 0.02 \left[ \frac{JCS_o}{a_j} \right] + 2JRC_o - 10 \quad \text{Equation 6.4}$$

in UDEC an improvement of the above relations is used for any load cycle  $i$  :

$$V_{mi} \cong A_i + B_i[JRC_o] + C_i \left[ \frac{JCS_o}{a_{j_n}} \right]^{Di} \quad \text{Equation 6.5}$$

$$K_{ni} = 0.0178 \left[ \frac{JCS_o}{a_{j_n}} \right] + 1.748JRC_o - 7.155 \quad \text{Equation 6.6}$$

where:

$JCS_o$ =joint compressive strength at reference lab scale.

$JRC_o$ =joint roughness coefficient at reference lab scale.

$a_{jn}$ =joint aperture at zero normal stress

A,B,C and D empirical parameters based on load cycle number whose values are given by Bandis et al. (1986).

For unloading cycles the previous relations for maximum rebound opening and unloading modulus are used in UDEC. A new  $a_{jn}$  used for unloading is the previous  $a_{jn}$  reduced by the permanent deformation  $u_{irr}$ .

$$u_{irr} = \left[ C_1 - C_2 \cdot \left( \frac{JCS_o}{a_{j_n}} \right) \right] \frac{u_{nl}}{100} \quad \text{Equation 6.7}$$

where,

$C_1, C_2$  parameters. Tables for  $C_1, C_2$  are given by Bandis et.al (1986)

$u_{nl}$  is the maximum closure for a complete load cycle.



An example from Bandis & Bakhtar (1985) showing the behavior under normal loading is shown in the spreadsheet implementation according of the Barton-Bandis model. For illustrative purposes the following values are taken as input:

Table 6.1: Example values for joint shear strength comparisons using the Barton-Bandis model (After Bandis, 1985)

Barton- Bandis parameter	case 1	case 2
JCS (MPa)	100	100
JRC	5	15
$\sigma_c$ (MPa)	150	150

From the specific examples it is possible to notice the difference in behavior of the two joints that differ only in the roughness parameter. According to Bandis et al. (1986) final closure under normal repetitive loading is more complete in the case of the smooth joint (JRC=5) than in the case of the rough joint (JRC=15), which has been validated also by laboratory measurements.

Table 6.2 : Example of joint closure under normal loading JRC=5, JCS=100 MPa,  $\sigma_c=150$  MPa.

Barton Bandis Joint Model - Behavior under normal loading

Created by : Norwegian Geotechnical Institute

NORMAL CLOSURE CALCULATION

INPUT PARAMETERS			$\sigma_n$	CYCLE 1	CYCLE 2	CYCLE 3	CYCLE 4	CYCLE 5	
JRC	5		LOAD	50	50	50	50	0	MPa
JCS	100		UNLOAD	0	0	0	0	0	MPa
SIGMAC	150		APERTURE	0.200	0.081	0.062	0.057	0.056	mm
			KNP	9.4E+03	3.2E+04	6.0E+04	7.0E+04	3.3E+01	

OUTPUT PARAMETERS

LOADING		KNi	10.49	23.60	30.14	33.01	33.44	33.44	MPa/mm
		VMI	-0.165	-0.059	-0.038	-0.034	-0.033	-0.033	mm
		$\alpha$ (hyperbolic)	0.095	0.042	0.033	0.030	0.030	0.030	
		b (hyperbolic)	0.578	0.712	0.875	0.899	0.903	0.903	

UNLOADING		KNi'	23.60	30.14	33.01	33.44	33.44	33.44	MPa/mm
		VIRR	-0.119	-0.019	-0.006	-0.001	0.000	0.000	mm
		DSM	-0.119	-0.138	-0.143	-0.144	-0.144	-0.144	
		SIRR	-0.119	-0.138	-0.143	-0.144	-0.144	-0.119	
		AJ'	0.042	0.033	0.030	0.030	0.030	0.030	
		BJ'	1.034	0.823	0.945	0.909	0.909	0.909	
		VMI'	-0.041	-0.040	-0.032	-0.033	-0.033	-0.033	

CONSTANTS

	CYCLE 1	CYCLE 2	CYCLE 3	CYCLE 4
A	-0.2960	-0.1001	-0.1031	-0.1031
B	-0.0056	-0.0073	-0.0074	-0.0074
C	2.2410	1.0082	1.1350	1.1350
D	-0.2450	-0.2300	-0.2510	-0.2510
C1	84.77	44.37	31.38	20.00
C2	0.02	0.01	0.01	0.01
JRC <sup>2.5</sup>	56			

DATA CYCLE 1	NORMAL STRESS							
			delta E	E	e	delta e	COND m2	COND cm2
0.0	0.000	0.00	200.00	200.00	0.00	-8.4771	-4.4771	
2.5	-0.097	97.47	102.53	102.53	97.47	-9.0575	-5.0575	
5.0	-0.123	122.51	77.49	77.49	122.51	-9.3007	-5.3007	
7.5	-0.134	133.99	66.01	66.01	133.99	-9.4399	-5.4399	
10.0	-0.141	140.57	59.43	59.43	140.57	-9.5312	-5.5312	
12.5	-0.145	144.84	55.16	54.43	145.57	-9.6075	-5.6075	
15.0	-0.148	147.83	52.17	48.68	151.32	-9.7045	-5.7045	
17.5	-0.150	150.05	49.95	44.63	155.37	-9.7799	-5.7799	
20.0	-0.152	151.75	48.25	41.64	158.36	-9.8402	-5.8402	
22.5	-0.153	153.11	46.89	39.33	160.67	-9.8896	-5.8896	
25.0	-0.154	154.21	45.79	37.51	162.49	-9.9309	-5.9309	
27.5	-0.155	155.12	44.88	36.03	163.97	-9.9658	-5.9658	
30.0	-0.156	155.89	44.11	34.81	165.19	-9.9958	-5.9958	
32.5	-0.157	156.54	43.46	33.78	166.22	-10.0218	-6.0218	
35.0	-0.157	157.11	42.89	32.91	167.09	-10.0447	-6.0447	
37.5	-0.158	157.61	42.39	32.15	167.85	-10.0648	-6.0648	
40.0	-0.158	158.04	41.96	31.49	168.51	-10.0827	-6.0827	
42.5	-0.158	158.43	41.57	30.92	169.08	-10.0988	-6.0988	
45.0	-0.159	158.77	41.23	30.41	169.59	-10.1133	-6.1133	
47.5	-0.159	159.08	40.92	29.95	170.05	-10.1264	-6.1264	
50.0	-0.159	159.36	40.64	29.54	170.46	-10.1383	-6.1383	

Table 6.3: Example of joint closure under normal loading JRC=15, JCS=100 MPa,  $\sigma_c=150$  MPa.

Barton Bandis Joint Model - Behavior under normal loading

Created by : Norwegian Geotechnical Institute

NORMAL CLOSURE CALCULATION

INPUT PARAMETERS			$\sigma_n$	CYCLE 1	CYCLE 2	CYCLE 3	CYCLE 4	CYCLE 5	
JRC	15		LOAD	50	50	50	50	0	MPa
JCS	100		UNLOAD	0	0	0	0	0	MPa
SIGMAC	150		APERTURE	0.600	0.410	0.380	0.361	0.351	mm
			KNP	2.1E+03	2.0E+04	2.6E+04	2.8E+04	2.4E+01	

OUTPUT PARAMETERS

LOADING		KNi	22.03	23.41	23.75	23.99	24.14	MPa/mm
		VMI	-0.260	-0.075	-0.066	-0.063	-0.061	mm
		$\alpha$ (hyperbolic)	0.045	0.043	0.042	0.042	0.041	
		b (hyperbolic)	0.175	0.568	0.637	0.666	0.684	

UNLOADING		KNi'	23.41	23.75	23.99	24.14	24.14	MPa/mm
		VIRR	-0.190	-0.030	-0.018	-0.010	0.000	mm
		DSM	-0.190	-0.220	-0.239	-0.249	-0.249	
		SIRR	-0.190	-0.220	-0.239	-0.249	-0.190	
		AJ'	0.043	0.042	0.042	0.041	0.041	
		BJ'	0.967	0.978	0.893	0.804		
		VMI'	-0.044	-0.043	-0.047	-0.052		

CONSTANTS

	CYCLE 1	CYCLE 2	CYCLE 3	CYCLE 4
A	-0.2960	-0.1001	-0.1031	-0.1031
B	-0.0056	-0.0073	-0.0074	-0.0074
C	2.2410	1.0082	1.1350	1.1350
D	-0.2450	-0.2300	-0.2510	-0.2510
C1	84.77	44.37	31.38	20.00
C2	0.02	0.01	0.01	0.01
JRC <sup>2.5</sup>	871			

DATA CYCLE 1	NORMAL STRESS							
		delta E	E	e	delta e	COND m2	COND cm2	
0.0	0.000	0.00	600.00	413.12	0.00	-7.8470	-3.8470	
2.5	-0.079	78.98	521.02	311.51	101.61	-8.0922	-4.0922	
5.0	-0.121	121.15	478.85	263.13	149.98	-8.2388	-4.2388	
7.5	-0.147	147.37	452.63	235.10	178.01	-8.3367	-4.3367	
10.0	-0.165	165.25	434.75	216.89	196.23	-8.4067	-4.4067	
12.5	-0.178	178.23	421.77	204.14	208.98	-8.4593	-4.4593	
15.0	-0.188	188.08	411.92	194.72	218.40	-8.5004	-4.5004	
17.5	-0.196	195.81	404.19	187.48	225.64	-8.5333	-4.5333	
20.0	-0.202	202.03	397.97	181.75	231.37	-8.5602	-4.5602	
22.5	-0.207	207.15	392.85	177.10	236.02	-8.5827	-4.5827	
25.0	-0.211	211.44	388.56	173.25	239.87	-8.6018	-4.6018	
27.5	-0.215	215.09	384.91	170.02	243.10	-8.6182	-4.6182	
30.0	-0.218	218.22	381.78	167.26	245.86	-8.6324	-4.6324	
32.5	-0.221	220.94	379.06	164.88	248.23	-8.6448	-4.6448	
35.0	-0.223	223.33	376.67	162.81	250.31	-8.6558	-4.6558	
37.5	-0.225	225.45	374.55	160.99	252.13	-8.6656	-4.6656	
40.0	-0.227	227.33	372.67	159.38	253.74	-8.6743	-4.6743	
42.5	-0.229	229.01	370.99	157.94	255.18	-8.6822	-4.6822	
45.0	-0.231	230.54	369.46	156.65	256.47	-8.6893	-4.6893	
47.5	-0.232	231.91	368.09	155.48	257.64	-8.6958	-4.6958	
50.0	-0.233	233.17	366.83	154.42	258.70	-8.7018	-4.7018	

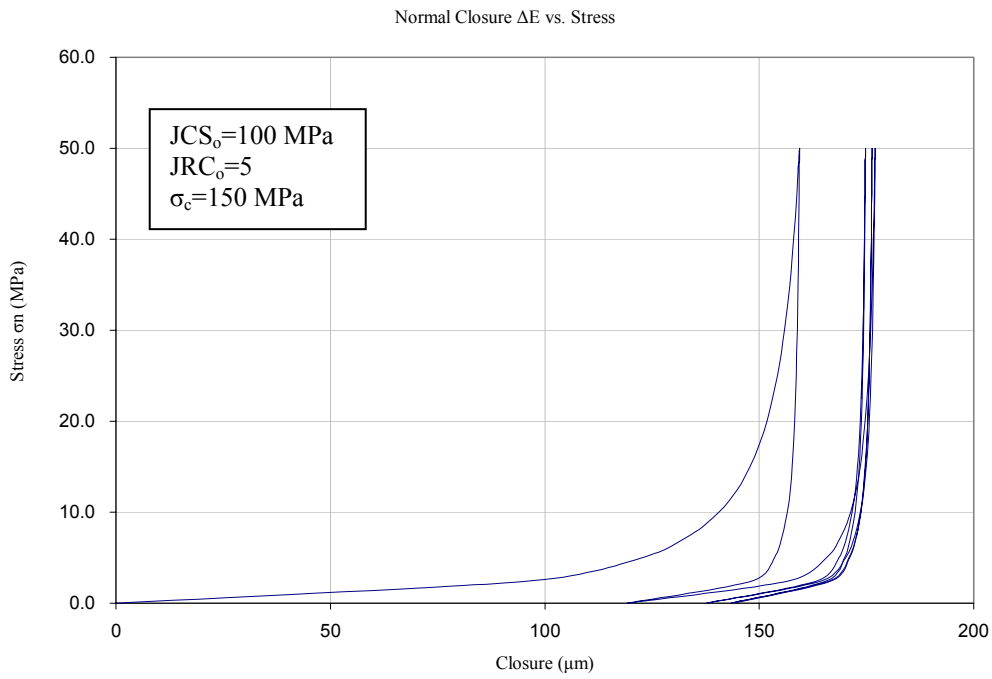


Figure 6.4: Normal closure under cyclic normal loading of the joint (case 1, after Bandis et al., 1985)

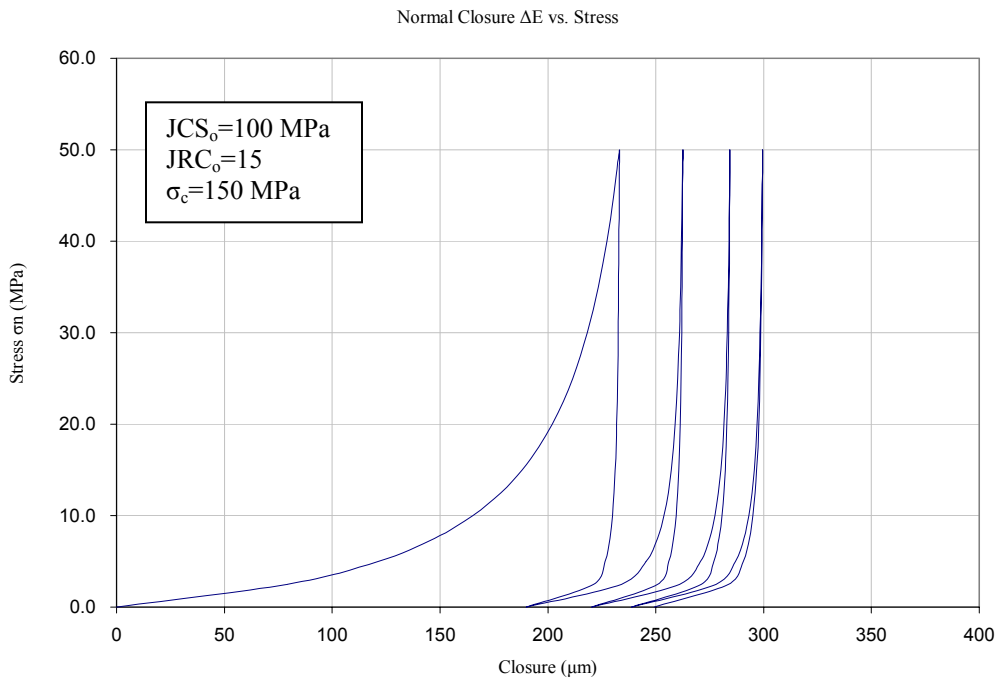


Figure 6.5: Normal closure under cyclic normal loading of the joint (case 2, after Bandis et al., 1985)

### 6.3.2 Shear behavior

The behavior of jointed masses in UDEC-BB is modeled using an empirical though sophisticated “mobilized roughness” method. According to the method the frictional strength for any shear displacement is:

$$\phi_{mob} = JRC_{mob} \cdot \log\left(\frac{JCS}{\sigma_n}\right) + \phi_r \quad \text{Equation 6.8}$$

with the  $\phi_r$  obviously not factored since it is the “last” available strength of a discontinuity.

According to Barton & Bandis (1985) the response history of a discontinuity during shearing has as follows:

1. Friction is mobilized under shearing.
2. Dilation begins upon mobilization of roughness
3. Peak shear strength is reached when  $JRC_{mob}/JRC_{peak}=1.0$  and  $\delta/\delta_{peak}=1.0$ .
4. Dilation declines as roughness is locally destroyed.
5. Residual strength is reached.

Barton & Bandis suggest the following empirical expression of the deformation at peak strength:

$$\delta_{peak} = \frac{L_n}{500} \left[ \frac{JRC_n}{L_n} \right]^{0.33} \quad \text{Equation 6.9}$$

UDEC uses the following relations for the shear behavior:

$$\tau = \sigma_n \cdot \tan\left(\phi_r + JRC \cdot \log\left(\frac{JCS}{\sigma_n}\right)\right) \quad \text{Equation 6.10}$$

where:

A roughness contribution factor is defined as follows:

$$RUFF = JRC_n \cdot \log\left(\frac{JCS_n}{\sigma_n}\right) \quad \text{Equation 6.11}$$

The RUFF factor was used by Bandis et al. (1986) to estimate the following ratio  $JRC_{mob}/JRC_n$  at low shear displacements ( $\delta/\delta_{peak} < 0.3$ ):

The mobilized roughness coefficient is expressed as:

$$JRC_{mob} = B \cdot JRC_n \quad \text{Equation 6.12}$$

Barton, Bandis & Bakhtar (1985) suggest a table with predefined values of the ratio B depending on the relative shear displacement.

The increment of normal joint deformation due to dilation only, during shearing is estimated by the following relationship:

$$\Delta_{un} = \Delta_{us} \cdot \tan \left( 0.5 \cdot JRC_{mob} \log \left( \frac{JCS_n}{\sigma_n} \right) \right) \quad \text{Equation 6.13}$$

where  $\Delta_{us}$  the shear displacement of the joint.

A dedicated spreadsheet was developed using Excel to evaluate the shearing resistance of discontinuities with the Barton-Bandis model. The Barton-Bandis parameter values used for the previous normal-loading spreadsheet were used. Along with the spreadsheet specific plots of the variation of the JRC and JCS parameters versus joint length are shown. Finally a shear stress-horizontal displacement plot is also shown. In cases where laboratory representation of the sample behavior is investigated, then  $L_n=L_o$ .

Table 6.4: Example of Barton-Bandis shear behavior model (case 1).

UDEc 3.1 - Barton - Bandis Shear Behavior Model									
Original spreadsheet by E.Hoek									
<b>Input Parameters</b>									
Joint No:			n/a	example					
Basic or Residual Friction Angle			26	phir	deg				
LAB Joint Roughness Coefficient			5	JRCo					
LAB Joint Compressive Strength			100	JCSo	mpa				
Lo	Lab scale Joint length		0.1	m					
Ln	Field Scale Joint length		0.1	m					
Testing or Field $\sigma_n^*$			50	Mpa					
Uniaxial Intact Rock Strength			150	Mpa					
*For Lab DSS performance use $L_o=L_n$ , and $\sigma_n = \sigma_{DSS}$									
For field performance use $\sigma_n$ range of field.									
<b>Output</b>									
Minimum Normal Stress (BB<70 deg)			0.000	MPa					
0.1	JRCn		5.00						
	JCSn		100.00						
$\delta$ peak			0.0007	m					
Roughness Contribution			1.505	RUFF					
Initial Aperture** ( Barton & Bakhtar)			0.2	mm					
<b>Non Linear MC Strength Envelope</b>									
Normal Stress	Shear Strength	$\delta(\tau)$	Friction Angle (deg)	Cohesive Strength (MPa)					
MPa	MPa			MPa					
0.0000	0.000	2.423	67.58	0.000					
0.1000	0.087	0.803	38.76	0.007					
0.2000	0.165	0.761	37.25	0.013					
0.4000	0.312	0.720	35.75	0.024					
0.8000	0.592	0.681	34.25	0.047					
1.6000	1.119	0.643	32.75	0.090					
3.2000	2.116	0.607	31.25	0.174					
6.4000	3.994	0.571	29.75	0.337					
<b>Strength Parameters vs. Length</b>			<b>udec parameters</b>						
Ln	JRCn	JCSn	A	B	$\delta x$ mm	JRC mob	$\tau$ developed	Dilation	$\Sigma$ (Dilation)
0.10	5.00	100.00	0.00	-17.27	0.00	-86.37	0.00	0.00	0.00
0.20	4.67	90.13	0.20	-4.32	0.15	-21.59	17.71	-0.01	-0.01
0.30	4.48	84.81	0.30	0.00	0.22	0.00	24.39	0.00	-0.01
0.40	4.35	81.23	0.45	0.50	0.33	2.50	25.20	0.00	-0.01
0.50	4.26	78.55	0.60	0.75	0.44	3.75	25.62	0.00	0.00
0.60	4.18	76.43	0.80	0.90	0.58	4.50	25.87	0.01	0.01
0.70	4.12	74.69	1.00	1.00	0.73	5.00	26.03	0.01	0.01
0.80	4.06	73.20	1.50	0.90	1.09	4.50	25.87	0.01	0.03
0.90	4.01	71.92	2.00	0.85	1.45	4.25	25.78	0.02	0.04
1.00	3.97	70.79	3.00	0.75	2.18	3.75	25.62	0.02	0.07
1.10	3.93	69.79	4.00	0.70	2.91	3.50	25.54	0.03	0.09
1.20	3.90	68.88	6.00	0.60	4.36	3.00	25.37	0.03	0.13
1.30	3.87	68.06	8.00	0.55	5.82	2.75	25.29	0.04	0.17
1.40	3.84	67.31	10.00	0.50	7.27	2.50	25.20	0.05	0.22
1.50	3.81	66.62	20.00	0.40	14.55	2.00	25.04	0.08	0.29
1.60	3.79	65.98	40.00	0.30	29.09	1.50	24.88	0.11	0.41
1.70	3.77	65.38	60.00	0.20	43.64	1.00	24.71	0.11	0.52
1.80	3.74	64.82	80.00	0.10	58.18	0.50	24.55	0.08	0.60
1.90	3.72	64.30	100.00	0.00	72.73	0.00	24.39	0.00	0.60
2	3.706	63.804							

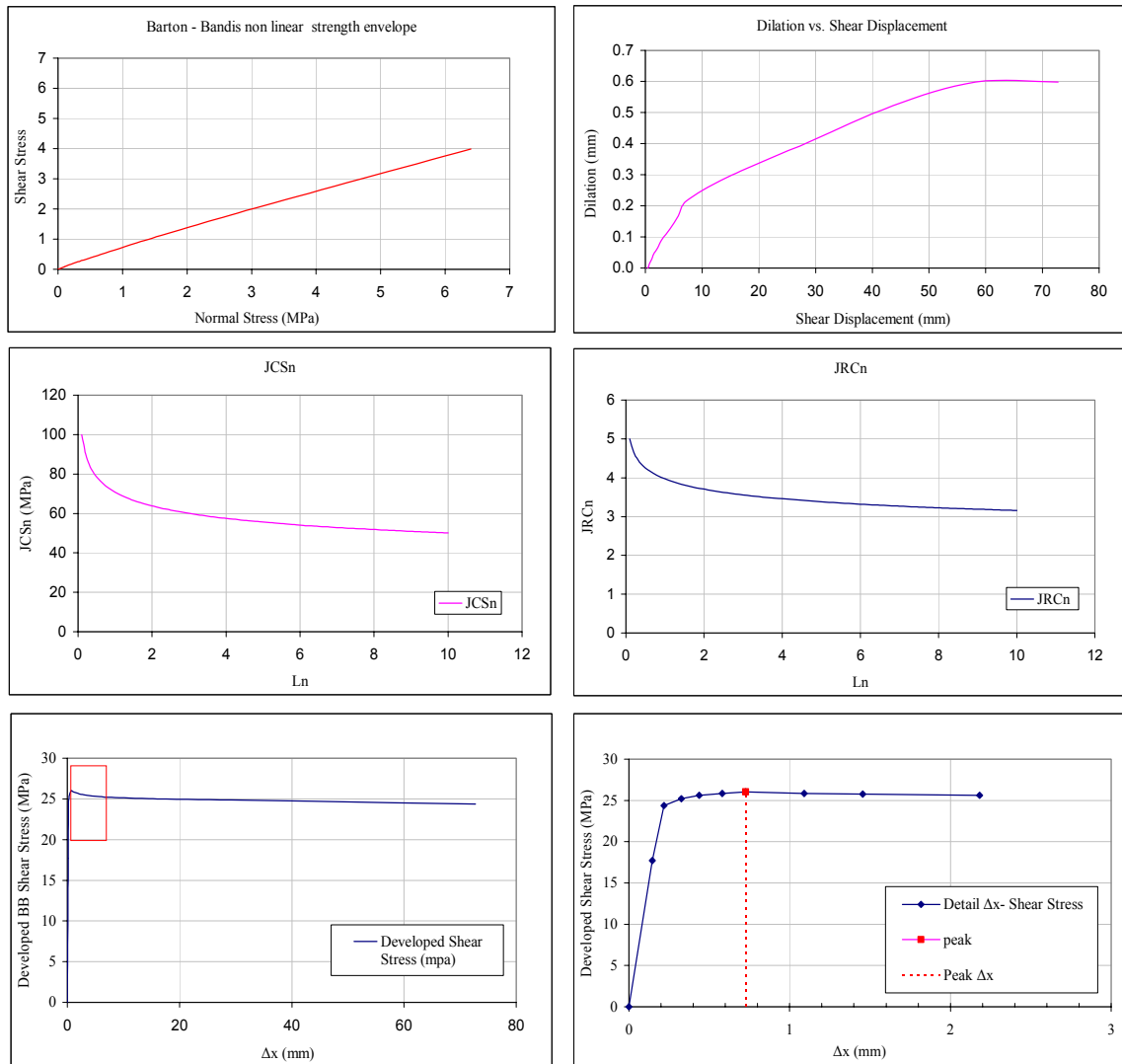


Figure 6.6: a: Non linear Barton-Bandis failure envelope, b: dilation vs. shear displacement, c,d: JCS and JRC versus joint length, e & f: shear strength versus horizontal displacement (case 1).



Table 6.5: Example for Barton-Bandis model (case 2).

UDEc 3.1 - Barton - Bandis Shear Behavior Model									
Original spreadsheet by E.Hoek									
<b>Input Parameters</b>									
Joint No:			n/a	example					
Basic or Residual Friction Angle			26	phir	deg				
LAB Joint Roughness Coefficient			15	JRCo					
LAB Joint Compressive Strength			100	JCSo	mpa				
Lo	Lab scale Joint length		0.1	m					
Ln	Field Scale Joint length		0.1	m					
Testing or Field $\sigma_n^*$			50	Mpa					
Uniaxial Intact Rock Strength			150	Mpa					
*For Lab DSS performance use $Lo=Ln$ , and $\sigma_n = \sigma_{DSS}$									
For field performance use $\sigma_n$ range of field.									
<b>Output</b>									
Minimum Normal Stress (BB<70 deg)			0.117	MPa					
0.1	JRCn		15.00						
	JCSn		100.00						
$\delta$ peak			0.0010	m					
Roughness Contribution			4.515	RUFF					
Initial Aperture** ( Barton & Bakhtar)			0.6	mm					
<b>Non Linear MC Strength Envelope</b>									
Normal Stress	Shear Strength	$\delta(\tau)$	Friction Angle (deg)	Cohesive Strength (MPa)					
0.1166	0.320	1.776	60.61	0.113					
0.2166	0.486	1.557	57.29	0.148					
0.4332	0.796	1.340	53.27	0.216					
0.8664	1.331	1.154	49.09	0.331					
1.7327	2.252	0.994	44.82	0.530					
3.4655	3.836	0.854	40.49	0.877					
6.9309	6.552	0.730	36.13	1.492					
13.8619	11.174	0.619	31.74	2.600					
<b>Strength Parameters vs. Length</b>			<b>udec parameters</b>						
Ln	JRCn	JCSn	A	B	$\delta$ x mm	JRC mob	$\tau$ developed	Dilation	$\Sigma$ (Dilation)
0.10	15.00	100.00	0.00	-5.76	0.00	-86.37	0.00	0.00	0.00
0.20	12.18	73.20	0.20	-1.44	0.21	-21.59	17.71	-0.01	-0.01
0.30	10.79	61.00	0.30	0.00	0.31	0.00	24.39	0.00	-0.01
0.40	9.90	53.59	0.45	0.50	0.47	7.50	26.87	0.01	0.00
0.50	9.26	48.47	0.60	0.75	0.63	11.25	28.16	0.02	0.02
0.60	8.76	44.65	0.80	0.90	0.84	13.50	28.94	0.03	0.05
0.70	8.37	41.66	1.00	1.00	1.05	15.00	29.47	0.04	0.09
0.80	8.04	39.23	1.50	0.90	1.57	13.50	28.94	0.06	0.14
0.90	7.76	37.20	2.00	0.85	2.09	12.75	28.68	0.07	0.21
1.00	7.52	35.48	3.00	0.75	3.14	11.25	28.16	0.09	0.31
1.10	7.31	33.99	4.00	0.70	4.18	10.50	27.90	0.12	0.42
1.20	7.12	32.69	6.00	0.60	6.27	9.00	27.38	0.15	0.57
1.30	6.95	31.53	8.00	0.55	8.36	8.25	27.13	0.18	0.75
1.40	6.80	30.50	10.00	0.50	10.45	7.50	26.87	0.21	0.96
1.50	6.66	29.56	20.00	0.40	20.90	6.00	26.37	0.33	1.29
1.60	6.53	28.72	40.00	0.30	41.80	4.50	25.87	0.49	1.78
1.70	6.41	27.94	60.00	0.20	62.70	3.00	25.37	0.49	2.27
1.80	6.30	27.23	80.00	0.10	83.60	1.50	24.88	0.33	2.60
1.90	6.20	26.58	100.00	0.00	104.51	0.00	24.39	0.00	2.60
2	6.106	25.974							

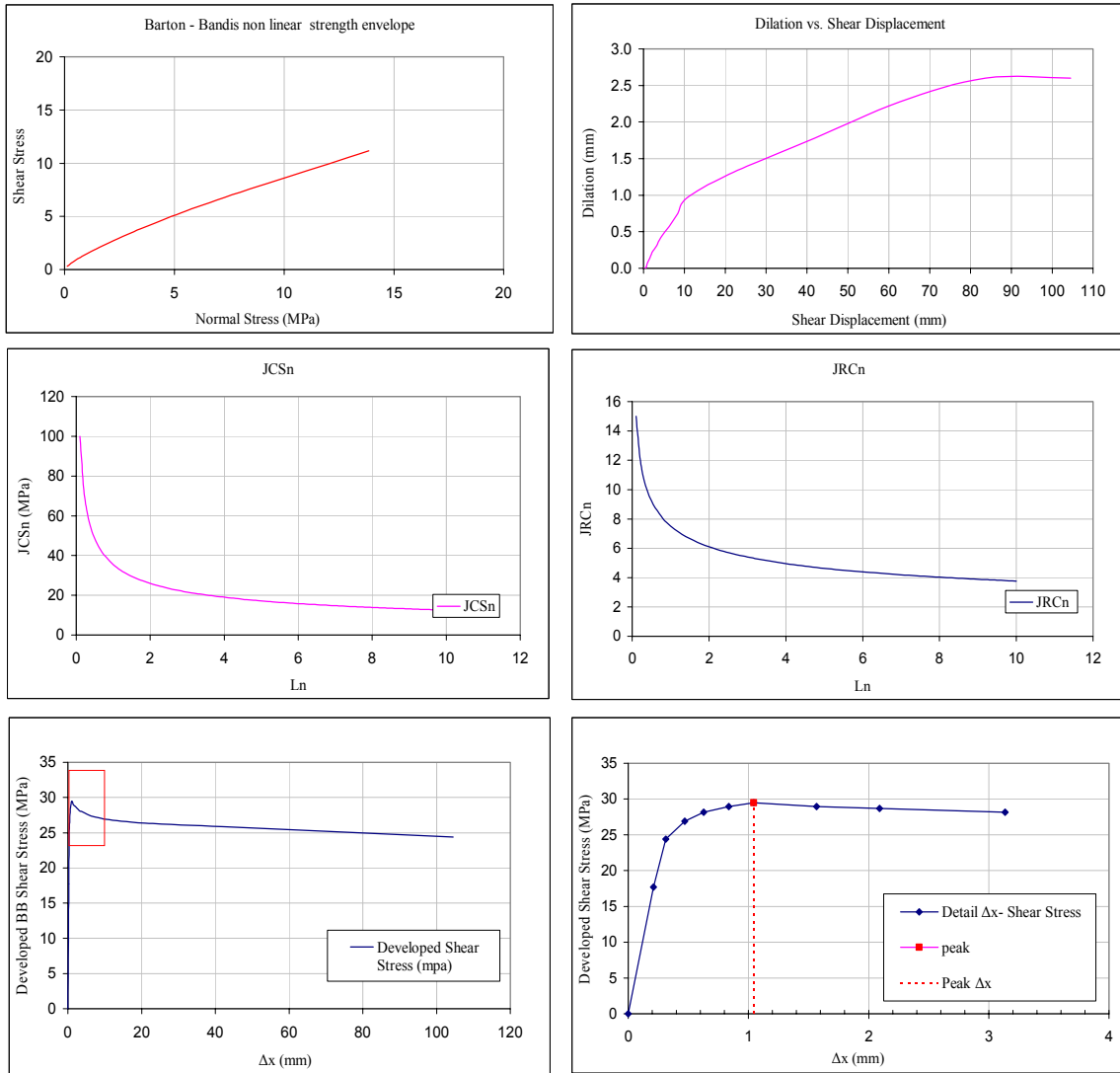


Figure 6.7: a: Non linear Barton-Bandis failure envelope, b: dilation versus shear displacement, c, d: JCS and JRC versus joint length, e & f: shear strength versus horizontal displacement (case 2).

## 6.4 Numerical modeling for the Shimizu tunnel No.3

Numerical investigations and analyses were performed for the Shimizu tunnel No.3 by consultants for the Japanese authorities (Japan Highways,1998) as well as from NGI for the Fuji Research Institute Corporation (1995). Initial studies were conducted by the use of three dimensional finite element analysis, as well as with two and three dimensional distinct element modeling. The complexity of this sequential excavation project and the involvement of various support systems throughout the tunneling lengths is certainly a problem that can only be examined by the use of a numerical code. Finite element modeling has been acknowledged to be an excellent tool aiding in the design of underground works offering great advantages and some degrees of simplicity when followed rationally and properly. However the ability to couple elastoplastic analysis with an elementary continuum logic and discrete behavior of a blocky system is considered as a very attractive alternative, giving further insight into different mechanisms involved in tunneling in a fractured rock mass such as the Shimizu tunnel No.3.

In numerical modeling several shortcomings are inevitable to some extent, the most important of them being the lack of adequate input to be used in numerical studies. This situation can be addressed by the adoption of a parametric numerical investigation that targets in better appreciation of the sensitivity of the predicted tunnel performance to variation in the model parameters. At the same time, study of the ground – support system interaction can be performed by using a variety of support system elements available in UDEC including rock bolts or reinforcement cables, steel beams and shotcrete. The proposed parametric analyses for the case can be subdivided into three main parts (figure 6.8). An initial simple continuum single tunnel model in UDEC is designed unsupported and analyzed. In this stage three parametric studies are performed:

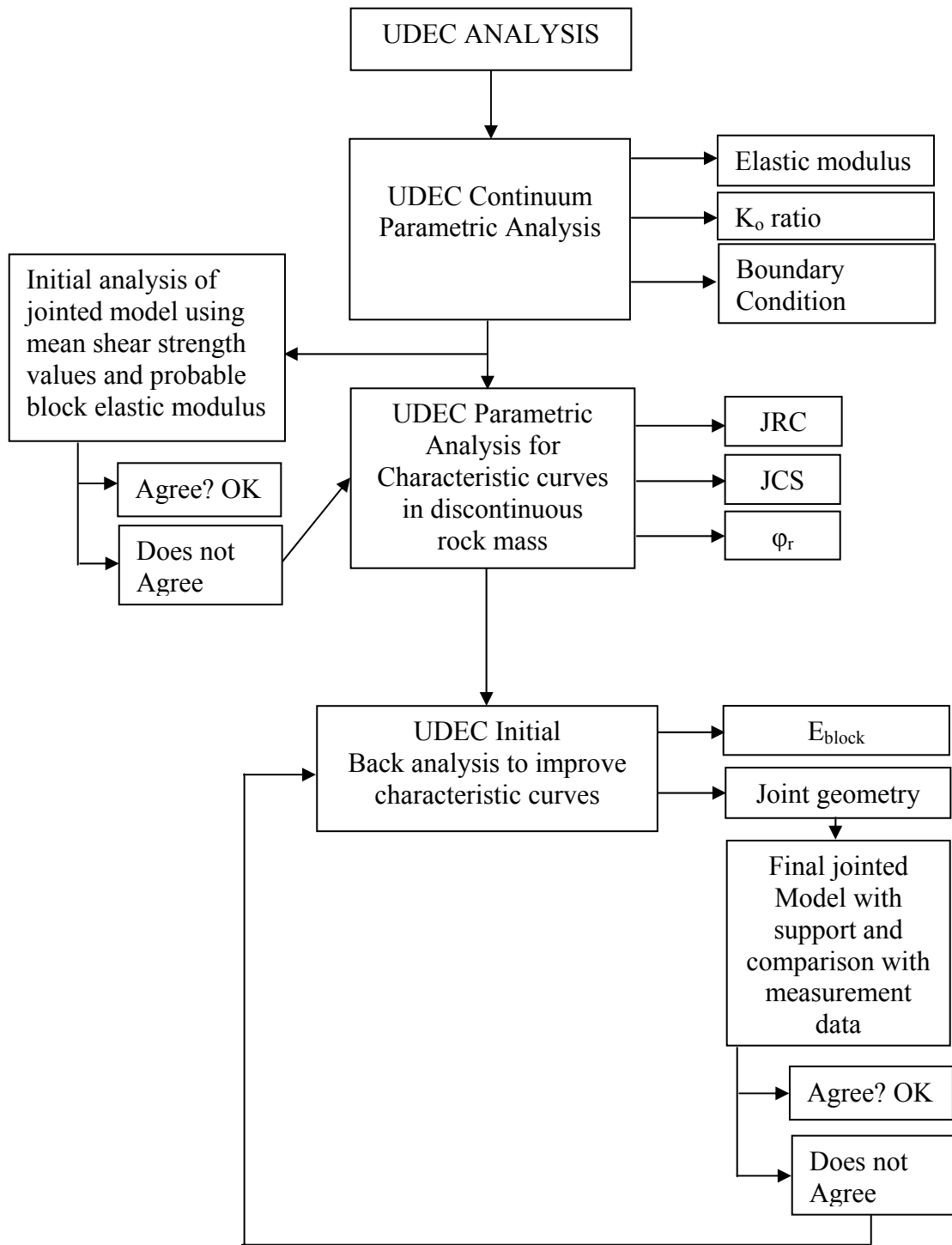


Figure 6.8: Method followed for numerical simulations with UDEC for the Shimizu tunnel No.3.

- a. A most probable and rational  $K_0$  ratio is adopted and the Elastic modulus is varied for the whole rock mass.
- b.  $K_0$  stress ratio is varied, assuming a constant elastic modulus. This procedure is followed for a lower and an upper bound value of elastic modulus.
- c. The effect of boundary condition is studied for the continuum. Models are constructed for conditions of insitu boundary stresses and zero lateral strain.

The simulation of the excavation even though it does not involve a support system yet, is conducted sequentially as the actual construction condition. This step is followed due to the fact that the analysis is elastoplastic and the deformations are highly stress path dependent in contrast to a purely elastic FEM or FDM solution where a theoretical unique solution exists no matter what the path is. It should be pointed out that UDEC cannot simulate a fully continuous excavated mass system but only an assemblage of blocks. Therefore, for continuum tunnel models artificial discontinuities are entered at locations where their existence does not influence the model and their properties are also specifically given high values (normal and shear stiffness, cohesion and tensile strength). This simulates “glued” fractures that do not affect the solution. Figures 6.9 and 6.10 show the model used in the above continuum approach and the associated finite difference zoning. In figure 6.11 the three excavation stages followed during numerical analysis are depicted.

In the second stage, a more complex model geometry is simulated in UDEC. The UDEC automatic fracture network generator is used with known spatial data as input, to construct a “stochastically” created block assemblage. This method utilized by UDEC permits the construction of a fracture network taking into account mean and standard deviation values for each of the spatial data assuming normally distributed parameters. Mahtab et al. (1992) discusses the variability of the possible distribution schemes for spacing and persistence, providing case study examples. It was found that very often lognormal or exponential distributions can be the case for statistically quantifying fracture geometrical data but there can also be cases where none of the often used distributions can be applied. In absence of field data the normal distribution assumed by

UDEC is used in the analysis. Optional modifications and additions may be made upon engineering judgment. The discontinuity network should conform to estimated Q or RMR values for the location of the tunnel section examined. To avoid highly complicated geometries and increase computational efficiency local refinements at the fracture geometry can be made upon judgment. Therefore far from the excavation fewer fractures are discretized. Close to the area of interest and where strain concentration is more likely to develop finer zoning was made to assist in plastic flow analysis inside the block material. The initial single tunnel jointed model is shown on figures 6.12 and 6.13.

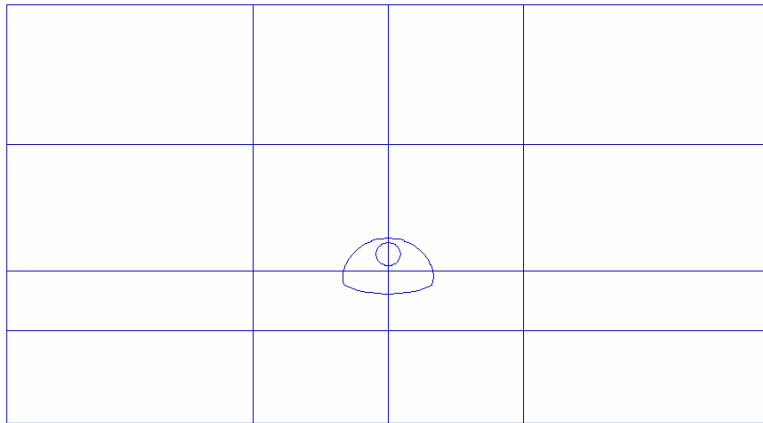


Figure 6.9: Artificial blocking for simple tunnel models in UDEC.

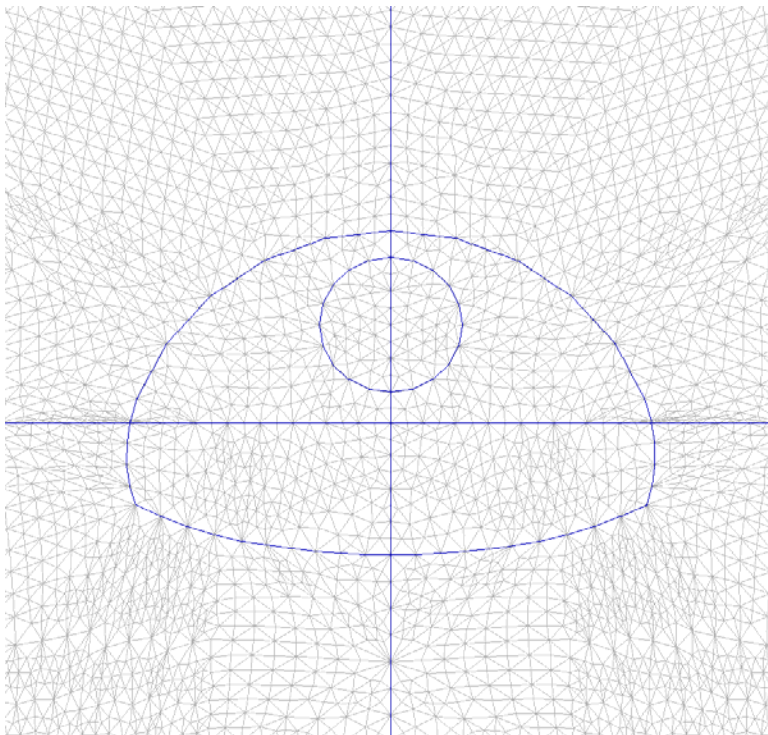


Figure 6.10: Finite Difference zoning in continuum models. Close to the tunnel the finite difference zone length becomes small to increase plastic flow precision.

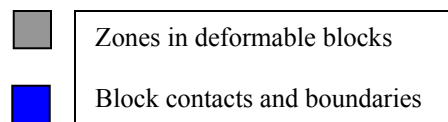
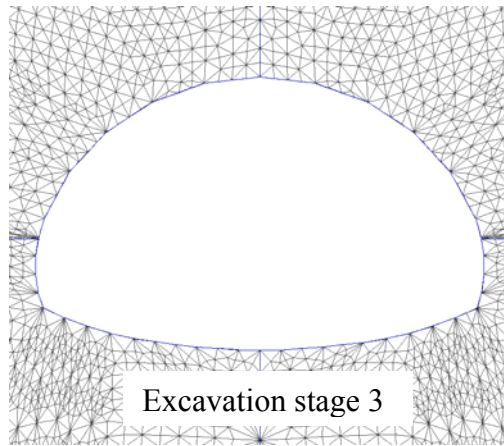
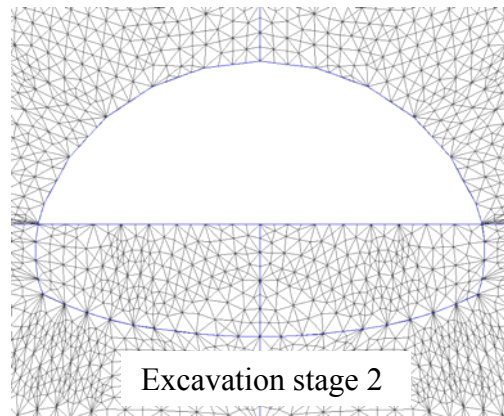
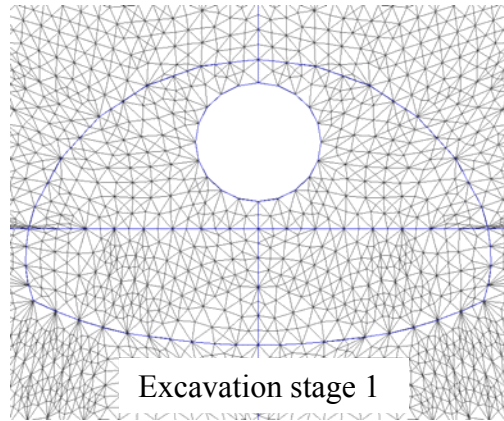


Figure 6.11: Excavation stages during numerical simulation.



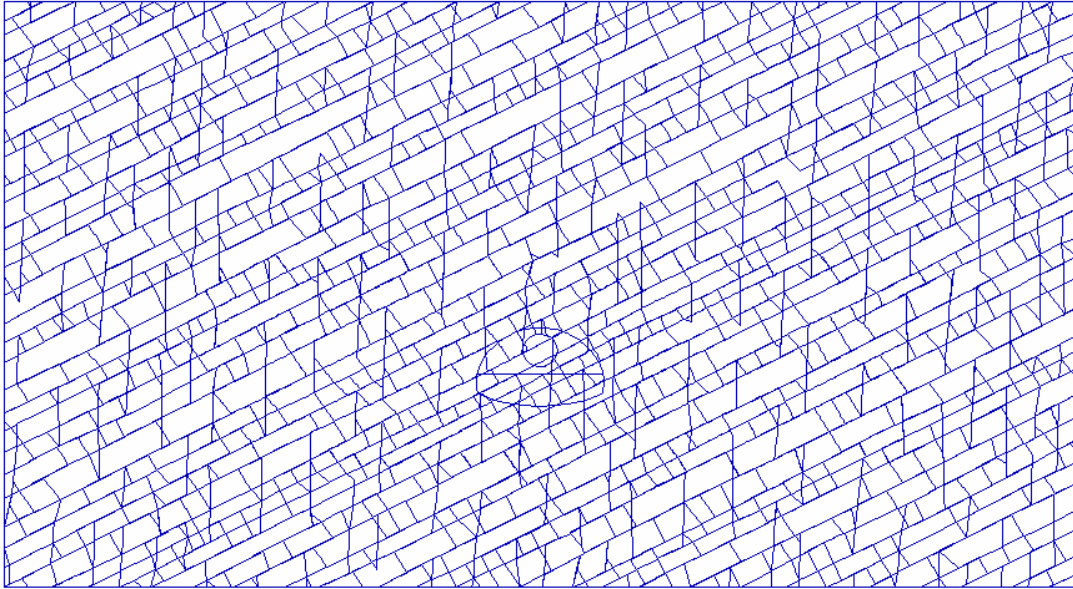


Figure 6.12: UDEC fracture network for single tunnel jointed model.

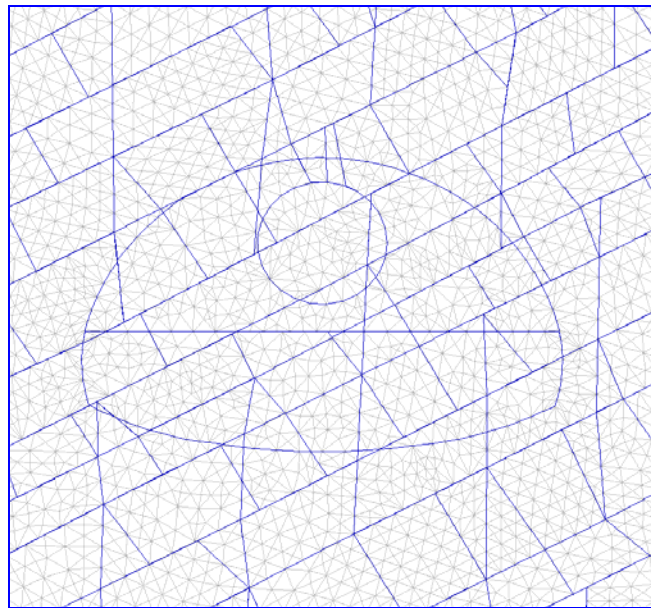


Figure 6.13: Refined finite difference zoning around tunnel region.

## 6.5 Simple continuum model analysis

For the purpose of evaluating the sensitivity of the tunnel response, a series of pseudo-continuum plane strain models were designed and analyzed in UDEC ver.: 3.1. Based on project reports for the Japan Highways, an empirical relation to describe the in situ stress ratio is the following:

$$K_o = \begin{cases} 0.25 + 0.01 \cdot h, & 20 < h < 75 \\ 1.0, & 75 \leq h \end{cases} \quad \text{Equation 6.14}$$

Monitoring data were available for the following chainage sections:

STA 912+60 , STA 912+75 , STA 913+65, STA 914+10.

The first two available measurement sections were located very close to the Western portal where highly disturbed and weathered ground existed with expected behavior and strength close to residual soil. For this range, no numerical analysis was conducted. The most complete available data existed for section STA 913+65. From the longitudinal geological profile this section is close to the contact between Wss sandstone and Walt sandstone-mudstone. Perhaps the most important issue in underground construction design is the knowledge of the in situ  $K_o$  ratio. In this case a parametric analysis was also performed to investigate the effects of the  $K_o$  ratio on the unsupported tunnel deformations.

From the longitudinal sections of figure 3.2 it is obvious that for the western sector the two tunnels even though are positioned at a center to center distance of 54.5 m they do not generally have the same overburden. For the section STA 913+65 the tunnel to Nagoya has a maximum overburden of about 83.0 m and the tunnel to Tokyo an overburden of about 60.0 m. Since data were available only for the tunnel to Tokyo, an overburden thickness of about 83.0 m was assumed in the analyses.

### 6.5.1 Effects of the elastic modulus

As an initial approach an overburden of about 83.0 m and an average nearly isotropic  $K_o$  ratio in the order of 0.83 was used to investigate different elastic moduli for the ground. The assumptions for the initial stress conditions used are as follows:

Average depth of tunnel = 83.0 m

$K_o = 0.83$

$\sigma_v = 2.08$  MPa

$\sigma_h = 1.72$  MPa.

In the analysis, no attempt was made to simulate the exact topographical cross section area at the specified chainage but a level ground was used as a first approximation. Under the above assumptions a series of analyses was conducted for unsupported tunnels in a continuous mass having the following properties:

$\phi' = 38^\circ$

$c' = 2.0$  MPa

$\nu = 0.3$

$\psi = 0^\circ$

Elastic modulus range = 2.0, 4.0, 5.0, 6.0, 8.0, 10.0, 12.0 GPa.

For each excavation stage, sufficient cycling time was allowed in order for equilibrium to develop and a steady state solution can be achieved at each step. The equilibrium was verified and recorded by the use of time history plots generated by the program during the analysis. These plots included the unbalanced forces developed in the model, while others recorded the tunnel convergence at specified locations as well as the stresses. For the purposes of the present study, plots for two cases,  $E = 4000$  MPa and  $E = 12000$  MPa will be shown. Figure 6.15 shows the initial stress state after consolidation stage and equilibrium. Figure 6.17 presents the deformations of the unsupported TBM 5.0 m opening. From the DEM analysis (in reality pure Finite Difference analysis for these models) calculated deformations for the pilot tunnel are presented in Table 6.6:

Table 6.6: Results for pilot opening deformations with no support from different methods.

Location	Deformation $\delta$ (mm) from method :		
	UDEC	Elastoplastic Analysis (Salencon)	Elastic $K_o$ Analysis
TBM roof (crown)	1.52	$\sigma_{av}=1.76$ MPa	1.6
TBM wall (spring line)	1.22	$\delta=1.46$	1.2

It becomes immediately apparent that even from the simplified elastoplastic analysis, by assuming an average isotropic condition in a spreadsheet calculation included in Table 6.7, the average deformation from UDEC and closed form solution are in close agreement. The above spreadsheet calculation predicts elastic behavior and no plastic yielding. For this reason a more elaborate elastic analysis shown in spreadsheet Table 6.8 gives even closer deformation results to UDEC for the problem of a circular problem in a biaxially stressed field.

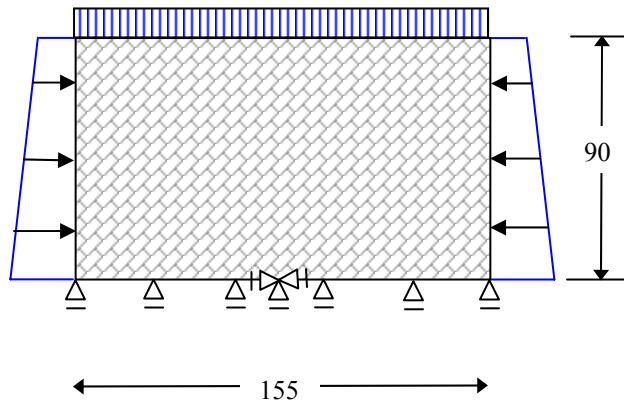


Figure 6.14: Simplified model used for continuum parametric analyses, by using prescribed lateral pressure boundary conditions.

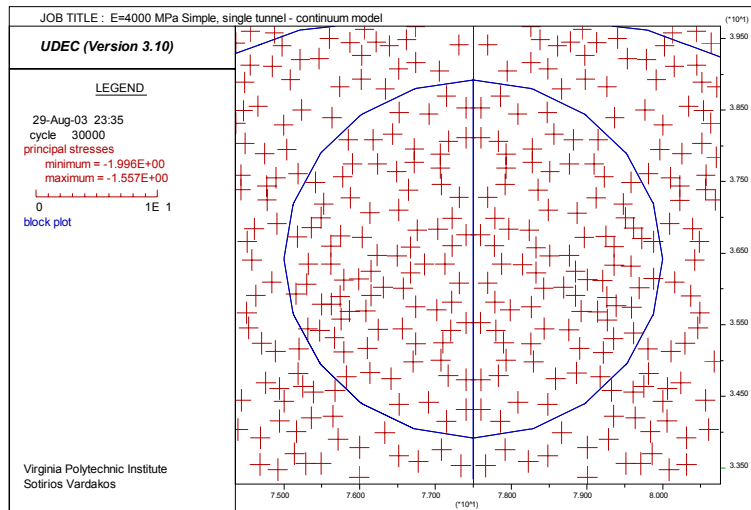


Figure 6.15: Stresses close to TBM opening in continuum model.

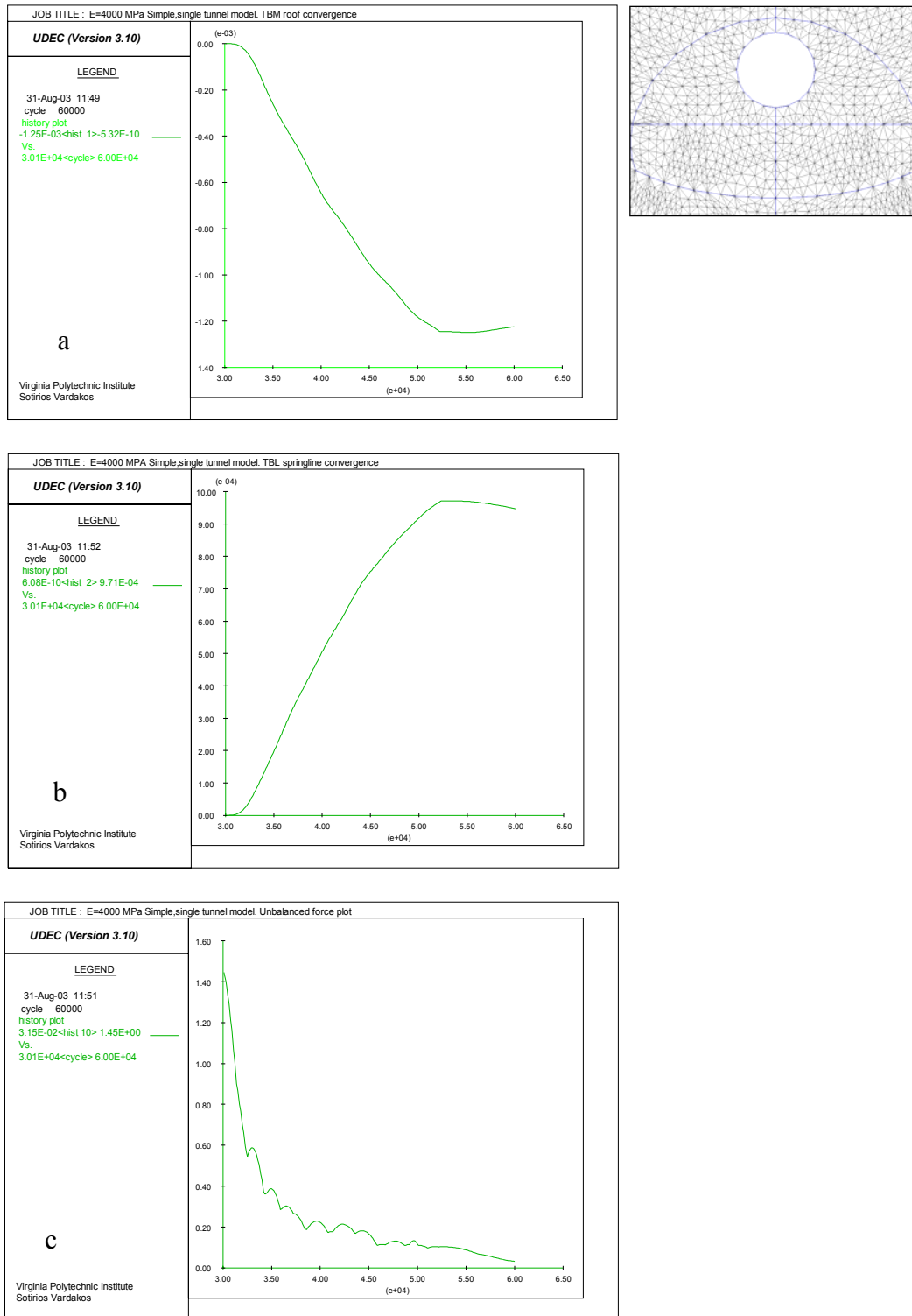


Figure 6.16: (a): E=4000 MPa model, TBM roof convergence vs. cycle time, (b): Springline convergence, (c): Unbalanced force plot.

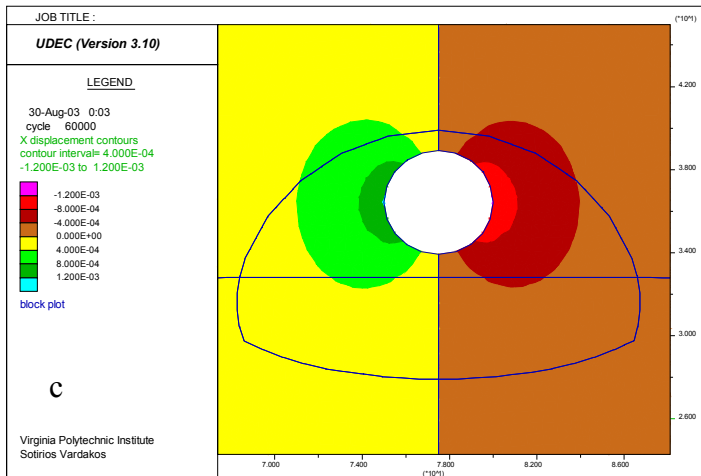
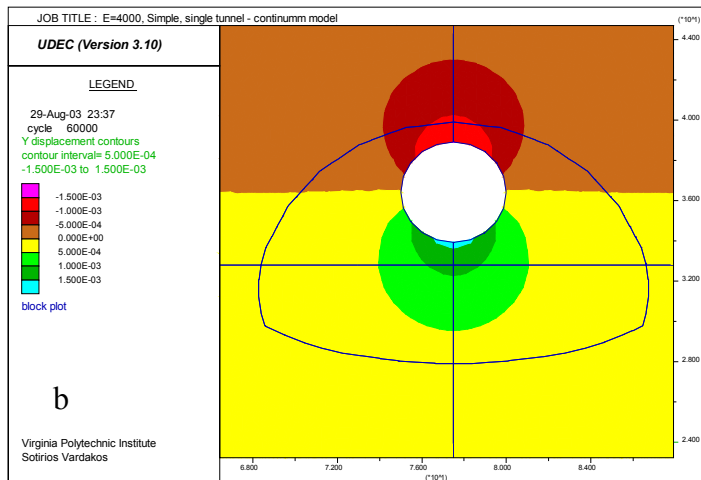
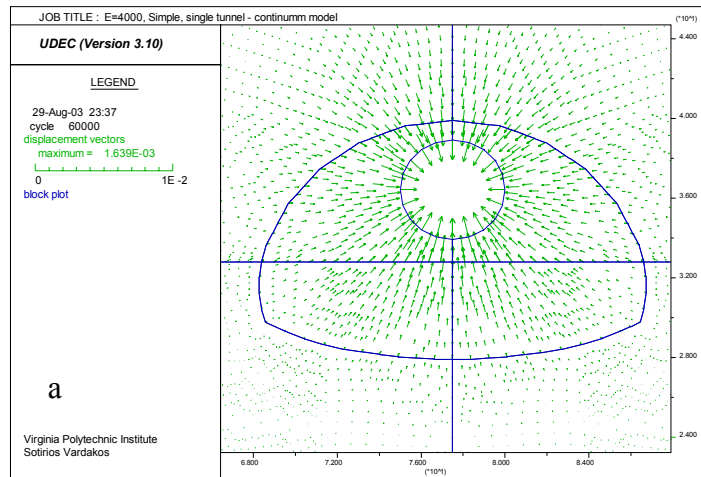


Figure 6.17: E=4000 MPa model, (a): Pilot tunnel total displacements, (b): Vertical displacements shaded contours, (c): Horizontal displacements shaded contours.

Table 6.7: Simplified elastoplastic analysis using a spreadsheet calculation for pilot tunnel, assuming E=4000 MPa. (After Kavvadas, 2001)

INPUT PARAMETERS			
Isotropic Stress	1.8 MPa		
Radius R	2.5 m		
c	2 MPa		
φ	38 degrees		
E(mod)	4000 MPa		
v poisson	0.3		
p <sub>i</sub>	0 MPa		

OUTPUT			
N <sub>φ</sub> =K <sub>p</sub>	4.204		
K <sub>o</sub> elastic	0.429		
Λ=	4395.604		
Overload Factor			
N <sub>s</sub> =	0.439		
D=	5384.615		
const C=	0.655		
r <sub>p</sub> (theoretical)=	2.1903		
c min =	0.878 MPa		
N <sub>s</sub> max=	1.00		
Condition for Analysis	Elastic		

STRESSES AND DEFORMATIONS														
ELASTIC REGION						PLASTIC								
for r<r plastic														
final stresses				final deformations			if no plastic c2=		if there is plastic region c2=			plastic		u at plastic radius
radius (r <sub>min</sub> =R)	σ <sub>r</sub>	σ <sub>θ</sub>	u actual*100	σ <sub>r</sub>	σ <sub>θ</sub>	u <sub>r</sub>	σ <sub>r</sub>	σ <sub>θ</sub>	u <sub>r</sub>	σ <sub>r</sub>	σ <sub>θ</sub>	u <sub>r</sub>		
2.51	0.014	3.586	0.146	0.014	3.586	0.001	-0.244	3.844	0.001667	0.033	8.340	0.001667156		
2.6	0.136	3.464	0.141	0.136	3.464	0.001	-0.105	3.705	0.001610	0.343	9.642	0.00160941		
2.8	0.365	3.235	0.131	0.365	3.235	0.001	0.158	3.442	0.001495	1.121	12.912	0.001494388		
3	0.550	3.050	0.122	0.550	3.050	0.001	0.369	3.231	0.001395	2.031	16.739	0.001394715		
3.2	0.701	2.899	0.114	0.701	2.899	0.001	0.542	3.058	0.001308	3.086	21.172	0.001307508		
3.4	0.827	2.773	0.108	0.827	2.773	0.001	0.686	2.914	0.001231	4.296	26.259	0.001230567		
3.6	0.932	2.668	0.102	0.932	2.668	0.001	0.806	2.794	0.001162	5.673	32.051	0.00116218		
3.8	1.021	2.579	0.096	1.021	2.579	0.001	0.908	2.692	0.001101	7.231	38.597	0.001100994		
4	1.097	2.503	0.091	1.097	2.503	0.001	0.995	2.605	0.001046	8.979	45.947	0.001045929		
4.2	1.162	2.438	0.087	1.162	2.438	0.001	1.070	2.530	0.000996	10.931	54.154	0.000996111		
4.4	1.219	2.381	0.083	1.219	2.381	0.001	1.135	2.465	0.000951	13.100	63.269	0.000950823		
4.6	1.268	2.332	0.079	1.268	2.332	0.001	1.191	2.409	0.000910	15.496	73.344	0.000909475		
4.8	1.312	2.288	0.076	1.312	2.288	0.001	1.241	2.359	0.000872	18.134	84.433	0.000871573		
5	1.350	2.250	0.073	1.350	2.250	0.001	1.285	2.315	0.000837	21.026	96.587	0.000836704		
5.2	1.384	2.216	0.070	1.384	2.216	0.001	1.324	2.276	0.000805	24.183	109.862	0.000804518		
5.4	1.414	2.186	0.068	1.414	2.186	0.001	1.358	2.242	0.000775	27.621	124.311	0.000774717		
5.6	1.441	2.159	0.065	1.441	2.159	0.001	1.389	2.211	0.000747	31.350	139.988	0.000747045		

Table 6.8: Simplified elastic analysis assuming the same initial stresses generated by UDEC during model consolidation. The stresses after model consolidation may be yield to a slightly different K<sub>o</sub> ratio than the prescribed value.

INPUT PARAMETERS			
σ <sub>h</sub> (UDEC CONSOLIDATION)	1.61 MPa	horizontal K <sub>o</sub> =	0.847
σ <sub>v</sub> (UDEC CONSOLIDATION)	1.9 MPa		
Radius R	2.5 m		
c	N/A MPa		
φ	N/A degrees		
E(mod)	4000 MPa		
v poisson	0.3		
p <sub>i</sub>	0 MPa		

OUTPUT			
N <sub>φ</sub> =K <sub>p</sub>			
K <sub>o</sub> elastic	0.429		
Λ=	4395.604		
Bulk Modulus K =	3333.333 MPa		
Shear Modulus G =	1538.462 MPa		

STRESSES AND DEFORMATIONS							
	m	degrees	MPa	MPa	MPa	m	m
	r (distance)	θ from hor.	σ <sub>r</sub>	σ <sub>θ</sub>	τ <sub>rθ</sub>	u <sub>r</sub>	u <sub>θ</sub>
Springline	2.501	0	0.0016	4.0879	-0.0005	0.0012	0.0000
Crown	2.501	90	0.0012	2.9293	0.0005	0.00164	0.0000



A useful feature implemented in UDEC is used in order to locate and investigate areas with plastic yielding potential. Using this feature a strength/stress ratio plot can be constructed to estimate possible failures due to plastic yielding. The ratio is shown in figure 6.18:

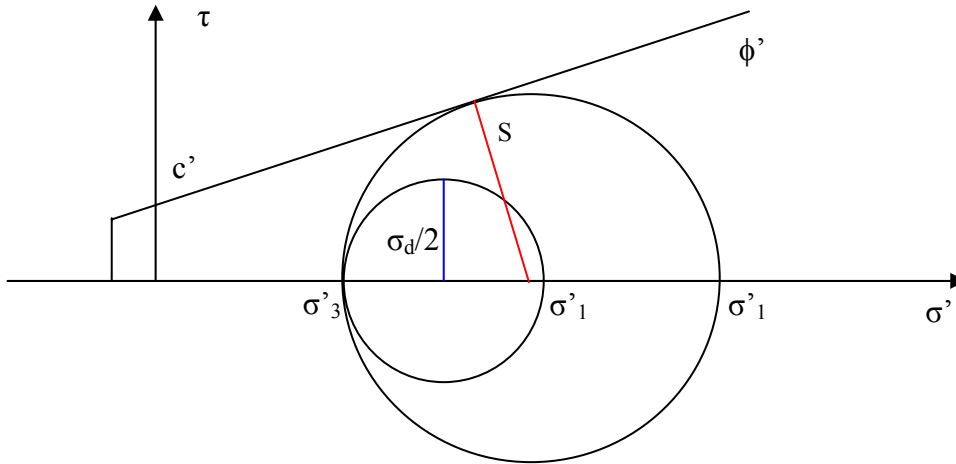


Figure 6.18: Definition of the strength over stress ratio as a means of estimating proximity to failure in UDEC.

The relation expressing the proximity to plastic failure is (assuming compression positive):

$$\frac{S}{\sigma_d/2} = \frac{\sigma'_{1f} - \sigma'_3}{\sigma'_1 - \sigma'_3} \quad \text{Equation 6.15}$$

where:

$$\sigma'_{1f} = \sigma'_3 \cdot K_p + 2c' \sqrt{K_p}$$

$$K_p = \frac{1 + \sin \phi'}{1 - \sin \phi'} = \tan^2(45 + \phi'/2)$$

The non yielding condition for the unsupported tunnel is also verified by UDEC plot in figure 6.19 b, which presents the mobilization of shear strength as a ratio of the available strength over the developed deviatoric stress which is above 2.0 for this case.

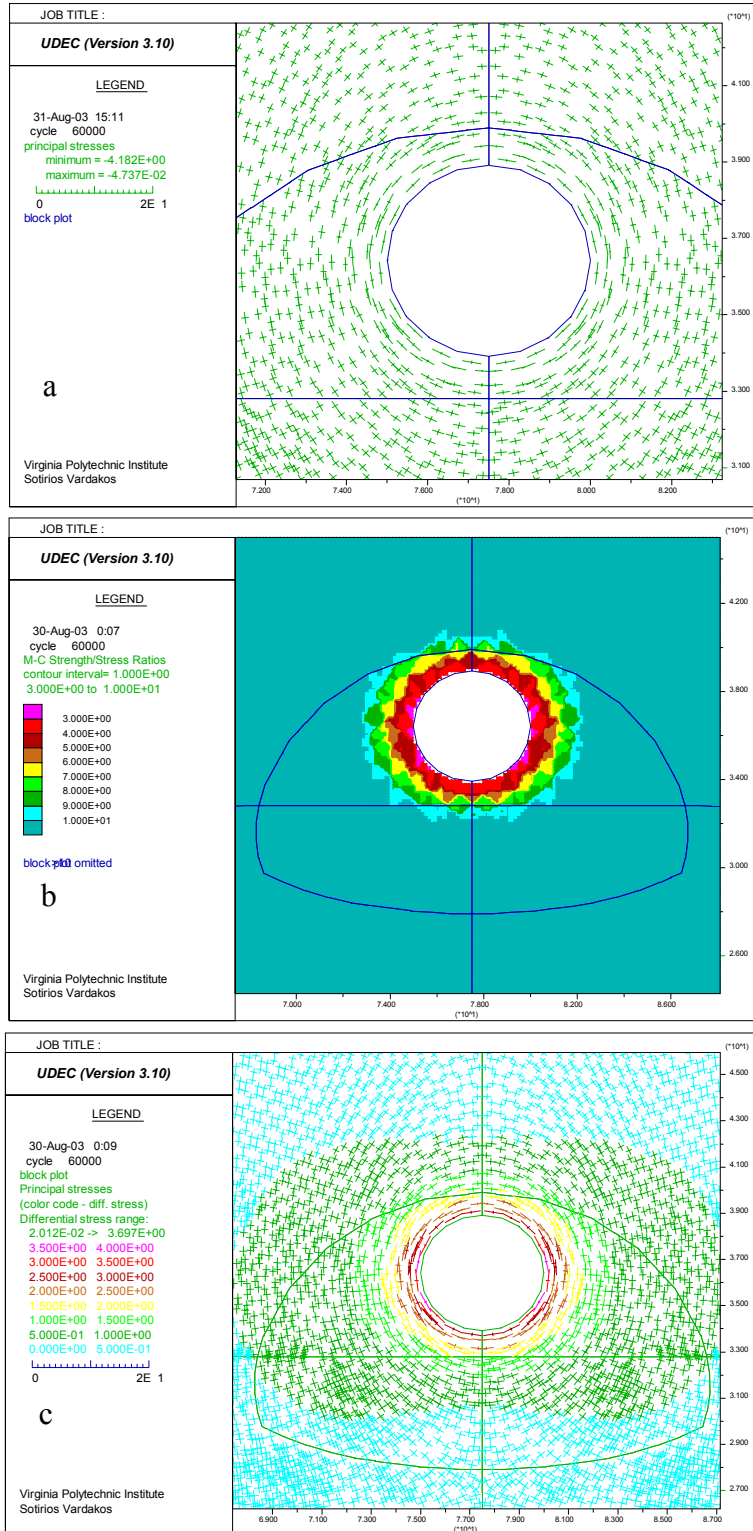


Figure 6.19: E=4000 MPa model, (a):principal stress tensors, (b): mobilization of shear strength, (c): color coded deviator stresses.

The next excavation stage includes removal of the top heading section elements and subsequent relaxation until equilibrium. From the UDEC analysis the following deformations are predicted:

Table 6.9: Tunnel deformations predicted by UDEC for top heading stage and by using an elastic modulus of  $E=4000$  MPa.

Location	Deformation $\delta$ (mm) from method :
	UDEC
Top Heading Roof	6.78
Top Heading Left roof point	5.95
Top Heading Right roof point	5.95
Floor Heave	7.6

In this case the unfavorable effect of the large span tunnel design becomes apparent by highly increased roof convergence to almost 7.0 mm from 1.6 mm. Figures 6.21 b,c show the vertical and horizontal displacements with shaded contouring. At the same time the floor is expected to heave for about 7.6 mm due to vertical unloading. For this condition, most of the deformations take place in the vertical direction and only small components in the order of 1.5 mm are developed in the horizontal direction, occurring mainly at a distance of 6.3 m from the crown. Figure 6.22 b shows the mobilization of shear strength in the rock mass surrounding the tunnel heading and figure 6.22 c presents the concentration of deviatoric stresses  $\sigma_1$ - $\sigma_3$ . From these plots the onset of plastic yielding is evident in the foundation area of the top heading (indicated by pink colored areas, where the strength ratio is 1.0) and is caused by the excessive concentration of stresses at these corner points. For this reason, the designs for the Shimizu No.3 tunnels included the existence of small buttresses at these foundation points in order to provide some safety by lateral confinement.

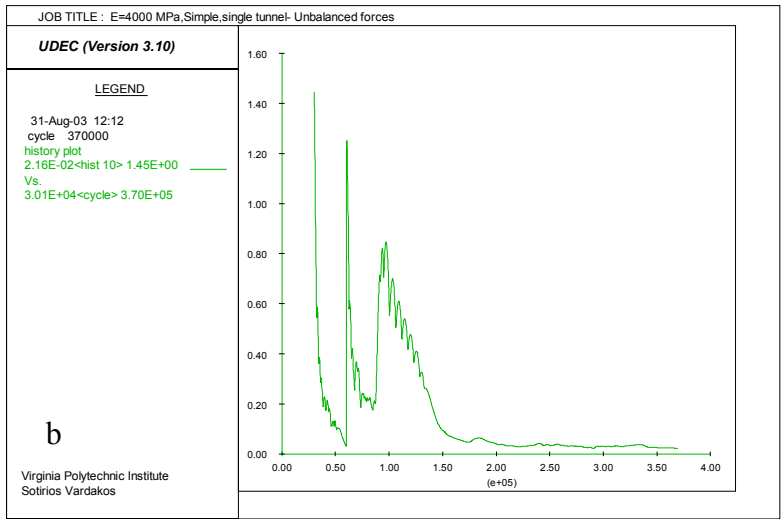
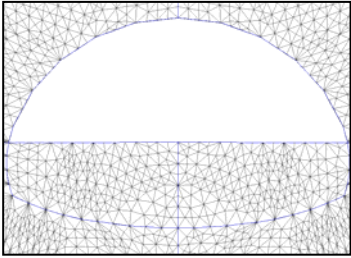
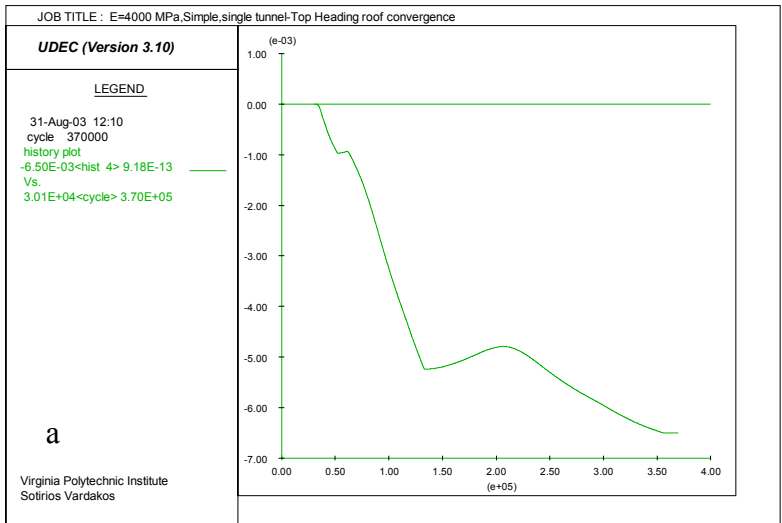


Figure 6.20: E=4000 MPa model, (a): Top heading excavation roof convergence, (b): Unbalanced force plot.

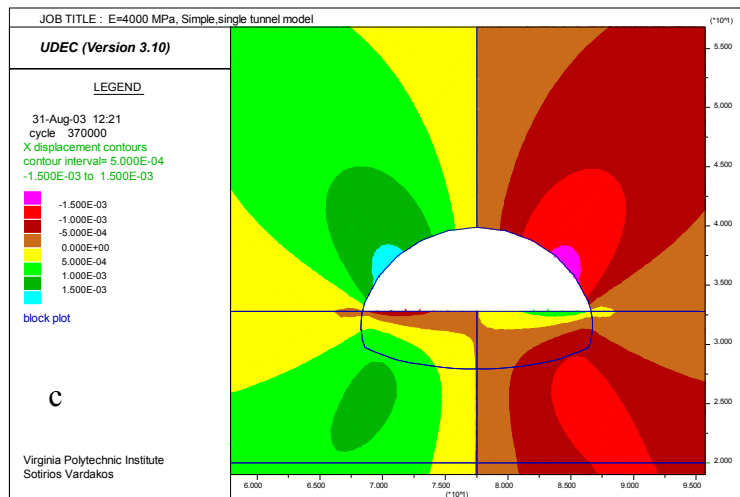
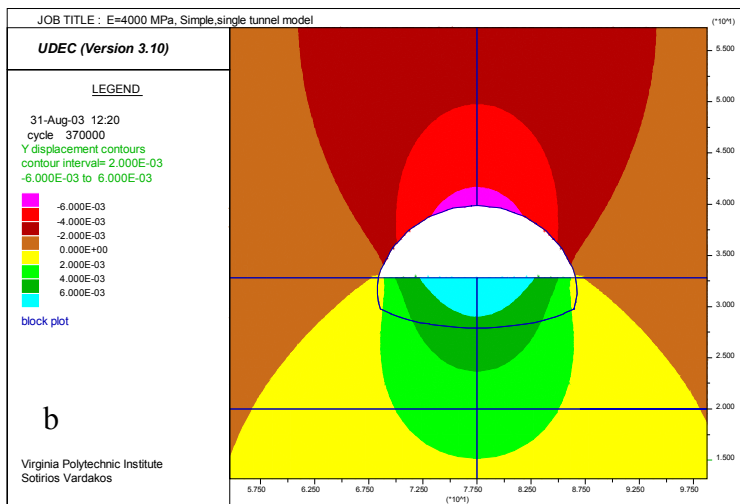
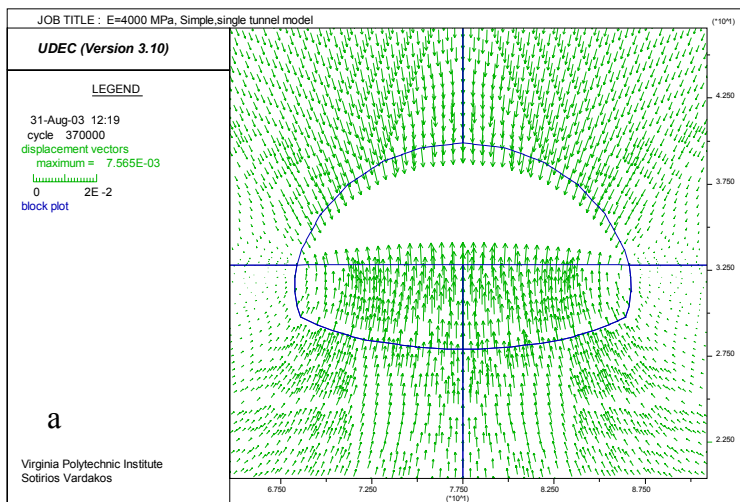


Figure 6.21: E=4000 MPa model, (a): Total displacements around top heading, (b): Vertical displacement shaded contour plot, (c): Horizontal displacements shaded contour plot.

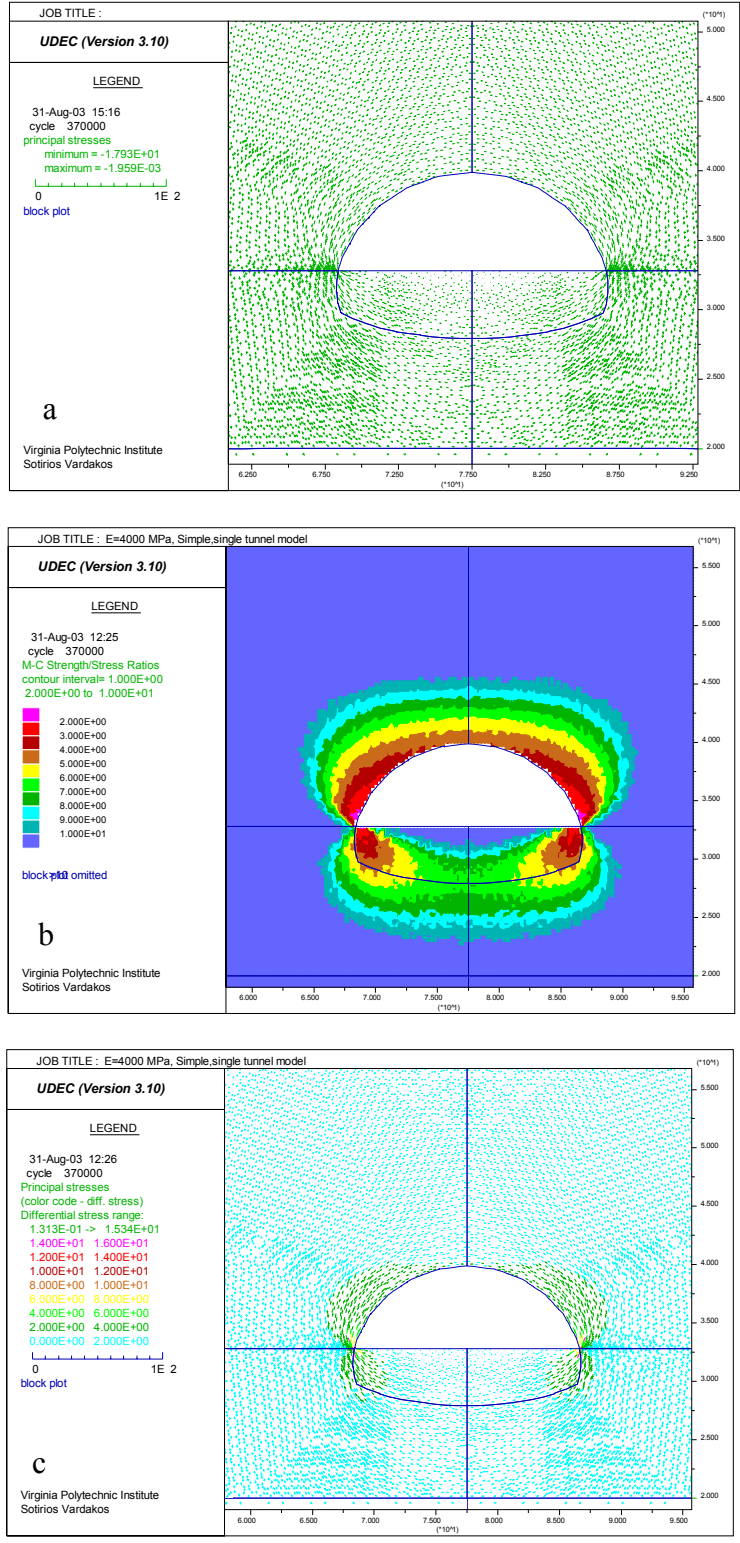


Figure 6.22: E=4000 MPa model, (a): Redistribution of stresses around top heading tunnel, (b): Strength/stress plot, (c): Deviatoric stresses.

The effects of the final stage of the excavation are shown in figures 6.24a, b, c. The vertical displacement of the roof does not practically change and most of the deformation happens on the floor and the walls. In reality this apparent stable behavior of the roof can be attributed to the elastoplastic model used. Due to unloading in the floor, an area around the tunnel develops where unloading causes strains, giving an “uplift” in the model. At the same time, there is an additional amount of vertical downward displacement which should theoretically be developed at the crown due to the relief of the excavation and the enlargement of the tunnel. However, the contribution of the bench excavation in development of downward strains and further settlement of the crown appears to be negligible.

The full excavated geometry causes the concentration of stresses at the foundation areas (elephant foot) and the installation of no support has as an effect the development of plastic yielding in these areas (figure 6.25c). This is immediately associated with the installation of three rock bolts per side as proposed by the Japan designs in order to minimize disturbance from the excavation sequence and improve stability by increasing the apparent horizontal pressure.

Table 6.10: Tunnel deformations predicted by UDEC for bench excavation stage assuming an elastic modulus of  $E=4000$  MPa.

Location	Deformation $\delta$ (mm) from method :
	UDEC
Bench stage Roof	6.79
Bench stage Left roof point	6.19
Bench stage Right roof point	6.19
Floor Heave	7.01

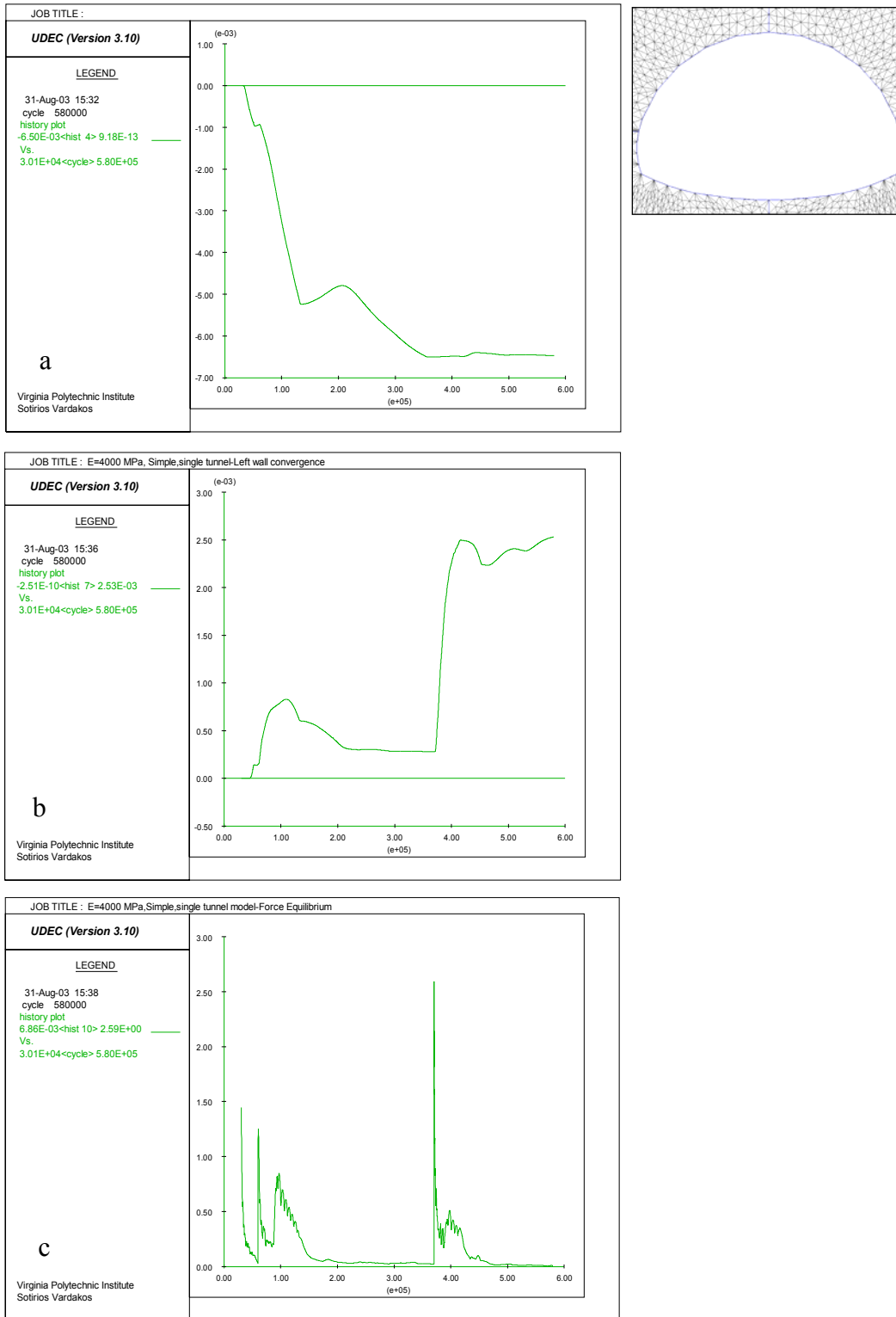


Figure 6.23: E=4000 MPa model, (a): Crownline convergence, (b): Left wall convergence (shoulder), (c) unbalanced forces plot.



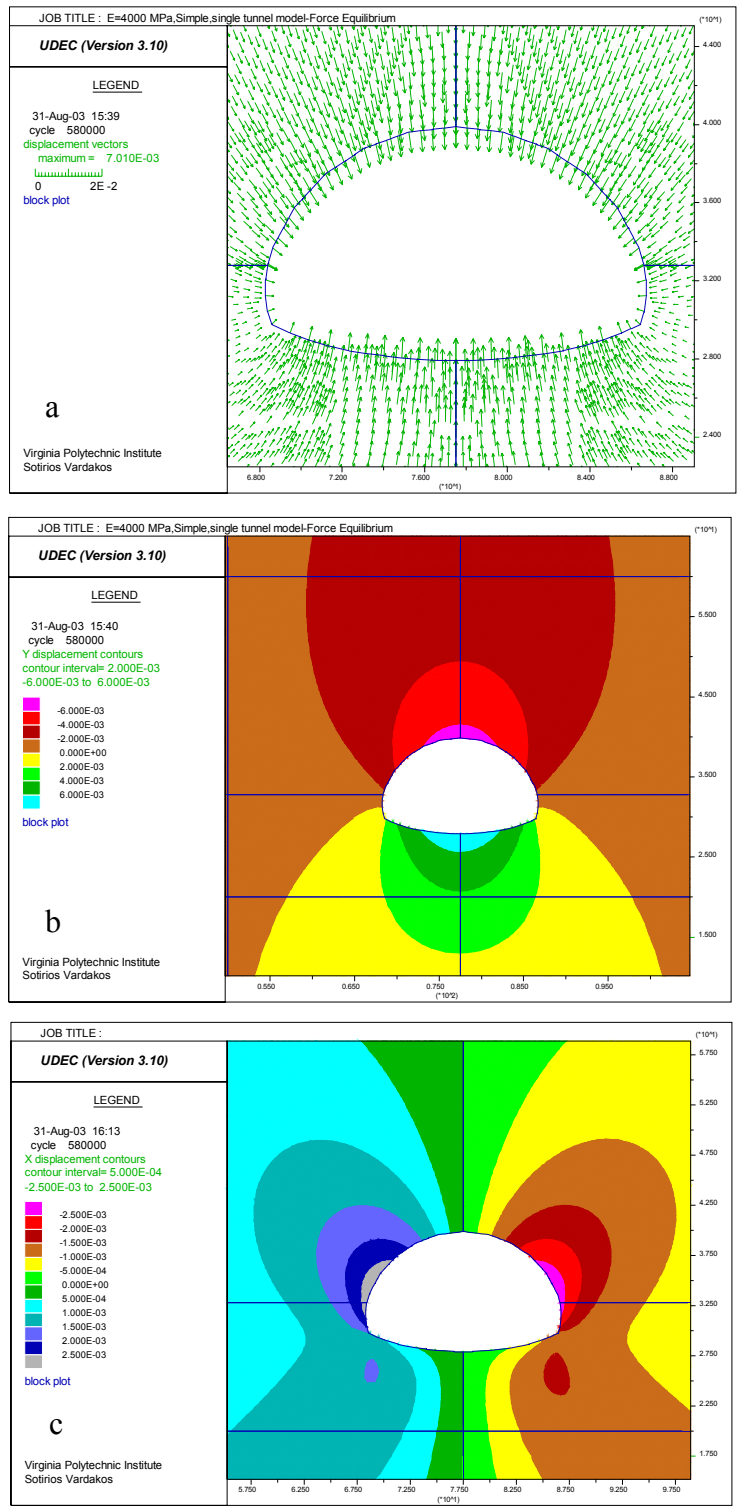


Figure 6.24: E=4000 MPa model, (a): Total displacements around final unsupported tunnel, (b): Shaded contours of vertical displacements, (c): Shaded contours of horizontal displacements.

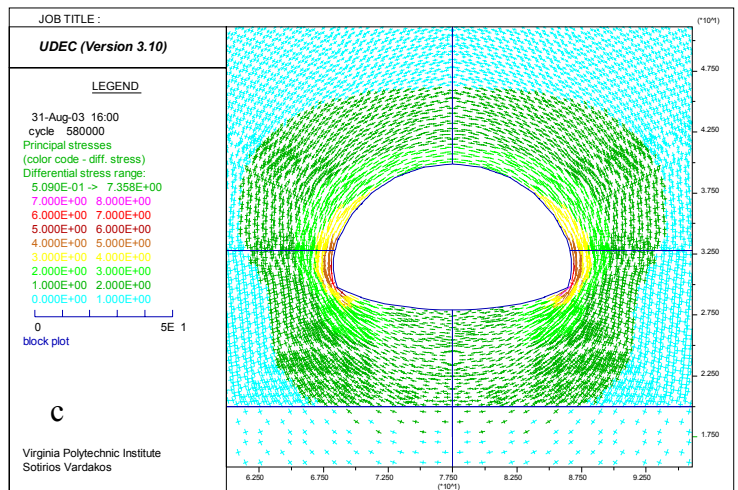
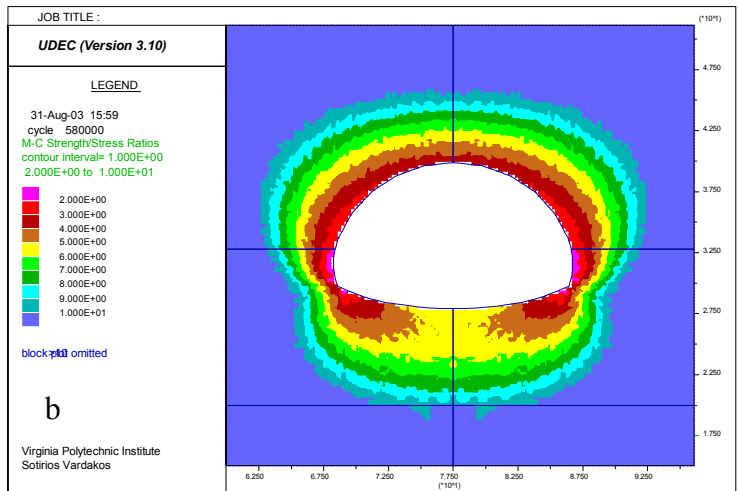
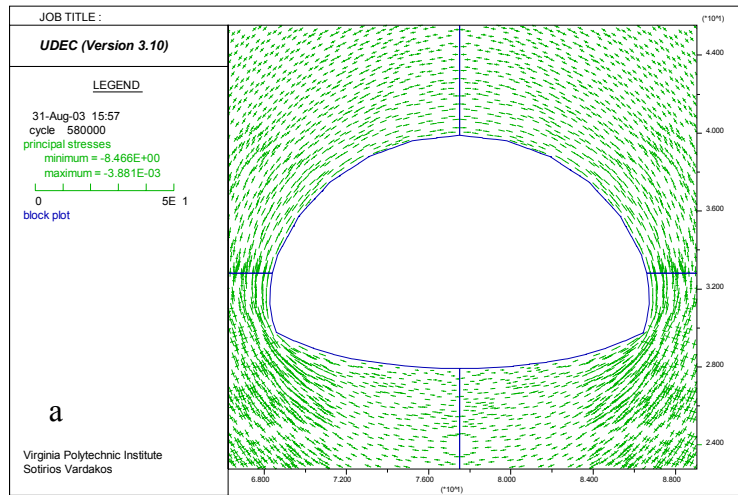


Figure 6.25: E=4000 MPa model, (a): Principal stresses around full excavation, (b): Strength/stress plot, (c): Deviatoric stresses.

Assuming now an increased elastic modulus of 12000 MPa, the analysis is repeated and the results recorded. Keeping all other parameters equal the initial excavation of the 12000 MPa model with the 5.0 m diameter tunnel boring machine causes the deformations depicted in figures 6.27 a,b,c. The closed form solution from the spreadsheet is also given for the problem of the circular tunnel, as a means to compare the deformations under nearly isotropic and anisotropic conditions. Results for comparisons are included in the following Table 6.11 and the results from the closed form solutions in Tables 6.12 and 6.13:

Table 6.11: Tunnel deformations predicted by different methods for pilot stage and by using an elastic modulus of  $E=12000$  MPa.

Location	Deformation $\delta$ (mm) from method :		
	UDEC	Elastoplastic Analysis (Salencon)	Elastic $K_o$ Analysis
TBM roof (crown)	0.49	$\sigma_{av}=1.76$ MPa	0.56
TBM wall (spring line)	0.39	$\delta=0.49$	0.40

From the above comparisons the deformations from UDEC are practically the same as the results of closed form solutions from the simplified elastoplastic and purely elastic analysis. It can also be noticed that the average deformations using the elastoplastic version (Salencon) and an average all around isotropic stress gives a result more compatible with the crown convergence (0.49 mm). In contrast to the 4000 MPa model the roof convergence has been decreased by 67.7%. Figure 6.27a shows the displacements of the excavation boundary, while figures 6.27b and 6.27c show shaded contour areas of vertical and horizontal displacements respectively. From figure 6.28b showing the mobilization of shear strength it is evident that no plastic deformations occur in the unsupported TBM opening and the mass remains in elastic state. Most deviatoric stress though is concentrated at the tunnel walls as shown in figure 6.28c.

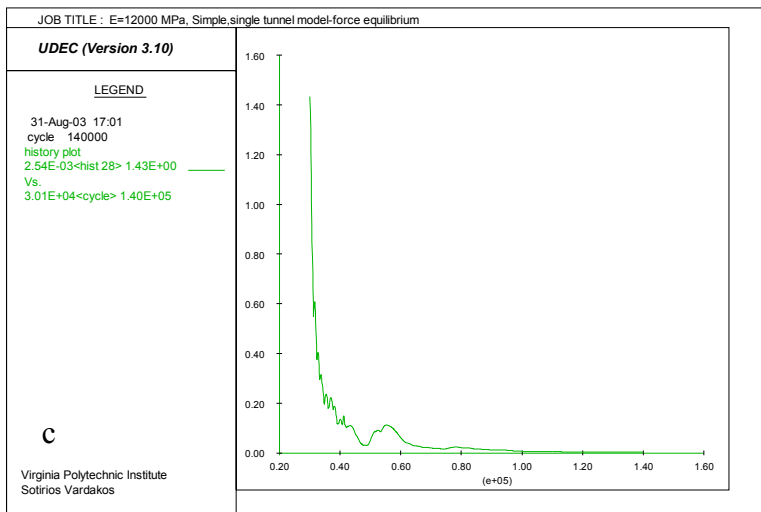
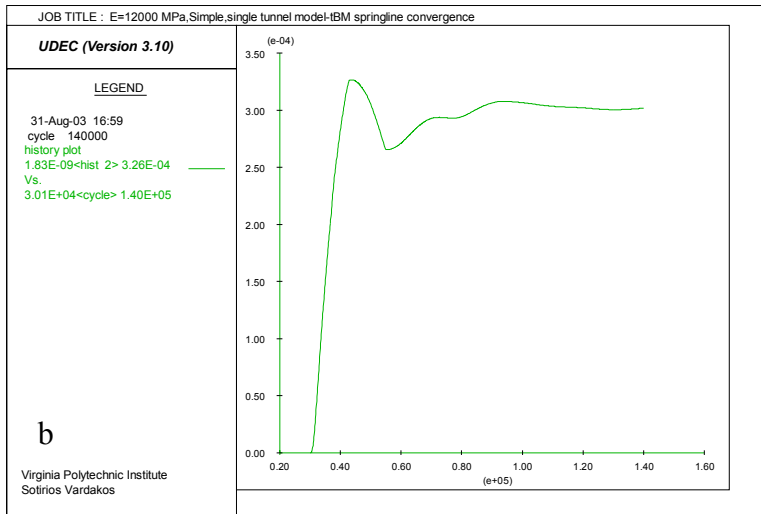
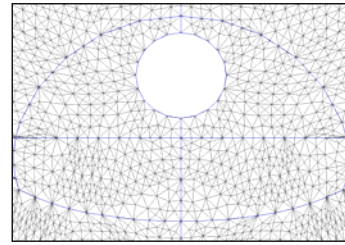
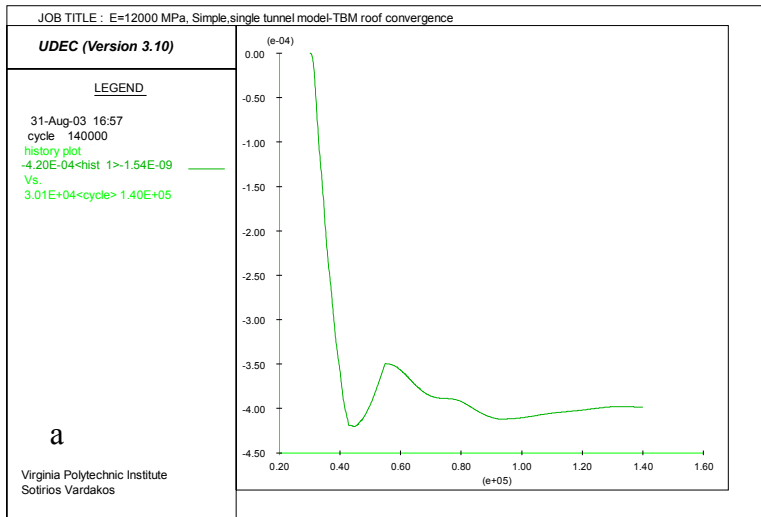


Figure 6.26: E=12000 MPa (a) Pilot tunnel roof convergence, (b): Tunnel springline convergence, (c): unbalanced force plot at end of solution.

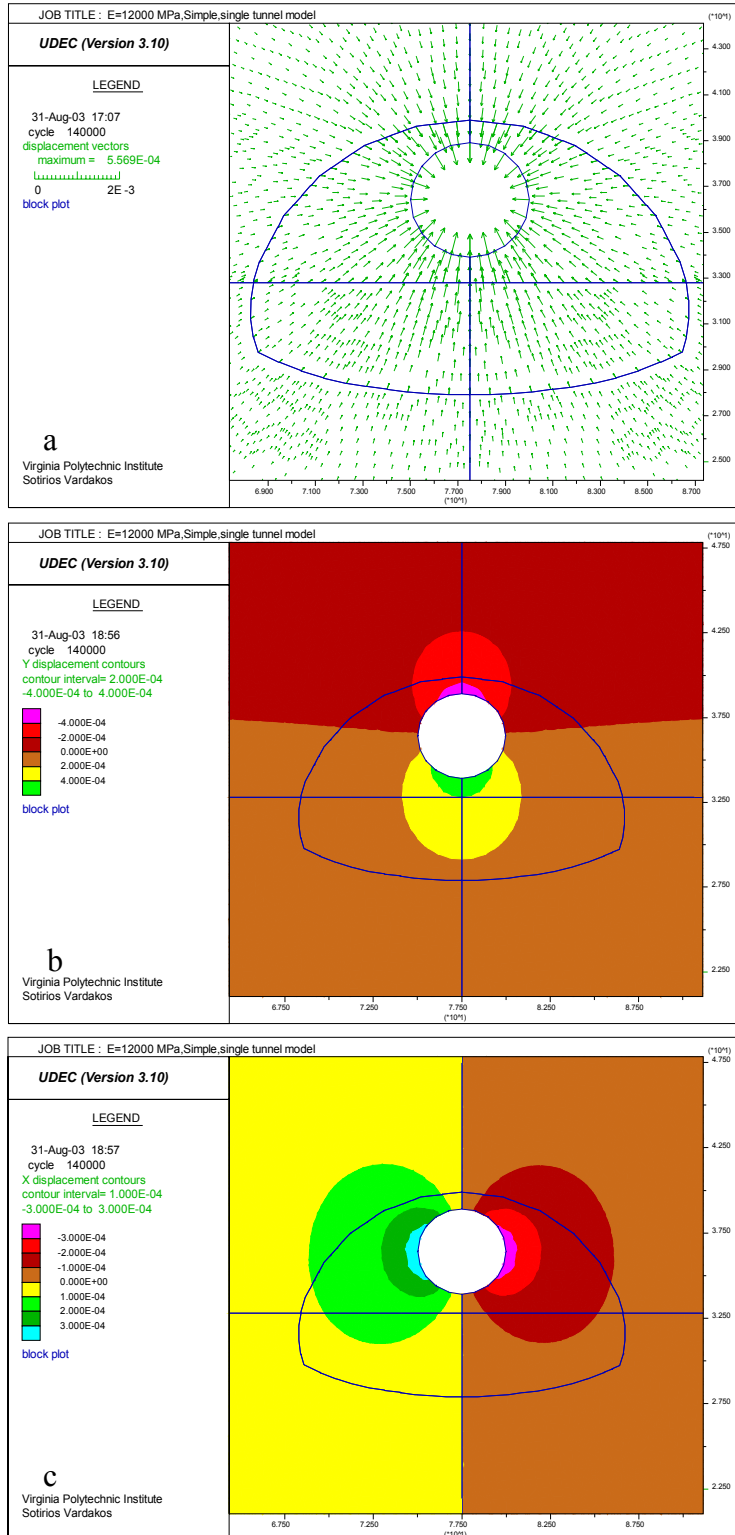


Figure 6.27: E=12000 MPa. (a): Total displacements around TBM opening, (b): Shaded contour plot of vertical displacements, (c): Shaded contour plot of horizontal displacements.

Table 6.12: Simplified elastoplastic analysis using a spreadsheet calculation for pilot tunnel, assuming E=12000 MPa. (After Kavvadas,2001)

INPUT PARAMETERS				STRESSES AND DEFORMATIONS												
Isotropic Stress	1.8 MPa			ELASTIC REGION					PLASTIC							
Radius R	2.5 m			for r<=R plastic												
c	2 MPa			if no plastic		if there is plastic region			plastic		u at plastic radius					
φ	38 degrees			c2=	0.001	c2=	0.001				0.0006					
E(mod)	12000 MPa			final stresses		final deformations		u <sub>r</sub>		σ <sub>r</sub>		σ <sub>θ</sub>				
v poisson	0.3			σ <sub>r</sub>	σ <sub>θ</sub>	u <sub>r</sub>	σ <sub>r</sub>	σ <sub>θ</sub>	u <sub>r</sub>	σ <sub>r</sub>	σ <sub>θ</sub>	u <sub>r</sub>				
p <sub>i</sub>	0 MPa			radius (r <sub>min</sub> =R)												
OUTPUT																
N <sub>φ</sub> =K <sub>p</sub>	4.204			2.51	0.014	3.586	0.049	0.014	3.586	0.000	-0.244	3.844	0.000556	0.033	8.340	0.000555757
Ko elastic	0.429			2.6	0.136	3.464	0.047	0.136	3.464	0.000	-0.105	3.705	0.000537	0.343	9.642	0.000536515
Λ=	13186.813			2.8	0.365	3.235	0.044	0.365	3.235	0.000	0.158	3.442	0.000498	1.121	12.912	0.000498186
Overload Factor				3	0.550	3.050	0.041	0.550	3.050	0.000	0.369	3.231	0.000465	2.031	16.739	0.000464968
N <sub>s</sub> =	0.439			3.2	0.701	2.899	0.038	0.701	2.899	0.000	0.542	3.058	0.000436	3.086	21.172	0.000435903
D=	16153.846			3.4	0.827	2.773	0.036	0.827	2.773	0.000	0.686	2.914	0.000410	4.296	26.259	0.000410259
const C=	0.655			3.6	0.932	2.668	0.034	0.932	2.668	0.000	0.806	2.794	0.000387	5.673	32.051	0.000387464
r <sub>p</sub> (theoretical)=	2.1903			3.8	1.021	2.579	0.032	1.021	2.579	0.000	0.908	2.692	0.000367	7.231	38.597	0.000367069
c min =	0.878 MPa			4	1.097	2.503	0.030	1.097	2.503	0.000	0.995	2.605	0.000349	8.979	45.947	0.000348714
N <sub>s</sub> max=	1.00			4.2	1.162	2.438	0.029	1.162	2.438	0.000	1.070	2.530	0.000332	10.931	54.154	0.000332107
Condition for Analysis	Elastic			4.4	1.219	2.381	0.028	1.219	2.381	0.000	1.135	2.465	0.000317	13.100	63.269	0.000317011
				4.6	1.268	2.332	0.026	1.268	2.332	0.000	1.191	2.409	0.000303	15.496	73.344	0.000303227
				4.8	1.312	2.288	0.025	1.312	2.288	0.000	1.241	2.359	0.000291	18.134	84.433	0.000290591
				5	1.350	2.250	0.024	1.350	2.250	0.000	1.285	2.315	0.000279	21.026	96.587	0.000278967
				5.2	1.384	2.216	0.023	1.384	2.216	0.000	1.324	2.276	0.000268	24.183	109.862	0.000268237
				5.4	1.414	2.186	0.023	1.414	2.186	0.000	1.358	2.242	0.000258	27.621	124.311	0.000258302
				5.6	1.441	2.159	0.022	1.441	2.159	0.000	1.389	2.211	0.000249	31.350	139.988	0.000249076

Table 6.13: Simplified elastic analysis assuming the same initial stresses generated by UDEC during model consolidation and an elastic modulus of E=12000 MPa.

INPUT PARAMETERS			STRESSES AND DEFORMATIONS						
σ <sub>h</sub> (UDEC CONSOLIDATION)	1.61 MPa	horizontal Ko=	0.834						
σ <sub>v</sub> (UDEC CONSOLIDATION)	1.93 MPa								
Radius R	2.5 m								
c	N/A MPa								
φ	N/A degrees								
E(mod)	12000 MPa								
v poisson	0.3								
p <sub>i</sub>	0 MPa								
OUTPUT									
N <sub>φ</sub> =K <sub>p</sub>									
Ko elastic	0.429								
Λ=	13186.813								
Bulk Modulus K =	10000.000 MPa								
Shear Modulus G =	4615.385 MPa								
			m	degrees	MPa	MPa	MPa	m	m
			r (distance)	θ from hor.	σ <sub>r</sub>	σ <sub>θ</sub>	τ <sub>rθ</sub>	u <sub>r</sub>	u <sub>θ</sub>
Springline			2.501	0	0.0017	4.1778	-0.0005	0.0004	0.0000
Crown			2.501	90	0.0012	2.8994	0.0005	0.00056	0.0000

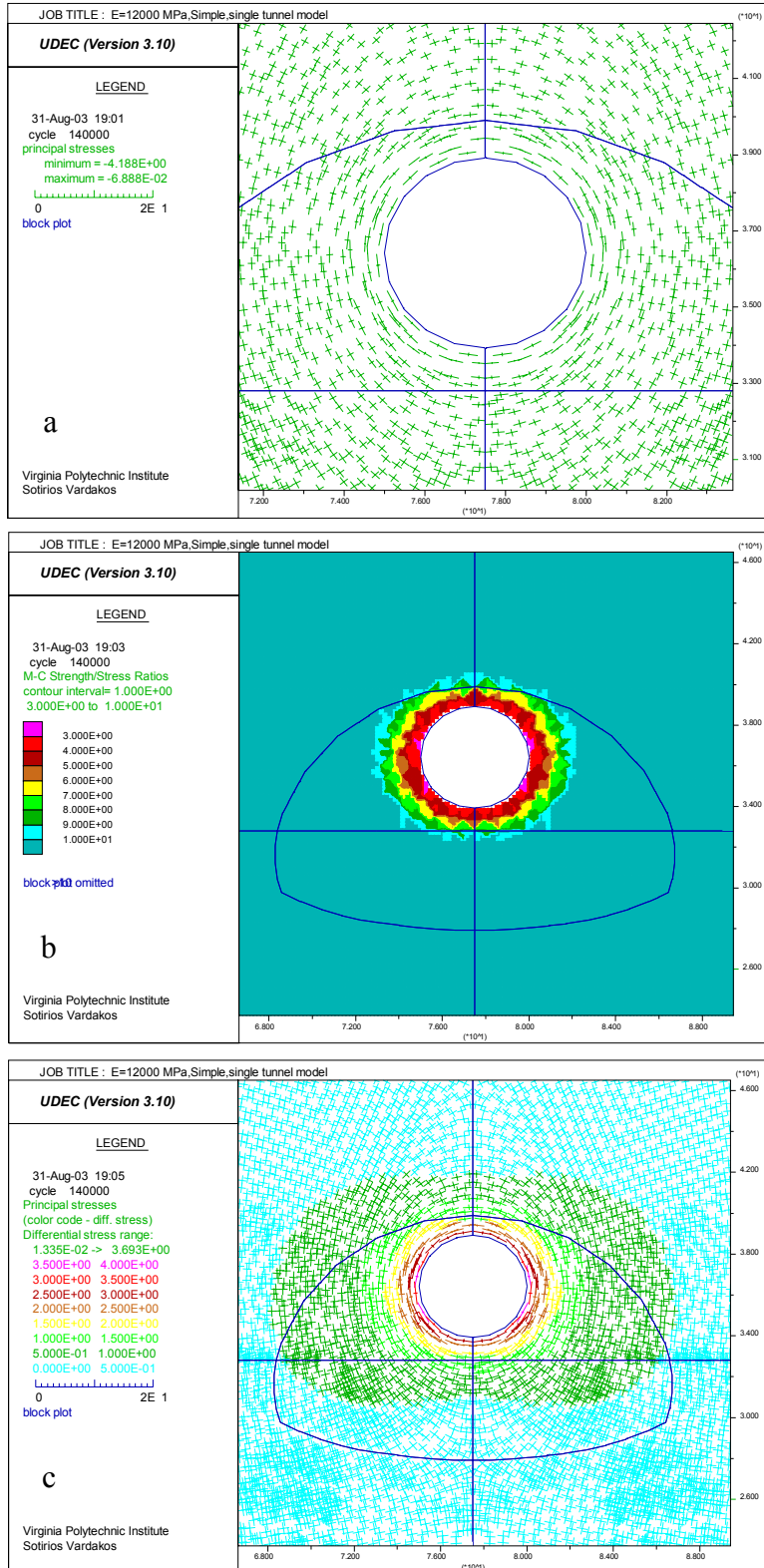


Figure 6.28: E=12000 MPa model, (a): Principal stresses around TBM opening, (b): Mobilization of shear strength around TBM tunnel, (c): Deviatoric stresses around pilot tunnel.

The next stage of the excavation causes the increase of roof convergence to approximately 2.3 mm while the roof deformation at a distance of 4.9 m from the centerline is about 2.0 mm. It is notable that the predicted floor heave exceeds the roof convergence by 1.4 mm. At this point the crown deformation is reduced by 66.7 % similarly to the reduction of the TBM tunnel convergence. From figure 6.30c the maximum expected horizontal deformation occurs in the roof at a distance of about 7.0 away from the centerline and is in the order of 1.0 mm, practically negligible. Similar to the 4000 MPa model the foundation of the top heading, causes concentration of the stresses close to that area and subsequently the shear strength is fully mobilized there (figure 6.31b).

Table 6.14: Tunnel deformations predicted by UDEC for top heading stage and by using an elastic modulus of  $E=12000$  MPa.

Location	Deformation $\delta$ (mm) from method :
	UDEC
Top Heading Roof	2.27
Top Heading Left roof point	2.0
Top Heading Right roof point	2.0
Floor Heave	3.7

The final excavation stage of the bench section does not cause any additional deformation of the tunnel roof as indicated by the analysis. The final floor heave has also the same magnitude as the crown convergence. In relation to the 4000 model, the roof convergence shows a reduction in the order of 65.6%. The walls of the tunnel at the springline level (5.7 m above the floor) show an inward displacement of 1.54 mm, that is a reduction of 58.6% over the 3.7 mm displacement in the 4000 MPa model. From figure 6.34b it becomes again evident that the most sensitive area is the foundation of the tunnel since failure initiates there for the unsupported excavation.



Table 6.15: Tunnel deformations predicted by UDEC for bench stage assuming an elastic modulus of  $E=12000$  MPa.

Location	Deformation $\delta$ (mm) from method :
	UDEC
Bench stage Roof	2.33
Bench stage Left roof point	2.14
Bench stage Right roof point	2.14
Floor Heave	2.29

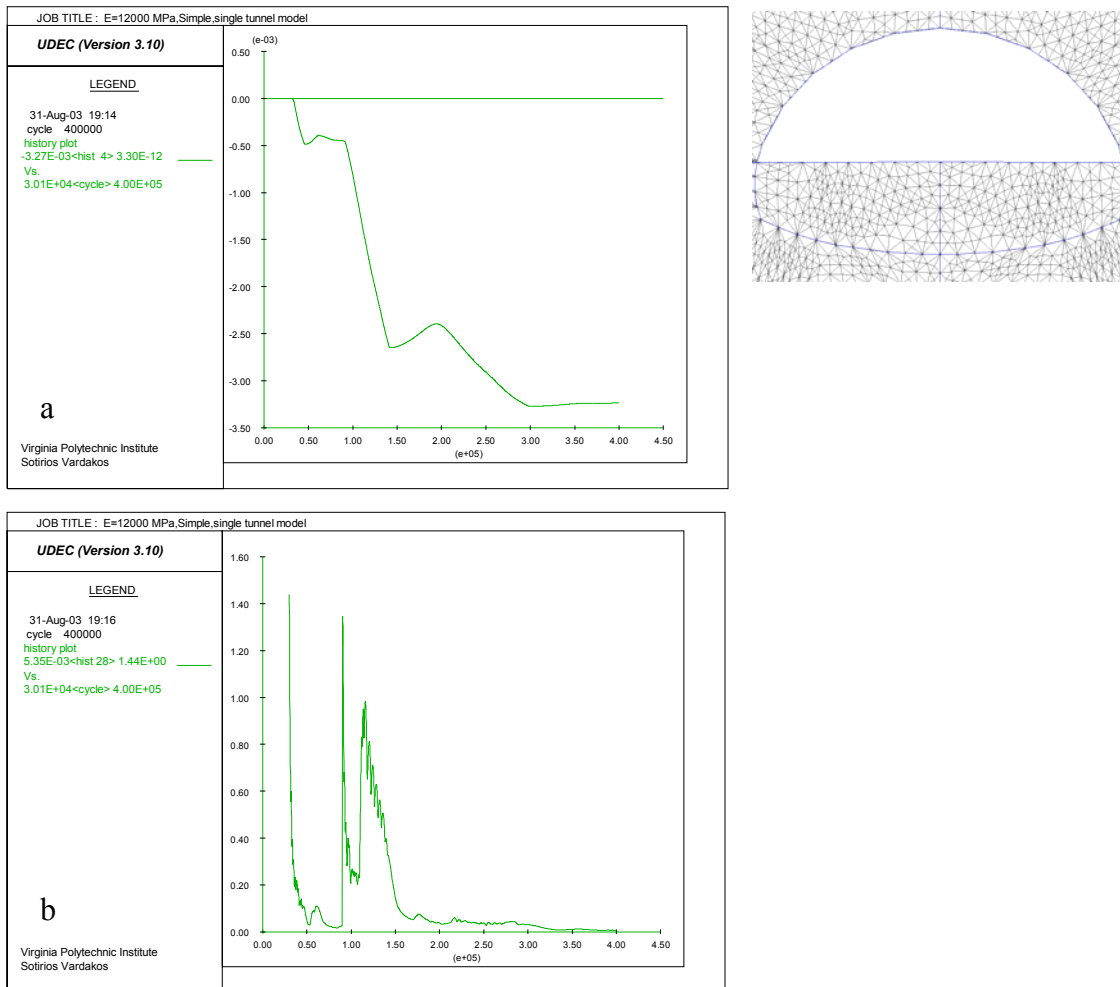


Figure 6.29:  $E=12000$  MPa. (a): Crownline convergence, (b): Unbalanced forces at end of solution.

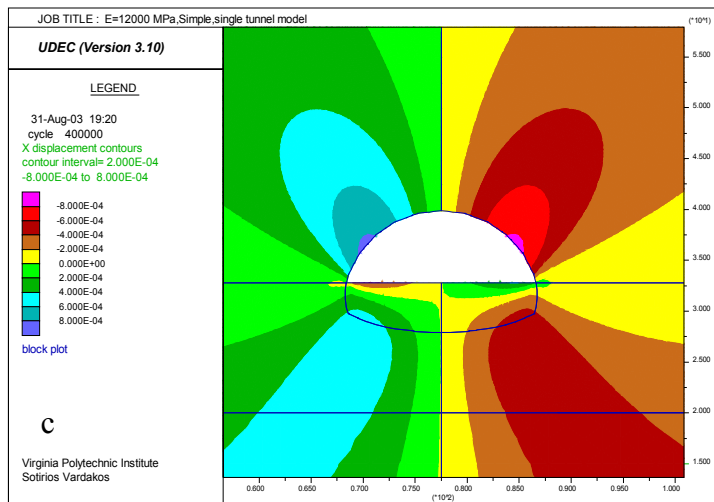
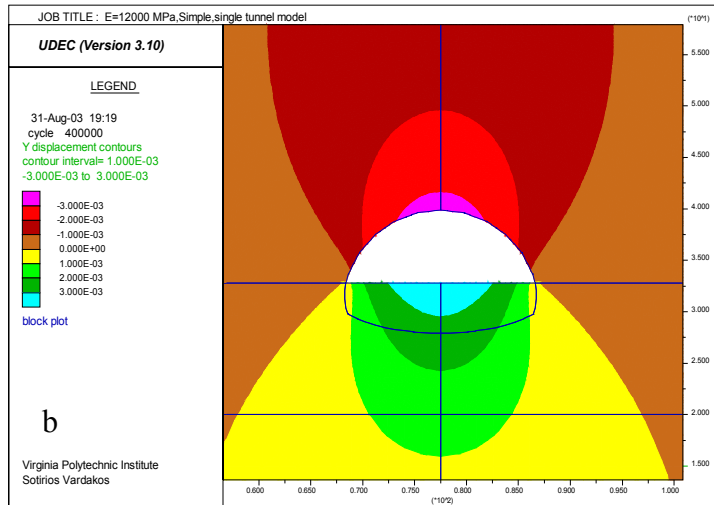
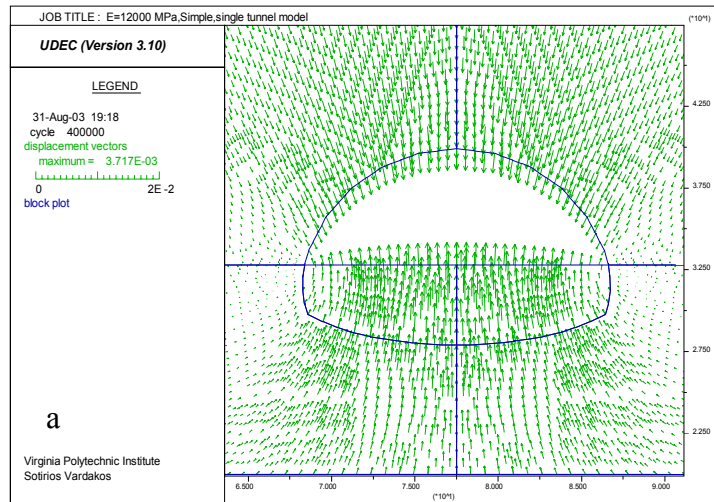


Figure 6.30: E=12000 MPa. (a): Total displacements around top heading stage, (b): Shaded contours of vertical displacements, (c): Shaded contours of horizontal displacements.

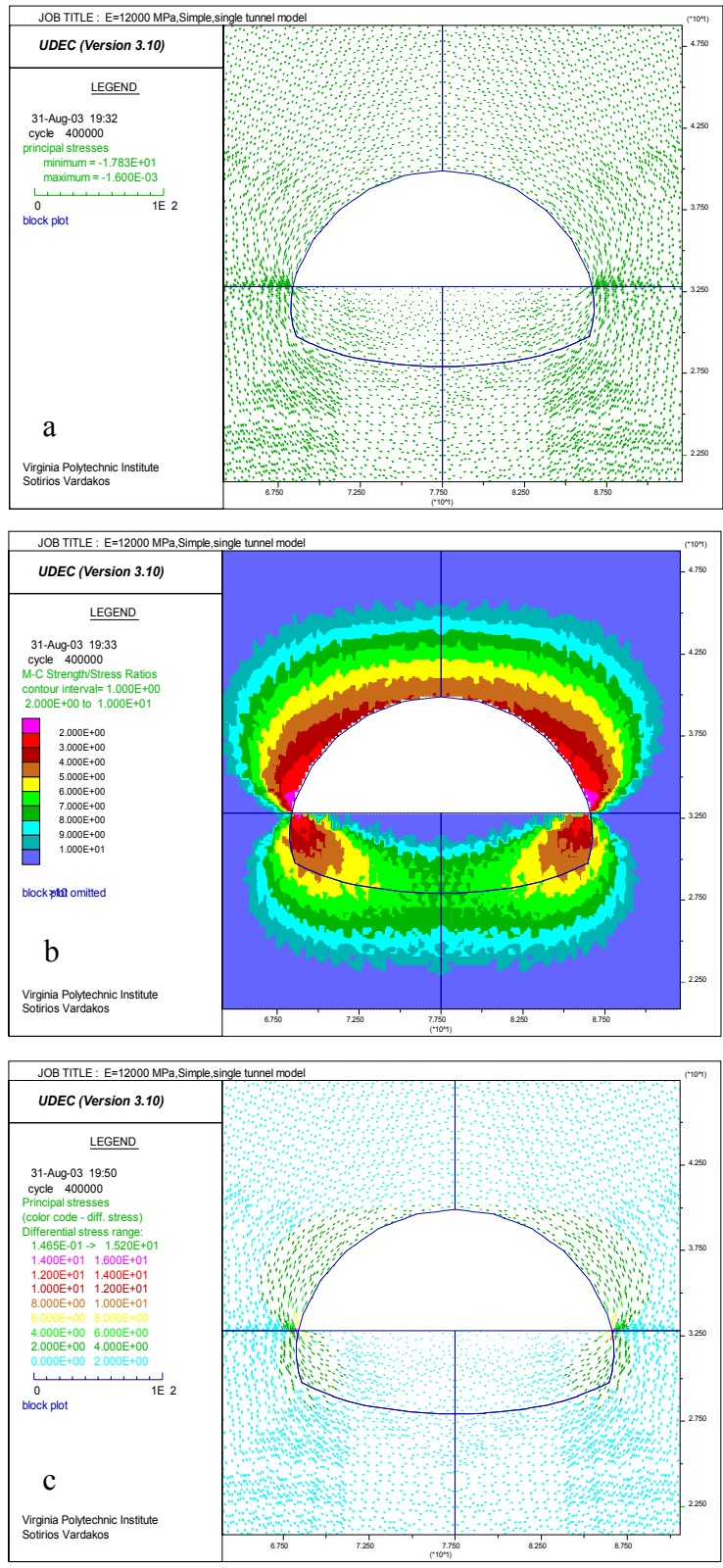


Figure 6.31: E=12000 MPa. (a)Principal stresses around top heading, (b): Strength mobilization plot, (c): Deviatoric stresses.

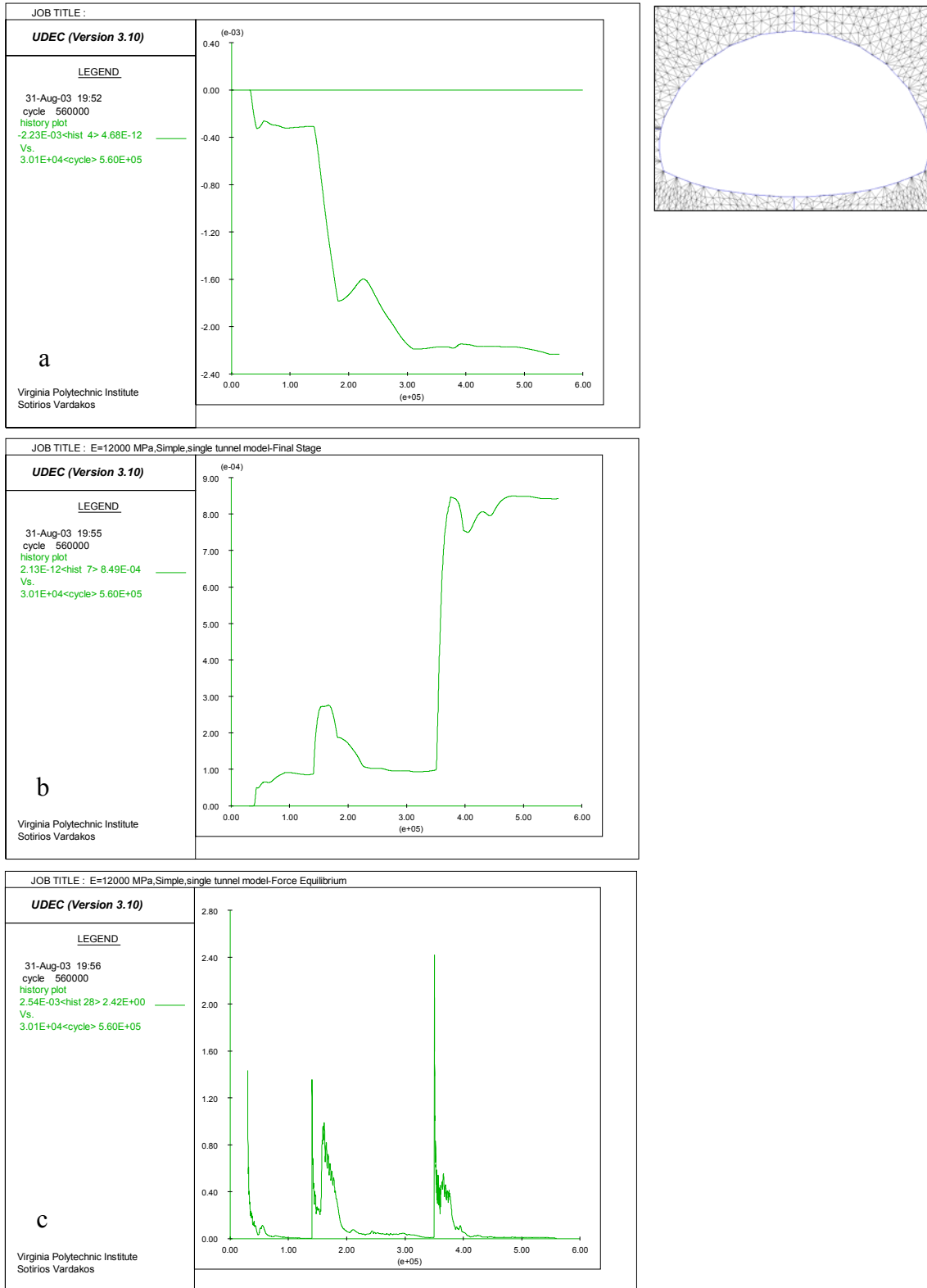


Figure 6.32: E=12000 MPa. (a): Crownline convergence vs. cycling, (b): Shoulder convergence, (c): Unbalanced force plot.

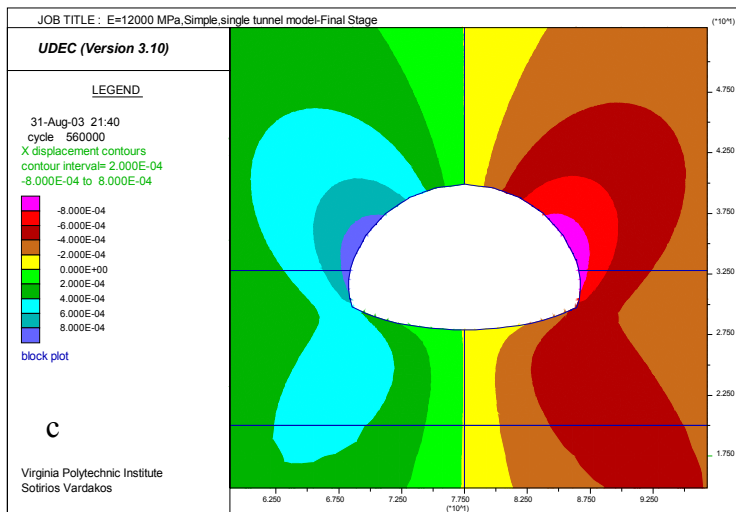
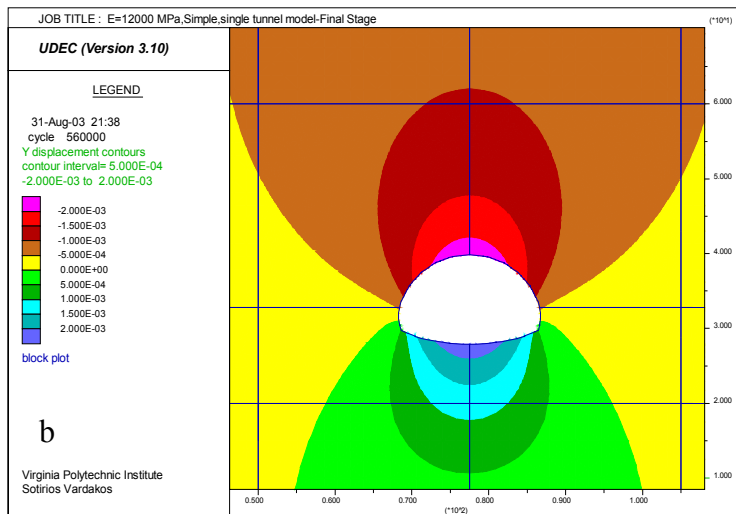
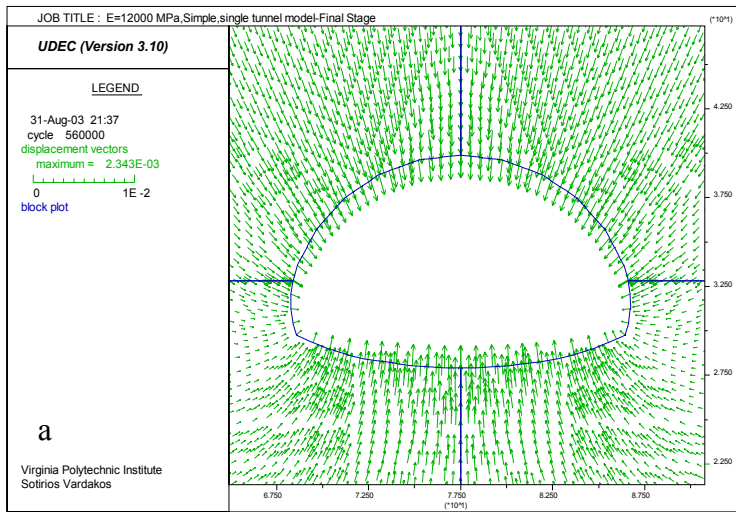


Figure 6.33: E=12000. (a): Bench excavation stage total displacements, (b): Shaded contours of vertical displacements, (c): Shaded contours of horizontal displacements.

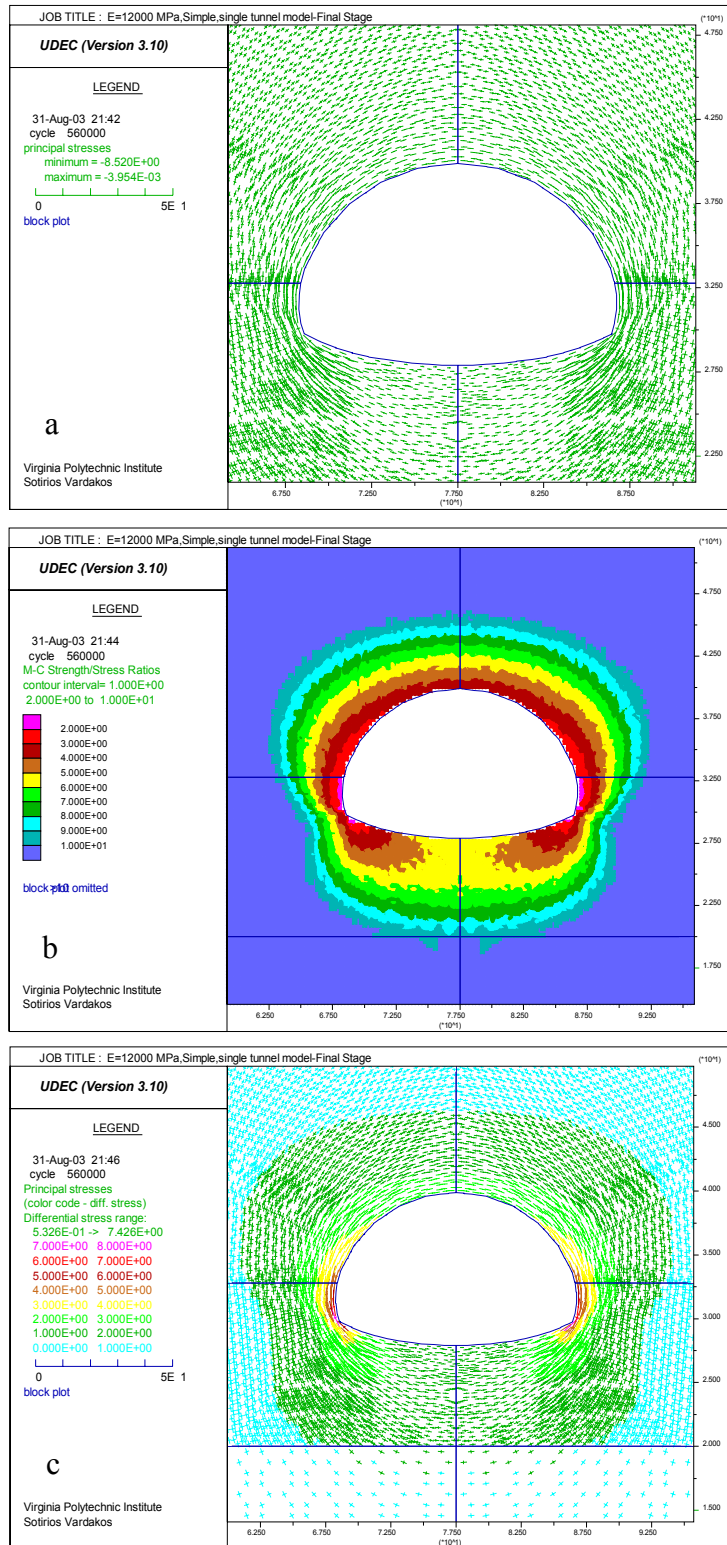
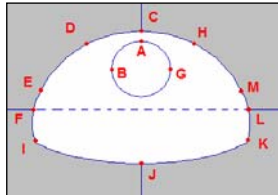


Figure 6.34: E=12000 MPa. (a)= Principal stresses around final excavation, (b):Mobilization of shear strength, (c): Deviatoric stresses.

The full results expressing the effects on the tunnel deformations by varying the elastic modulus of the rock mass are included in Table 6.16. The results are also plotted and shown cumulatively in figure 6.35. As expected from the parametric analysis the deformations are inversely proportional to the elastic modulus, it is possible to note the gradual decrease in the deformation recorded at various locations by increasing the elastic modulus. From the table it is also apparent that the variation of the elastic modulus has, as expected no affect on the stresses developed at the specified locations since the elastic modulus only affects the developed strains. The upper curves of points A and B for the crown and sidewall of the 5.0 m TBM opening reveal that there is little effect for an elastic modulus in the range 6000 – 12000 MPa and the deformations do not change appreciably. Further reduction of the elastic modulus below 6000 MPa causes more displacements while the rate of change increases also. In addition plots 6.23 and 6.32 for the 4000 and 12000 MPa models reveal that computing time needed for equilibrium is also increased by reducing the elastic modulus.

The greatest disturbance is caused by the excavation of the top heading. The geometry used is highly unfavorable in terms of vertical loads and the displacements mainly at the crownline rapidly develop. In actual conditions, the strain rate of the low modulus model should be significantly faster than the stiffer models (as opposed to the apparent cycling time to equilibrium). For modulus values below the range of 6000 MPa, the deformation increments, by comparing the roof of the TBM and the roof of the top heading, become progressively larger with a remarkable, practically quadrupled, deformation at  $E=2000$  MPa. The recorded plots are characteristic of this tunnel geometry and can be used to easily predict deformations using any intermediate modulus.

Table 6.16: Cumulative results for unsupported tunnel using continuum models using different elastic moduli.

LOCATION	Elastic Modulus						
	2000	4000	5000	6000	8000	10000	12000
maximum displacements	Pilot						
Pilot roof - A	3.05	1.52	1.19	0.96	0.73	0.60	0.49
Pilot left wall -B	2.40	1.22	0.96	0.77	0.58	0.47	0.39
Pilot right wall -G	2.40	1.22	0.96	0.77	0.58	0.47	0.39
stresses							
$\sigma_{\text{tangential}}$ roof - A	3.15	3.19	3.13	3.06	3.06	3.11	3.11
$\sigma_{\text{radial}}$ roof - A	0.53	0.51	0.50	0.51	0.51	0.52	0.52
$\sigma_{\text{tangential}}$ wall - G	4.24	4.17	4.11	4.06	4.10	4.16	4.18
$\sigma_{\text{radial}}$ wall - G	0.49	0.47	0.47	0.47	0.48	0.48	0.48
maximum displacements	Top Heading						
top heading roof - C	13.48	6.78	5.42	4.49	3.37	2.73	2.27
roof left - D	11.89	5.95	4.78	3.98	2.99	2.41	2.00
roof right - H	11.88	5.95	4.78	3.98	2.99	2.41	2.00
stresses							
$\sigma_1$ at left corner areas - F	9.39	9.41	9.41	9.37	9.32	9.45	9.42
$\sigma_1$ at right corner - L	9.48	9.50	9.50	9.46	9.41	9.54	9.50
maximum displacements	Bench Excavation						
roof - C	13.48	6.77	5.44	4.55	3.49	2.79	2.33
roof left - D	12.26	6.19	4.99	4.17	3.19	2.55	2.14
roof right - H	12.27	6.20	5.00	4.18	3.20	2.56	2.14
left wall - E	7.17	3.72	3.01	2.52	1.91	1.54	1.29
right wall - M	7.23	3.76	3.05	2.55	1.95	1.56	1.31
floor heave - J	13.86	7.01	5.58	4.60	3.42	2.74	2.29
stresses							
$\sigma_1$ at left elephant foot - I	8.36	8.46	8.47	8.47	8.49	8.51	8.52
$\sigma_3$ at left elephant foot - I	1.50	1.52	1.52	1.51	1.51	1.52	1.51
$\sigma_1$ at right elephant foot - K	8.21	8.32	8.33	8.32	8.35	8.37	8.38
$\sigma_3$ at right elephant foot - K	1.48	1.50	1.50	1.49	1.50	1.50	1.50
Notes:							
Stresses and Moduli in Mpa							
Deformations in mm							
Measurement Point locations:							



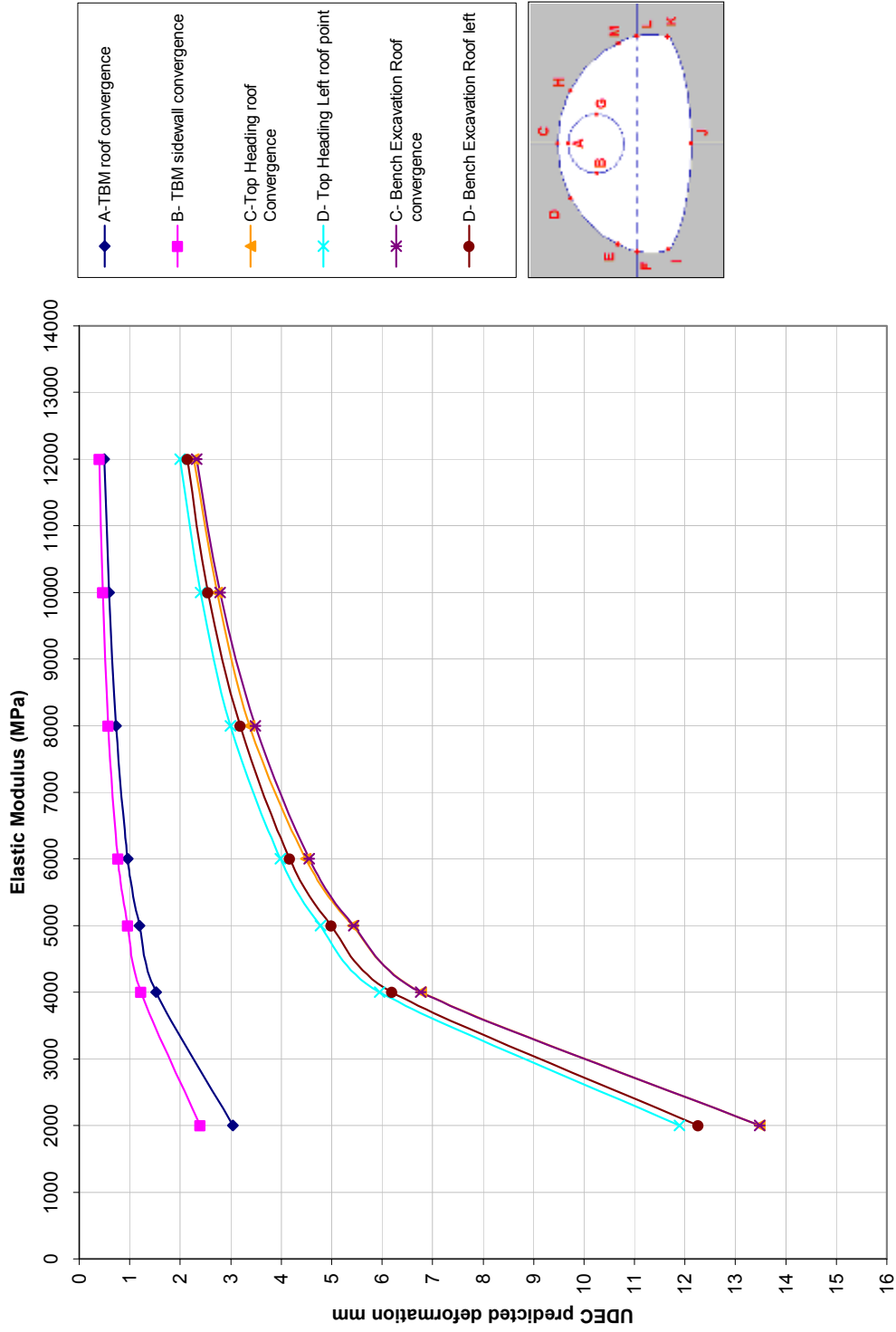


Figure 6.35: Plots of predicted deformation of continuum models, using UDEC for elastic moduli in the range from 2000 - 12000 MPa.

## 6.5.2 Effects of the $K_0$ stress ratio in simple models

Two parametric analyses were also conducted to investigate the effects of the  $K_0$  ratio in the stability of the unsupported single tunnel, one assuming an elastic modulus of  $E=5000$  MPa and one assuming a lower bound elastic modulus  $E=2000$  MPa. For the specific project and with respect to the western sector, considerable discrepancies and variations of the average elastic modulus had been so far reported. Geotechnical investigations had shown elastic moduli in the range 8.5-15 GPa (Barton, 1995) from geophysical exploration while laboratory tests on intact core samples showed higher elastic moduli than expected. On site geological reports from the JHPC refer to elastic moduli to as low as 1.0 GPa for western areas, when used in continuum modeling approaches.

Interesting data are given by Kikuchi<sup>6</sup> et al. (1984) who investigated the relationship between the elastic modulus and the unconfined compressive strength ( $q_u=\sigma_{ci}$ ) from various rock types predominant in Japan, including soft and hard rocks. It was suggested that an approximately linear relationship in a log-log plot ( $E$  vs.  $q_u$ ) expressed better the relation. These data refer to laboratory scaled strengths and moduli from various case histories and do not incorporate any reduction due to natural jointing in contrast to the previous estimation method. The relationship proposed from the Japan Nuclear Cycle and Development Institute (1999) is shown in the plot of figure 6.36 and it is:

$$E_i = 0.416 * \sigma_{ci}^{0.758} \quad \text{Equation 6.16}$$

This correlation does not account for any natural jointing and the rock mass should develop a much lower average stiffness. This value should only be considered as an upper bound expected intact modulus and limit any rock mass modulus estimates. The equation was also applied to compare modulus values from known uniaxial compression test data (figure 6.37). This figure shows both, the measured strengths and moduli as well as predicted moduli values using the above equation for the same uniaxial compression

---

<sup>6</sup> Geotechnical parameter data obtained from the Japan Nuclear Cycle-Development Institute (1999).

strengths. Actual data are shown to be close but relatively higher than what is empirically predicted. For the range of known compressive stresses the intact modulus is in the range:  $E_i=10.75\pm 1.86$  GPa.

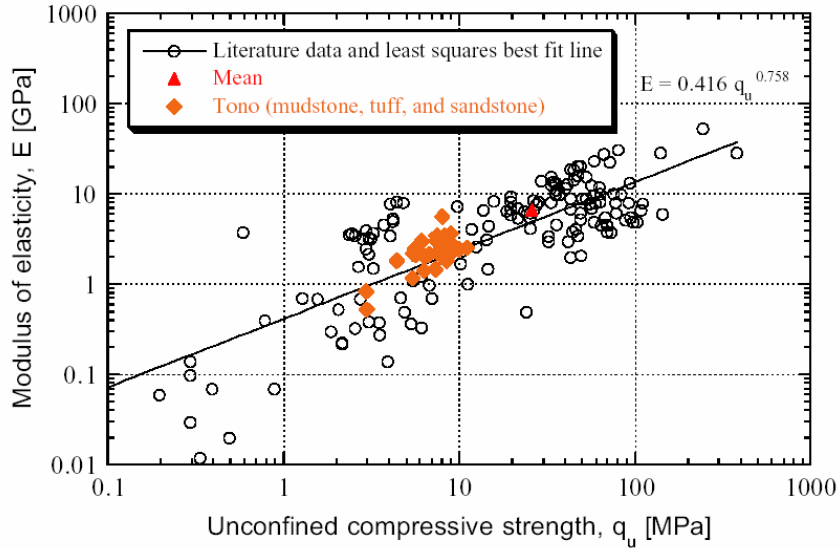


Figure 6.36: Elastic modulus and unconfined compressive strength from various soft rock types in Japan. (After Kikuchi et al., 1984)

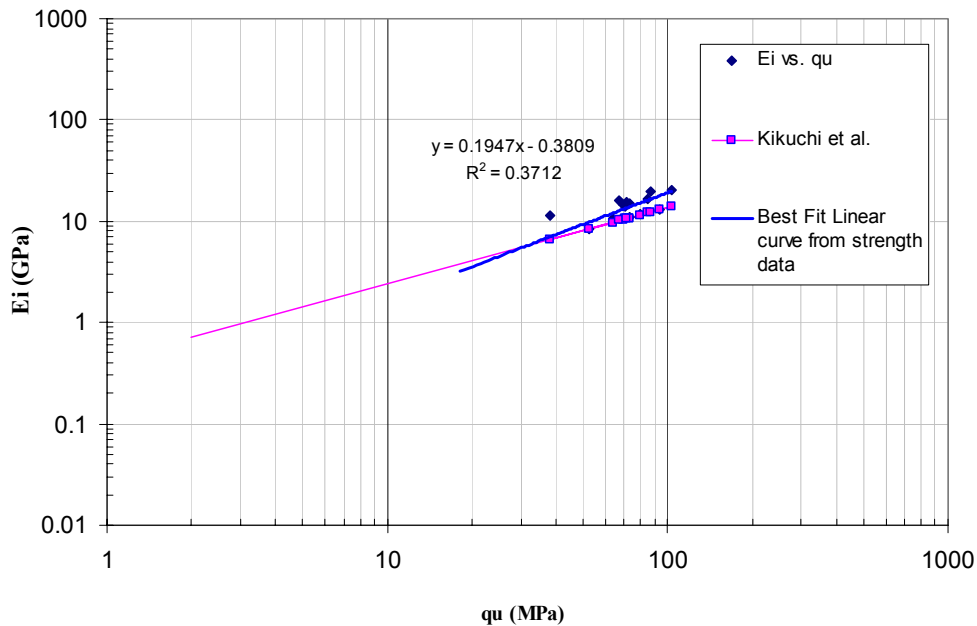


Figure 6.37: Correlations between the intact rock elastic modulus and the uniaxial compressive strength in the Wss sandstone of the Shimizu tunnel No.3 site.

For the chainage STA 913+65 geotechnical investigations have registered the geology at the specific station to be composed of moderately fractured sandstone with partially developed joints and rock mass rating quality is in the range 50-70 or in terms of the Q quality index  $Q \sim 2.0$ . From these classifications a relatively competent rock mass is theoretically anticipated. A correlation between the Japan classification system and the often used RMR and Q systems is presented as follows in Table 6.17:

Table 6.17: Correlation table between RMR, Q and Japan Highways' rock mass classification systems.

Method	Grading				
RMR	80-70	70-50	50-40	40-20	20-10
Q	40-10	10-4	4-1	1-0.1	0.1-0.01
JH Classification	B	CI	CII	DI	DII
JH Grade	90-75	75-60	60-40	40-20	20-10

Data depicted in figure 3.7 show RMR ratings for horizontal boring BH-1. Assuming the last 20.0 m of core length, an average value of  $RMR=48$  can be estimated. For this quality rating, correlations between RMR and elastic modulus by Serafeim & Pereira (1983) and Hoek & Brown (1997) suggest elastic moduli of 9.0 GPa and 6.0 GPa respectively assuming an average compressive strength of 40 MPa for the intact material:

$$E = 10^{\left(\frac{RMR-10}{40}\right)}, \text{ Serafeim \& Pereira (1983)} \quad \text{Equation 6.17}$$

$$E = \frac{\sqrt{\sigma_{ci}}}{10} 10^{\left(\frac{RMR-10}{40}\right)}, \text{ Hoek \& Brown (1997)} \quad \text{Equation 6.18}$$

The program Roclab (Rocscience Inc. 2002) was also used to estimate an average elastic modulus for the rock mass. Conservative assumptions made for the sandstone-mudstone formation according to the Hoek-Brown criterion are presented in Table 6.18 and the associated strength envelopes in  $\sigma_1$ - $\sigma_3$  and  $\sigma$ - $\tau$  space are shown in figure 6. 38:

Table 6.18: Estimated average elastic modulus using Hoek-Brown parameters.

Hoek & Brown Parameters			Result	
sigci	60	MPa	Hoek Brown mb	2.07
GSI	44		Strength s	0.0016
m <sub>i</sub>	17		parameters a	0.509
D	0.1			
Stress Range $\sigma_3 < 2.2$ MPa			$c'$	0.9 MPa
			$\phi'$	47.2 degrees
			Mohr Coulomb Fit	
			$\sigma_t$	-0.046 MPa
			$\sigma_c$	2.271 MPa
			$\sigma_{cm}$	11.27 MPa
			$E_m$	5209.5 MPa

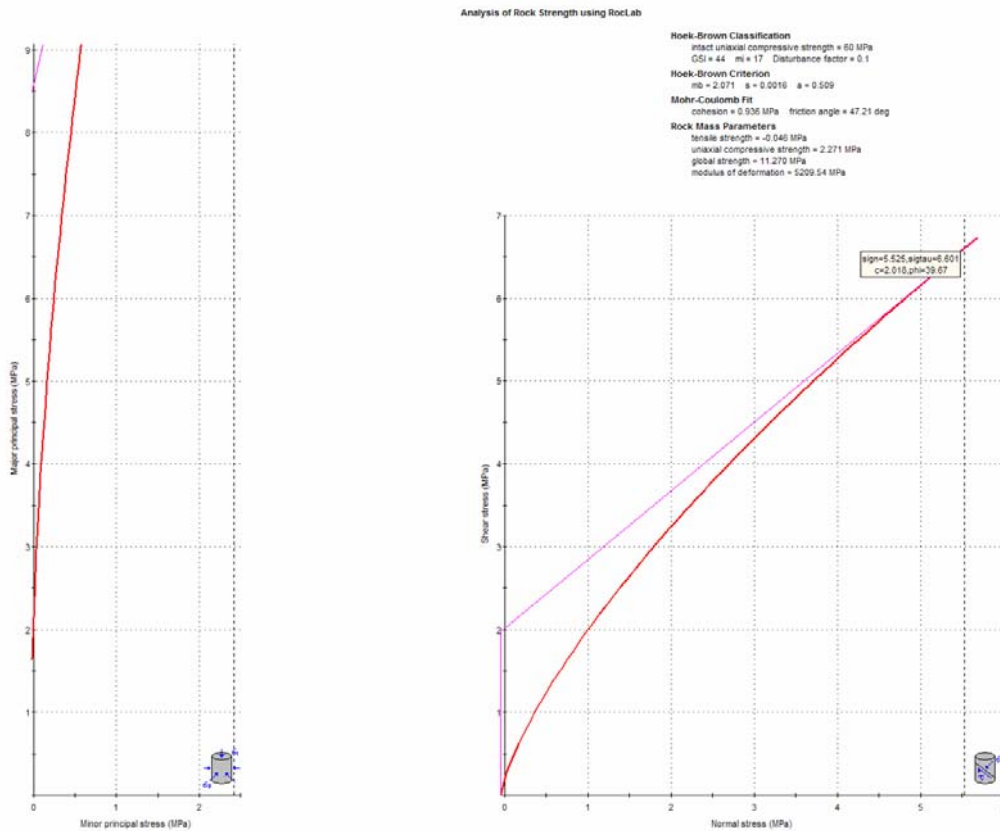


Figure 6.38 a,b: Non linear strength envelopes in  $\sigma_1, \sigma_3$  space and  $\sigma, \tau$  space using the Hoek-Brown criterion.

The program makes use of the equation 6.18 (Hoek, 1999) and as it becomes obvious the average modulus based on the above assumptions should be in the range of  $E=5200-5600$  MPa assuming some minor damaging effects during blasting and a conservative value of uniaxial compressive strength  $\sigma_{ci}=60-70$  MPa.

In this research a lower bound  $E=2.0$  GPa was considered to be the case for highly weathered Wss-Walt rock masses, which can be considered as a rational decision due to the proximity of the analyzed section with the weathered Walt unit. From the above correlations and characterization an average rock mass modulus of  $E=5000$  MPa is considered for this research as a logical starting value. This value should be implemented in a continuum analysis approach (i.e., FEM or FDM) while for discontinuum analyses its application may be conservative due to the fact that in such modeling an average elastic and anisotropic stiffness is developed by the model itself due to the jointing.

Empirical relations have also been developed to estimate the average elastic modulus of a fractured rock mass. For the case of uniaxial compression of rock that contains only one set of uniformly-spaced joints oriented normal to the direction of loading, the following equation can be used (Itasca, 2000):

$$\frac{1}{E_{mass}} = \frac{1}{E_i} + \frac{1}{s \cdot K_n} \quad \text{Equation 6.19}$$

where:

- $E_m$  = rock mass elastic modulus,
- $E_i$  = intact rock Young's modulus,
- $K_n$  = joint normal stiffness, and
- $s$  = joint spacing.

For the joint shear stiffness  $K_s$  the following relation is also proposed under the same assumptions:

$$K_s = \frac{G_m \cdot G_r}{s \cdot (G_r - G_m)} \quad \text{Equation 6.20}$$

where:

$G_m$  = rock mass shear modulus,

$G_r$  = intact rock shear modulus, and

$K_s$  = joint shear stiffness.

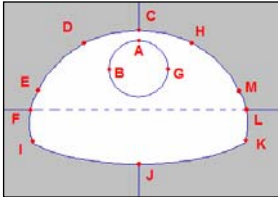
However, the complexity of the true rock mass due to the existence of multiple joint sets and complex loading do not allow for the application of such estimates. For this purpose a separate analysis using a jointed single tunnel model with a range of possible elastic moduli can aid in investigating the relation between deformations in both models and their reliance on the intact block elastic modulus used.

Results of the parametric analysis are cumulatively presented in Table 6.19. Results for  $K_o$  ratios of 0.5, 0.83, 1.0 and 1.2 are shown for the two elastic moduli used. For the  $K_o=0.83$  ratio a comparison of the models using a zero lateral strain condition is also included to address the issue of boundary conditions. Plot in figure 6.15 shows the variation in displacement of different measurement points at the excavation boundaries, over the changing  $K_o$  ratio for  $E=2000$  MPa. It should also be clarified that the displacements measured are total, i.e., they do not refer to a reference direction, horizontal or vertical. For the cases of crown and floor measurements the deformations are entirely developed in the vertical direction.

Table 6.19: Results of continuum parametric analysis for different  $K_0$  values and elastic moduli.

	$\varepsilon_x=0$					$\varepsilon_x=0$				
Insitu $K_0$ ratio:	0.5	0.83	0.83	1	1.2	0.5	0.83	0.83	1	1.2
Elastic Modulus:	5000	5000	5000	5000	5000	2000	2000	2000	2000	2000
<b>LOCATION</b>										
<b>maximum displacements</b>										
Pilot roof - A	1.36	1.19	1.19	1.13	1.07	3.45	3.05	2.90	2.86	2.55
Pilot left wall -B	0.45	0.96	0.96	1.19	1.49	0.96	2.40	2.30	3.05	3.66
Pilot right wall -G	0.45	0.96	0.96	1.18	1.49	0.96	2.40	2.30	3.05	3.66
<b>stresses</b>										
$\sigma_{\text{tangential}}$ roof - A	1.45	3.13	3.14	3.90	4.90	1.30	3.15	3.06	3.99	4.87
$\sigma_{\text{radial}}$ roof - A	0.29	0.50	0.50	0.59	0.71	0.30	0.53	0.51	0.63	0.73
$\sigma_{\text{tangential}}$ wall - G	4.62	4.11	4.11	3.96	3.72	4.72	4.24	4.07	4.02	3.62
$\sigma_{\text{radial}}$ wall - G	0.48	0.47	0.47	0.68	0.47	0.49	0.49	0.48	0.49	0.48
<b>maximum displacements</b>										
Top heading roof - C	5.86	5.42	5.62	5.24	5.02	14.57	13.48	13.97	13.05	12.46
Top Heading roof left - D	4.99	4.78	4.97	4.73	4.73	12.45	11.89	12.34	11.79	11.77
Top Heading roof right - H	5.00	4.78	4.97	4.73	4.73	12.44	11.88	12.32	11.79	11.77
<b>stresses</b>										
$\sigma_1$ at left corner areas - F	9.78	9.41	9.38	9.24	9.02	9.78	9.39	9.40	9.21	8.97
$\sigma_1$ at right corner - L	9.85	9.50	9.47	9.33	9.11	9.86	9.48	9.49	9.30	9.06
<b>maximum displacements</b>										
bench excavation										
roof - C	6.01	5.44	5.65	5.19	4.89	14.76	13.48	14.02	12.98	12.30
roof left - D	5.24	4.99	5.15	4.94	4.97	12.86	12.26	12.70	12.19	12.22
roof right - H	5.25	5.00	5.16	4.96	4.98	12.86	12.27	12.71	12.21	12.24
left wall - E	2.23	3.01	3.01	3.54	4.29	5.37	7.17	7.23	8.40	10.14
right wall - M	2.25	3.05	3.05	3.57	4.32	5.42	7.23	7.29	8.47	10.22
floor heave - J	5.81	5.58	5.52	5.48	5.35	14.36	13.86	13.64	13.64	13.37
<b>stresses</b>										
$\sigma_1$ at left elephant foot - I	8.24	8.47	8.49	8.58	8.74	8.13	8.36	8.38	8.49	8.65
$\sigma_3$ at left elephant foot - I	1.47	1.52	1.53	1.53	1.53	1.45	1.50	1.51	1.52	1.52
$\sigma_1$ at right elephant foot - K	8.10	8.33	8.35	8.44	8.60	7.99	8.21	8.24	8.34	8.51
$\sigma_3$ at right elephant foot - K	1.45	1.50	1.51	1.51	1.51	1.43	1.48	1.49	1.50	1.51

Notes:  
 Stresses and Moduli in Mpa  
 Deformations in mm  
 Measurement Point locations:





For comparison purposes analyses conducted for the cases of  $K_o=0.5$  and  $K_o=1.2$  will be described. It becomes obvious from the plot that as the horizontal pressure increases ( $K_o$  increases) points located in the roof of the excavations show progressively lower downward displacement, a behavior logically expected even from the theory of elasticity. In contrast as the  $K_o$  ratio is increased points located in the sidewalls (points E and M) show larger inward displacements. It is most interesting to observe that as the  $K_o$  value increases from the nearly isotropic  $K_o=0.83$  to  $K_o=1.2$  most deformations recorded in the analyses with reference to the top heading and bench excavation stages, exhibit convergence trend to the range of 12 mm. More specifically for the TBM excavation stage the following deformations are shown in the following table (the values from Table 6.19 have been rounded to the closest decimal).

Table 6.20: Comparison of predicted deformations by UDEC for the unsupported pilot opening for two extreme values of  $K_o$ , assuming  $E=2000$  MPa.

Excavation stage: TBM	$K_o=0.5$	$K_o=1.2$
Location	Deformations ( $\delta$ in mm)	
Crownline	3.5	2.6
Springline	1.0	3.7

The above results reveal a 25.7% reduction for the crownline displacement and a 270% increase in the springline convergence. This trend is also apparent from general Table 6.19 where the crownline deformations do not change between the two extremes appreciably as opposed to the springline displacements. The next excavation stage (top heading) causes some additional convergence to the roof bringing the total deformation to the values represented in Table 6.21:

Table 6.21: Comparison of predicted deformations by UDEC for the unsupported top heading stage for two extreme values of  $K_o$ , assuming  $E=2000$  MPa.

Excavation stage: Top Heading	$K_o=0.5$	$K_o=1.2$
Location	Deformations ( $\delta$ in mm)	
Top Heading Roof	14.6	12.5
Top Heading left (4.9 m off centerline)	12.5	11.8

It is shown again that the deformations are relatively reduced by increasing the  $K_o$  ratio from 0.5 to 1.2. The roof convergence is reduced by 14.65% while at a distance of 4.9 m from the centerline the total convergence is reduced only by 5.6%. The final excavation stage does not produce any additional deformations of practical concern and the two curves expressing the roof displacements at the end of the numerical analysis, practically converge. It is notable though that the inward displacement of the tunnel sidewalls after the bench excavation increases quite rapidly and is the most sensitive to  $K_o$ . More specifically the deformation calculated for  $K_o=0.5$  is about 5.4 mm while for  $K_o=1.2$  is in the order of 10.1 mm, expressing an increment of 87%. From the above it becomes obvious that high  $K_o$  ratios can contribute favorably to stability especially for this type of geometry with a high horizontal/vertical axis, geometry ratio. A rational result is to expect high support loads for low  $K_o$  ratios and thus more expensive and higher capacity support measures.

In figures 6.39 to 6.44, a direct comparison between the  $K_o=0.5$  and  $K_o=1.2$  models is illustrated. Figures 6.39a, b, 6.41a, b and 6.43a, b show the redistributed stresses around the tunnel for the TBM excavation, top heading and bench excavation stages respectively. From the shear strength mobilization it is obvious that for any of the cases deformations around the 5.0 m openings are elastic and no plastic zone is formed. For the  $K_o=0.5$  case a considerable area over the roof of the tunnel heading becomes relieved of hoop stresses after the construction that suggests the caution for any structurally controlled unstable rock masses. Figures 6.42b, 6.42d show the deviatoric stress concentrations around the top heading stage. For  $K_o=0.5$  critical areas are the foundations of the top excavation where failure starts if the tunnel is left unsupported.

Adversely for the case of  $K_o=1.2$  (figure 6.42d) more shearing strength is mobilized over above and below the excavated space. This mobilization has the advantage of relieving the excessive concentrations around the temporary foundation areas and localized failure does not commence. Similarly the final excavation stage causes initiation of failure at the tunnel foundations for the  $K_o=0.5$  case while the  $K_o=1.2$  models exhibit more stable behavior. In the last case maximum deviator stresses are still developed at the foundations but due to the wider mobilization of shear strength around the tunnel, predicted failure is only localized. Results from the parametric analysis conducted, for  $E=5000$  MPa reveal similar behavior. The results from the analysis are represented in the following table for the pilot opening:

Table 6.22: Continuum analysis results for cases of  $K_o=0.5$  and  $K_o=1.2$ , assuming  $E=5000$  MPa.

Excavation stage: TBM	$K_o=0.5$	$K_o=1.2$
Location	Deformations ( $\delta$ in mm)	
Crownline	1.36	1.1
Springline	0.5	1.5

The above results suggest a reduction in the order of 19% for the TBM roof convergence and an increase of about 200% for the sidewalls. The top heading stage promotes the deformation of the roof to the following values:

Table 6.23: Continuum analysis results for cases of  $K_o=0.5$  and  $K_o=1.2$ , assuming  $E=5000$  MPa.

Excavation stage: Top Heading	$K_o=0.5$	$K_o=1.2$
Location	Deformations ( $\delta$ in mm)	
Top Heading Roof	5.9	5
Top Heading left (5.0 m off centerline)	5	4.7

From the above it can be seen that the crownline shows a 14.3% reduction in deformations while roof points located about 5 m from the centerline do not show any appreciable change in total displacement. Finally for the bench excavation the crown

deformation presents a reduction in the order of 18.3% and sidewalls show an increase of 92.8%.

Table 6.24: Continuum analysis results for bench excavation stage, assuming  $E=5000$  MPa.

Excavation stage: Bench	$K_0=0.5$	$K_0=1.2$
Location	Deformations ( $\delta$ in mm)	
Bench Roof (C)	6	4.9
Bench sidewalls	2.2	4.3

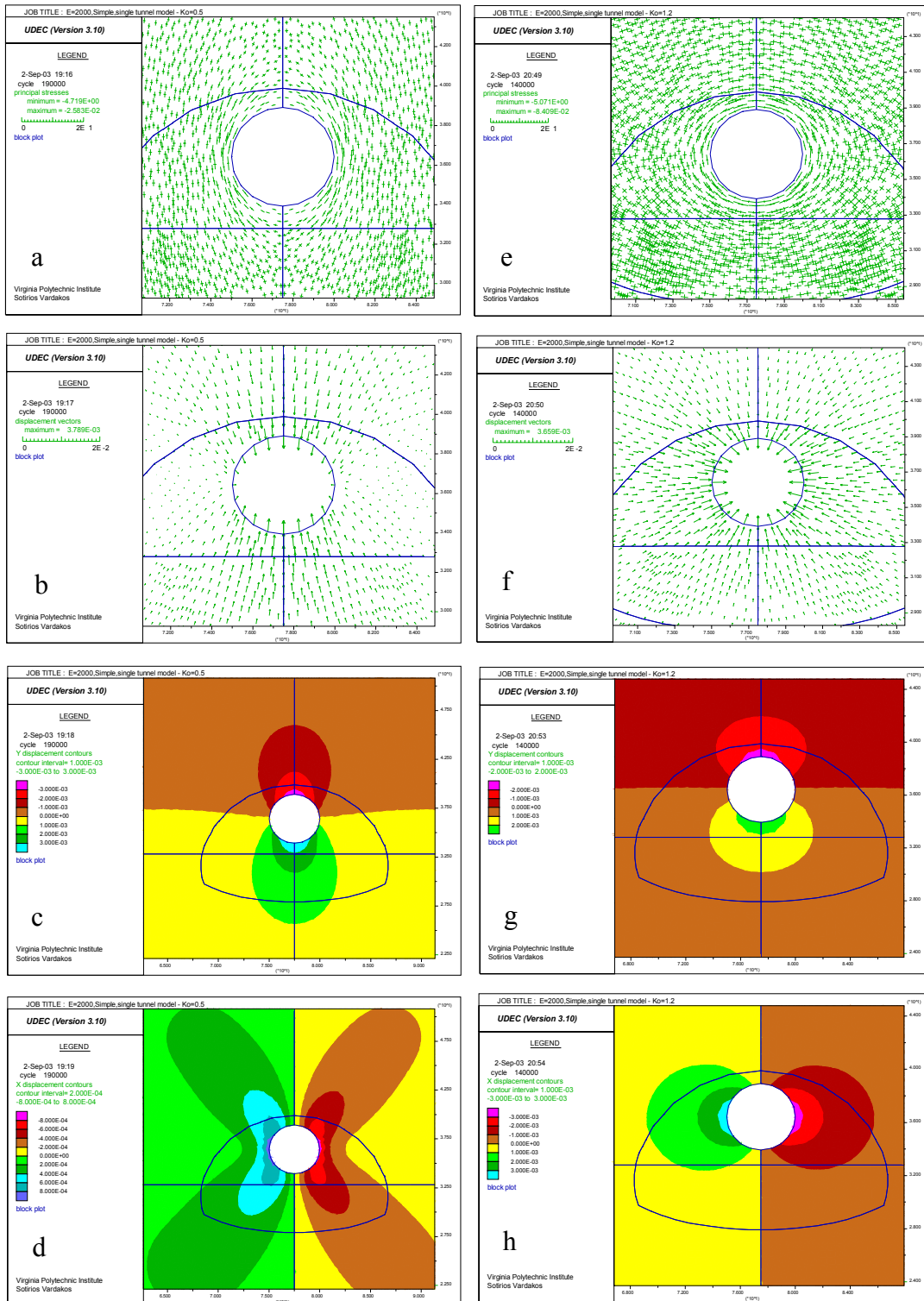


Figure 6.39:  $K_0=0.5$ , (a): Stress redistribution, (b): Total displacements, (c): Shaded contours for vertical displacements, (d): Shaded contours for horizontal displacements.  $K_0=1.2$ , (e): Stress redistribution, (f): Total displacements, (g): Shaded contours for vertical displacements, (h): Shaded contours for horizontal displacements.

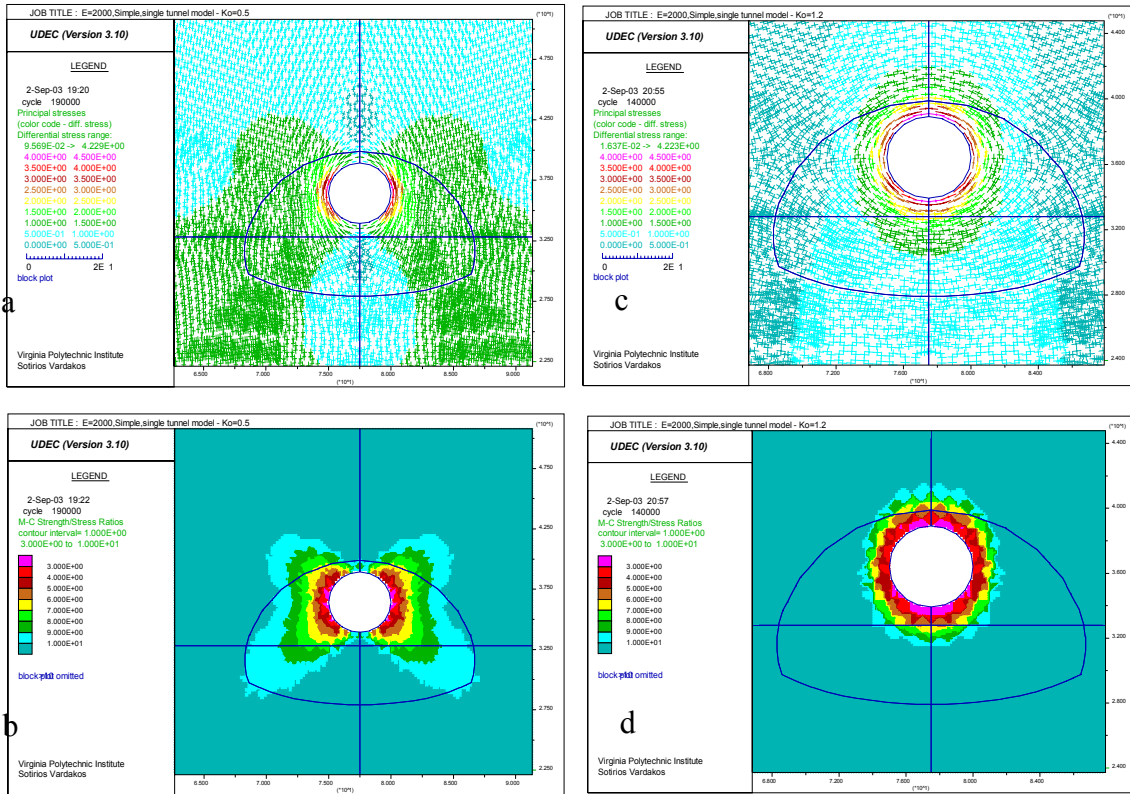


Figure 6.40: TBM pilot tunnel-  $K_0=0.5$ , (a): Deviatoric stresses, (b):Strength/stress ratio.  $K_0=1.2$ , (c): Deviatoric stresses, (d):Strength/stress ratio.

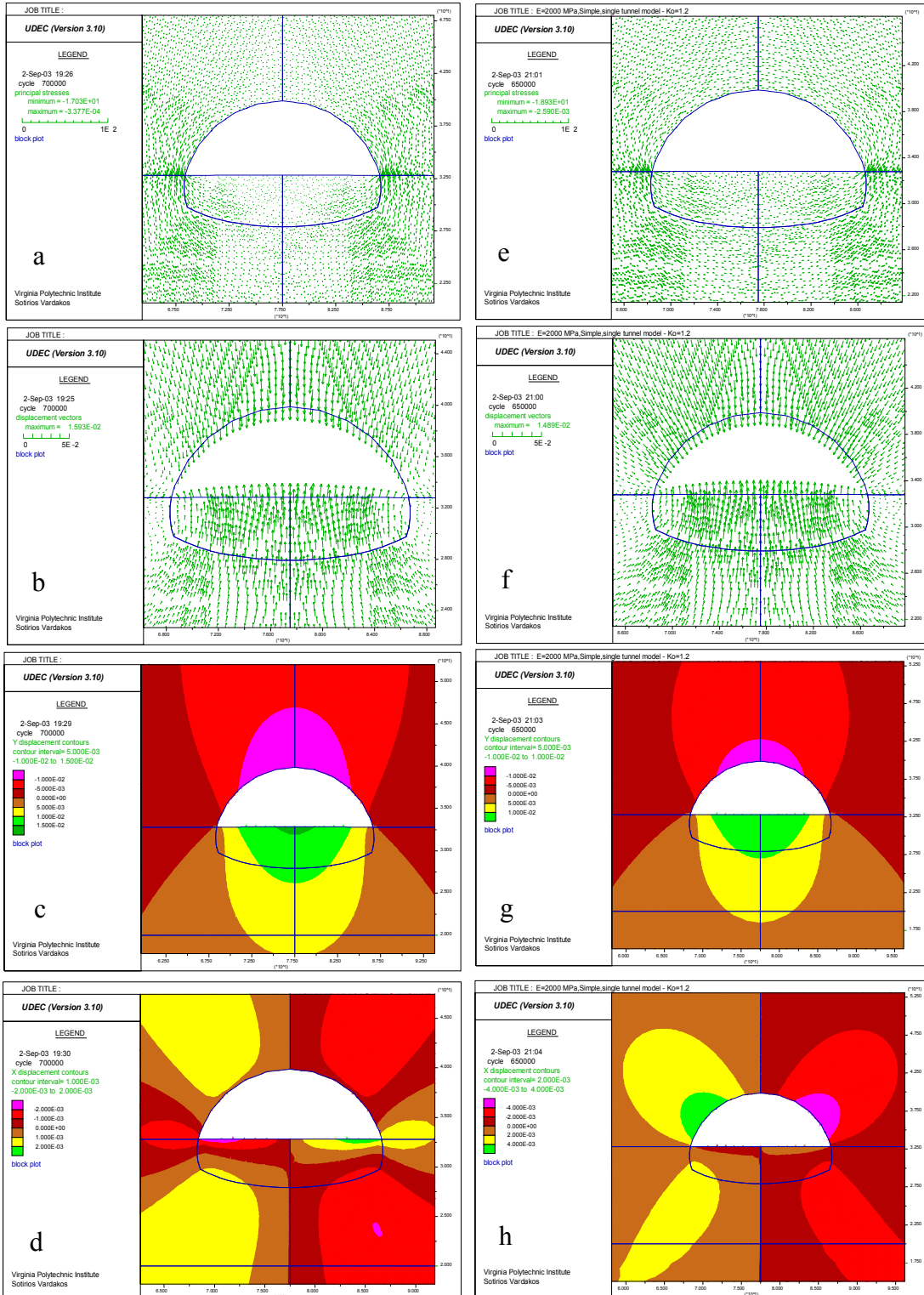


Figure 6.41: Top Heading-  $K_o=0.5$ , (a): Total displacements, (b): Stress redistribution, (c): Shaded contours for vertical displacements, (d): Shaded contours for horizontal displacements.  $K_o=1.2$ , (e): Stress redistribution, (f): Total displacements, (g): Shaded contours for vertical displacements, (h): Shaded contours for horizontal displacements.

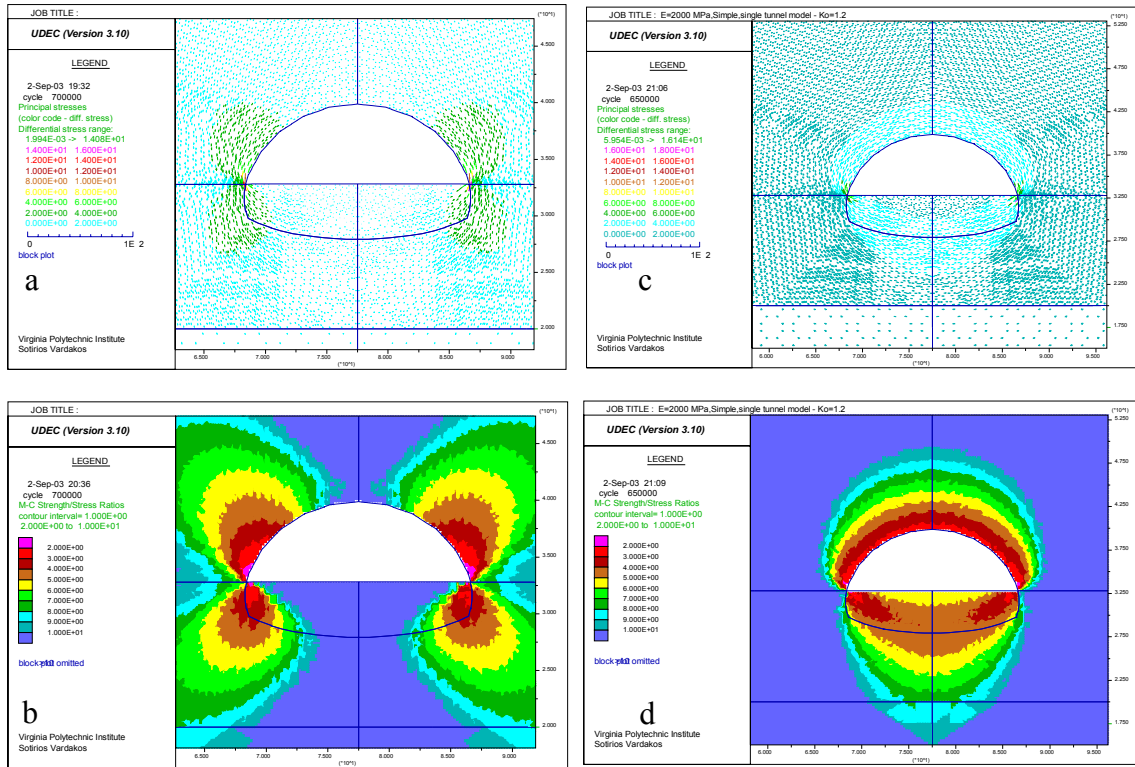


Figure 6.42:  $K_0=0.5$ , (a): Deviatoric stresses, (b): mobilization of shear strength.  $K_0=1.2$ , (c): Deviatoric stresses, (d): Mobilization of shear strength.



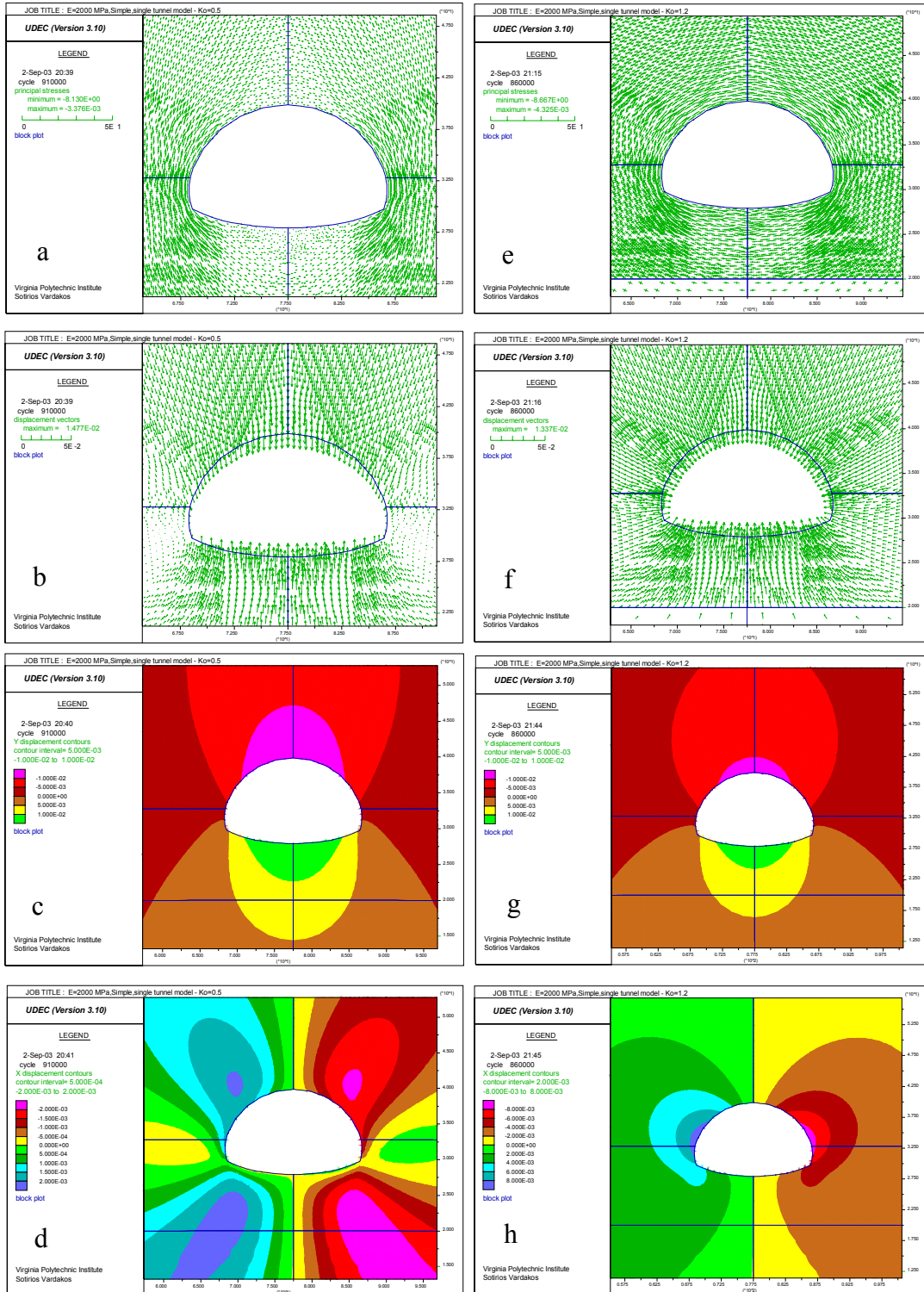


Figure 6.43:  $K_0=0.5$ , (a): Stress redistribution, (b): Total displacements, (c): Shaded contours for vertical displacements, (d): Shaded contours for horizontal displacements.  $K_0=1.2$ , (e): Stress redistribution, (f): Total displacements, (g): Shaded contours for vertical displacements, (h): Shaded contours for horizontal displacements.

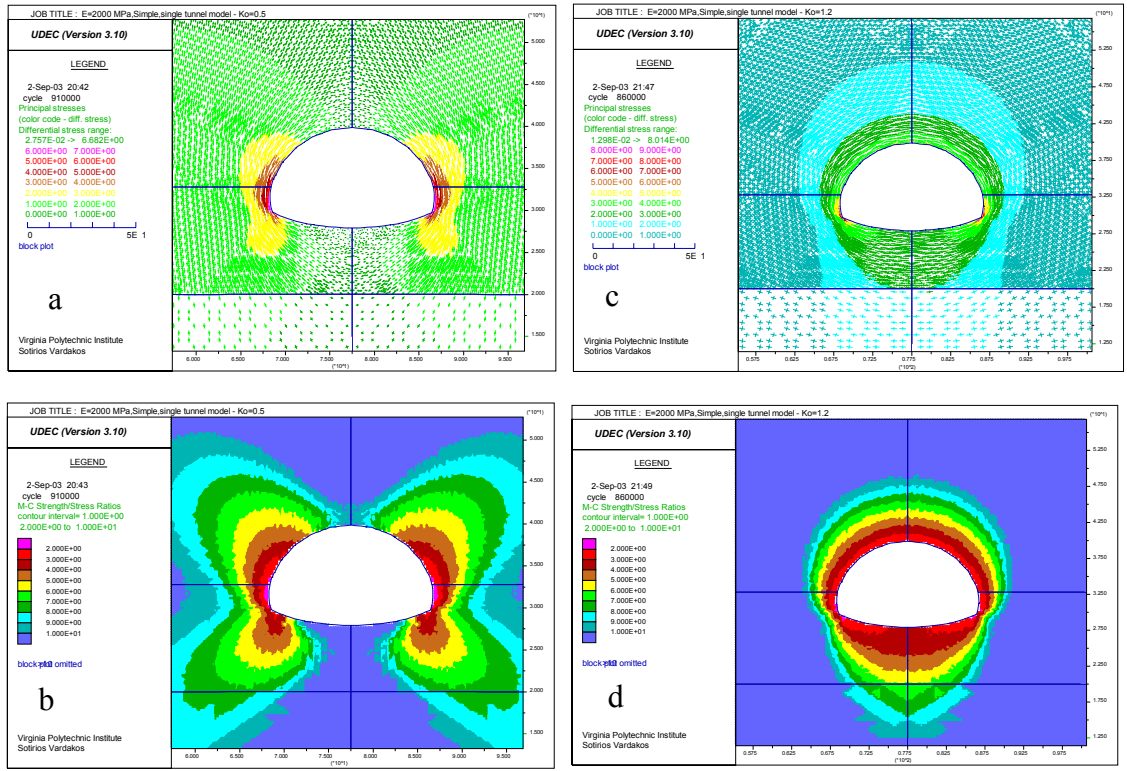


Figure 6.44:  $K_0=0.5$ , (a): Deviatoric stresses around tunnel at bench stage, (b): Mobilization of shear strength and overstressing of shoulder area.  $K_0=1.2$ , (c): Deviatoric stresses around tunnel at bench stage, (d): More uniform mobilization of shear strength for  $K_0=1.2$  case and more stable tunnel.

A separate numerical analysis was also performed to assess the issue of boundary condition choice for the continuum approach. Two analyses were executed assuming a  $K_0$  ratio of 0.83 and about 80 m of tunnel overburden. Figure 6.45 presents a simplified plane strain model with the boundary conditions used. Vertical boundaries were fixed with horizontal fixities while the bottom boundary was fixed in the vertical direction. The  $K_0$  condition was applied by initial consolidation of the model using prescribed insitu stress equations expressing stress versus depth in the three principle directions, thus assuming an initial stress regime with vertical and horizontal principle stresses.

Results from general Table 6.19 are also plotted in figures 6.46 and 6.47. It becomes obvious that the zero lateral strain models behave practically in the same way as the boundary stress models and differences are only minor. For both the  $E=2000$  MPa and  $E=5000$  MPa models, the differences can be only located in the roof convergence at locations C and D and has no practical significance. The great similarity can be attributed to the great lateral extent of the zero lateral strain models, in such a way that the stress-strain development close to the area of interest is not affected by the existence of boundary fixities. At this point this comparison though it holds for pseudo-continuum approaches, should be separately be verified for jointed models. Numerical analysis showed that there are no appreciable differences in computing time for the two cases and both model cases converge approximately at the same time.

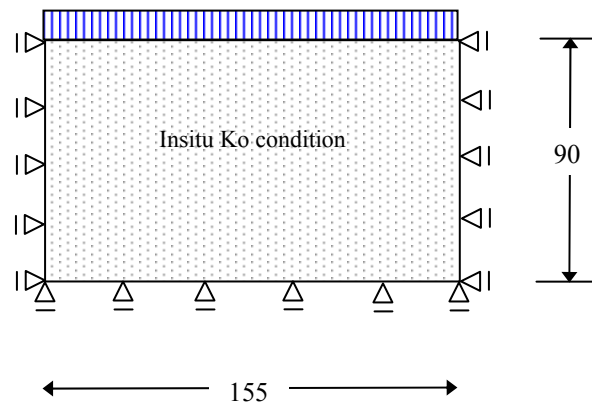


Figure 6.45: Simplified model for parametric analysis, using a zero lateral strain boundary condition.

E=2000 MPa - Convergence vs. insitu  $K_0$  ratio in UDEC pseudo-continuum models

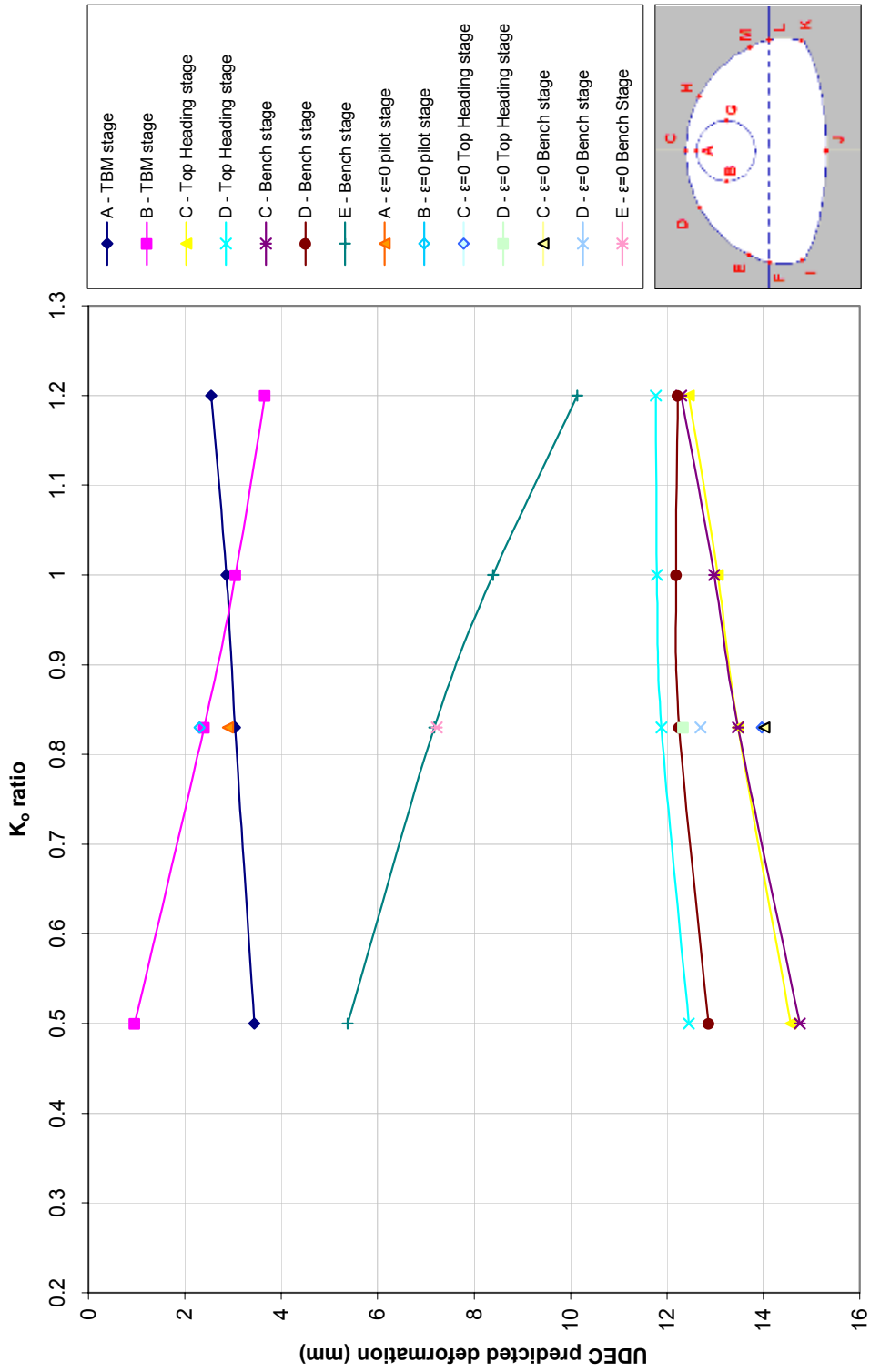


Figure 6.46: Plots of deformation versus  $K_0$  ratio for E=2000 MPa for continuum parametric analyses.

E=5000 MPa - Convergence vs. insitu  $K_0$  ratio in UDEC pseudo-continuum models

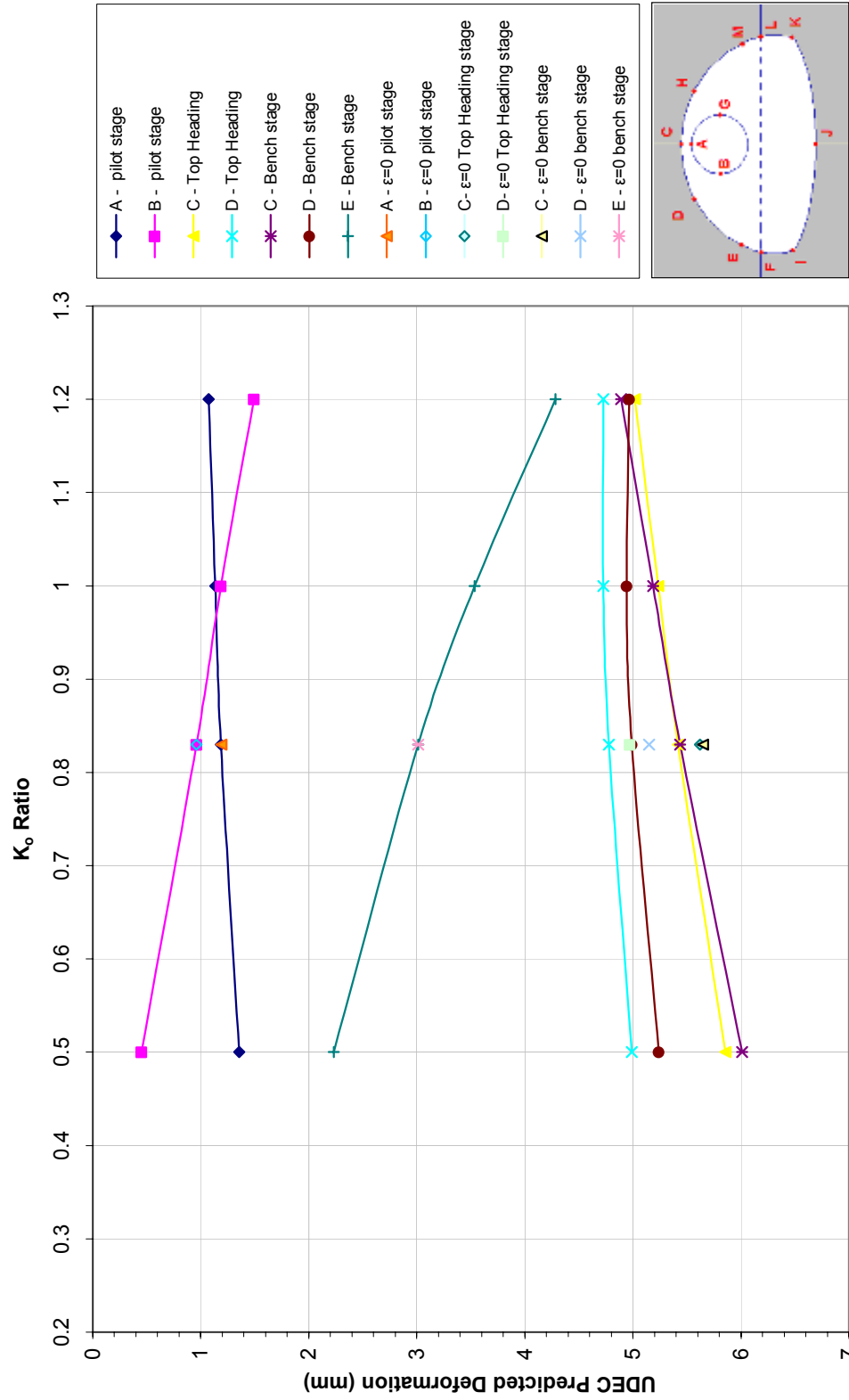


Figure 6.47: Plots of deformation versus  $K_0$  ratio for E=5000 MPa for continuum parametric analyses.

## 6.6 Monitoring data from the Shimizu tunnel No.3 site

During the tunnel construction the observational method was applied in order to verify the support system choices and data were recorded at specific locations along the tunnel drives. The field measurements performed at the Shimizu tunnel No.3 included:

1. Displacements of tunnel boundary.
2. Displacements of surrounding rock mass.
3. Rock bolt axial forces.
4. Sprayed concrete stress development.
5. Ground pressures.
6. Steel beam element stresses.
7. Vacuum permeation tests.
8. Secondary lining internal pressures.

Limited data for displacements, rock bolt forces, shotcrete and steel stress were available for the two chainage stations: STA 913+65 and STA 914+10, where most support ground conditions were practically the same and the support system used varied slightly only in the means of a less rigid steel beam (H150).

Displacement measurements on the tunnel boundary are usually conducted with three dimensional convergence measurements from a Total Station device, or with a tape extensometer. In the first method, special reflex targets are installed via supporting bolt-studs at the tunnel boundary. The total station device measures by laser beam reflection the coordinates of each point. From the coordinate measurements independent point deformation or any relative deformation between two points can be made. A series of measurements in time at the same location can reveal the deformation trends of the excavation. According to Kavvas (2001), the normal magnitude of accuracy for such measurements depending on the atmospheric conditions in the tunnel can be in the order of 2-4 mm. The metal tape extensometer offers greater accuracy in the order of 0.5 mm at the expense of manual measurement between selected points. Monitoring data for the

stations STA 913+65 are shown in figures 6.50, 6.51 and for STA 914+10 in figures 6.52 and 6.53.

Displacements in the surrounding rock mass were made by using 12.0 m long multipoint extensometers in the roof of the tunnel and 12.0 m long single rod extensometers at peripheral points (figure 6.49). In the multipoint extensometer the head is fixed at a position (i.e., for a vertical boring its position is the end of the borehole) and includes many rod extensometers that are also fixed at various depths. With this equipment the relative deformation between the head and the individual rod ends can be measured.

Bolt axial forces can be measured by installed measurement anchors or with a specially designed pressure cell. The measurement anchor allows the measurement of axial force distribution on the anchor body. It is usually a hollow steel anchor in which a compact type of extensometer is enclosed. Extensometer measuring wires are preinstalled at specified equal distances inside the rockbolt and their deformation can be related to the rock bolt axial force via its elastic properties. The anchor cell can only measure one point load and is placed at the point of fixity of the anchorage. Both of these devices can measure pressure changes as the anchorage receives load during advance and results can be used to check the bearing capacity of the installed bolts and any potential problems from bolt overloading. Monitoring data from extensometer and measurement anchors are shown in figures 6.54a-6.54j.

Shotcrete stress is measured usually via dedicated flat pressure cells encapsulated in the body of the lining during construction. Cells can be accommodated to measure tangential and radial stress in the shotcrete and are usually installed in pair one perpendicular and one tangential to the tunnel radius. Stresses in steel sets are usually measured by strain gages installed on the body of the steel sets. Measurement data for shotcrete and steel set stresses are shown in figures 6.54 and 6.55.

# Standard Cross Section

(mm)

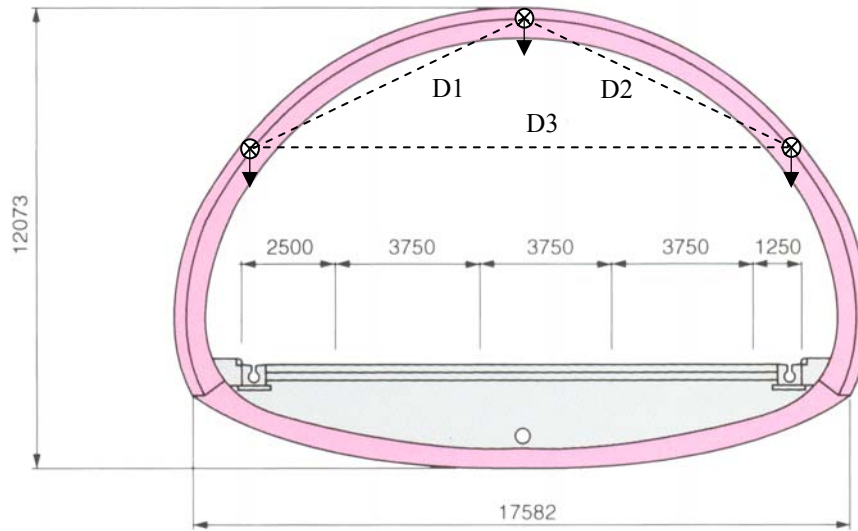


Figure 6.48: Shimizu tunnel No.3 section geometry and locations of reflex targets for three dimensional geodetical surveying.

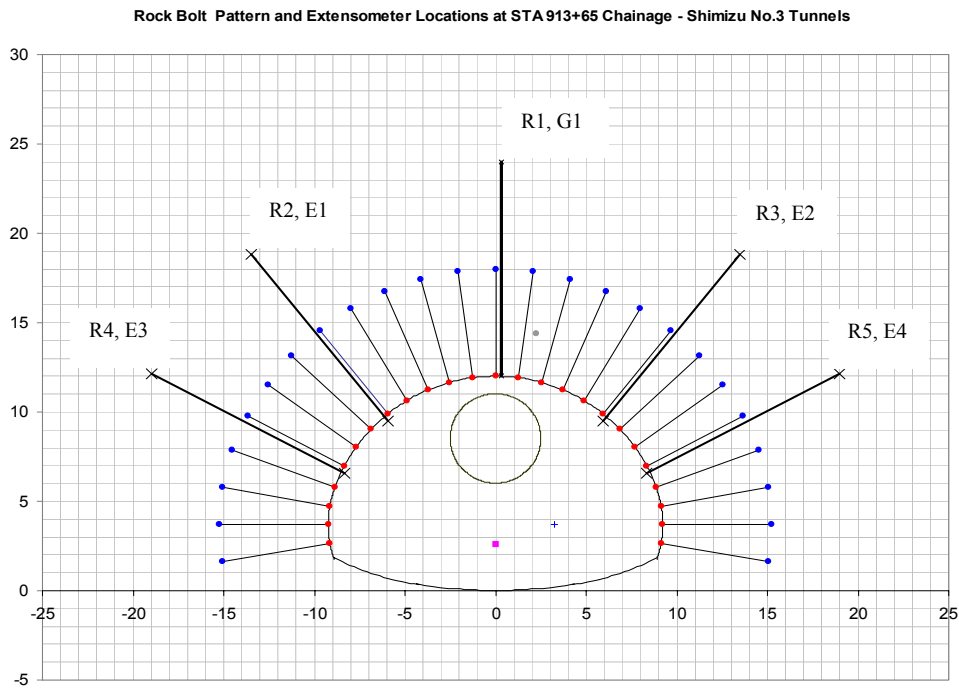


Figure 6.49: Measurement locations at STA913+65 section. R=measurement anchors, E=extensometers.



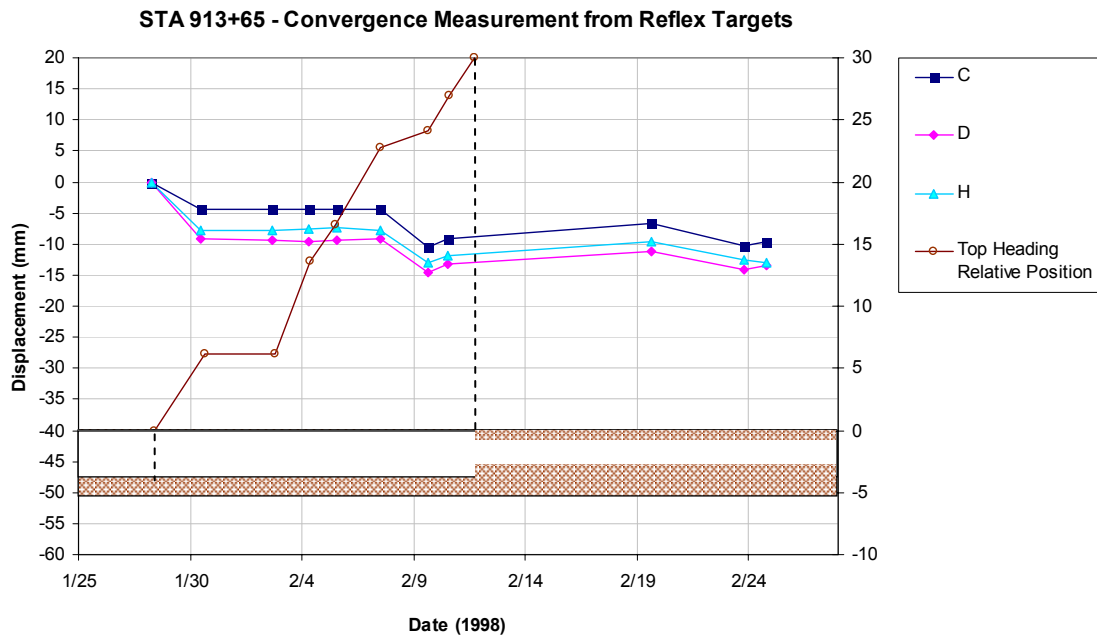


Figure 6.50: Monitoring data from 3D surveying in tunnels at chainage 913+65. Vertical deformation versus time at locations C,D,H. The advance of the top heading from the chainage 913+65 is also presented (After Japan Highways,1998).

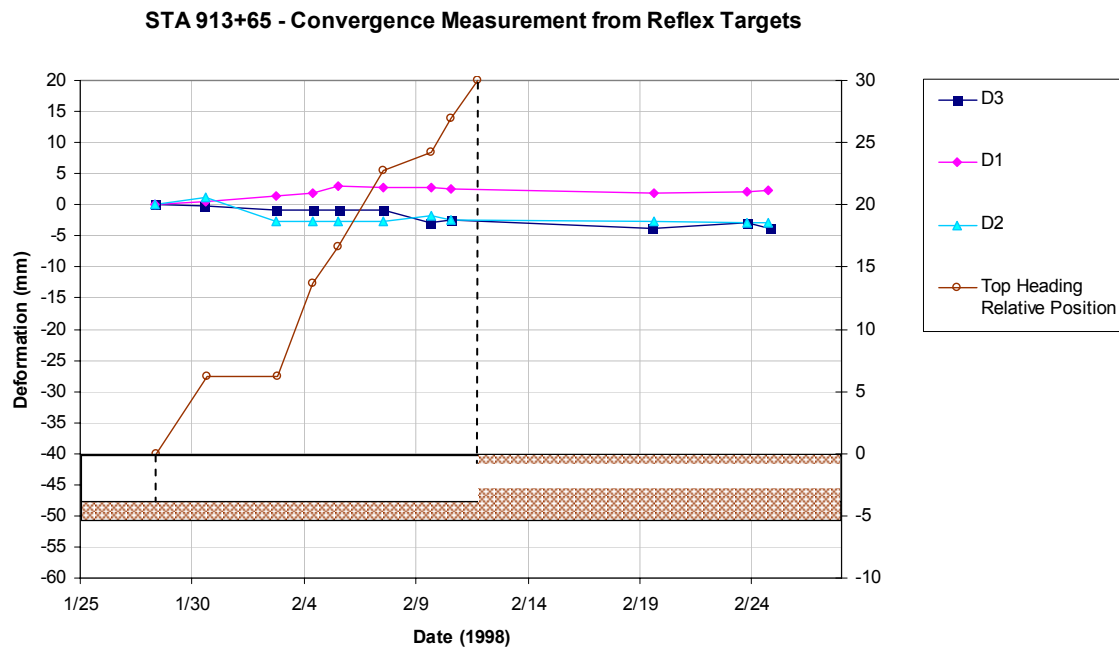


Figure 6.51: Length closure versus time at for D1,D2 and D3 reference distances. The advance of the top heading from the chainage 913+65 is also presented (After Japan Highways, 1998).

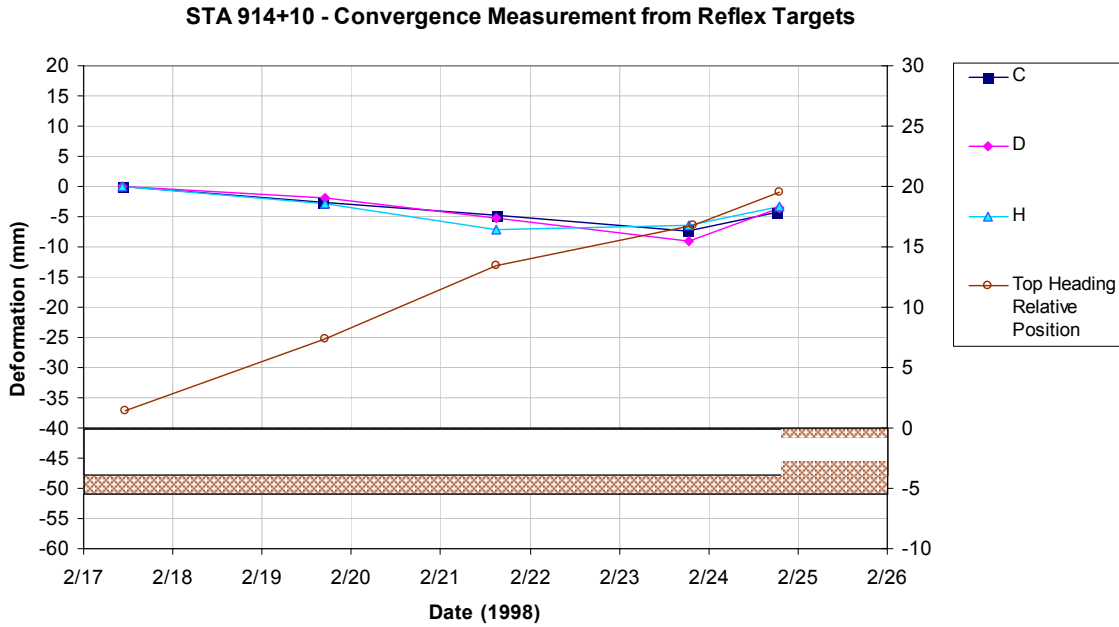


Figure 6.52: Monitoring data from 3D surveying in tunnels at chainage 913+65. Vertical deformation versus time at locations C,D,H. The advance of the top heading from the chainage 914+10 is also presented (After Japan Highways,1998).

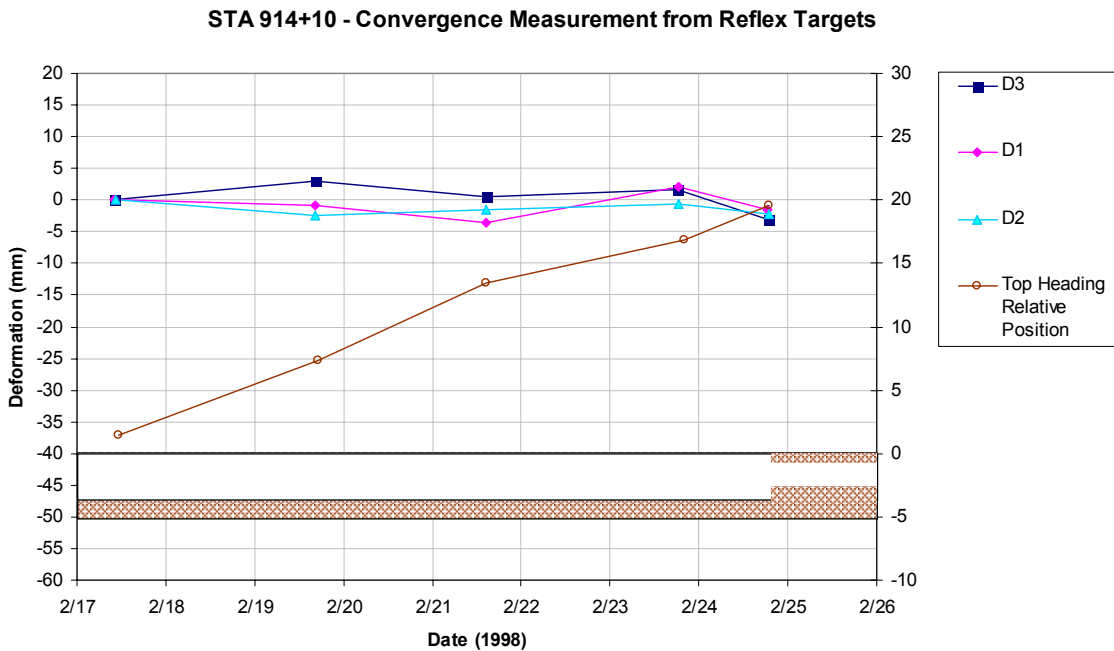
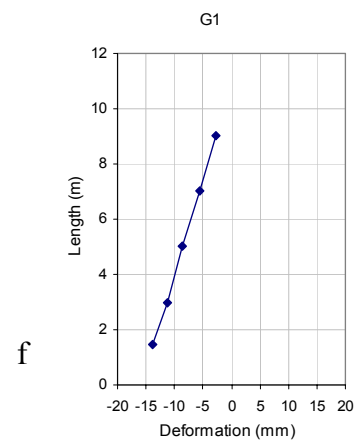
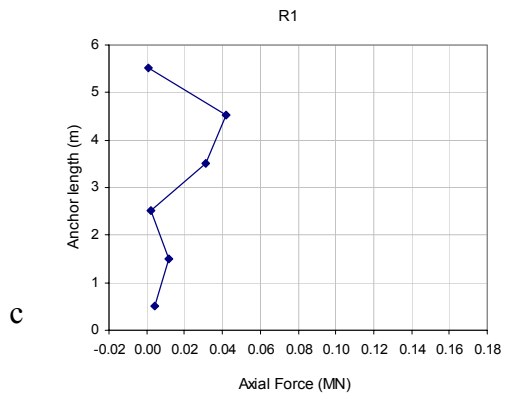
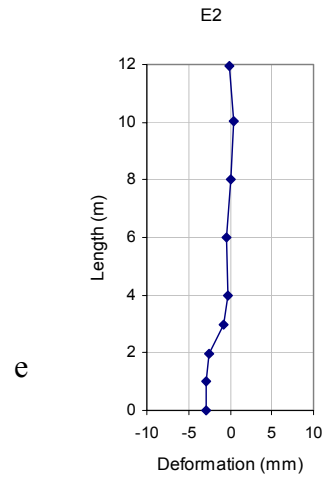
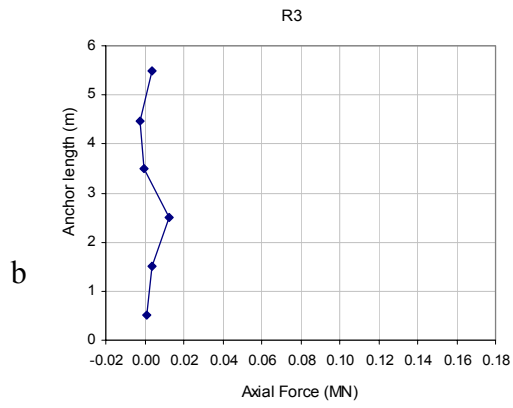
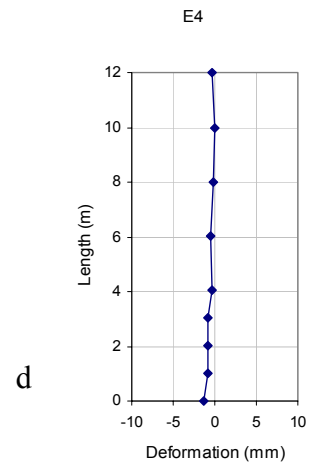
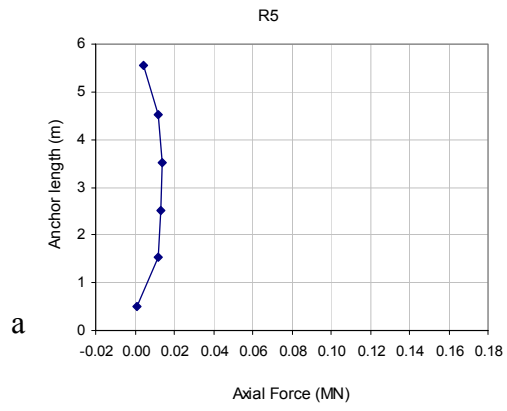


Figure 6.53: Length closure versus time at for D1,D2 and D3 reference distances. The advance of the top heading from the chainage 914+10 is also presented (After Japan Highways, 1998).



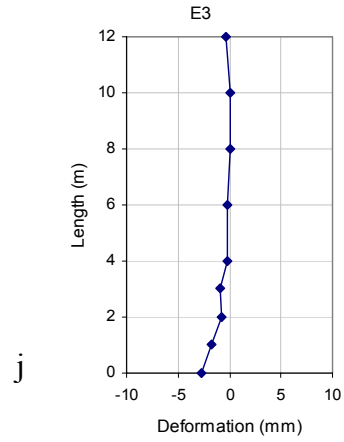
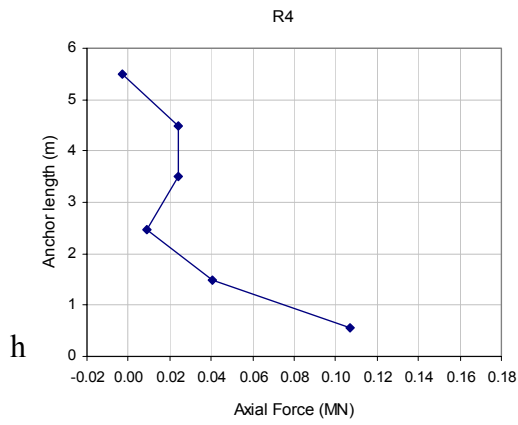
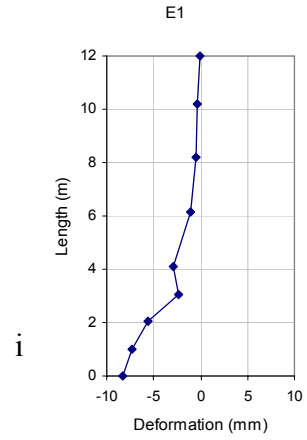
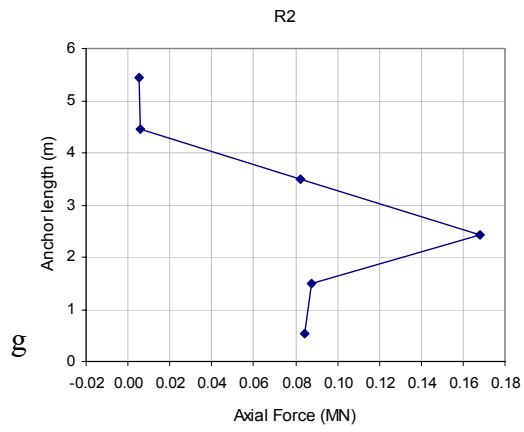


Figure 6.54 a-j: Results from extensometer and measurement anchor locations around top heading at 913+65 chainage.

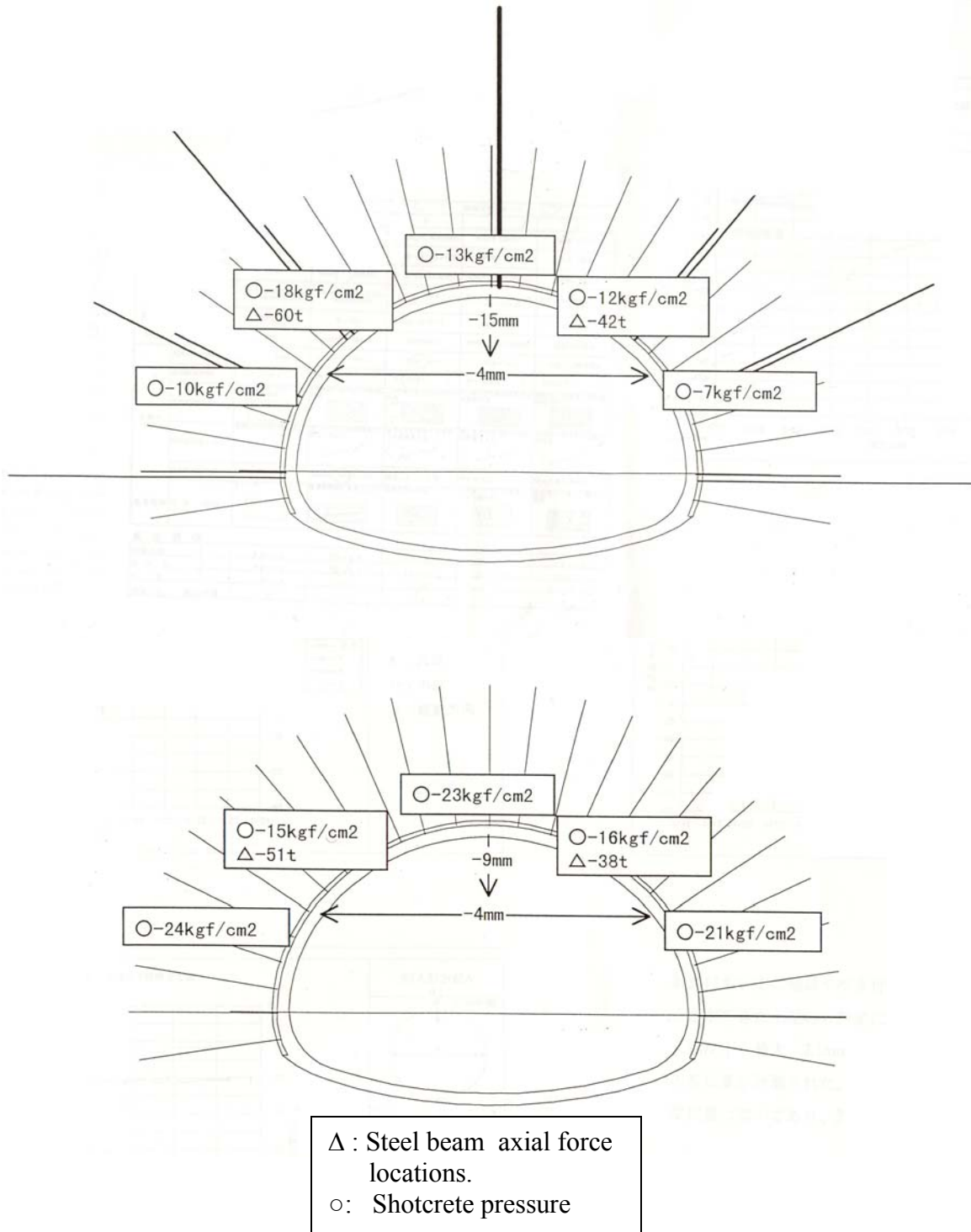


Figure 6.55 : Locations of primary lining stress measurement elements for chainage:  
a) STA 913+65 and b) STA 914+10.

## 6.7 Single tunnel jointed model analyses

### 6.7.1 General

An initial study for the applicability of the convergence-confinement method in conjunction with the distinct element numerical analysis was performed in order to investigate the effects of gradual unloading. A single tunnel jointed model was constructed based on models initially presented by NGI (1995), by using the stochastic joint generator of UDEC and with orientation data described in chapter 3. In this case due to the great lateral extent of the model and for the sake of efficiency and reduction of computing time, only one out of ten joints are practically included and explicitly simulated in UDEC. Certain reductions in parameters such as the block elastic modulus had to be made to account for the non-simulated jointing.

For this type of initial analysis the following assumptions were made:

- $E_{\text{block}}=5000 \text{ MPa}$
- $c'=2 \text{ MPa}$
- $\phi'=38^{\circ}$
- $\psi=0^{\circ}$
- $\gamma=25 \text{ kN/m}^3$
- Tunnel overburden thickness for chainage STA 913+65 and STA 914+10 is approximately 80 m.
- $K_o=0.83$

With respect to the Barton-Bandis joint model the following parameters were used:

- Mean values of for the shear strength parameters of the discontinuities were used (available data by NGI, 1995) represented in Table 6.25.

Table 6.25: Mean values of joint strengths according to Barton and Gutierrez (1995)

Property	Bedding	Cross joints	
$JRC_o$	3	7	
$JCS_o$	30	40	MPa
$\phi_r$	25	30	Degrees
$\sigma_c$	50	50	MPa

- $E_{o \text{ bedding}} = 0.14 \text{ mm}$ ,  $E_{o \text{ cross joints}} = 0.33 \text{ mm}$  (from equation 6.1)
- $L_o = 0.1 \text{ m}$ ,  $L_n = 0.5 \text{ m}$ . The value of the natural joint length of 0.5 m was based on reports by Barton & Gutierrez (1995).
- The Barton-Bandis model in UDEC calculates automatically the stress dependent joint stiffness values, however limiting values of stiffness can be used so that :

$$K_n, K_s \leq 10 \cdot \max \left[ \frac{K + 4/3G}{\Delta z_{\min}} \right] \text{ (MPa/m)} \quad \text{Equation 6.21}$$

In the above relation  $\Delta z_{\min}$  is the minimum width of adjoining zones (=1.0 m) and K, G are the maximum bulk and shear moduli of the adjoining blocks. This relation is generally used to increase the numerical efficiency. In cases of high stiffness contrast between adjacent deformable zones and joints numerical issues may result. Higher stiffness values also result in greater solution times. At the same time a relatively high stiffness value should be used to avoid interpenetration (contact overlap) of joints which is a non physical condition. The above relation is a suggested estimate of appropriate maximum stiffness values to be used and is used by UDEC to limit displacement-hardening response under high cyclic loading.

- The tunnel is assumed to be excavated in three stages, a pilot stage, a top heading and a lower bench stage. At the end of each excavation stage support is assumed to be installed. However available measurement data for comparisons existed only for the top heading excavation and for the left tunnel heading to Tokyo only. Therefore weight is given in analysis of this stage.

A difficulty in using UDEC is that there is no built in provision for a controlled relaxation analysis with simultaneous ground-support interaction. This simulation was done manually first by constructing complete characteristic curves using gradual relaxation from 0 to 100%. The procedure chosen during the initial analysis is described herein. For each excavation stage the following procedure is followed:

1. Initial consolidation of model to equilibrium.
2. Deletion of excavated blocks in initial consolidated model and substitution of interior boundary tractions with factored values generated by external UDEC subroutine (programmed in FISH language).
3. Stepped reduction of interior boundary tractions by a reduction factor of  $1-\lambda_i$  ( $i$ =step number) down to complete relaxation (100%) and cycling each time to equilibrium. Recording of equivalent internal pressure vs. displacement on roof or walls of excavation.
4. Construction of approximate characteristic curves.
5. Construction of calculated displacements vs. cycle time (UDEC computational engine time) at the same specified locations.
6. Assumption for a relaxation factor  $\lambda$ , or approximate calculation of the loss factor  $\lambda$  under the specific case (elastic or plastic) at the distance  $d$  where support is installed, through the Panet curve for the specific  $N_s$  value.
7. Re-cycling of model dynamically from previous step to match the displacement for the desired loss factor  $\lambda$ . The required cycling time before support installation is taken from the displacement-cycling curve.
8. Implementation of support measures in distinct element model.
9. Further cycling to equilibrium. The support is now loaded.
10. Proceed to the next stage of excavation.

Specifically during the controlled unloading of the model (tunneling simulation) the following steps are considered and executed:

1. Gradual unloading of TBM  $D=5.0$  m circular opening by 10 step increments to full removal of interior gridpoint forces. Construction of characteristic curve for TBM tunnel. These curves are not used for the convergence-confinement method but only for an initial investigation of the rock mass behavior.
2. Deletion of top heading blocks and gradual unloading of excavation by 10 steps to full unloading. Construction of characteristic curve for top heading.



### 6.7.2 Advantages and disadvantages of the method

The above method has two promising advantages. Especially when using a two dimensional numerical analysis (plane strain), perhaps it is the only means of addressing the issue of third dimensional effects in deformations, especially close to the tunnel front, and provide an estimate of support delays and unavoidable pre deformations before installation of support. When using a complex model including jointing such as in UDEC it is desired to construct “tailor” made characteristic curves for the unsupported ground, for the specific jointed model and for multiple excavation stages including the TBM phase, the top heading and or even the bench excavation. Having a curve specifically generated for the model used, is a way to directly incorporate parameters affecting the model deformations and related to the existence of the fractures.

This method however includes some additional drawbacks as well. The applicability of the Panet curves shown in figure 5.1 have been generated under the assumptions of homegenous ground stressed to isotropic state and exhibiting elastic-perfectly plastic behavior. The applicability of the convergence-confinement method has been discussed by various researchers and engineers. Nashri et al. (2003) describes problems for unsafe and unreliable use of the convergence-confinement method for irregular tunnel geometries by a case study for the Magenta station of the Paris Subway (EOLE) where tunnels deviated greatly from the circular reference geometry and final predicted deformation estimates where in disagreement with measured values. In the design and analysis of tunnels with the convergence-confinement method the choice of the most appropriate stress relaxation factor  $(1-\lambda)$  is of great importance and should be verified by measured displacements during tunneling (Kavvadas, 2000; Nashri, 2003).

It is also disputable if the same unloading factor must be used for the whole tunnel boundary during a plane strain numerical study. Clearly the three dimensional distribution of stresses is more complex specially close to the tunnel face, or close to excavation connection steps, a fact that undermines the above assumption of constant

unloading, the more the geometry deviates from the circular shape and thus the use of this method becomes complicated.

Furthermore, some other geomechanical issues must be noted. This method has been implemented and utilized with success in a variety of commercially available Finite Element software mainly. However, the adoption of this method in Distinct Element modeling may be more challenging. It is important to note some potential differences in the solution of the two methods, the immediate excavation unloading and the gradual controlled unloading, as these two procedures may yield to numerically different results. In the case of an isotropic homogenous elastic medium the developed deformations are theoretically stress path independent. However in a more complex medium like the UDEC generated model where the behavior is also controlled by the joint deformability, there may be a case when immediate full unloading due to excavation, will lead to irreversible (plastic) movements of some joints, thus contributing some apparent plastic strain in the total strain of the model. This can happen if during the dynamic cycling to equilibrium some momentarily excessive stresses may overcome available strength and joints may seem to displace. In this case the final deformations recorded under full unloading may be larger at some extent than a progressively unloaded model. These differences should be a function of the parameters controlling their elastoplastic response and the relative size of the opening with respect to the joint set frequencies. Despite these potential difficulties this method is certainly promising and its application could provide some insight on the issues of three dimensional effects when using a plane strain model.

### 6.7.3 Analysis results from initial jointed model

Plots in figures 6.56 show recorded deformation after the first excavation stage at the crown for the cases of full and gradual unloading of a circular 5.0 m diameter tunnel in  $E=5000$  MPa elastoplastic rock. Figures 6.57 show the mobilization of shear strength at both cases. In the following Table 6.22 results from the UDEC analyses are shown. From these results it is evident that the immediately excavated tunnel shows relatively greater deformations by an order of 2.1 mm. From the parametric analysis plot in figure

6.11 it is apparent that the required elastic modulus value in order to get comparable displacements would be 3000-3300 MPa. Table 6.22 includes results of the elastoplastic analysis (isotropic loading) and results from a closed form solution based on elastic deformations of an opening in a biaxially stressed field. The immediately unloaded model in UDEC shows close agreement with the elastic  $K_o$  solution and is in relative agreement with the elastoplastic analysis estimates.

Table 6.26: Comparison of predicted deformations for pilot tunnel using UDEC and simple elastoplastic analyses.

Method:	UDEC full unloading	UDEC gradual unloading	Elastoplastic analysis using $\sigma_{av}$ .		Elastic using $K_o$ ratio.	
E mod.	5000	5000	3000	3200	3000	3200
Insitu Stress	$\sigma_v=1.87$ $\sigma_h=1.58$	$\sigma_v=1.87$ $\sigma_h=1.58$	$\sigma_{av}=1.7$		$\sigma_v=1.87$ $\sigma_h=1.53$	
$\delta$ crown	2.1	1.75	1.84	1.73	2.17	2.04
$\delta$ wall (R) (L)	1.95 1.854	1.55			1.5	1.4
Stresses in MPa, deformations in mm, $\epsilon \neq 0$ models.						

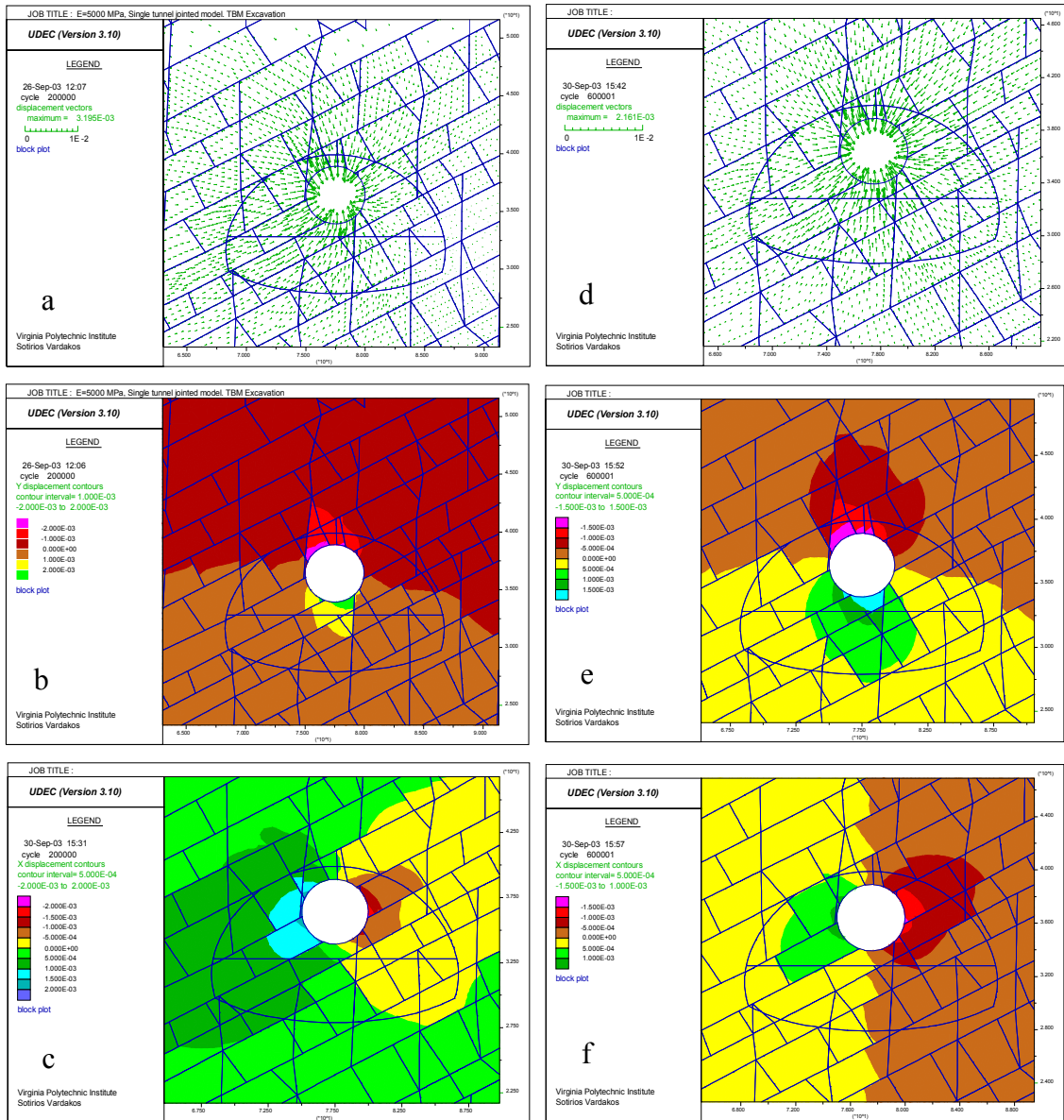


Figure 6.56: Final deformation results from dynamic (left column) and controlled relaxation analysis (right column) for pilot opening in jointed mass. The dynamic solution reveals slightly higher deformations. a & d) Total displacement plots, b & e) shaded contours of vertical displacements, c & f) shaded contours of horizontal displacements.

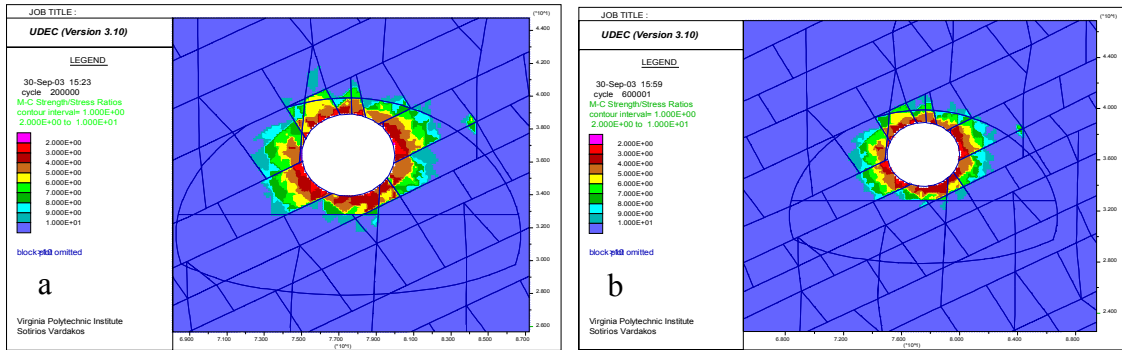


Figure 6.57: Strength / stress results from (a) dynamic and (b) controlled relaxation analysis, for pilot tunnel in jointed mass. In both cases no plastic yielding occurs in the rock mass.

#### 6.7.4 DEM constructed characteristic curves for the initial jointed model

During gradual unloading the stresses and deformations at specific locations where monitored and recorded. Data were recorded for the following points, most of which were also points of on site measurement:

Pilot Tunnel : A (crown), B (springline)

Top Heading : C (crown), C2 (crown+2.0 m), C3 (crown+3.4 m), C4 (crown+6.0m) -  
D (roof left) – H (roof right).

It should also be mentioned that monitored stresses and deformations do not refer to the exact same point since stresses are calculated in the finite difference CST zone, while deformations occur at gridpoints. However attention was given during the code structure so that these points are in the closest possible distance. Boundary gridpoint deformations could not be recorded in a history plot after excavation (even though they are calculated) and thus the closest gridpoint inside the rock mass was recorded instead. Therefore the UDEC constructed series of convergence plots which do not represent exact behavior of the boundary and only an approximation can be made from them. However an approximate correction for this can be made by constructing independent plots.

For the boundary convergence plots, deformation is recorded manually for the specific boundary gridpoint of interest (for the stepped analysis) and for each step a factoring by  $(1-\lambda_i)$  of the initial zone stress, immediately adjacent and towards the inside of the excavation is made. Thus the characteristic curve can be used in the performance analysis. For points located above the tunnel geometry, vertical stresses ( $\sigma_y$ ) are recorded at the immediately adjacent finite difference zone towards the tunnel. Stress values are the ones calculated by UDEC for each step, instead of being factored from the initial ones after the pilot excavation stage. It is also expected that the starting deformation for  $\lambda=0.0$  is not zero but is equal to the amount of gridpoint deformation due to the initial unloading of the pilot tunnel. However these assumptions in the construction of the convergence curves do not introduce errors in the analysis since what is more important is the

recording of the deformation on these points for a given boundary loss factor and not for a loss factor at an internal rock mass point.

Representative results of the trial analysis are shown in figures 6.58-6.60. The constructed curves show displacements versus equivalent support pressure at the crown and sidewall during gradual unloading, as also estimated convergence during immediate full unloading. From these figures it is apparent that the pilot opening behaves elastically and no failure zone is expected to develop. It is also noticeable that a difference between the gradual unloading solution and the dynamic solution for immediate unloading exists. The expected difference is in the order of:  $2.1 - 1.75 \approx 0.35$  mm and suggests some degree of shearing in the joints during the dynamic solution which led to an increase of displacements. For the practical application of the current tunnel analysis this behavior is not considered to be significant especially when comparisons are made with measured displacements since the error of the measurement methods and equipment is very often in the range of 2.0 mm.

Figure 6.59 shows convergence curves at the crown (C) and two roof points at a distance of 6.7 m off the centerline (D and H), during excavation of the top heading. From these curves it becomes evident that the surrounding rock mass behaves elastically until a maximum deformation of 8.0 mm for the crown and 6.0 mm for offset roof points, passed which a non linear deformation occurs and the deformations increase rapidly upon any further pressure reduction. While this effect resembles to the plastic behavior convergence model of Pacher (plastic zone starts developing around the opening) it is clearly attributed to the kinematic response of an unstable rock block (wedge). However this numerical study in UDEC reveals also a disadvantage. If it is hypothesized that the tunnel section is unloaded gradually via the convergence confinement approach, then a kinematically unstable block seems to be stable even for loss factors  $\lambda$  above 0.25, which expresses a theoretical loss factor at the face of the tunnel. In contrast an unstable wedge would most probably be detached from its surroundings. In hard rocks instability of the wedge may be more pronounced and the only native source of resistance would be the dilative behavior of the wedge surfaces, which would work towards self anchoring of the

block. From the continuum parametric analysis in UDEC the crown deformation limit of the unsupported tunnel (6.0-7.0 mm) occurs for a rock mass elastic modulus of about  $3500 \pm 300$  MPa. Therefore so far it can be deduced that the difference between the elastic modulus used in the two solutions of the simple and jointed model is in the order of  $1500 \pm 300$  MPa and can be useful for a reference relation between the two approaches.

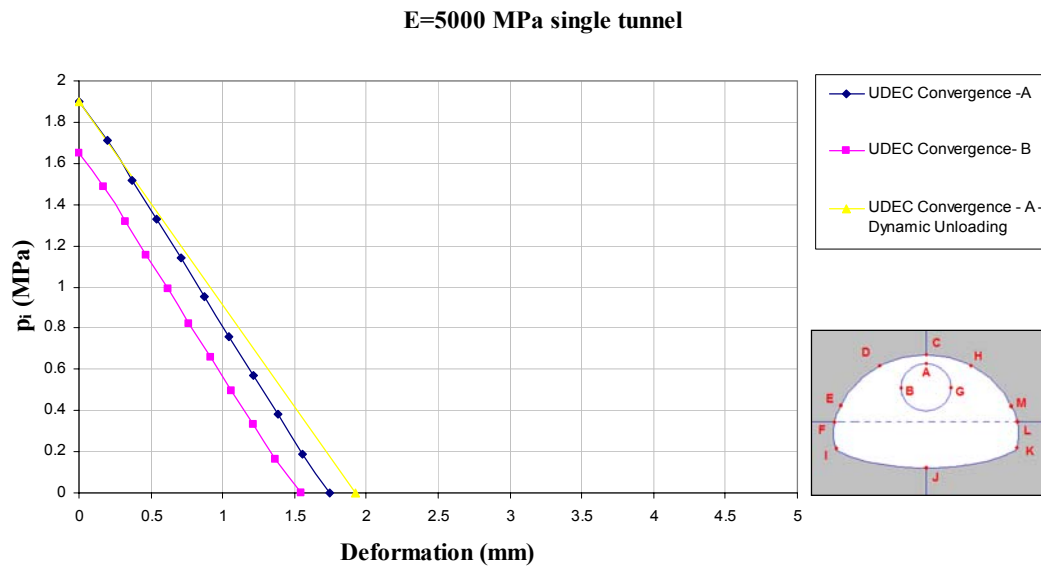


Figure 6.58: Characteristic curves in jointed model using  $E=5000$  MPa, for  $D=5.0$  pilot opening using controlled deformation in UDEC.

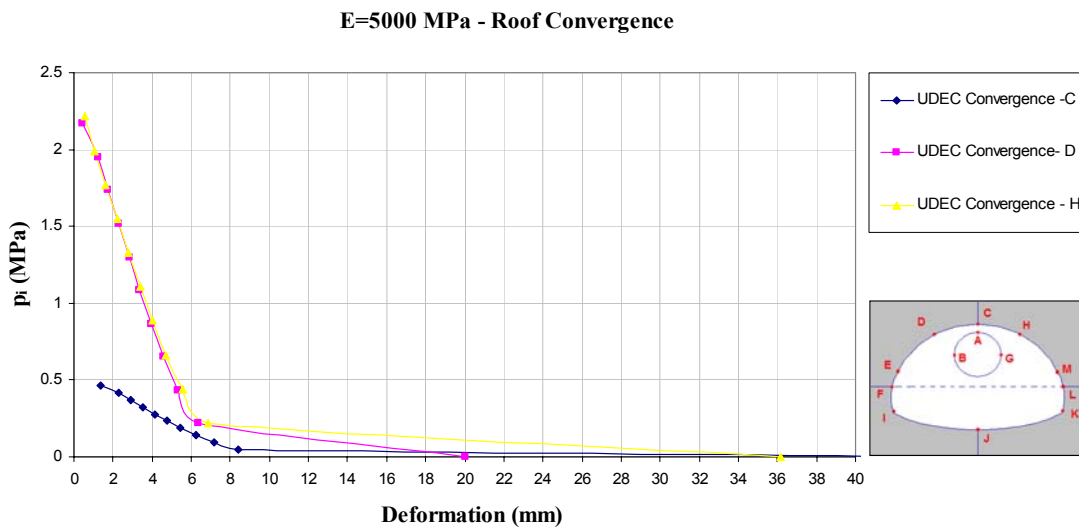


Figure 6.59: Characteristic curves in jointed model using  $E=5000$  MPa, for top heading using controlled deformation in UDEC. At a loss factor of  $\lambda=0.9$  unstable rock blocks start detaching from the surrounding rock mass.



E=5000 MPa Centerline Convergence UDEC Estimates

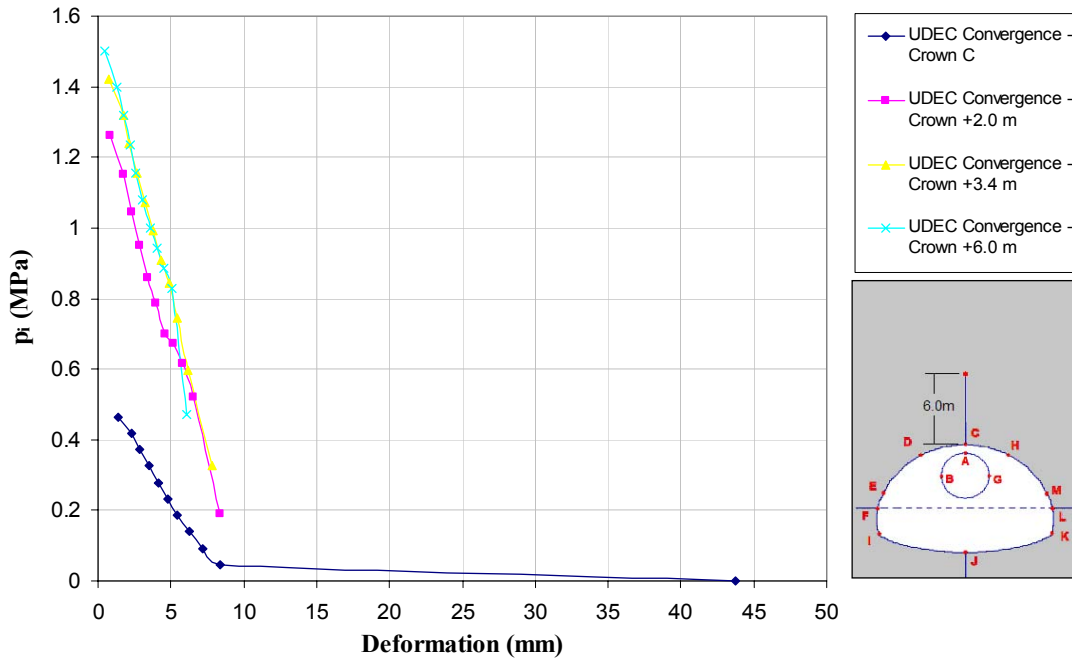


Figure 6.60: Approximate characteristic curves in jointed model using  $E=5000$  MPa for points located at the crown (C) and at 2.0, 3.4 and 6.0 m above the crown.

From this trial analysis it is evident that two different approaches exist so far. Using a plane strain continuum approach not involving structurally controlled mechanisms of instability can be advantageous when the convergence confinement method is to be used. The loss factor of Panet (1986) can be applied under the assumption of elastic perfectly plastic rock and nearly isotropic conditions. However in a distinct element model the concept of gradual unloading can yield to misleading results if not considered properly. In the later case it is evident that the roof blocks start deforming non linearly from  $\lambda=0.8-0.9$ . In the case of an elastic ground response and assuming an average tunnel span of 12.5 m this should occur at a distance of one to two diameters behind the face of the tunnel heading or at about 6.0-12.0 m behind the face of the particular tunnel in strict terms. The Distinct element method then becomes more appropriate for cases where behavior of the model is more dictated by kinematic behavior of jointed rock mass under sudden imposed changes instead for use in a transient problem involving deviations from the plane strain concept due to proximity with geometry changes etc. Therefore two mechanisms can be observed with the distinct element modeling.

A local failure mode can be observed due to the detachment of rock blocks. The detachment can be initially prevented by applying spot bolting, a usual procedure during rock tunneling. Upon immediate and full unloading of the excavation UDEC will develop large total strains (advantageous here over the FEM or FDM) including detachment of a block while at the same time the second mechanism of stress redistribution in the vicinity of the opening will commence. UDEC will finally let the excavated space create its own natural arching and reach a mechanically acceptable geometry of equilibrium. One important and widely accepted fact is nevertheless proved by UDEC gradual unloading analysis. The kinematically unstable block starts deforming non-linearly (onset of detachment) only at a loss factor of  $\lambda=0.8-0.9$  which means 10-20% of the initial stress exists as equivalent internal pressure. This reveals the great value of rock bolt support that can increase stability only with small tension levels (or equivalently compression of the rock mass).

Therefore the question arises on how three dimensional effects can be accounted in a rational fashion in UDEC with out sacrificing the appealing discrete element modeling in favor for a continuum model. In the tunnel section 913+65 high rock mass ratings were reported as stated before with the existence of fractures at an average spacing of 50 cm (Japan Highway's Tunneling Division report). As it is also reported no pre-reinforcement works were performed to reinforce the tunnel in that section (figure 3.8) from the pilot stage. There can be a way to address this issue by still applying the convergence-confinement method. Clearly if the primary support installation in UDEC commences immediately so that any unstable blocks are prohibited to slide, then this approach would be unconservative and not rational since the rock mass would not be let to arch naturally. In the proposed method the mobilization of the second mechanism is exploited and the convergence method is applied.

For the above reasons it can be proposed to stabilize initially unstable block elements by spot bolting at a short cycling time right after the excavation of the top heading with support elements such as bolts or cables that can be or not be included in the final support system used. The existence of local reinforcing elements in limited amount does not affect the global behavior and is only performed to avoid excessive loosening and great excavation geometry changes in the form of extensive apparent over-breaks. An alternate method especially for instances where the existence of these blocks is a question of probability (they may not actually exist), would be to artificially glue these blocks to the hosting rock mass. This approach avoids unwanted locally excessive over-excavations and permits application of a beam support element. The later method even though it provides an artificial local improvement in the system can be advantageous over any other method if better tracking of deformations at the tunnel boundary is needed so that it can be directly associated with a relaxation factor. For the first method analysis is performed by tracking the movement of the closest stable blocks at the roof (where ground arching starts developing due to stress redistribution), while in the second tracking at the boundary can be directly done. For both methods deformation tracking can be manually done in small step increments of cycling time and the construction of a convergence curve, installation of the support could be performed at the

specified loss factor (i.e.,  $\lambda=0.5$ ) during deformation of the rock mass as it is recorded by the gradual unloading solution. In figure 6.61 a general scheme of the trial iterative procedure followed during application of the Pacher curves is shown.

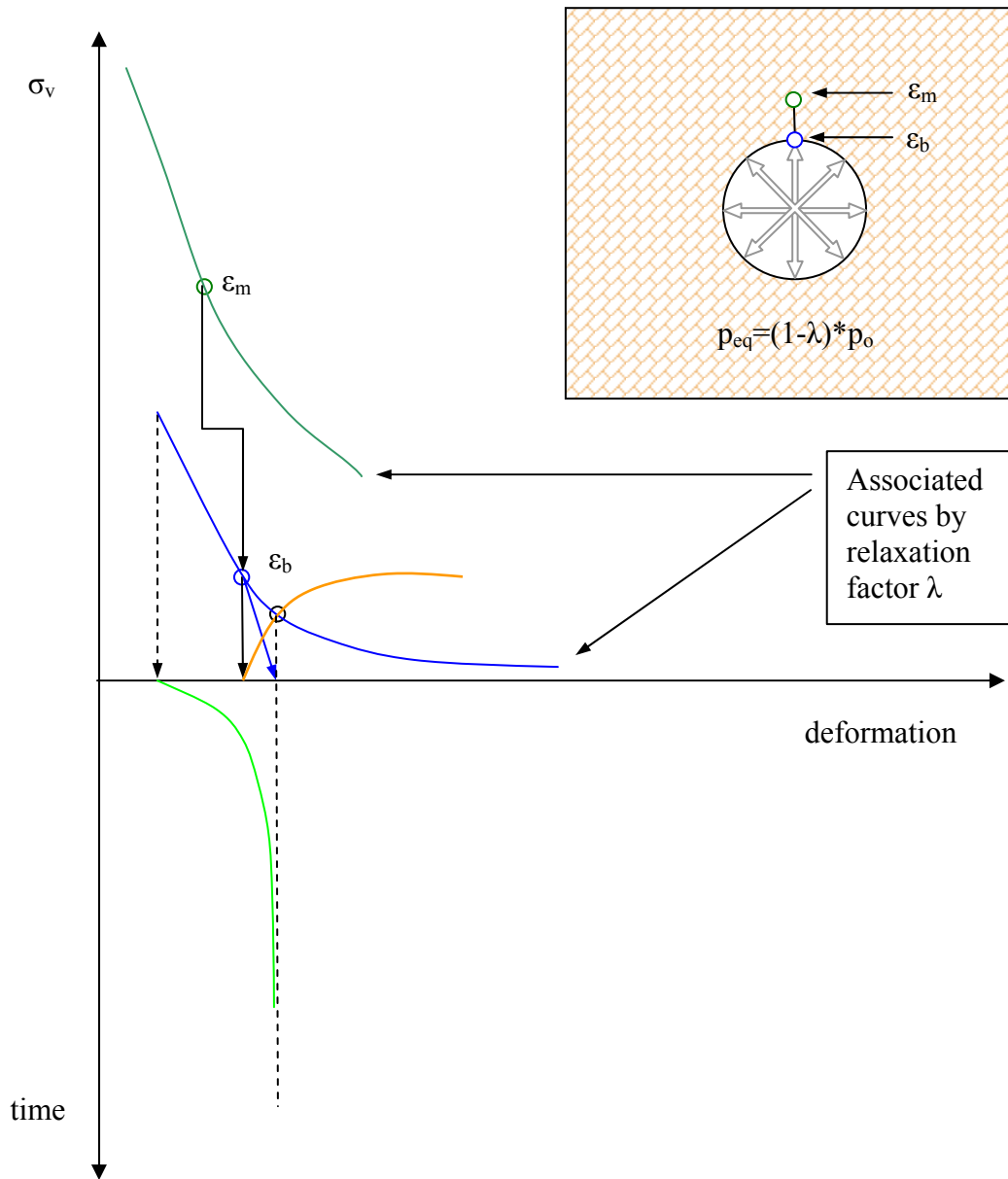


Figure 6.61: Schematic representation of the convergence-confinement principle used in the initial UDEC analysis. Curve  $\epsilon_b$  is calculated for the boundary of the excavation. Curve  $\epsilon_m$  is calculated for an internal point in the rock mass close to the boundary but stable enough so that large displacements do not occur. Both curves are associated simultaneously by the exactly known loss (relaxation) factor  $\lambda$  which is used to “drive the analysis”.

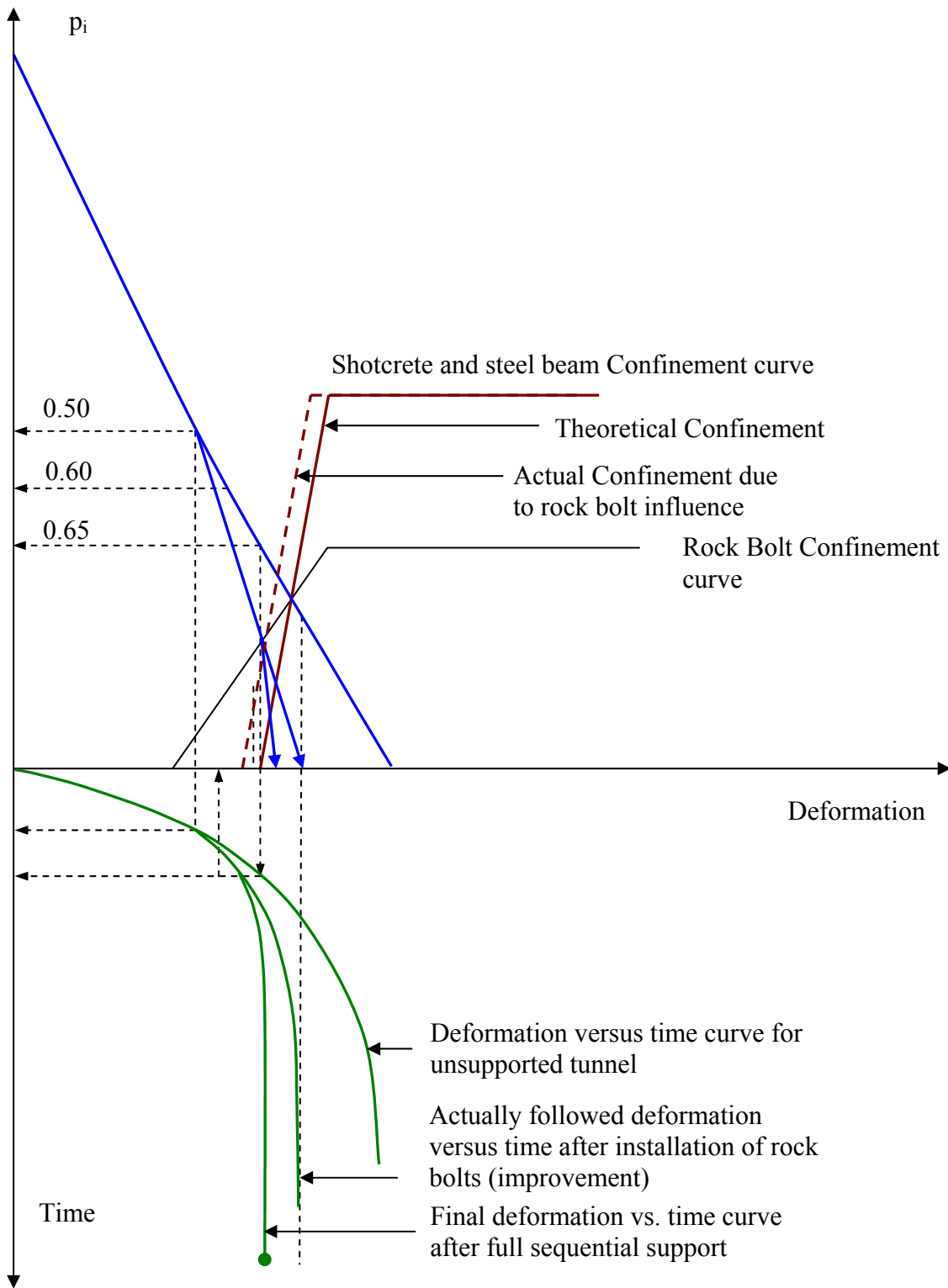


Figure 6.62: Schematic representation of ground-support interaction used in UDEC.

An initial analysis was performed following the above proposed steps and the results are presented herein. After the pilot tunnel excavation to 100% unloading with no application of support measures, as was described by the designs, the top heading excavation started and the tunnel crown displacement at different locations was tracked for an assumed loss factor  $\lambda=0.5$ . For the most stable point C4 located at 6.0 m above the crown the vertical displacement is in the order of 3.1 mm. The corresponding cycling time from the UDEC history plot of this point (figure 6.63) is 1600 cycles. Therefore a dynamic cycling of 1600 cycles is allowed during top heading excavation before placement of the rock bolt support. Assuming now that the loss factor for installation of the steel beam H200 and the normal shotcrete of  $t=20$  cm thickness, is in the range of  $\lambda=0.65$ , then the vertical deformation of the C4 point is about 3.8 mm, from the convergence plot for the unsupported tunnel. For this deformation a cycle time difference of  $205013-201586\approx 3500$  cycles is estimated by the history plot of point C4. This is the time allowed after placement of the upper heading rock bolts, before installation of the steel beams and shotcrete. However as it becomes apparent from the simplified schematic in figure 6.62 due to the improvement effect of the rock bolt installation the final actual relaxation factor that occurs before installation of the shotcrete and beams should be somewhat lower than 0.65 (assumed in the above cycling estimates). This slight difference means that the beam and shotcrete support is installed slightly sooner than a theoretical stage of a factor  $\lambda=0.65$  but this is not considered to introduce significant errors in the analysis. These steps were written on a code file and subsequently executed in UDEC.

For the rock bolts material parameter calculation a spreadsheet was formulated to assist in computations. Formulation is based on a model proposed by Lorig (1985) and takes into account not only axial capacity of the elements but also resistance in shearing. The model can also consider rock bolt spacing and rock bolt grout properties. The table with computations is included in Table 6.27. For the 6.0 m long rockbolts a cement based concrete grout was assumed to have been used and factor of 0.5 to account for application quality, was also assumed as a conservative assumption, due to physical loss of grout inside fissures and cracks which reduces the developed capacity of the reinforcing

element. With respect to the bench excavation tunnel deformation data were not available and thus analysis had to be empirically performed in the plane strain models. Furthermore previous studies performed with continuum models showed little difference in the incremental crown displacement between the two stages and thus analysis approach is rather limited.

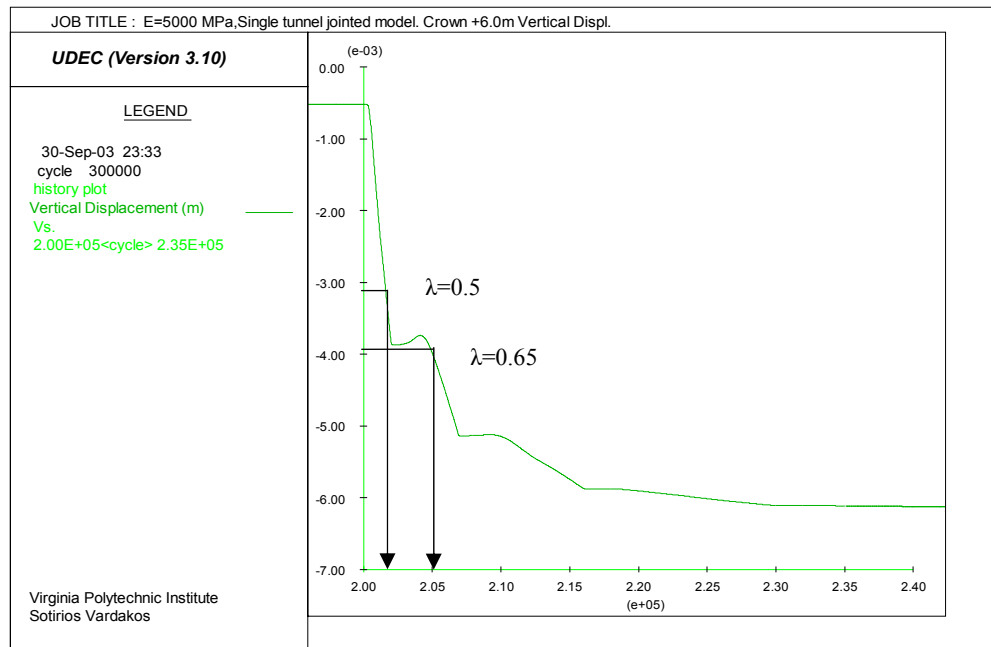


Figure 6.63: Deformation versus cycling time at 6.0 m above the crown of the top heading and tracking of the cycling time for the corresponding loss factor.

The relations proposed by Gerdeen et al. (1977) and used by Lorig (1985) for the calculation of the rock bolt properties are included herein:

$d_a$  = bolt diameter (mm)

$d_h$  = hole diameter (mm)

$G_g$  = Grout Shear Modulus (MPa)

$E_g$  = Grout Elastic modulus (MPa)

$G_{gf}$  = Factored grout Shear Modulus to account for quality of application (MPa)

$E_{gf}$  = Factored grout Elastic modulus to account for quality of application (MPa)

$E_b$  = Bolt Elastic modulus (MPa)

Bolt spacing =  $S$  (m)

$F_a$  = Ultimate axial bolt capacity (MN)

$F_s$  = Bolt shear capacity (MN)

The normal stiffness for fully grouted rock bolts is calculated as:

$$k_n = \sqrt{\frac{0.5 \cdot C_{gf} \cdot E_b}{\left(\frac{d_h}{d_a}\right) - 1}} \quad \text{Equation 6.22}$$

$$K_a = \frac{\pi \cdot k \cdot d_a}{S} \quad \text{Equation 6.23}$$

For the Shear Stiffness it is:

$$\text{Second moment of inertia of bolt section} = I = \frac{\pi \cdot d_a^4}{64} \quad \text{Equation 6.24}$$

$$K = \frac{2 \cdot E_{gf}}{\left(\frac{d_h}{d_a}\right) - 1} \quad \text{Equation 6.25}$$

$$\beta = \left(\frac{K}{4 \cdot E_b \cdot I}\right)^{0.25} \quad \text{Equation 6.26}$$

$$K_s = \frac{E_b \cdot I \cdot \beta^3}{S} \quad \text{Equation 6.27}$$



The maximum axial force is :

$$F_{a \max} = \frac{F_a}{S} \quad \text{Equation 6.28}$$

The maximum shear force is :

$$F_{s \max} = \frac{F_s}{S} \quad \text{Equation 6.29}$$

Table 6.27: Calculation of rock bolt input parameters in UDEC (After Lorig, 1985).

INPUT PARAMETERS:			
Bolt Diameter:	$d_a$	0.022	m
Hole Diameter:	$d_h$	0.035	m
F.S on grout properties:		0.5	
Grout Shear Modulus:	$G_g$	13000	MPa
Grout Elastic Modulus:	$E_g$	15000	MPa
Bolt Young Modulus:	$E_b$	2.1E+05	MPa steel
Bolt Spacing:	$S$	1.2	m
Ultimate Axial Bolt Strength:	$F_a$	0.176	MN 18 tn
Bolt Shear Limit:	$F_s$	0.1232	MN
OUTPUT PARAMETERS :			
Factored Grout Shear Modulus:		6500	MPa
Factored Grout Elastic Modulus:		7500	MPa
1/2 Active Length : = 2* $d_a$		0.044	mm (UDEC input)
NORMAL STIFFNESS:			
$k$ :		33985.29	
$K_a$ :		1957.412	(UDEC input)
SHEAR STIFFNESS :			
$I$ :		1.15E-08	
$K$ :		25384.62	
$\beta$ :		40.26314	
$K_s$ :		131.3475	(UDEC input)
MAXIMUM AXIAL FORCE:			
$F_a \max$ :		0.146667	(UDEC input)
MAXIMUM SHEAR FORCE :			
$F_s \max$ :		0.102667	(UDEC input)

Due to the encapsulation of the H200 beams in the shotcrete the primary support lining was transformed into a single equivalent steel section. The transformation is based on the assumption that the developed compressive or tensile strains of the longitudinal fibers are proportional to the distance from the section neutral axis and also on the assumption that planar sections before bending remain planar after bending as well.

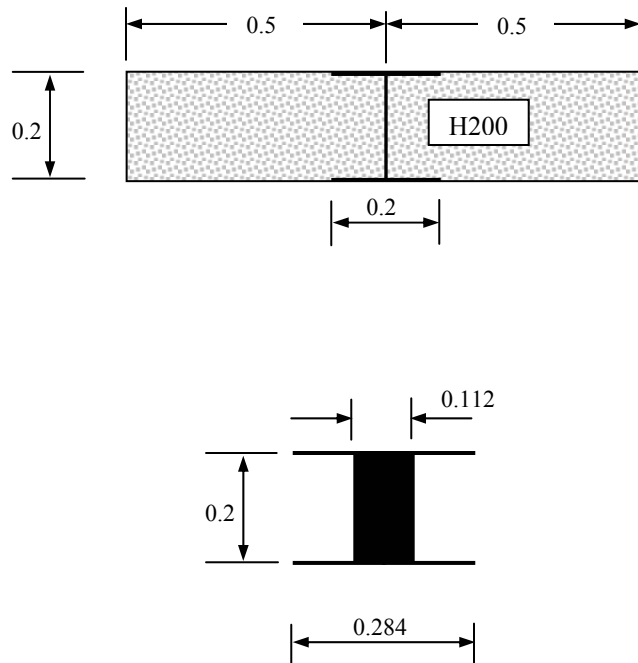


Figure 6.64: Equivalent steel beam for shotcrete-steel beam lining used for support (lengths in meters).

$$F_{\text{tot eq}} = F_{\text{H200}} + n \cdot F_c \quad \text{Equation 6.30}$$

$$n = \frac{E_c}{E_s} = \frac{21000}{200000} = 0.105 \quad \text{Equation 6.31}$$

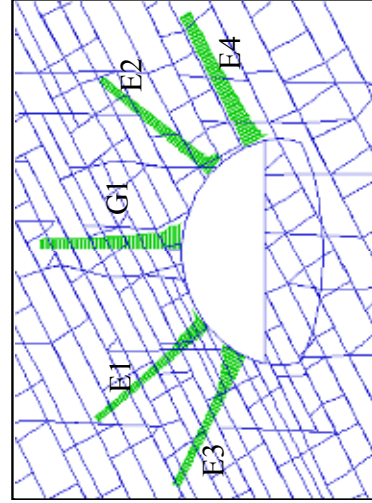
$$I_{\text{tot eq}} = 11126.4 \cdot 10^{-8} \text{ m}^4$$

$$F_{\text{tot eq}} = 0.02655 \text{ m}^2$$

UDEEC equivalent H steel section shape factor = Web area/ Total section area= 0.7433.

Table 6.28: Comparison between predicted results for top heading using UDEC and measurement data.  
 E=5000 MPa jointed model.

Method	UDEC Solution			Onsite Measurements			
	Uncorrected Deformation (mm)	Rock Bolt Maximum load (MN)	Axial Force on Composite beam (MN/m)	Deformation (mm)	Rock Bolt Maximum load (MN)	Axial Force on Steel section (MN)	Axial Force in Shotcrete (MN)
Crown (C)	10.1	(G1)	-	9.5	(G1)	-	-
Crown (D)	10.2	-	-	13	-	-	-
Crown (H)	12.1	-	-	13	-	-	-
Ext. E4/R5	3	0.019	0.223	1	0.013		0.137
Ext. E2/R3	11.1	0.127	0.196	3	0.01	0.412	0.235
Ext. G1/R1	11.2	0.089	0.121	14-15	0.042	-	0.255
Ext. E1/R2	13	0.049	0.159	8	0.168	0.588	0.353
Ext. E3/R4	4.6	0.027	0.163	3	0.108	-	0.196



Note:

- E=Extensometer location
- R= Measurement Anchor location
- C, D, H onsite data are from 3D convergence surveying by Total Station.
- E1,2,3,4 & G1 data are from extensometer measurements.

### 6.7.5 Discussion of results for initial DEM analysis

Figure 6.65 shows shaded contours of predicted vertical displacements at the end of the top heading construction and figure 6.66 presents the predicted nodal deformation along lines where 12.0 m extensometers were installed. From figure 6.67 which presents contours of the mobilized shear strength, it becomes apparent that there are two distinct regions above and beneath the tunnel which have been distressed due to excavation. The top region is evidence for potentially unstable rock blocks and is supported by the rock bolts and the primary lining of the structure. In that region the predicted axial rock bolt forces are also maximized.

As it is shown in figures 6.50 and 6.51 of measured displacements, the top heading excavation at the chainage of 913+65 was performed on the 1/27/98. Measurement equipment was installed on the 1/28/98 in that section and the excavation of the heading drive was continued. On the 2/16/98 the top heading face arrived at the chainage 914+10 covering about 45 m of tunnel length. From the three dimensional convergence measurement (geodetical) it is seen that by the date of 2/26/98, top heading deformations had been almost stabilized. For that time, the crown deformation records show about 9.5 mm of displacement and offset roof points D and H show about 13 mm of convergence. This is in relative disagreement with the trend of continuum element modeling that has the offset points converging less than the crown. However the Distinct element model, shows that such differences can occur mainly due to the existence of non-uniform displacements of blocks. At this stage there should be two issues acknowledged:

- Predicted deformation results from UDEC have not yet been corrected, to take into account effects of previous deformations, before installation of the measurements.
- The final predicted deformations from UDEC are not in general agreement with the concept of convergence-confinement since equilibrium should have been achieved in theoretically lower deformations.

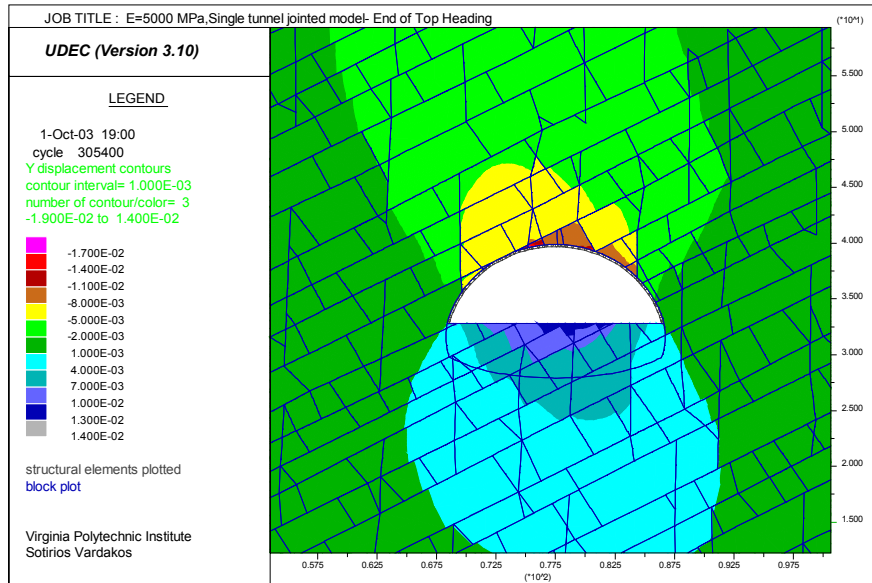


Figure 6.65: Shaded contours of vertical displacements after installation of support in top heading, assuming a block elastic modulus of  $E=5000$  MPa.

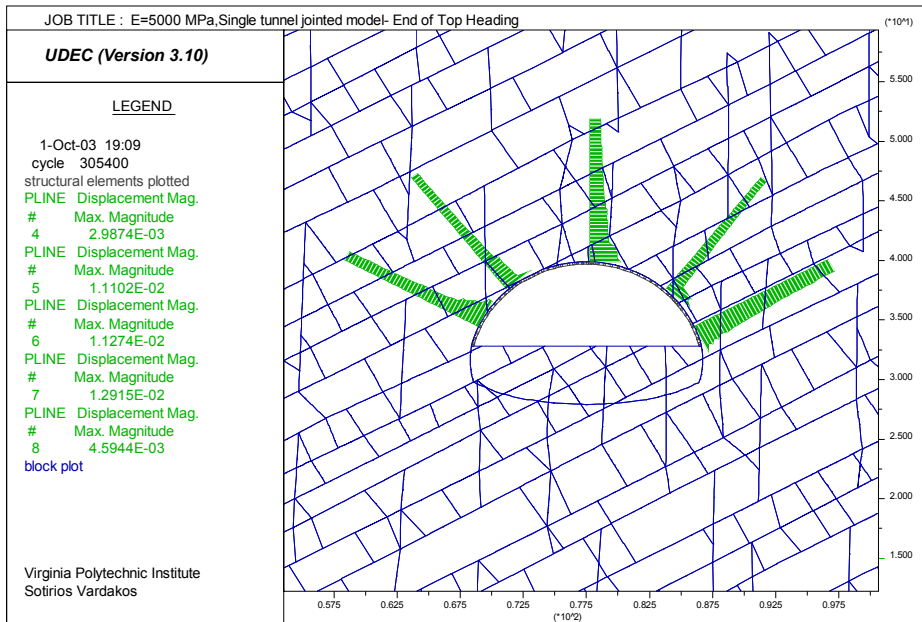


Figure 6.66: Deformations along directions of extensometer locations in top heading.

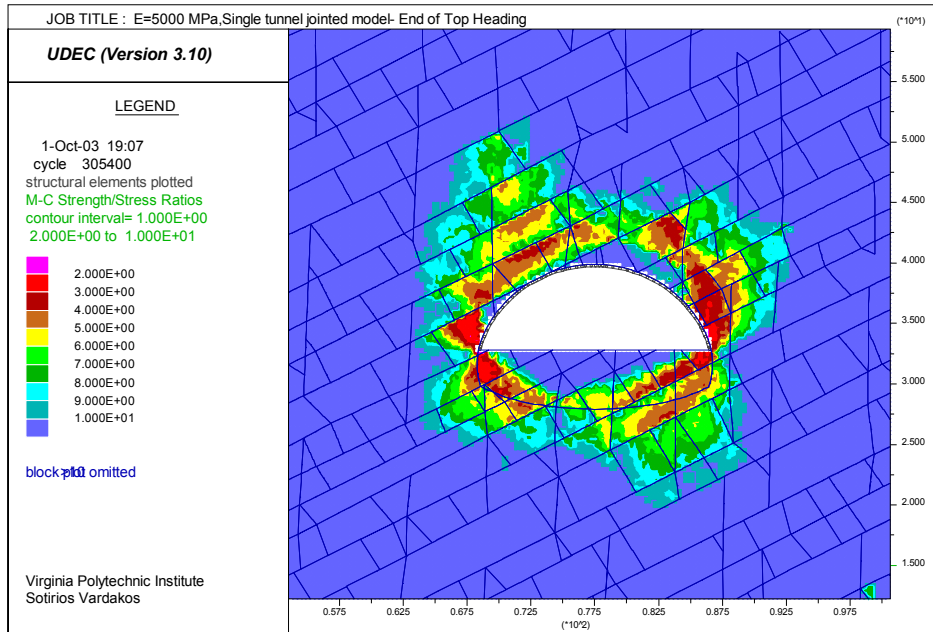


Figure 6.67: Strength/stress plot for supported top heading excavation. It is shown that there is a region of distressed blocks above the tunnel as well as at the temporary floor level. Stress concentration around the edges tends to cause initialization of plastic yielding at these points.

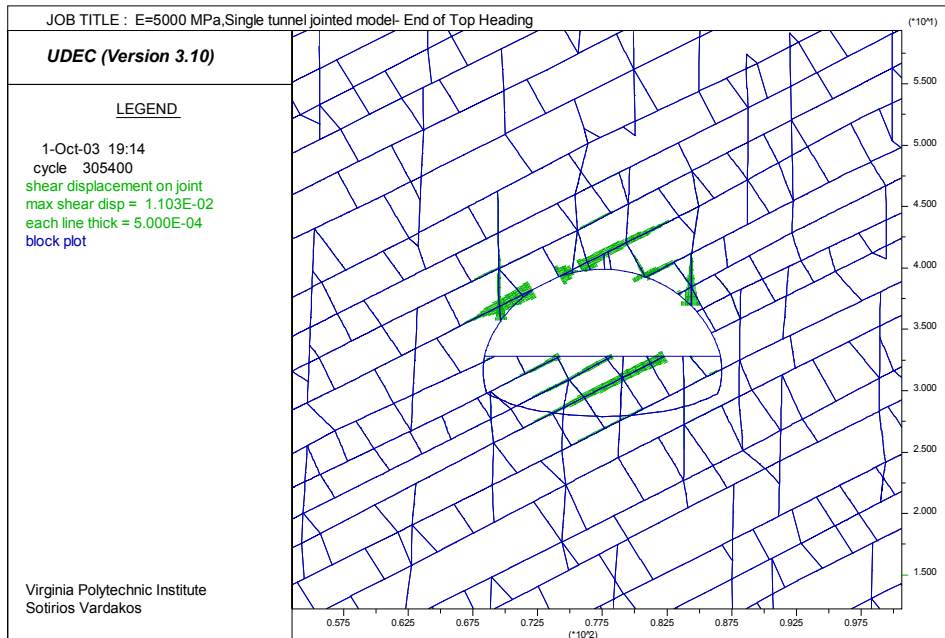


Figure 6.68: Shear displacements around supported top heading, using E=5000 MPa.

Data from the extensometer and measurement anchors give further insight to the displacement trends. Extensometers G1, E1 and E3 reveal that more deformations occur in the left half of the top heading geometry, a fact also recorded by the rock bolt axial forces, which show relatively higher values at these locations, while in the case of location D (R2 measurement bolt) a threshold axial load close to the maximum nominal capacity of the bolt occurs. The deformation recorded by the multi point extensometer at the roof is recorded to be greater than the geodetical survey value at a value of about -14 mm. From figure 6.54f the deformation distribution also appears to be relatively uniform with no sudden increments.

Numerical analysis does not predict axial force values which fit well to the measured ones and this can be attributed to the unknowns involved in the spatial data during construction of the distinct element model, since the existence or not of a fracture can change the rock bolt axial force estimates. It is also apparent that the axial forces measured inside the primary lining materials of the top heading are higher than what is estimated by the numerical code which would mean that the lining material does not appear to be loaded at it is in actual conditions. At this point it should also be recognized that the interaction between shotcrete and steel beams is in reality much more complex than what is assumed by the composite section and certain differences may exist. Figure 6.69 shows a magnified deformed block plot (x60) in contrast to the original geometry. It becomes apparent that the UDEC model behaves anisotropically since more strain is developed on the left side of the model especially in the direction perpendicular to the bedding planes and this is most probably the basis of explanation of the true tunnel behavior. From this analysis it becomes obvious that there is a difference between the controlled relaxation and the dynamic solution which may lead to uncertain estimates of the loss factor. The application of the relaxation method was made under the assumption of similar ground response during a dynamic solution. The final results show that this does not necessarily happen and by the time the measured point above the crown has reach a desired relaxation, the actual excavation boundary has been equivalently relaxed even more and thus has greater initial displacements than anticipated. Thus loads are under predicted and a better approach must be made.

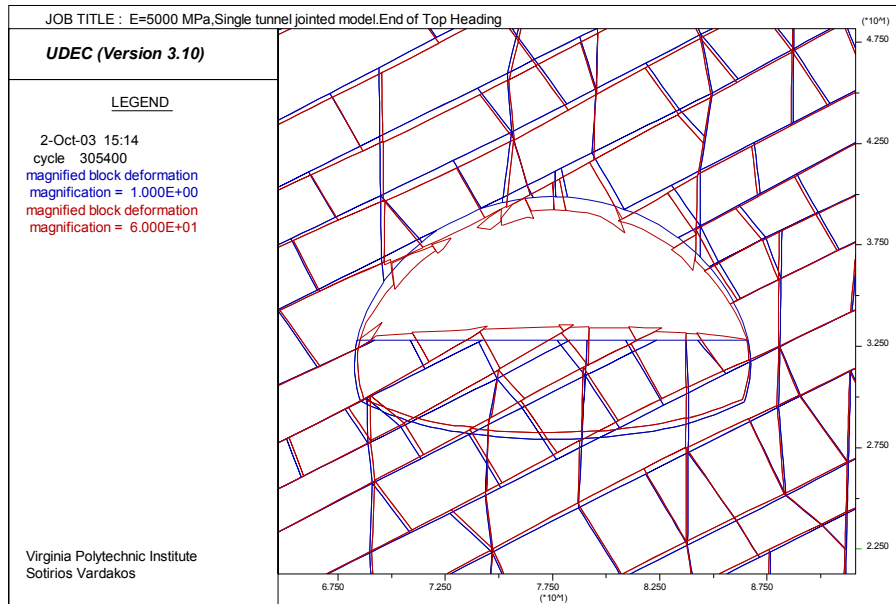


Figure 6.69: Comparison between original geometry and deformed block geometry after excavation in jointed model.

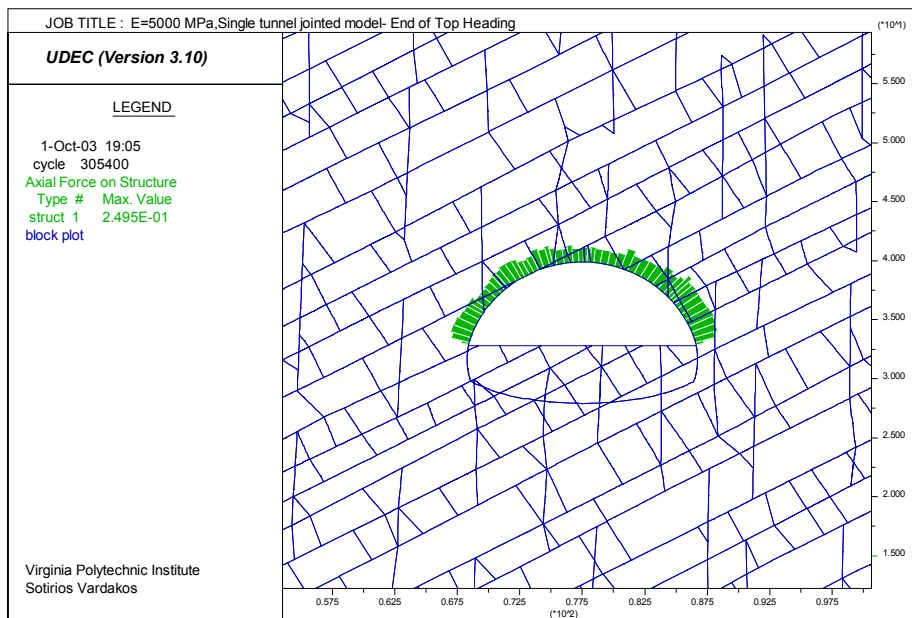


Figure 6.70: Axial forces on composite beam structure for jointed model by using E=5000 MPa.



## CHAPTER 7 : Parametric analysis for characteristic curves

### 7.1 General procedure

At this stage four series of parametric analyses were performed, in order to study the sensitivity of the UDEC models and the variation of the convergence (characteristic) curves, by varying different parameters of the problem. The parametric analysis was based on the  $E=5000$  MPa, single tunnel jointed model and the following parameters were investigated:

1. Relative location of the tunnel with respect to the most influencing joint set. Two single tunnel jointed models were analyzed assuming an elastic modulus of  $E=5000$  MPa and by shifting vertically the tunnel position (or equivalently the location of the fracture network). A more rigorous analysis would require several variations of fracture geometry or tunnel relocation, but it exceeds the scope of the present work.
2. Influence of the Joint Roughness Coefficient ( $JRC_o$ ) in the model stability.
3. Influence of the Joint Wall Compressive strength ( $JCS_o$ ) in the model stability.
4. Influence of the residual friction angle  $\phi_r$  in the model behavior.

### 7.2 Vertically relocated tunnel models

#### 7.2.1 Downward relocation of the tunnel

In this case a model was constructed in UDEC, where the tunnel was assumed to be relocated downwards in relation to its former position in the  $E=5000$  MPa jointed model. In order to keep all other things equal, including stresses (for comparison purposes) an equivalent upward shifting of the bedding plane fracture network was performed, since it is the most influential on the tunnel stability. Based on the initially constructed geometry of UDEC  $E=5000$  model, the true spacing and standard deviation was measured from three scanlines perpendicular to the sandstone bedding. Data for the bedding intersections were recorded and statistically examined in order to evaluate an approximate value for the amount of vertical relocation. Data are shown in Table 7.1.



From the analysis, was concluded that UDEC had initially constructed a bedding spacing (rounded):

$$s=2.9\pm 0.6 \text{ (m)}.$$

Therefore it was decided to equivalently shift the location of the beddings in the vertical direction by:

$$\delta y = \frac{s}{\cos(dip)} = \frac{0.6}{\cos(28)} = 0.67 \text{ m}$$

Based on the above the new model was constructed and subsequently analyzed only unsupported in order to examine the dependency of the convergence curves on bedding location. Results of the analysis are shown in figures 7.1 and 7.2. From the results it is apparent that the convergence analysis for the pilot opening shows relatively more displacements than in the case of the original geometry. Maximum vertical displacement in the opening is about 2.1 mm in comparison to 1.8 mm of the previous analysis. The springline also shows an increase in deformation to 1.85 mm from 1.6 mm. Nevertheless the convergence curves constructed for the top heading excavation reveal the true effects of the new geometry. The tunnel behaves much more uniformly and in the cases of the crownline point C and roof point D, no unstable rock blocks are formed. The deformations equilibrate at a final solution of about 10 mm for the crown and 8.0 mm for point D. In point H a wedge formation causes sudden increment of deformations after reduction to a critical pressure. By comparing figures 7.2 and 6.59, it can be concluded that there is no appreciable difference of the top heading convergence between the two analyses and the gradual unloading solution is practically the same. The difference can be observed at the final stage of unloading where the new geometry proves to be more favorable to stability than the previous.

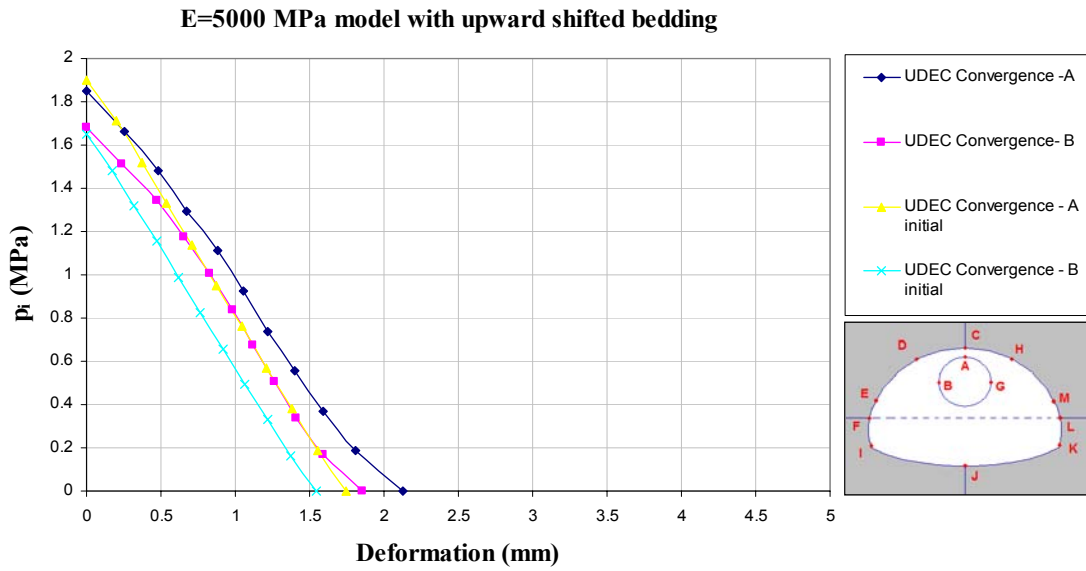


Figure 7.1: Characteristic curves in jointed model using E=5000 MPa with upward shifted bedding.

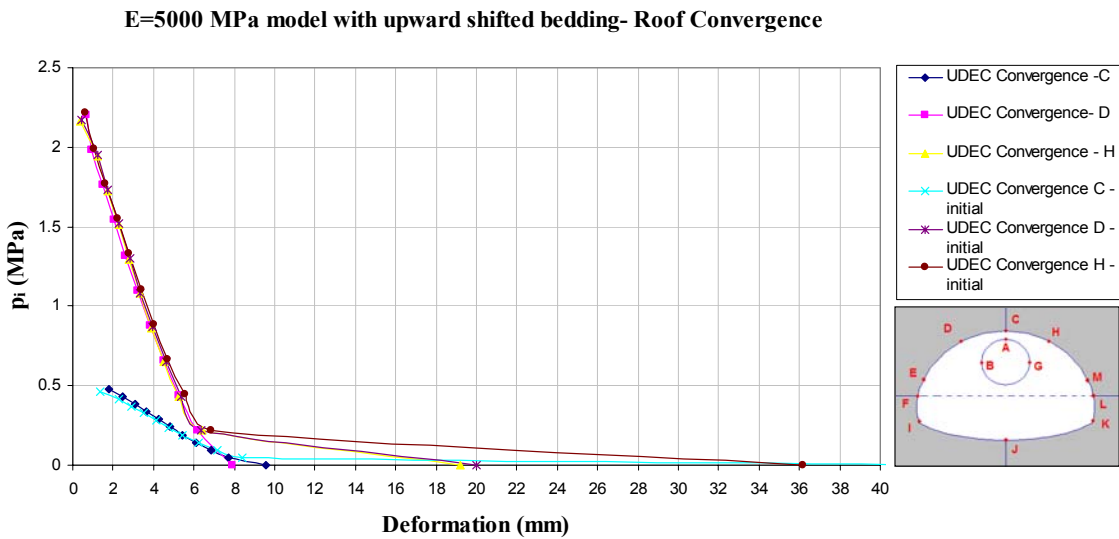


Figure 7.2: Characteristic curves in jointed model using E=5000 MPa with upward shifted bedding.

## 7.2.2 Upward relocation of the tunnel

In this analysis an equivalent downward shifting of the sandstone bedding plane was performed. Analysis was based again on the unsupported tunnel to investigate the influence on the ground characteristic curves. Results of this analysis are shown in figures 7.3 and 7.4. From this analysis it is also apparent that the ground response curves for the top heading excavation are in close agreement with the ones from the initial  $E=5000$  MPa model. Again most differences are exhibited at the last stage of unloading since in this case only one out of three unstable rock blocks stabilizes in contrast to the initial  $E=5000$  model. Therefore, it is concluded that for the range of “equivalent” tunnel relocation assumed in the previous analysis, the convergence curves remain practically the same and can also be used for a full excavation-support interaction analysis.

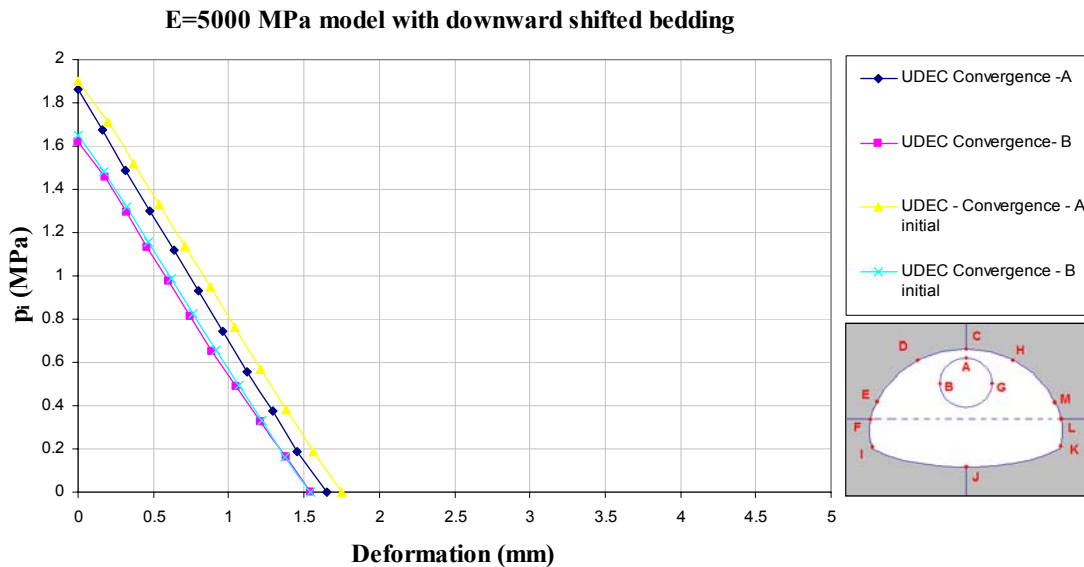


Figure 7.3: Characteristic curves in jointed model using  $E=5000$  MPa with downward shifted bedding.

**E=5000 MPa model with downward shifted bedding- Roof Convergence**

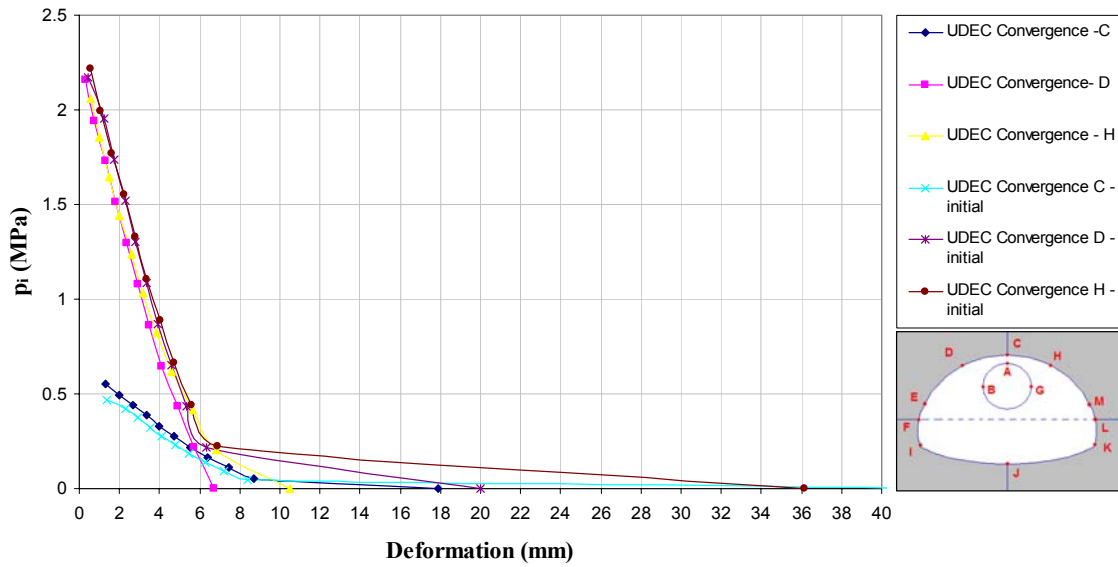


Figure 7.4: Characteristic curves in jointed model using E=5000 MPa with downward shifted bedding.

### 7.3 Influence of the Joint Roughness Coefficient ( $JRC_o$ )

In this series of analyses the influence of the joint roughness coefficient  $JRC_o$  on the convergence curves was examined. For both joint sets, bedding and random cross joints the mean values were decreased and increased by their standard deviation respectively. Due to these changes the initial aperture value used as input in the numerical code, was also changed accordingly by using the relationship 6.1 for consistency, while all other parameters were kept constant. The values used have as follows:

$$JRC_o = \overline{JRC_o} \pm \delta(JRC_o) \quad \text{Equation 7.1}$$

$$E_o \approx \frac{JRC}{5} \left( \frac{0.2\sigma_c}{JCS} - 0.1 \right) \quad \text{(Equation 6.1)}$$

Bedding:  $JRC_o = 3 \pm 1$

Cross Joints:  $JRC_o = 7 \pm 3$

$\sigma_c = 50$  MPa.

Table 7.2: Parameter values used in UDEC to examine the influence of the Joint Roughness Coefficient ( $JRC_o$ ) on the convergence curves.

Parameter Value:	Mean			M+Std.dev		M-Std.dev	
	JRC	JCS	$E_o$	JRC	$E_o$	JRC	$E_o$
Bedding	3	30	0.140	4	0.186	2	0.093
Cross Joints	7	40	0.330	10	0.300	4	0.120
Note: Aperture $E_o$ in (mm).							

Convergence curves for the pilot and the top heading stages, are depicted in figures 7.5 and 7.6. From the curves for the pilot opening, becomes apparent that there is a trend for reduction of the recorded radial deformations even though the strength via the Barton-Bandis criterion has been reduced. This difference is very small for practical purposes and is most probably attributed to the simultaneous change in the theoretical initial aperture of the joints. The convergence curves constructed for the top heading roof, do

not show any appreciable difference (minor differences) and it can be deduced that the Roughness coefficient does not practically influence the behavior of the tunnel significantly to become an issue.

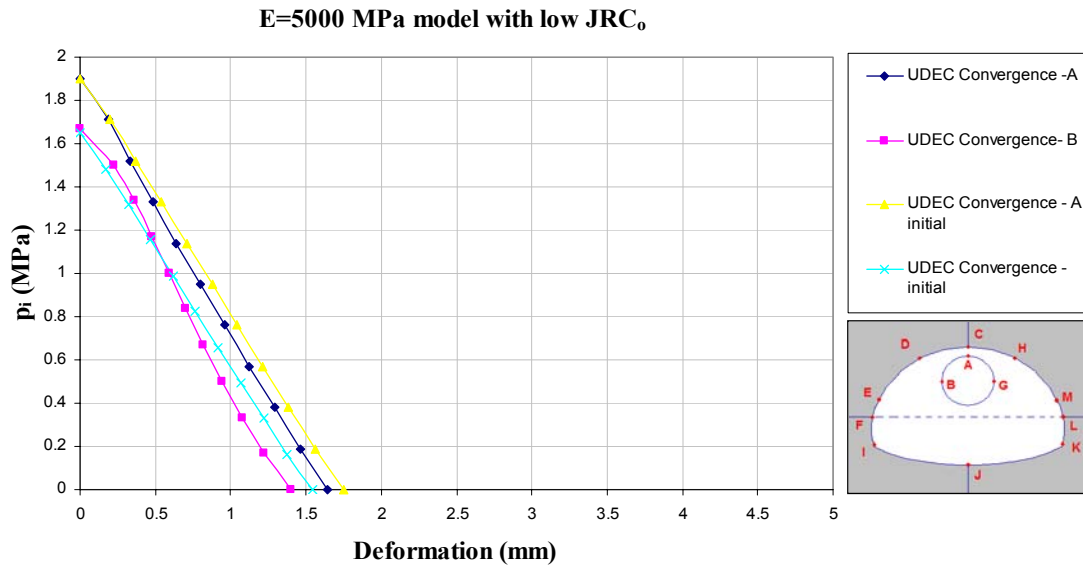


Figure 7.5: Characteristic curves for pilot tunnel in jointed model using E=5000 MPa with low JRC parameter.

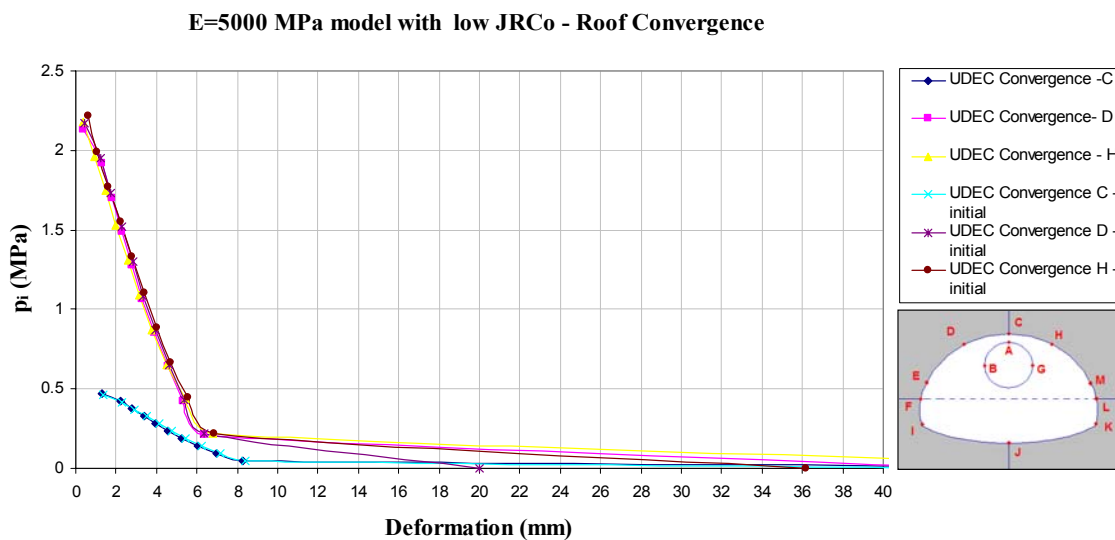


Figure 7.6: Characteristic curves for top heading in jointed model using E=5000 MPa with low JRC parameter.



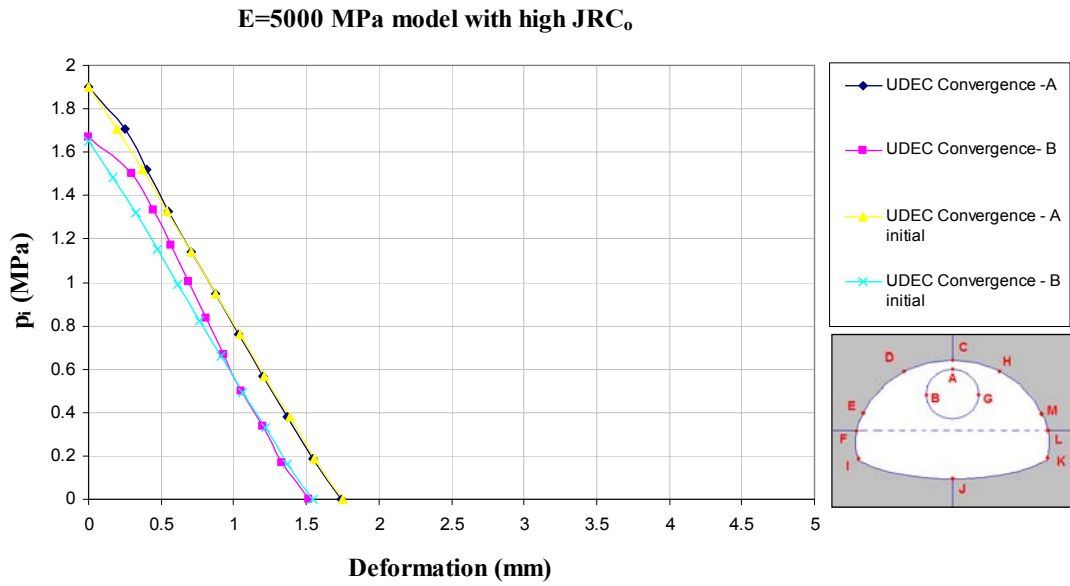


Figure 7.7: Characteristic curves for pilot tunnel in jointed model using E=5000 MPa with increased JRC parameter.

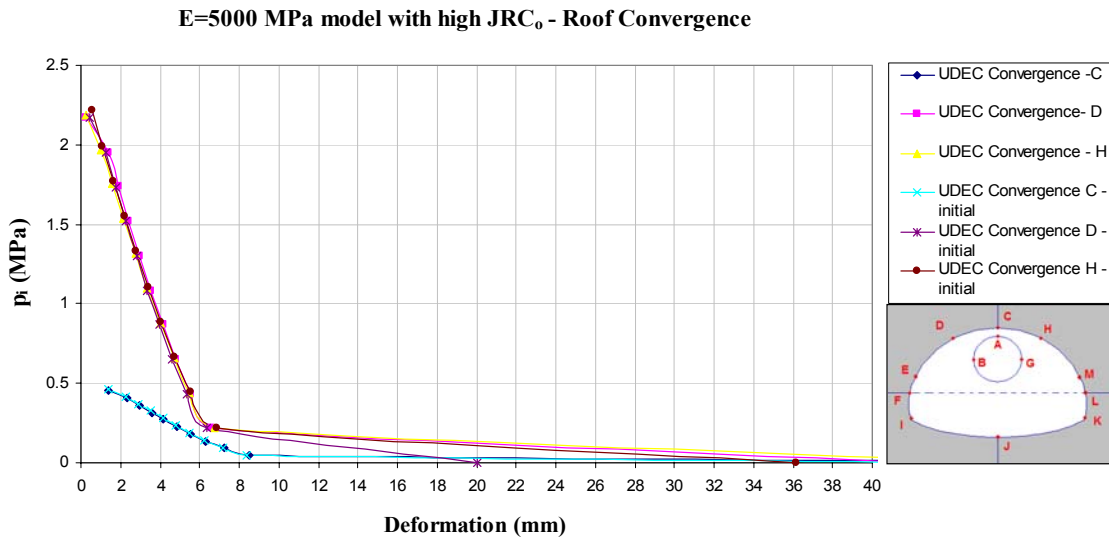


Figure 7.8: Characteristic curves for top heading excavation in jointed model using E=5000 MPa with increased JRC parameter.

## 7.4 Influence of the Joint Wall Compressive Strength ( $JCS_o$ )

In this series of analyses the influence of the joint wall compressive strength  $JCS_o$  on the convergence curves was examined. For both joint sets, bedding and random cross joints the mean values were decreased and increased by their standard deviation respectively. Due to these changes the initial aperture value used as input in the numerical code, was also changed accordingly by using the relationship 6.1 for consistency, while all other parameters were kept constant. The values used have as follows:

$$JCS_o = \overline{JCS_o} \pm \delta(JCS_o) \quad \text{Equation 7.2}$$

Table 7.3: Parameter values used in UDEC to examine the influence of the Joint Compressive Strength ( $JCS_o$ ) on the convergence curves.

Parameter Value:	Mean			M+Std.dev		M-Std.dev	
	JCS	JRC	$E_o$	JCS	$E_o$	JCS	$E_o$
Bedding	30	3	0.14	40	0.09	20	0.24
Cross Joints	40	7	0.33	60	0.093	20	0.56
Note: Aperture $E_o$ in (mm).							

Results shown in figures 7.9 to 7.12 once more show, that the convergence curves do not appreciably deviate from the curves constructed by using the mean strength parameters for practical engineering purposes. However the deformations exhibit a small trend to increase when the  $JCS_o$  is reduced while they tend to decrease when the  $JCS_o$  is increased again. In this case the increment in the JCS values causes a simultaneous reduction in the initial aperture values, therefore a more compact model is initially constructed thus a slight increase in strength and reduction in deformations would be theoretically expected. The exact opposite phenomena happen for a reduction in the compressive strength parameter.

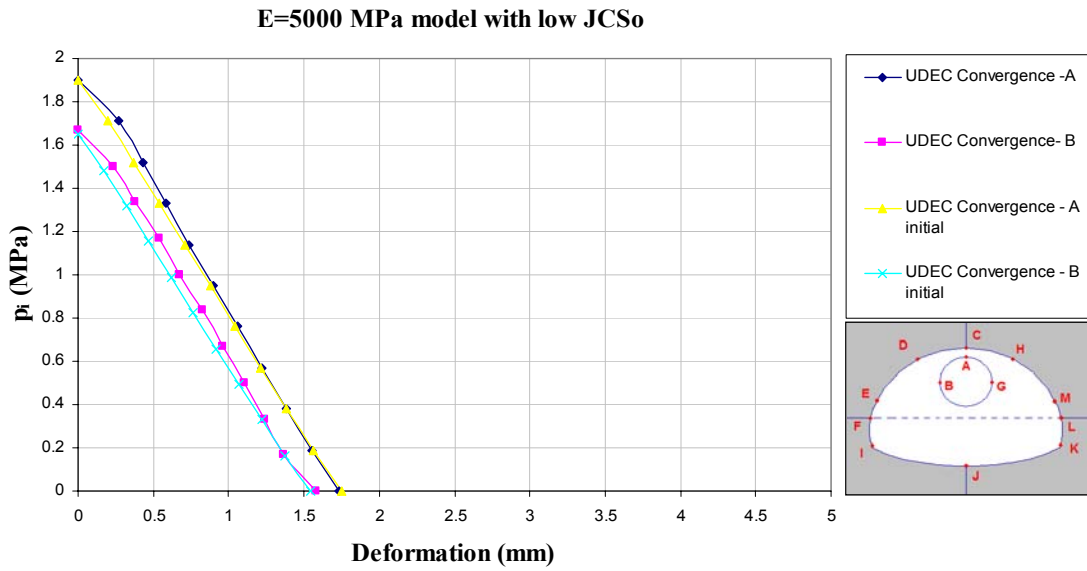


Figure 7.9: Characteristic curves for pilot tunnel in jointed model using E=5000 MPa with low JCS parameter.

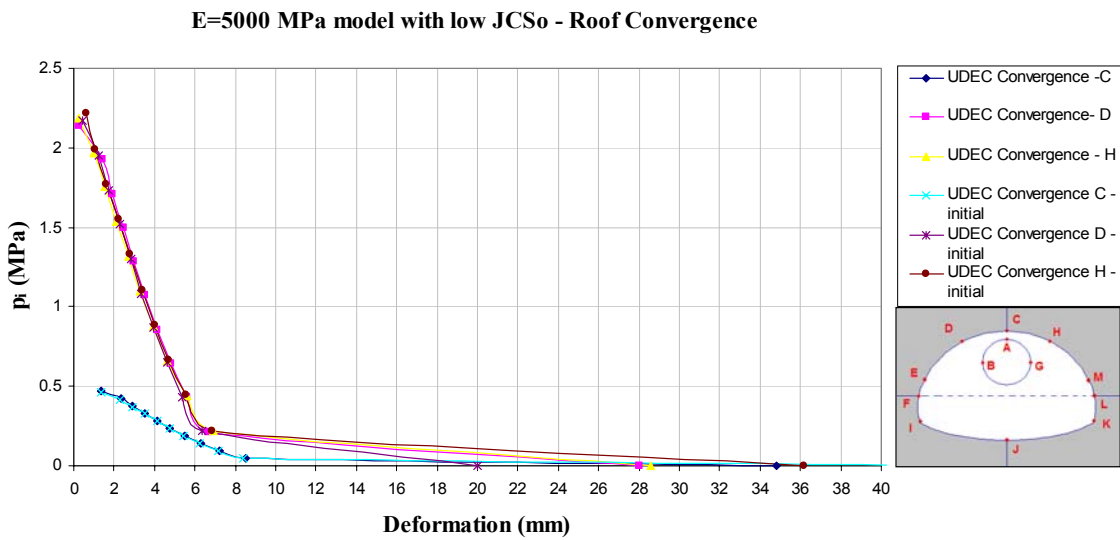


Figure 7.10: Characteristic curves for top heading excavation in jointed model using E=5000 MPa with low JCS parameter.

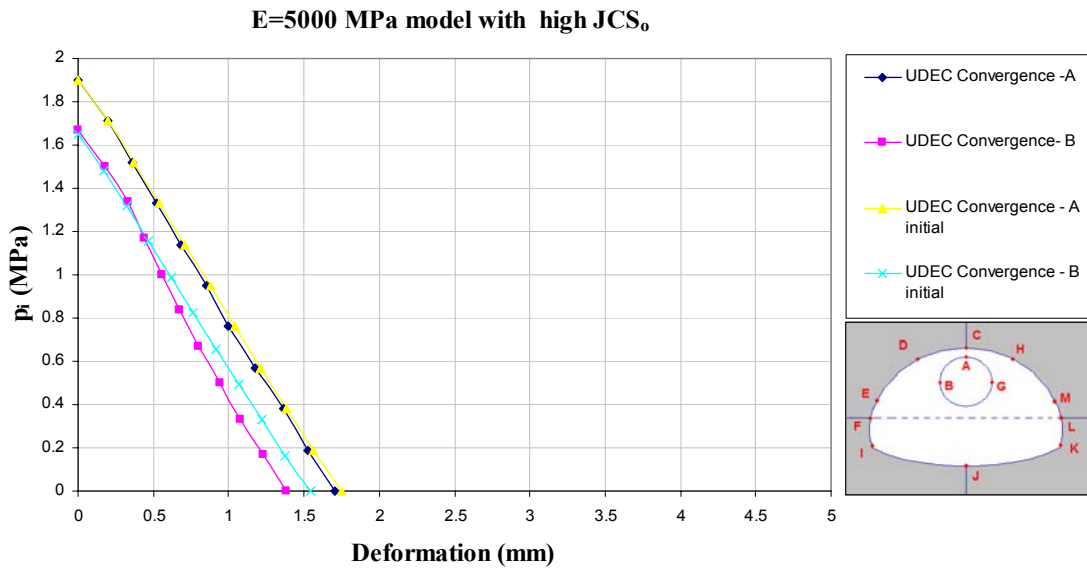


Figure 7.11: Characteristic curves for pilot tunnel in jointed model using E=5000 MPa with high JCS parameter.

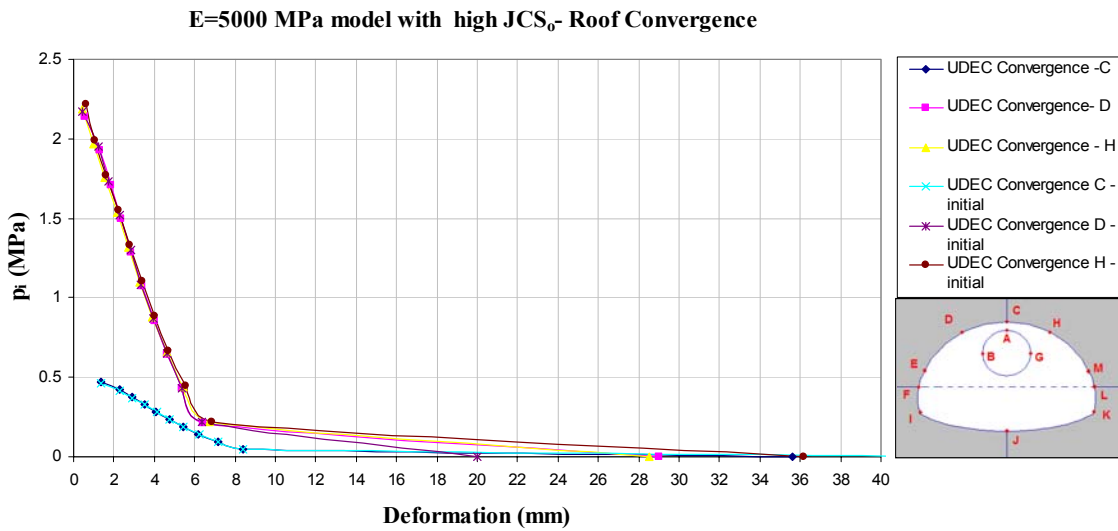


Figure 7.12: Characteristic curves for top heading excavation of tunnel in jointed model, using E=5000 MPa with high JCS parameter.

## 7.5 Influence of the residual friction angle $\phi_r$ in the model behavior

For this case the initial model was used to investigate the influence of the joint residual friction angle on the convergence curves. The friction angle  $\phi_r$  was varied as follows:

Bedding:  $\phi_r = (25 \pm 5)^\circ$

Cross Joints:  $\phi_r = (30 \pm 5)^\circ$

The results from this analysis are shown in figures 7.13 to 7.16. From figure 7.13 becomes apparent that there is minor difference in the curves created for the unsupported pilot tunnel while figure 7.14 shows that the reduction in the residual friction angle (and thus joint strength) causes development or more deformation as it is logically expected. On the contrary, the increase in the residual friction angle results in slightly less deformation at full relaxation as shown in figures 7.15 and 7.16. However all the recorded differences are not considered to be significant for practical engineering purposes and therefore the convergence curves constructed by UDEC are not generally very sensitive on parameter statistical fluctuations, a very important desired feature in a so multi-parametric problem as a rock tunnel where uncertainties can prevail easily.

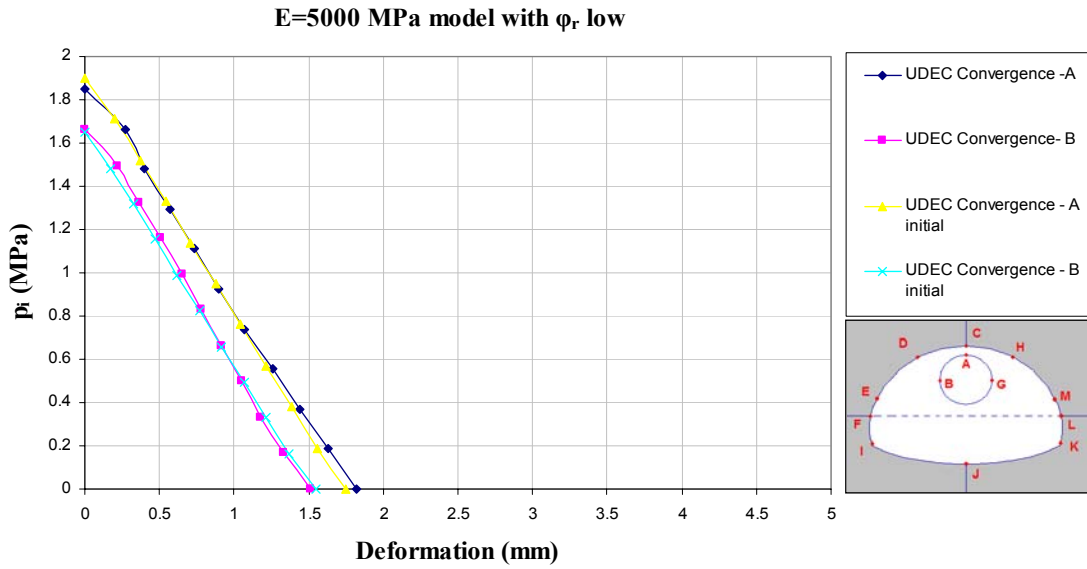


Figure 7.13: Characteristic curves for pilot tunnel in jointed model using  $E=5000$  MPa and assuming reduced residual friction angle  $\phi_r$ .

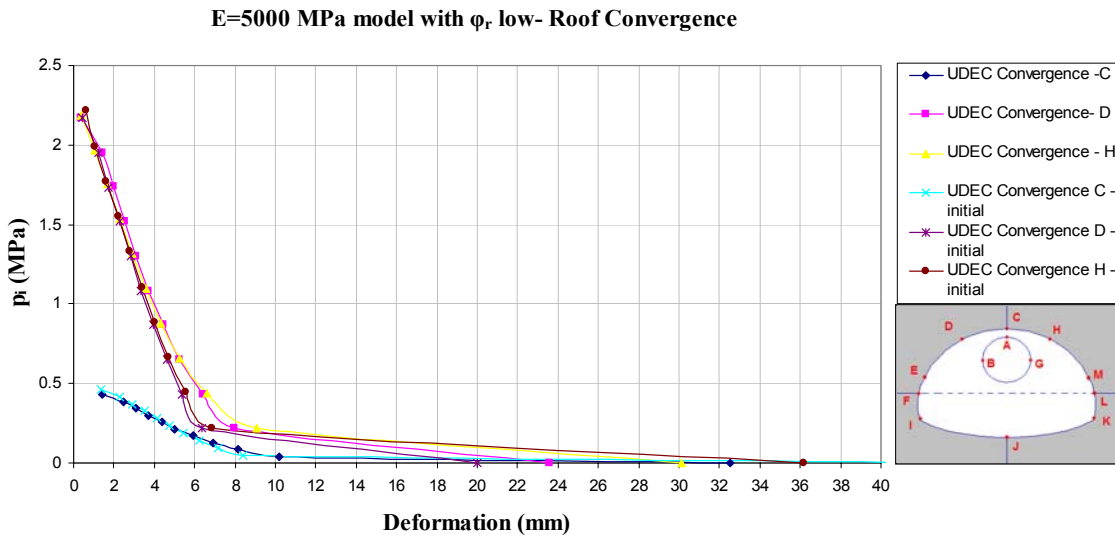


Figure 7.14: Characteristic curves for top heading stage in jointed model using  $E=5000$  MPa and assuming reduced residual friction angle  $\phi_r$ .

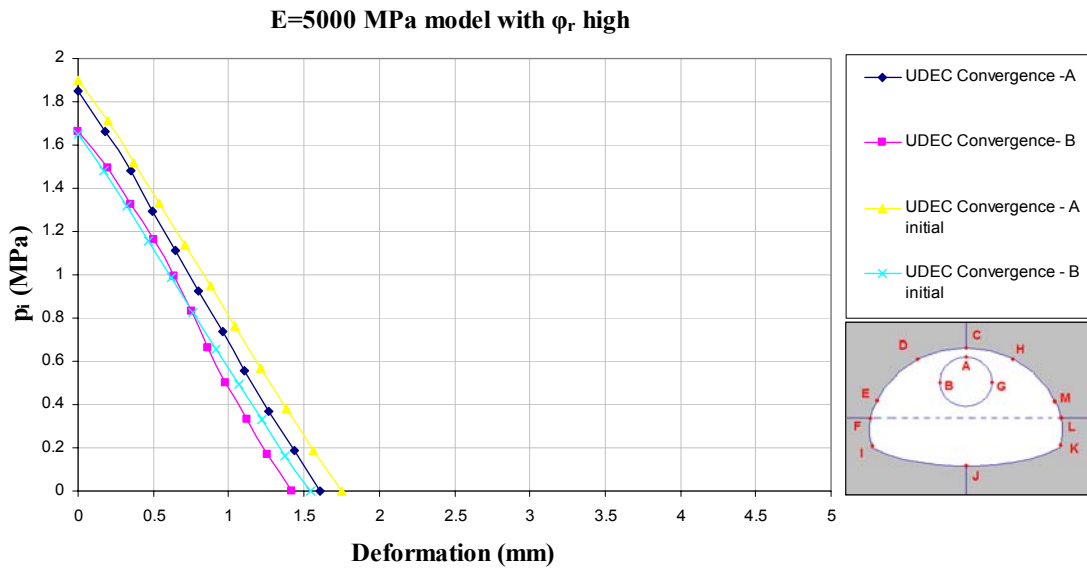


Figure 7.15: Characteristic curves for pilot tunnel in jointed model using  $E=5000$  MPa and assuming increased residual friction angle  $\phi_r$ .

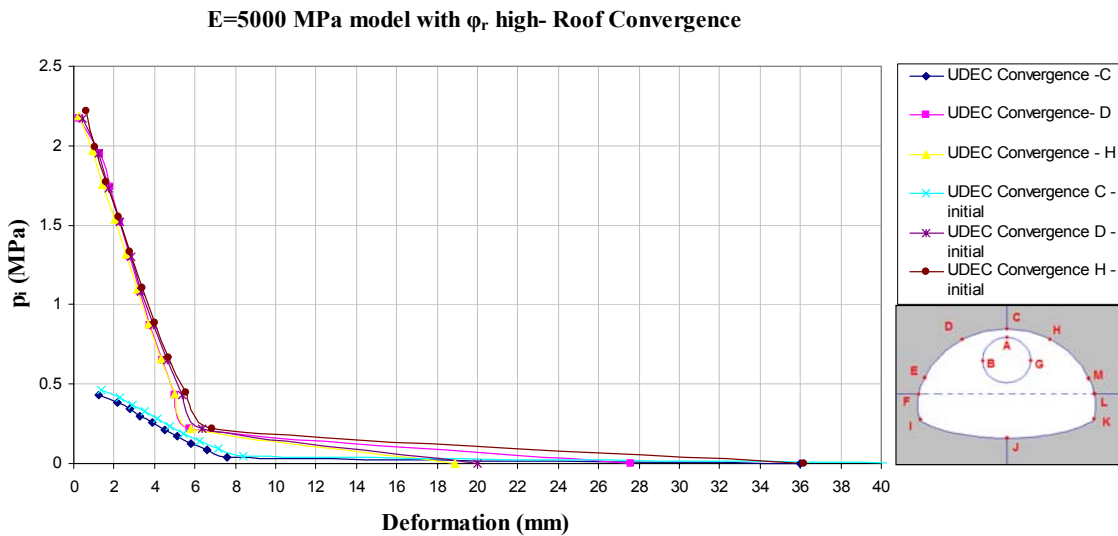


Figure 7.16: Characteristic curves for top heading stage in jointed model using  $E=5000$  MPa and assuming increased residual friction angle  $\phi_r$ .

## CHAPTER 8 : Back-analyzed models

### 8.1 General considerations

So far it has been shown by the parametric studies, that the effects of statistical variation of different parameters, involving mainly the shear strength or the location of the discontinuities, do not alter appreciably the expected stress redistribution around the tunnel. The constructed “characteristic” curves for the pilot tunnel and top heading excavation stages reveal that the overall behavior is not expected to change significantly. The fracture network utilized in the parametric analyses (NGI, 1995) was initially designed to include approximately of 1 out of 10 discontinuities per joint set for efficiency purposes. This fact especially in the case of the bedding is causing the model to behave more rigidly than it should be, even with a globally reduced block elastic modulus in the range of 5000 MPa. It was also observed that even with a lower modulus of  $E=5000$  MPa used for distinct blocks predicted deformations did not fit well with measured data in the analyzed section. This fact suggests that lower stiffness values or a different model closer to what should be really anticipated, should be examined.

A logical reason to the question of why did this initial overestimation of stiffness occur may be found to the way that these values were taken beforehand. First of all the implementation of limited geophysical testing (downhole seismic measurements) in the specific area may have resulted in erroneous estimations or it did not capture well and in detail some local irregularities of the sedimentary rock formations. Furthermore a great deal of rock mass classification was performed during boring of the pilot tunnel. Without doubt procedures involving geotechnical investigation by the pilot tunnel are of paramount importance for the type of the work. However the fact that the pilot was excavated by a tunnel boring machine may have led to some rock mass quality overestimations due to the uniformity and smoothness of the excavation profile. In addition during the top heading and bench excavations the drill and blast technique was invoked which also causes further disturbance and loosening of the surrounding rock mass thus a reduction in its elastic-plastic properties. These elements should not be



overlooked during the analysis of any underground engineering work and their influence should be weighted during designs.

Therefore a refinement of the initial model used can be made by back analysis in order to better agree with the measured results. Different methods can be followed at this stage. A possible method is to further reduce the elastic modulus of the rock blocks in order to increase the developed strains and approach the measured displacements for the case of the STA 913+65 chainage. Another method is to increase the level of design accuracy in the joint network especially in the bedding orientation and reanalyze the problem and evaluate the effects of the new geometry. All methods necessitate the development of new convergence curves for the top heading excavation. In the last case the main advantage is the self development of an anisotropic elastic modulus in the UDEC model. All cases are followed and subsequently analyzed.

In order to study and investigate the top heading excavation behavior under different possible conditions, the following analyses were initially conducted to further study the sensitivity of the convergence curves, mainly for the top heading excavation:

1. An analysis using the same as the  $E_{\text{block}}=5000$  MPa jointed model by reducing the global elastic modulus to 3800 MPa.
2. A locally refined single tunnel jointed model with closer spacing of the bedding close to the excavated region assuming  $E_{\text{block}}=5000$  MPa.
3. A locally refined jointed model (as in case 2) by reducing the global elastic modulus to  $E_{\text{block}}=4300$  MPa.
4. A locally refined jointed model (as in case 2) by further reduction of the global elastic modulus to  $E_{\text{block}}=3000$  MPa

## 8.2 Ground characteristic curves for back analysis

### 8.2.1 Single tunnel jointed model with $E=3800$ MPa

In this case the elastic modulus of the rock mass was reduced globally from  $E=5000$  MPa down to  $E=3800$  MPa. This reduction was made empirically by comparing the deformation curves of figure 6.35 of the continuum approach. From these plots it is seen that in order to get convergence values in the desired amount of roof displacement range even on unsupported excavations, the average elastic modulus should be reduced to a value of approximately 2000 MPa. In specific monitored deformations have revealed that after support of the top heading, measured deformations from extensometers should be at about 10-15 mm for the crown, 8 mm at about 6.0 m the left of the centerline and around 3 mm at 6.0 m to the right of the centerline. In fact if the measured deformations by surveying are considered then the deformation range may be even larger.

As a rough guideline this should suggest a block modulus in the range of  $E=2000+(1500\pm 300)$  MPa. The stiffer modulus value of 3800 was initially assumed. The same procedure steps were followed during the analysis, new convergence curves were constructed. The following table 8.1 shows results of the pilot tunnel stage from the two numerical analyses, under immediate and controlled unloading, as well as from simplified elastic and elastoplastic analysis. It is apparent that in this case the solution difference between the two numerical solutions in UDEC is increased. For the crownline it becomes 0.5 mm and for the springline it is about 0.9 mm. Results from the elastic and elastoplastic analyses, by using an equivalent modulus  $E=2300$  MPa, yield comparable results with the immediate unloading UDEC solution. Results of the numerical analysis for the unsupported top heading are shown in figures 8.1 and 8.2. Figures 8.3, 8.4 and 8.5 show convergence curves produced during the controlled unloading of the excavated space.

Table 8.1: Comparison between UDEC and simplified elastoplastic analysis for pilot tunnel.

Method:	UDEC full unloading	UDEC gradual unloading	Elastoplastic analysis using $\sigma_{av}$ .	Elastic using $K_o$ ratio.
E mod.	3800	3800	2300	2300
Insitu Stress	$\sigma_v=1.9$ $\sigma_h=1.65$	$\sigma_v=1.9$ $\sigma_h=1.65$	$\sigma_{av}=1.7$	$\sigma_v=1.9$ $\sigma_h=1.65$
$\delta_{crown}$	2.6	2.14	2.4	2.8
$\delta_{wall (R)}$ $(L)$	2.5 2.2	1.6 1.8		2.2

Note: Stresses in MPa, deformations in mm,  $\epsilon \neq 0$  models.

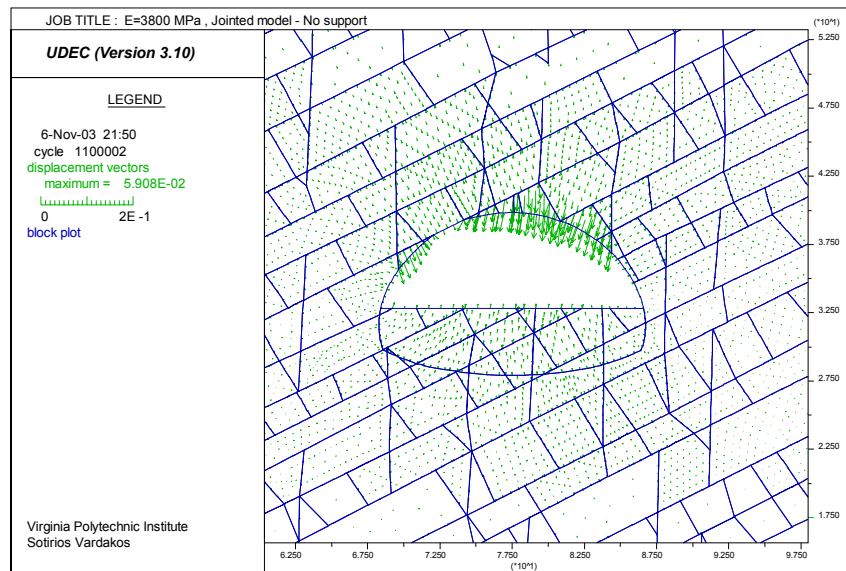


Figure 8.1: Maximum total displacements in unsupported top heading at 100% relaxation, by using  $E=3800$  MPa.

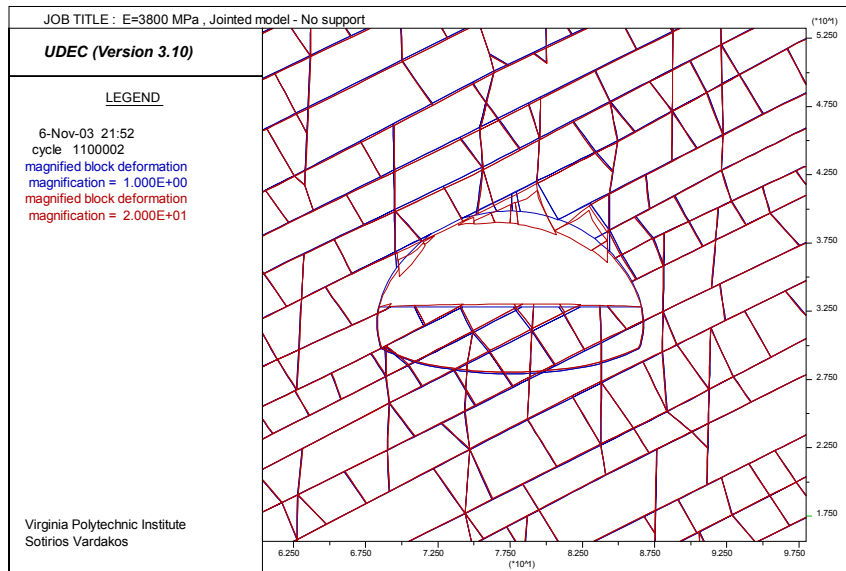


Figure 8.2: Comparison between initial and deformed fracture network (x20) at 100% relaxation of top heading in E=3800 MPa bedded sandstone.

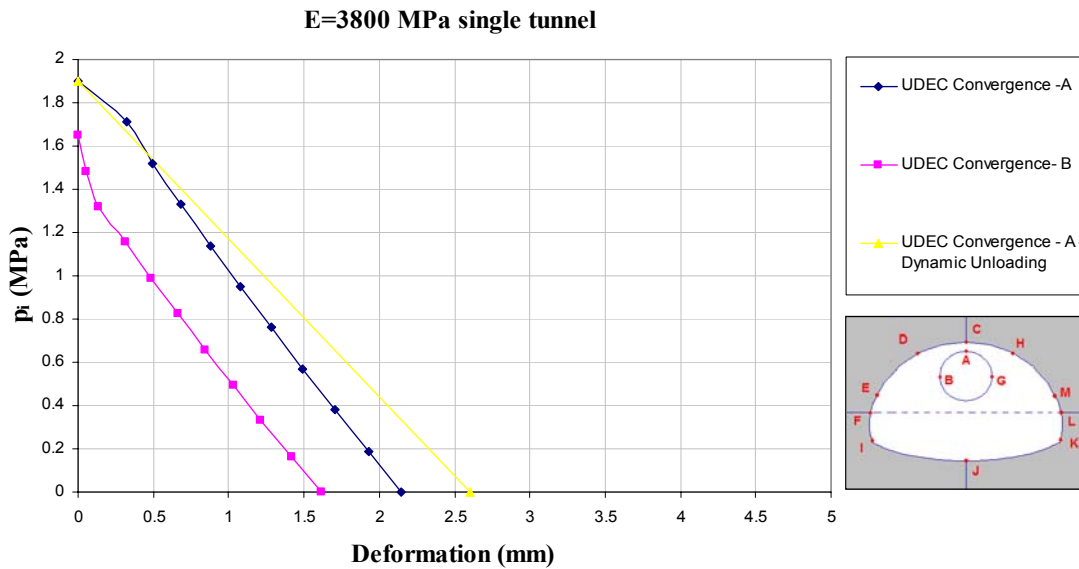


Figure 8.3: Convergence curves of pilot tunnel, using E=3800 MPa.

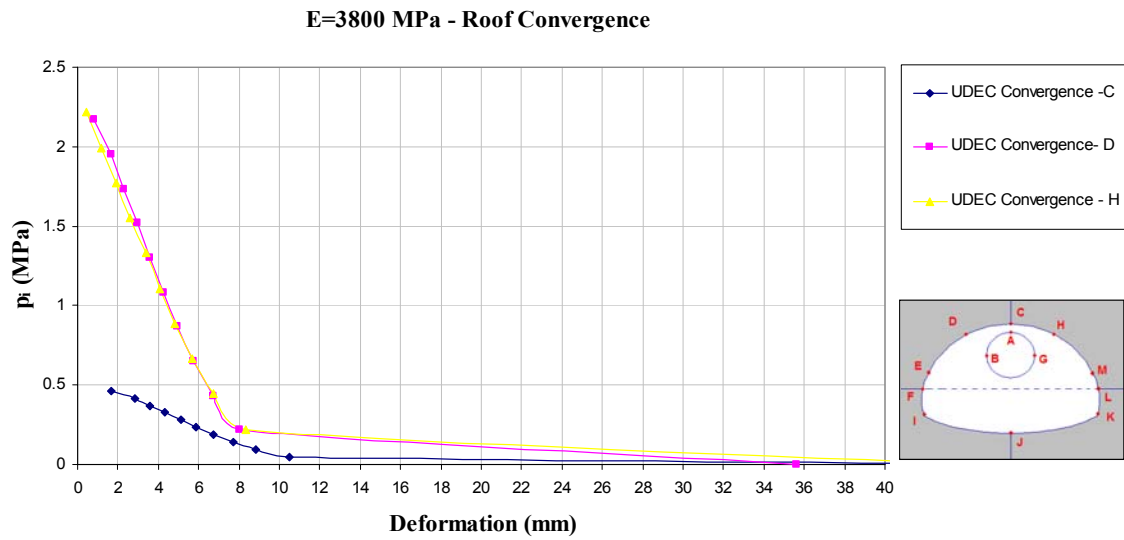


Figure 8.4: Convergence curves of top heading roof, assuming  $E=3800$  MPa.

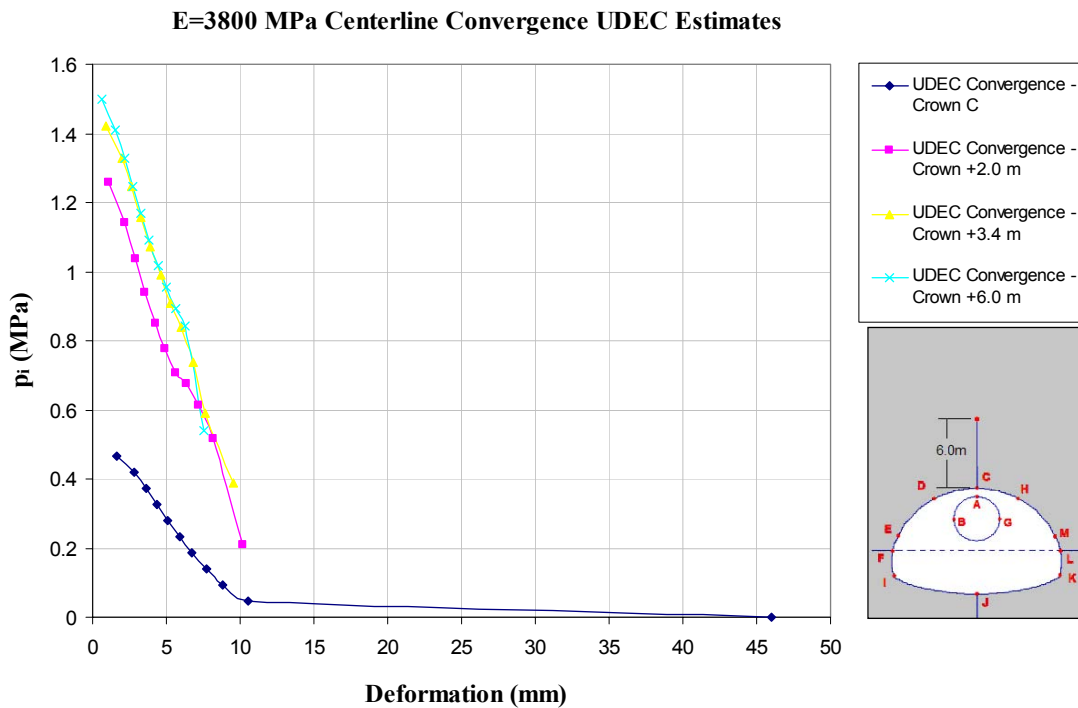


Figure 8.5: Convergence curves at 2.0, 3.4 and 6.0 m above the crown of top heading stage, by using  $E=3800$  MPa.

From the results it becomes apparent that the reduction of the block elastic modulus has as an effect the increase of all deformations and in specific an increment in the order of 2.0 mm before the critical support pressure is reached at the tunnel roof boundary. However even for high relaxation factors the desired range of deformations is not predicted and therefore the model needs revision. Figure 8.2 which shows a magnification of the displacements reveals that even though the global elastic modulus was decreased, the developed strains normal to the bedding plane have drastically increased more than in any other direction. This effect supports that a trial analysis using a closer to actual bedding spacing, at least in the affected region close to the tunnel opening may improve the results more. For this reason a new model with manual refinements based on the recorded rock mass conditions, is constructed to further investigate possible effects.

### 8.2.2 Jointed model including localized refinement

In figures 8.6 and 8.7, representative results of the numerical analysis are shown, for the case of an unsupported discontinuous model, in which local refinements in the sandstone bedding have been made by assuming  $E_{\text{block}}=5000$  MPa. The new bedding spacing is in the order of  $s=1.45\pm 0.26$  m based on close inspection of the constructed network. More refinements were made to the left half of the tunnel thus introducing an artificial anisotropy in the model more compatible with measured deformation behavior. For this analysis, convergence curves were constructed for the top heading excavation and they are depicted in figures 8.8, 8.9. From figure 8.8 it is apparent that the bedding spacing reduction immediately affects displacements in the tunnel roof which are now less uniform. In specific point D located the at the left half roof, is expected to deform about 7.5 mm for a loss factor of  $\lambda=0.9$  while the symmetrical point H at the right of the tunnel shows deformations in the order of 5.8 mm for the same degree of unloading. Convergence recorded at points above the crown of the excavation shows irregular behavior which is however expected due to the increased fracturing and stress redistribution. From the constructed characteristic curves it becomes apparent that even with zero installed support, predicted maximum deformations are still lower than the

values recorded insitu. Thus subsequent advancements and alterations need to take place for a better fit of numerically predicted results.

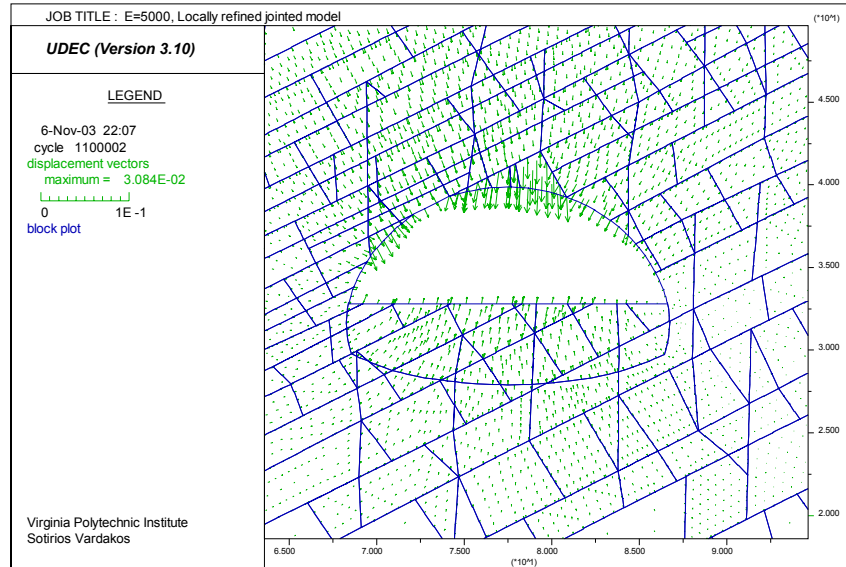


Figure 8.6: Total displacements for top heading excavation stage at 100% relaxation of locally refined jointed model assuming  $E=5000$  MPa.

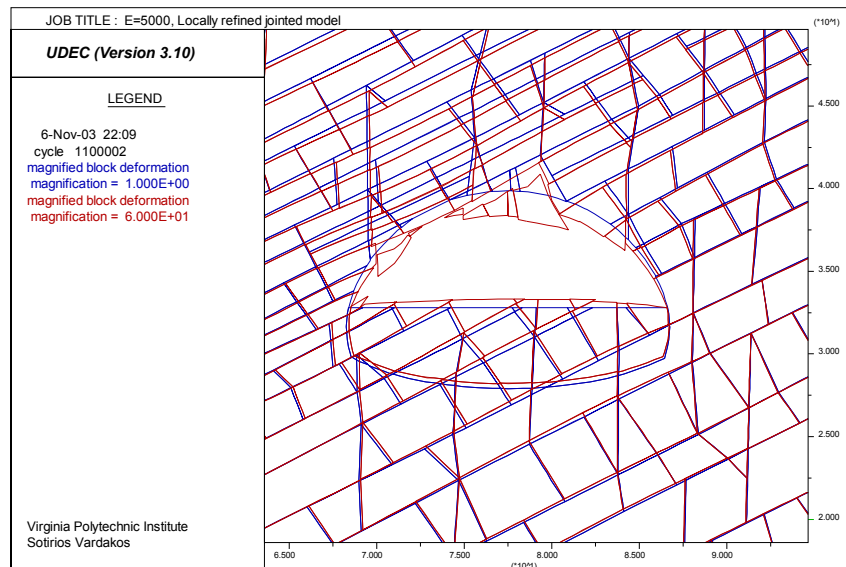


Figure 8.7: Comparison of initial and deformed fracture network (x60) at 100% relaxation of top heading in  $E=5000$  MPa closely bedded sandstone.

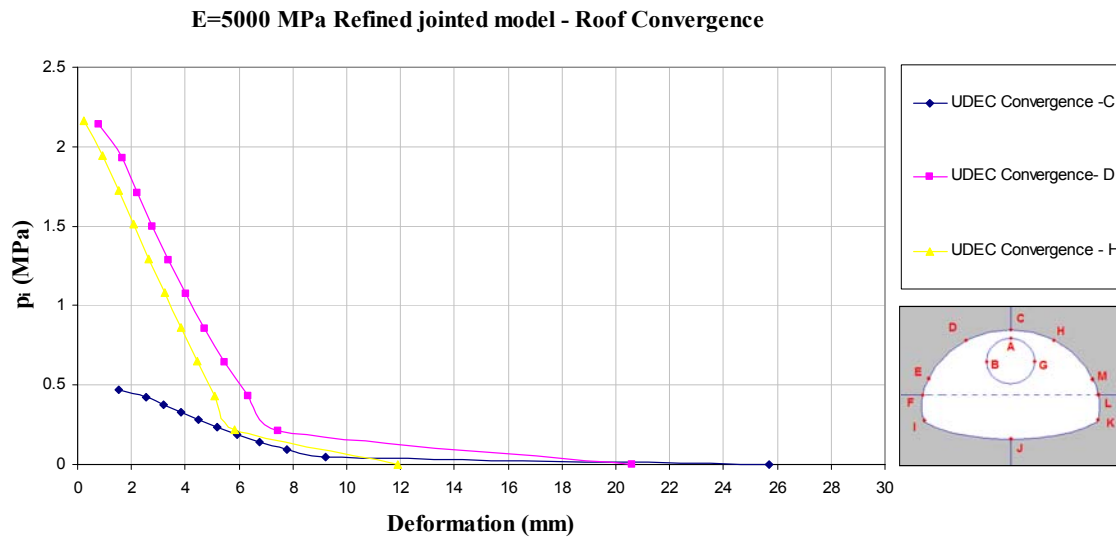


Figure 8.8: Convergence curves for top heading stage in locally refined jointed model. Point D located at the left of the crown exhibits more deformation in contrast to point H to the right, due to the effects of bedding induced anisotropy. This behavior is also recorded by onsite measurements from extensometers.

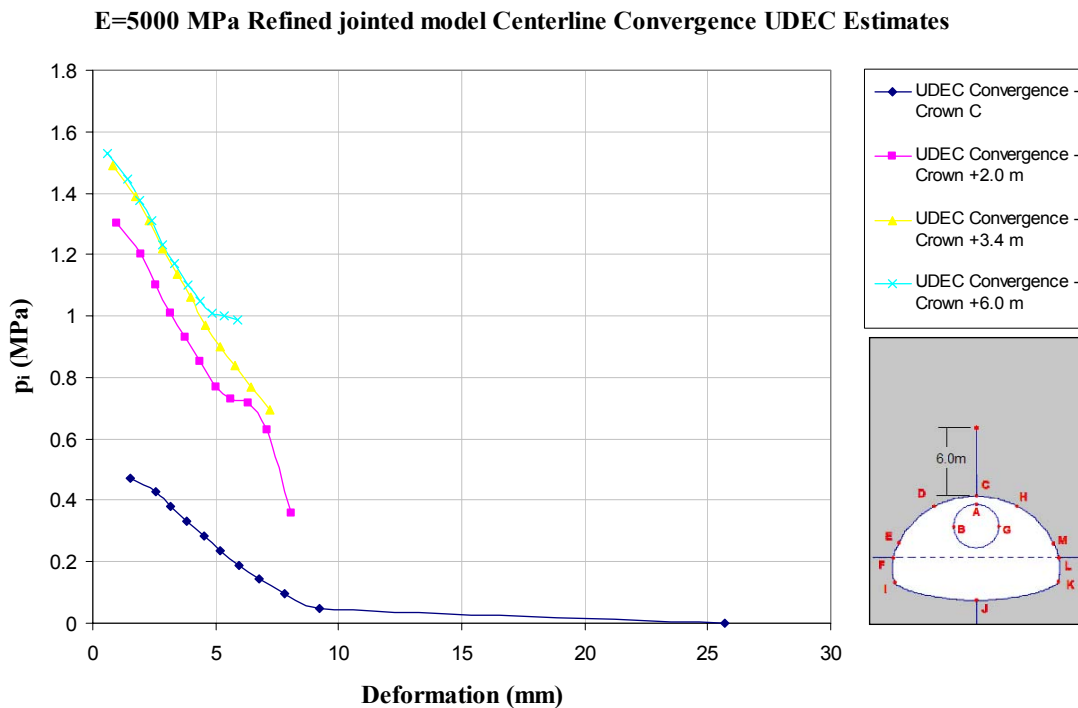


Figure 8.9: Convergence curves for top heading stage at three locations above the crown, for locally refined model.



### 8.2.3 Refined jointed model with $E=4300$ MPa block elastic modulus

A third back-analysis model was constructed, on the framework basis of the second by reducing the global elastic modulus to  $E=4300$  MPa. It was also considered to artificially assign higher stiffness values at certain unstable block surfaces (cross joint surfaces) close to the excavation boundary. This step does not alter the global behavior of the surrounding rock mass and is only conducted to prohibit highly irregular deformations during controlled unloading and assist in the construction of better convergence curves close to the boundary. Still the effects of the bedding induced anisotropy are included in the analysis as before, which is the key element in the present stress-deformation analysis. Interesting results from the analysis are shown in figures 8.10 to 8.12. In this case all deformations have been increased and there is a notable difference between the convergence of the left and right halve of the tunnel. Figure 8.11 shows a comparison of the initial and the deformed fracture geometry at full unloading with no support. It is evident that the predicted deformations even at a 100% of relaxation are lower than the recorded deformations after support installation, a fact which necessitates further back-analysis steps.

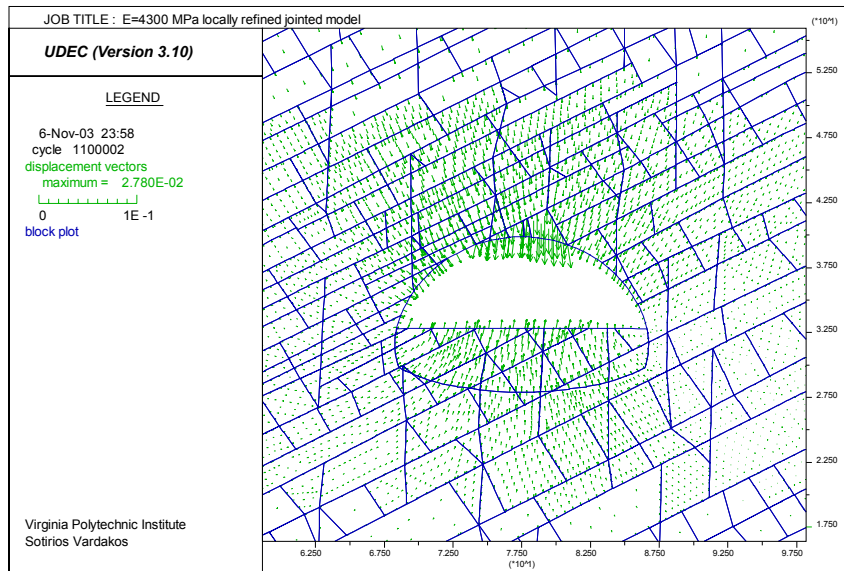


Figure 8.10: Total displacements for top heading excavation stage at 100% relaxation of locally refined jointed model, using Eblock=4300 MPa.

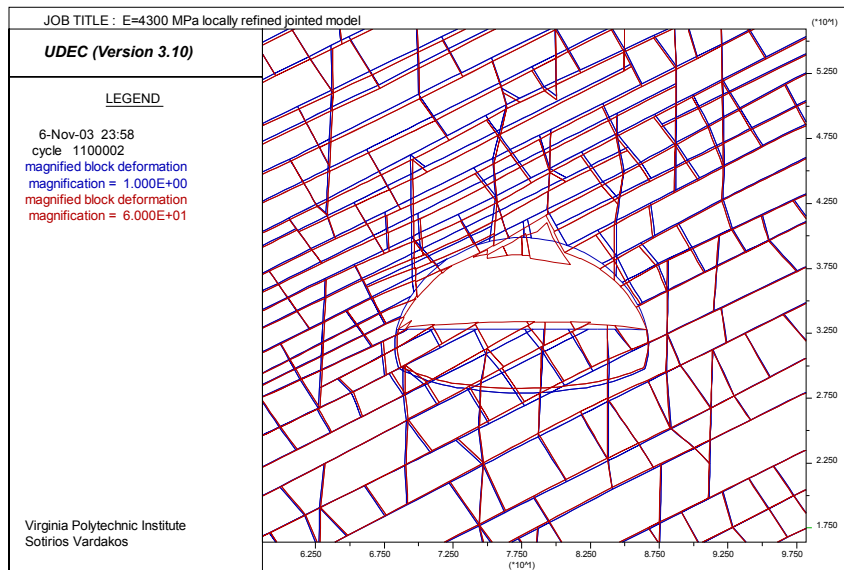


Figure 8.11: Comparison of initial and deformed fracture network (x60) at 100% relaxation of top heading in closely bedded sandstone assuming Eblock=4300 MPa.

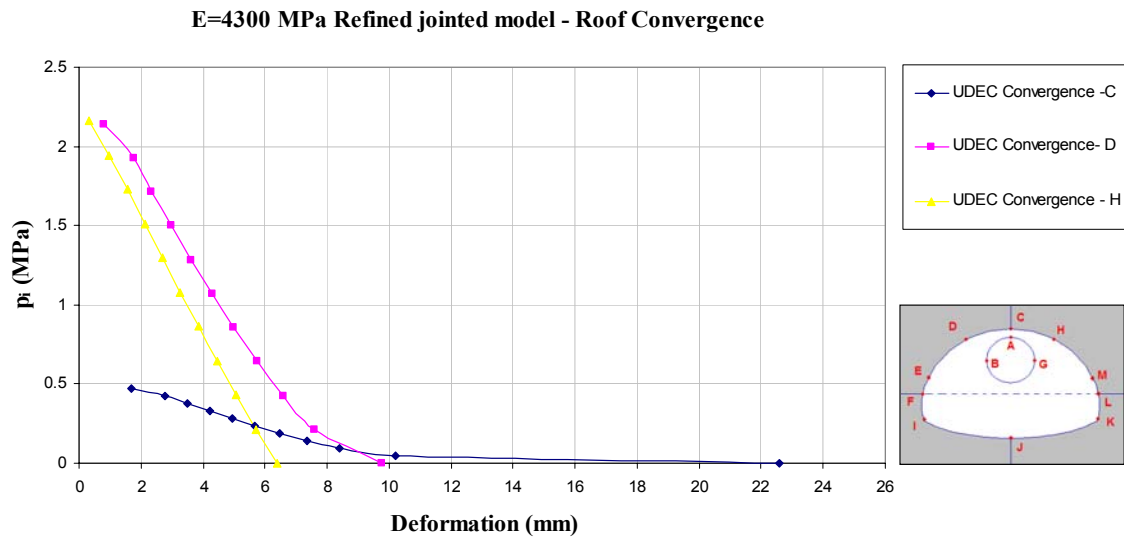


Figure 8.12: Characteristic curves for the top heading excavation in rock mass of  $E=4300$  MPa.

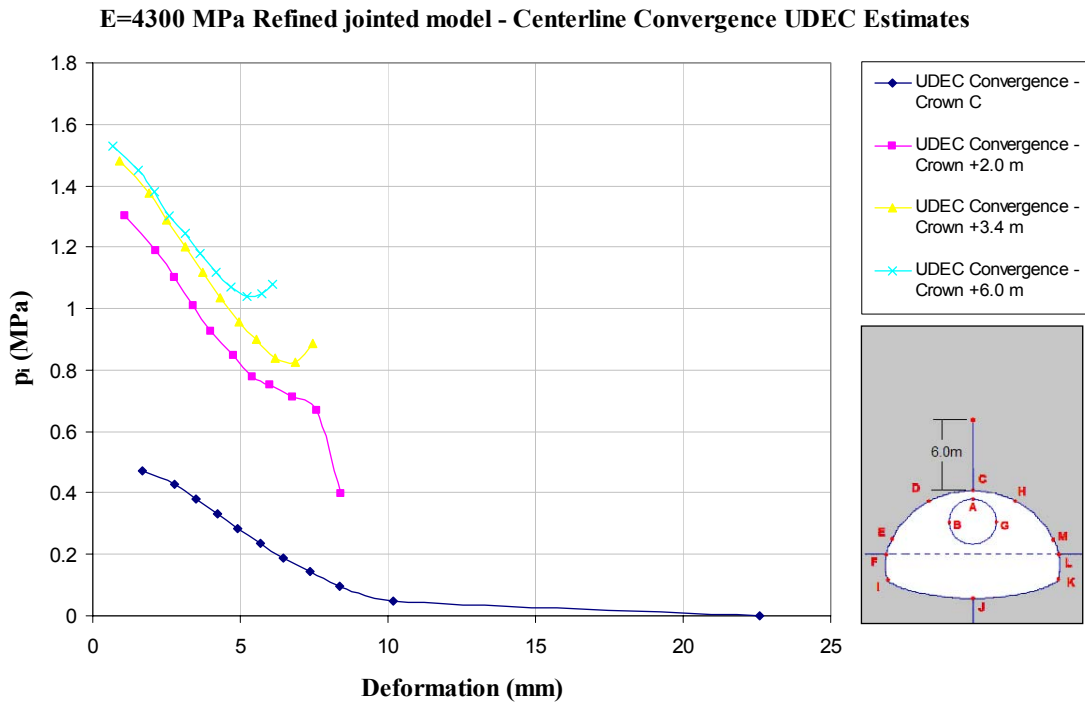


Figure 8.13: Approximate characteristic curves at the locations of 2.0, 3.4 and 6.0 m above the tunnel crown.

### 8.3 Final analysis with the distinct element and convergence-confinement methods

In this case a model based on the previous refined model was constructed and analyzed. From the previous analysis it became apparent that subsequent modifications of the geometry and the elastic properties of the bedded sandstone immediately affect the characteristic curves but the predicted maximum displacements were still lower than the measured ones. In order for the predicted displacements to reach the measured levels there can be two possible ways for addressing this. Either the fracture network has to be even more realistic to better represent the discontinuity features in the vicinity of the excavated region, or equivalently a reduction must be performed in the block elastic modulus so that more strain develops during the tunnel advance. For this analysis the second method is followed due to its computing efficiency advantage. A global elastic modulus of  $E_{\text{block}}=3000$  MPa was assumed, while certain cross joints in the vicinity of the boundary were assigned higher elastic properties since their existence was not verified by local measurement nor reported in geologic onsite report (Japan Highways, 1998).

On the basis of the above new convergence curves were constructed mainly for the excavation boundary at points C, D and H. Results of the controlled relaxation analysis are shown in figure 8.14. For this analysis it was assumed as in the initial model that the rock bolt support takes place approximately for a loss factor of about  $\lambda=0.5$ , while beam and shotcrete support is installed in one stage for a later loss factor of about  $\lambda=0.65$ . Once again the installation of the support systems is completed under dynamic cycling conditions and not during a numerically controlled deformation. From the convergence curves of figure 8.14 it is now obvious that maximum displacements have reached higher levels than previous analyses while at the same time the anisotropic behavior of the rock mass is evident. At 100% relaxation the left halve of the tunnel (measurement point D) converges by a final deformation of 12.5-13.0 mm, while at the right halve of the tunnel point H converges for a maximum of about 9.0 mm.

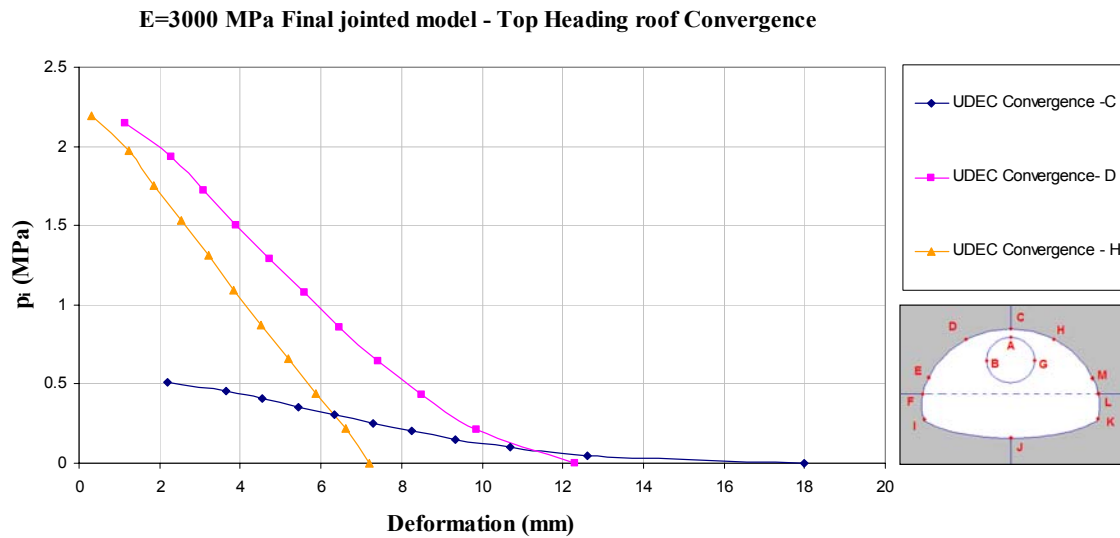


Figure 8.14 : Characteristic curves for top heading excavation assuming  $E_{block}=3000$  MPa.

A similar approach to the method followed in the initial  $E_{block}=5000$  MPa model was utilized here. The support was installed during the dynamic analysis at a cycle time estimated by tracking the deformations of three reference points of the roof (C,D,H) so that these can approximately match deformations for a specific loss factor  $\lambda$ , as recorded from the characteristic curves of figure 8.14. Assuming  $\lambda=0.5$  for the rock bolt installation the following deformations are compared and a decision is made for the necessary time delay:

Table 8.2 : Comparison table between results from convergence curves for  $\lambda=0.5$  and from dynamic UDEC solution during excavation, at two time points.

Method:	Crown (C)	Crown (D)	Crown (H)	Cycle time in dynamic solution
Convergence curves	7.6	5.78	4.5	
Dynamic Solution	6.6	6.94	4.9	5000
	7.9	7.8	5.4	6000

From the above table an interesting conclusion can be made. For a prescribed relaxation factor 0.5 the results of the controlled deformation analysis do not necessarily exactly match the results of the dynamic solution at any cycling time. Therefore only approximations for the required delay time can be made by utilizing the above method. More specifically it is apparent that the theoretical relaxation along the excavation boundary during the dynamic solution progress is not bound to be constant as theorized by the controlled deformation analysis and this is probably expressing the actual behavior of the rock mass. Therefore conclusions or decisions from table 8.2 must not be made in strict terms but some allowance must be given for related uncertainties. From the above an initial value of 5000 cycles is considered as a rational decision for a rock bolt pattern installed relatively close to the face. Similarly for a hypothetical relaxation factor in the range of  $\lambda=0.65$  a comparison presented in Table 8.3 can be made. From Table 8.3 it is derived that a cycle time of about 7000 cycles is required for an approximate loss factor of  $\lambda=0.65$  or an equivalent time of 2000 cycles needs to be executed by the code after the previous step.

Table 8.3: Comparison table between results from convergence curves for  $\lambda=0.65$  and from dynamic UDEC solution during excavation.

Method:	Crown (C)	Crown (D)	Crown (H)	Cycle time in dynamic solution
Convergence curves	9.3	7.2	5.7	
Dynamic Solution	9.1	7.7 – 8.7	5.9	7000

Results of the analysis are presented in figures 8.15 to 8.22. Before comparing the immediate total displacement results from the UDEC solution it is significant to recognize some factors contributing to these displacements and on the other hand to acknowledge when and where exactly did the recorded deformations start and when and where did they end. Figure 8.23 presents a simplified schematic representation of the measurement location.

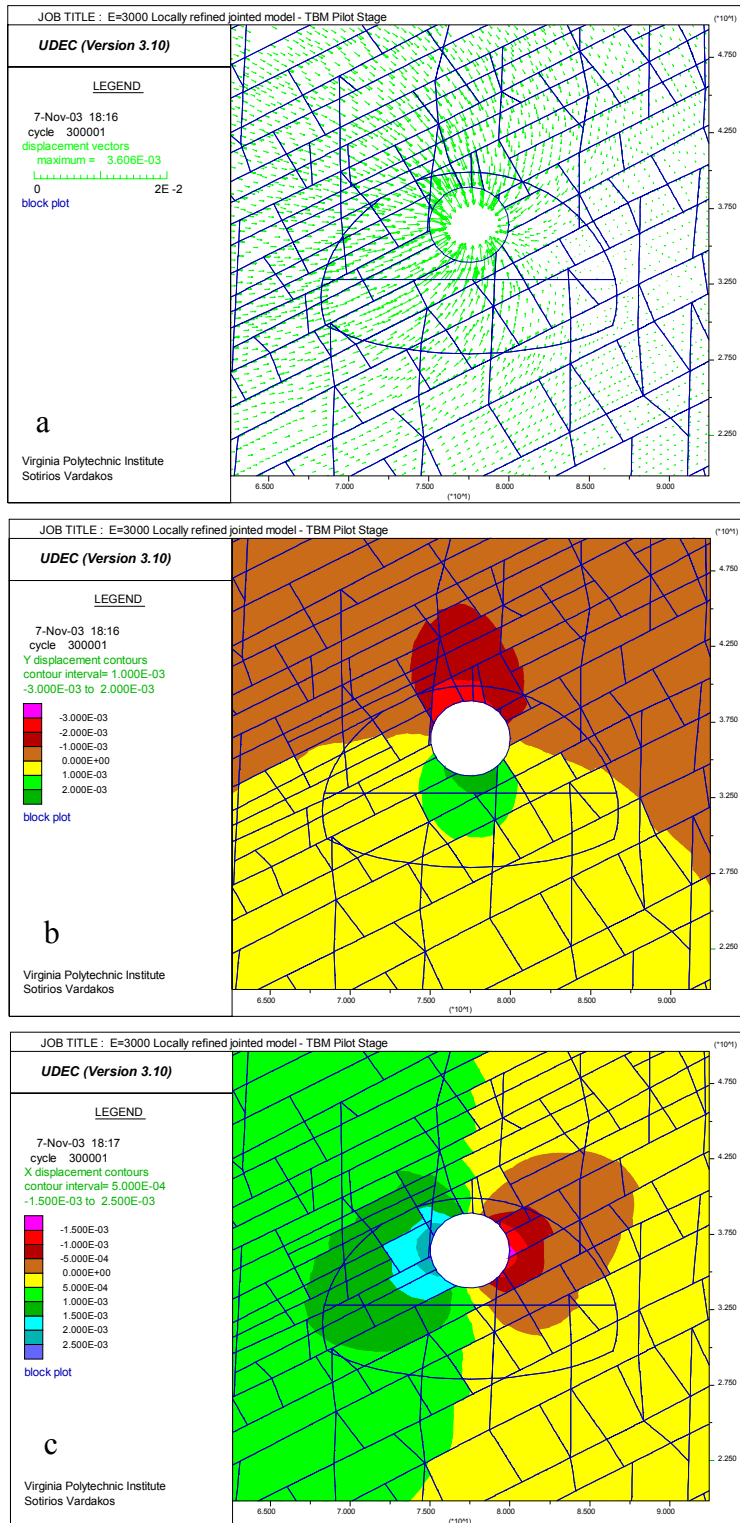


Figure 8.15: Results for pilot tunnel in 3000 MPa jointed model, a) Total displacements b) contours of vertical displacements, c) Contour plots of horizontal displacements.

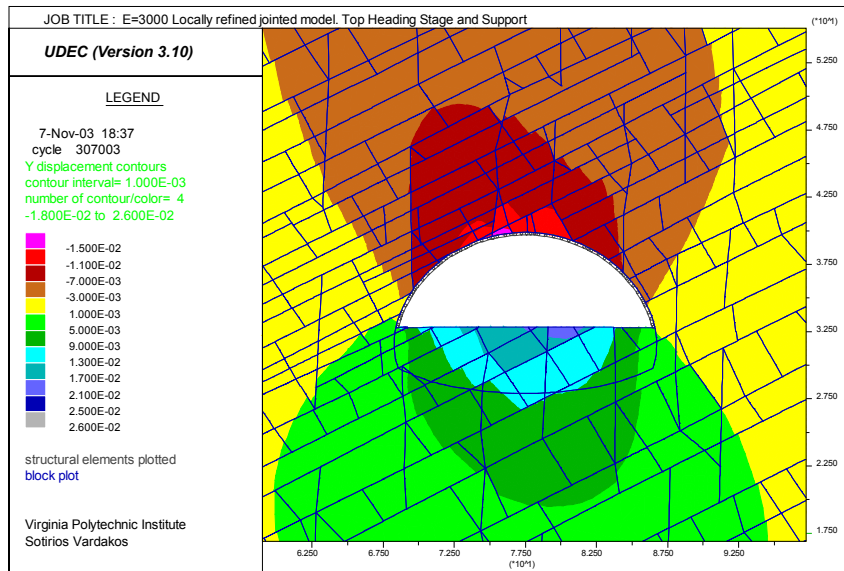


Figure 8.16: Shaded contours of vertical displacements after ground-support equilibrium for jointed model assuming  $E=3000$  MPa.

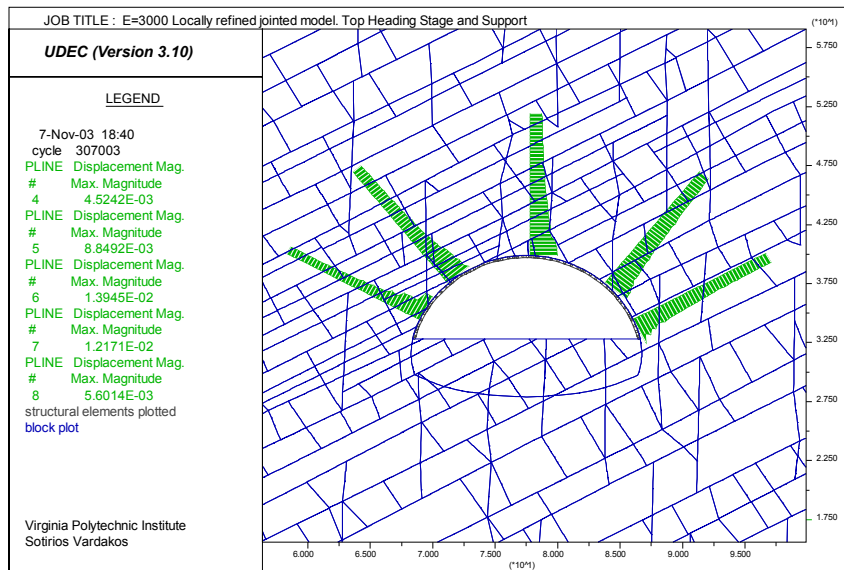


Figure 8.17: Predicted displacements along extensometer locations.



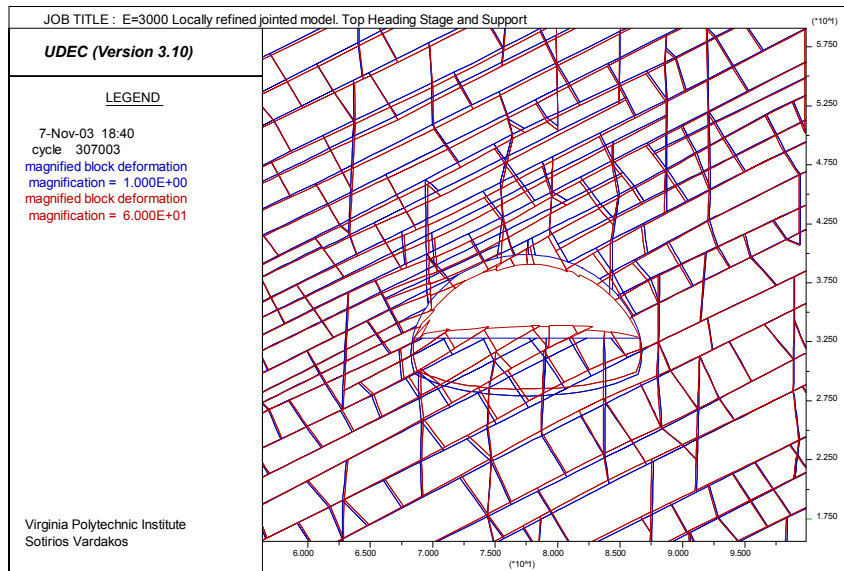


Figure 8.18: Comparison between original and deformed block assemblage (x60) at the end of top heading excavation and support for jointed model assuming  $E=3000$  MPa.

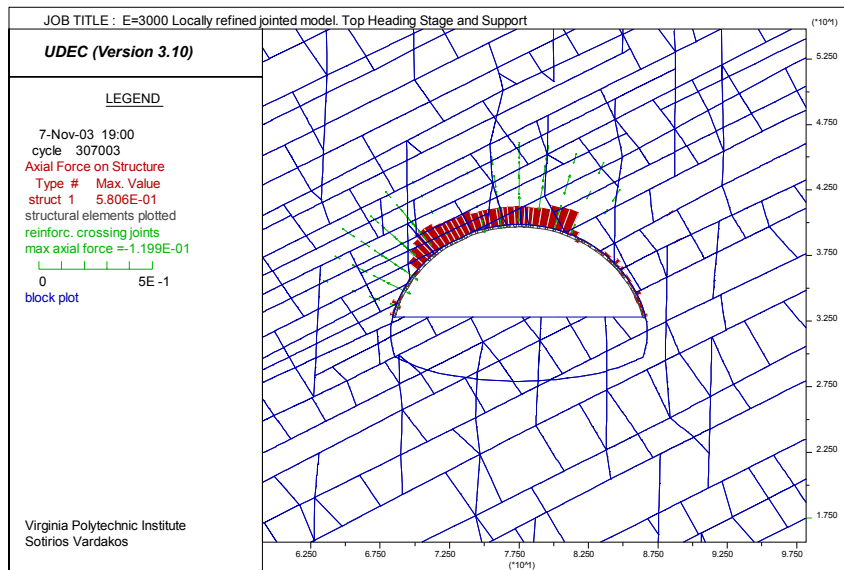


Figure 8.19: Distribution of axial forces on composite beam element and rock bolts axial forces (MN/m) for top heading.

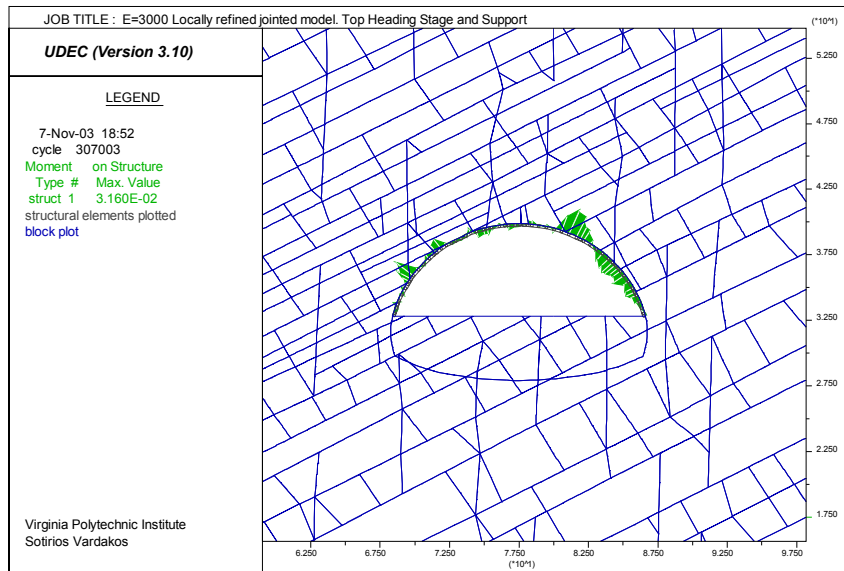


Figure 8.20: Distribution of bending moments on composite beam element simulating the primary lining (MN.m/m).

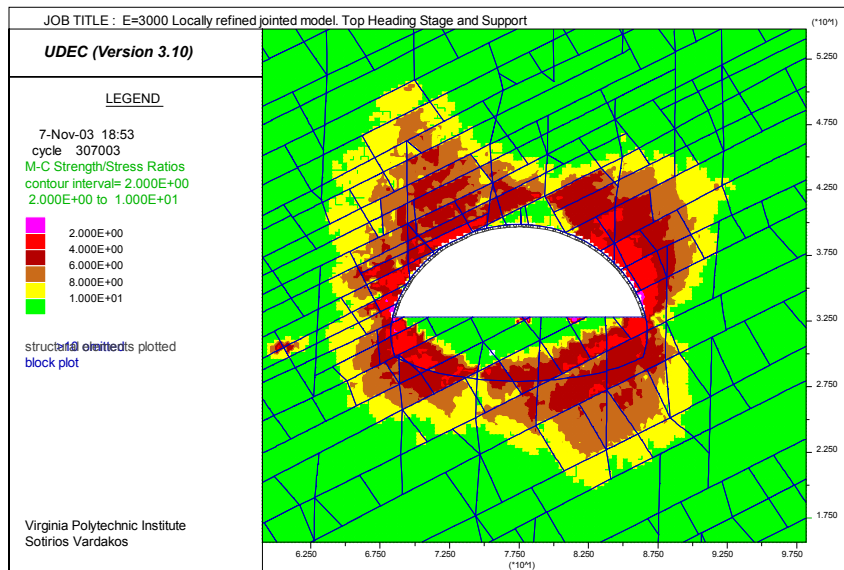


Figure 8.21: Mobilized shear strength around the tunnel at the end of top heading excavation stage and support.

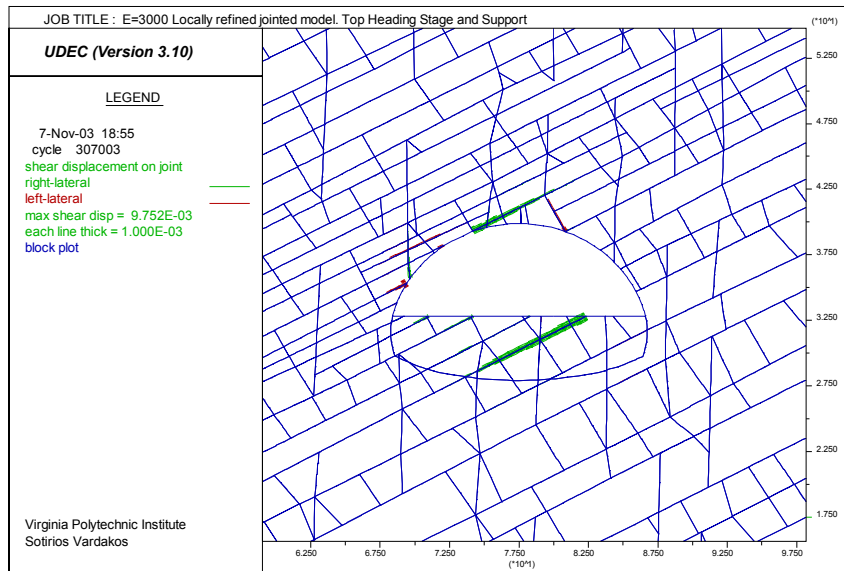


Figure 8.22: Shear displacements at the end of the top heading and support.

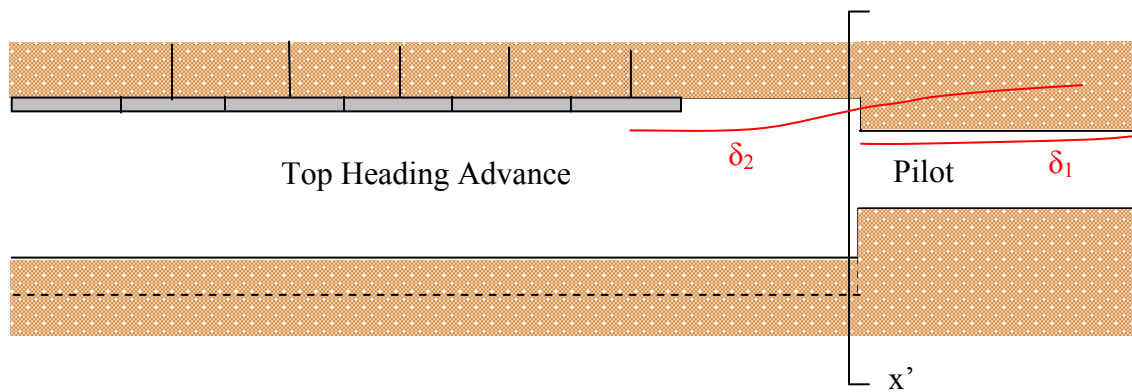


Figure 8.23: Schematic representation of measurement location and components of pre-convergence due to already completed excavation activity from the pilot opening and the proximity of the top heading.

Based on the available data monitoring equipment is installed at section xx' just after an excavation round of the top heading section. As always in this method the pilot tunnel has already been excavated. At section xx' before the monitoring equipment is installed, there have been two components of pre-convergence:

1. An initial amount of inward deformation due to the pilot tunnel excavation corresponding to 100% relaxation of the pilot opening since it was unsupported at the chainage STA 913+65.
2. An initial amount of pre-deformation at xx' due to the top heading advance.

There is also one more implication when it comes to extensometer measurements. These elements even though they can provide most valuable information with respect to strain development inside the rock mass, taken that they have been installed correctly, they may yield to lower measured deformations (i.e., at the excavation boundary) due to a simultaneous deformation towards the excavation room, of the fixed extensometer head at the end of the borehole. With respect to reflex target measurements, since they start from the same point where two components of boundary pre-convergence have occurred, then the values measured by the numerical code would need some theoretical correction as well. On the other hand the numerical analysis does not take these into effect and thus the finally predicted deformation results are calculated cumulatively from the history of all stages.

The only quantitatively correct way to investigate so complicate three dimensional effects is a dedicated three dimensional continuum or discontinuum model analysis, however unavailable in this case. An approximate correction is required in any case for the plane strain problem imposed here in order to be able to compare deformations on the same basis. It must also be recognized that reinforcement and support loads are correctly predicted by UDEC since their interaction with the system has only to do with deformations occurring after a relaxation factor of  $\lambda=0.5-0.65$ .

In order to remove these effects it was assumed that when the top heading excavation front reaches the station STA913+65 then it is assumed that in addition to

previous convergence due to the TBM excavated tunnel, there is an additional incremental convergence corresponding to an approximate confinement loss of  $\lambda=0.2-0.25$ , due to the three dimensional effect of the top heading advance. Both these deformations can be accounted by measuring the corresponding deformations at the locations of interest, at the second stage (assuming i.e.,  $\lambda=0.2$ ). Then by subtracting the pre-convergence values from the final values of excavation boundary deformation we can estimate true incremental deformation of the top heading that should be recorded by the geodetic surveying. For the extensometer measurements a third type of correction should also be included to account for the deformation of the fixed extensometer head. This deformation even if it is unknown as an actually measured magnitude, it can be estimated by the results of the numerical code.

Therefore by assuming an approximate top heading loss factor  $\lambda=0.2$ , exactly at the transition of the pilot tunnel to the top heading (measurement section) the deformations at the measurement boundary locations are measured. Past that point the incremental deformation of the extensometer heads, may be estimated by the difference between the total head deformation at  $\lambda=0.2$  and the final total head deformation at the state of equilibrium between the support and the rock mass. Quantitatively this can be expressed as:

$$\delta_{\text{extens.b}} = \delta_{\text{UDEEC eq.b}} - [\delta_{\text{UDEEC } \lambda=0.2.b} + (\delta_{\text{UDEEC eq.h}} - \delta_{\text{UDEEC } \lambda=0.2.h})] \quad \text{Equation 8.1}$$

where:

- $\delta_{\text{extens.b}}$  = excavation boundary deformation measured at extensometer locations (in situ monitoring data).
- $\delta_{\text{UDEEC eq.b}}$  = excavation boundary deformations predicted by numerical code at extensometer locations after final equilibrium with support.
- $\delta_{\text{UDEEC } \lambda=0.2.b}$  = excavation boundary deformations predicted by numerical code at extensometer locations during controlled relaxation analysis, for  $\lambda=0.2$ .
- $\delta_{\text{UDEEC eq.h}}$  = deformation at location of extensometer head at state of final ground-support equilibrium.

- $\delta_{\text{UDEC } \lambda=0.2. h}$  = deformation at location of extensometer head, for loss factor  $\lambda=0.2$  (state of transition between pilot tunnel and top heading).

Based on the above assumptions the total values of deformation are included in Table 8.4 along with the corrected values. From the results becomes apparent that generally there is a relatively good overall agreement between predicted and measured displacements. Some minor differences may have also been due to the fact that the original design incorporated two temporary low height buttresses at the foundation levels so that stresses redistribute more favorably.

In more detail and with respect to convergence at crown location C the numerical code gives a total displacement in the range 12-18 mm, and a corrected extensometer maximum deformation of 10.2. Multipoint extensometer G1 has recorded a relative deformation in the range 14-15 mm. Point D is relatively good agreement already with an approximately corrected boundary deformation of 9.3 mm versus 13 mm indicated by three dimensional surveying. Deformations under the same practically geotechnical conditions (figure 6.52) show that the convergence for the section STA 914+10 is about 9.0 mm. Point H at the tunnel roof presents the most contradicting values in terms of measurement. Extensometer data have recorded a maximum of 3.0 mm of displacement while three dimensional surveying by total station has shown almost 12 mm of displacement. Based on the corrections the extensometer deformation is about 6.5 mm while the correction for the surveyed value gives about 7.1 mm. Generally such differences are logical and should be expected to some extent, and they are function of the measuring device or method accuracy, conditions and variables of measurement such as temperature, air moisture, dust or others. For the section STA 914+10 the corresponding deformation should be about 5.0-7.0 mm which is even closer to the predicted value. At the location of extensometer E4 the corrected displacement is about 0.9 mm which is practically the same as the measured relative deformation of 1.0 mm. At the location of extensometer E1 predicted deformation after correction is about 6.7 mm while measured extensometer deformation is in the range of 8.0 mm. Finally the

deformations at location E3 are predicted by UDEC to be in the order of 3.6 mm while actual measurements recorded 3.0 mm.

Therefore based on the assumptions and approximations regarding the approximate relaxation factors used for the analysis and especially considering some of the unknowns of the actual construction and unknowns regarding the rock mass properties or even the exact initial stress state there is a fair agreement of measured and predicted displacements.

The second parameter of the back analysis would be the predicted rock bolt axial forces. It is shown that the general trend of low axial loads at the right half and higher axial loads to the left half of the tunnel has been successfully captured. This coupled with the anisotropic behavior can be regarded as a rational result. It should also be recognized that attempting to entirely simulate the actual tunneling conditions may be a difficult if not impossible target to succeed, nevertheless important facts concerning the load distribution and development in the reinforcing elements are well proved. Accepting some rational allowance for the interpretation of the rock bolt loads it is predicted that some elements are highly stressed, as it has been documented by the monitoring data (figure 6.54g). At the location of measurement anchors R3 and R4, predicted axial loads by UDEC are slightly overestimated while in location R1 the numerical solution predicts a maximum load of approximately 0.137 MN while the measured value is in the order of 0.039 MN. This difference most probably can be attributed to an apparently unstable block tending to move downwards in the UDEC model. The uniformity of figures 6.54c and 6.54f suggests that that specific block may not truly exist and thus the actual rock bolt force can be lower. Despite this fact the rock bolt forces to the left of the tunnel even at a level close to the temporary working level, are reasonably close to the measured values. In general, as outlined in paragraph 6.7.2 attempt of the back analysis to nearly match rock bolt displacements is impractical since the number of unknowns is increased, and main uncertainties with factors such as the fracture geometry or the installation quality of rock bolts are parameters difficult to simulate explicitly.

Because of the limitations of the numerical model used to simulate a composite support member (using the Timoshenko beam theory) and the unknown actual interaction between the two components, the shotcrete lining and the steel members the results should not be evaluated explicitly. However results of the analysis record high axial loads in the general range of the monitoring data. From figure 8.19 it becomes apparent that most critical loads develop mainly at the left halve of the tunnel roof, while in figure 8.20 it is shown that the maximum bending moment of  $3.2 \cdot 10^{-2}$  MN.m/m develops close to the location of point H. In that area the beam element received more shear loads from the rock mass, since the rock bolts are not receiving high loads due to less jointing intensity. To this phenomenon also contributes the formulation of the rock bolt reinforcement of UDEC 3.1, according to which rock bolts can pick up axial loads only when intersecting deformable joints, as opposed to various finite element or finite difference numerical codes that calculate the deformation of the reinforcement based on interaction with a continuum host medium.

Figures 8.24-8.33 present the tunnel deformations, and support system loads after the completion of the bench excavation. Data for this analysis were not available thus this is included only for illustration purposes. For this stage it was assumed that the rest of the excavation is completed in one stage (bench and invert are treated as one excavation) and support in the means of rock bolts and shotcrete-steel beam primary lining are executed in short time after some relaxation of the model to simulate a short delay. As far as the lining is concerned the original design specified that the steel and shotcrete support ends at the foundation level (elephant foot) while the invert and final lining is one member is composed of 30 cm thick reinforced concrete. In the analysis only a 30 cm concrete invert is simulated.

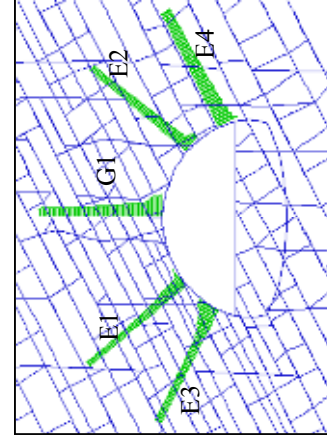


Table 8.4: Comparison between predicted results for top heading using UDEC and measurement data.  
E=3000 MPa refined jointed model.

Method	UDEC Solution			Onsite Measurements				
	Total/Corrected* Deformation (mm)	Rock Bolt Maximum load (MN)	Axial Force on Composite beam (MN/m)	Deformation (mm)	Rock Bolt Maximum load (MN)	Axial Force on Steel section (MN)	Axial Force in Shotcrete (MN)	
Crown (C)	15/10.5	(G1)	-	9.5	(G1)	-	-	
Crown (D)	12.4/9.3	-	-	13	-	-	-	
Crown (H)	8.9/7.1	-	-	12	-	-	-	
Ext. E4/R5	3.7/0.9	<0.01	11	1	0.013		0.137	
Ext. E2/R3	8.8/ 6.45	0.035	16	3	0.01	0.412	0.235	
Ext. G1/R1	13-18/10.2	0.147 (av.= 0.078)	47	14-15	0.042	-	0.255	
Ext. E1/R2	12.2/6.7	0.141	64	8	0.168	0.588	0.353	
Ext. E3/R4	5.6/ 3.55	0.141	15	3	0.108	-	0.196	

Note:

- E=Extensometer location, R= Measuring anchor location
- C, D, H onsite data are from 3D convergence surveying by Total Station.
- E1,2,3,4 & G1 data are from extensometer measurements.
- \* Correction is approximate based on assumptions regarding pre-convergence.



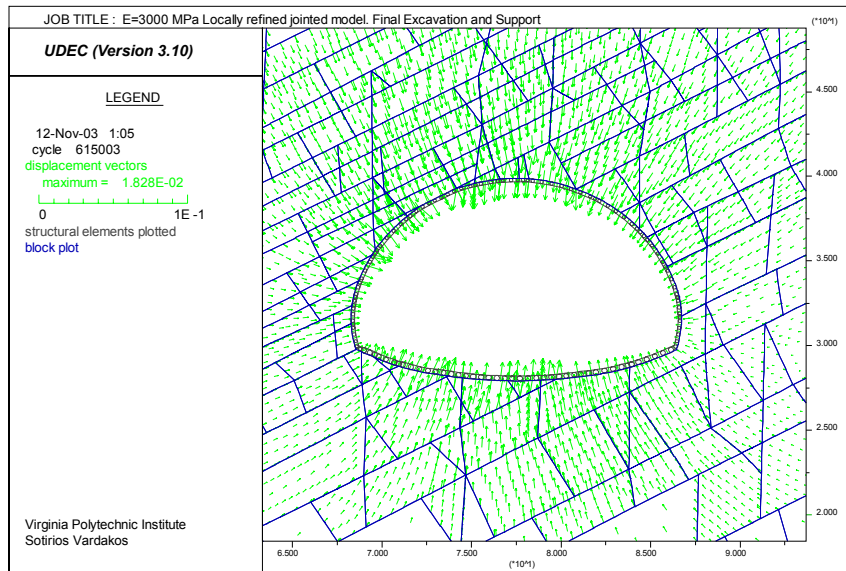


Figure 8.24: Total displacement vectors at the end of construction.

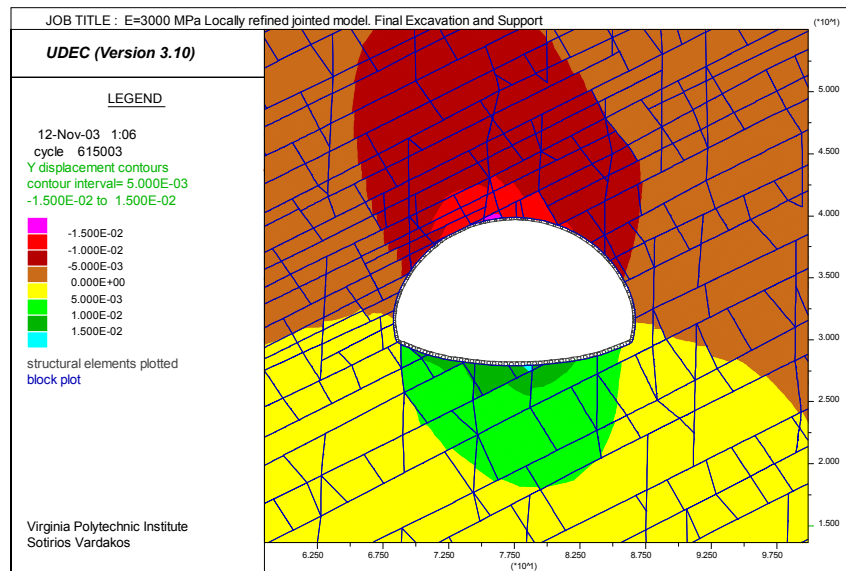


Figure 8.25: Shaded contours of vertical displacements at the end of construction.

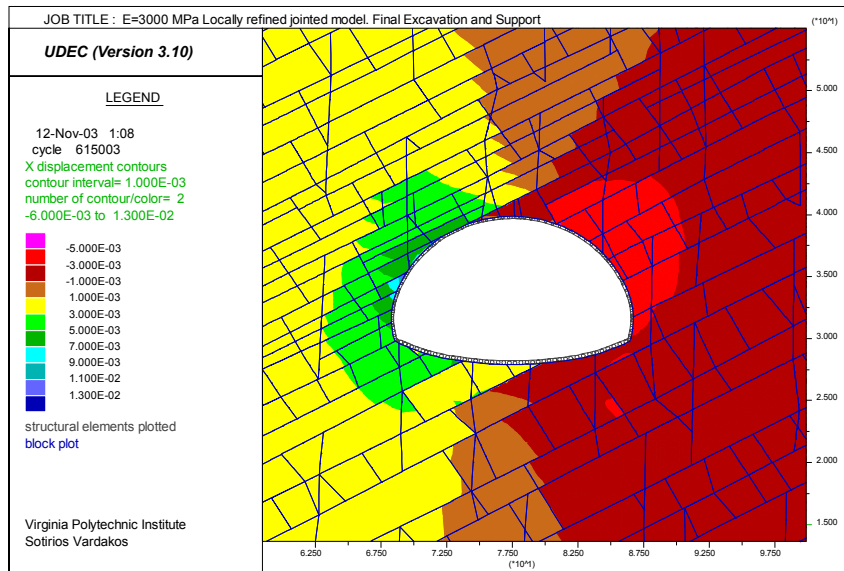


Figure 8.26: Shaded contours of horizontal displacements at the end of construction.

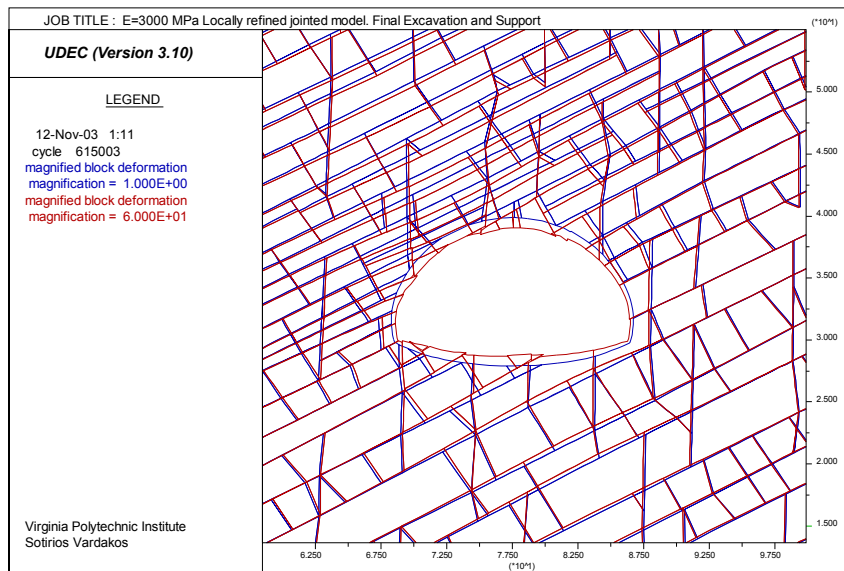


Figure 8.27: Comparison between initial and deformed block geometry after completion of excavation and support.

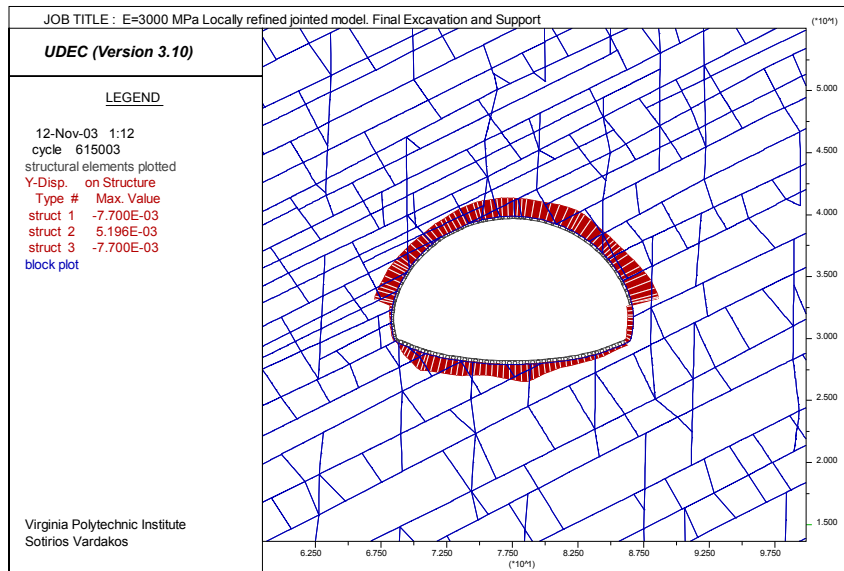


Figure 8.28: Vertical displacements (m) of composite beam element at the end of construction.

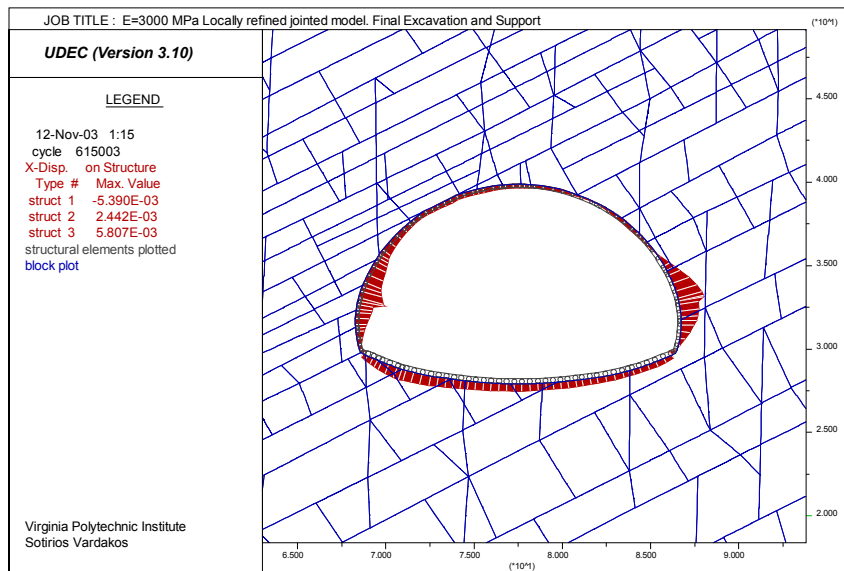


Figure 8.29: Horizontal displacements developed at the composite beam after bench excavation and support.

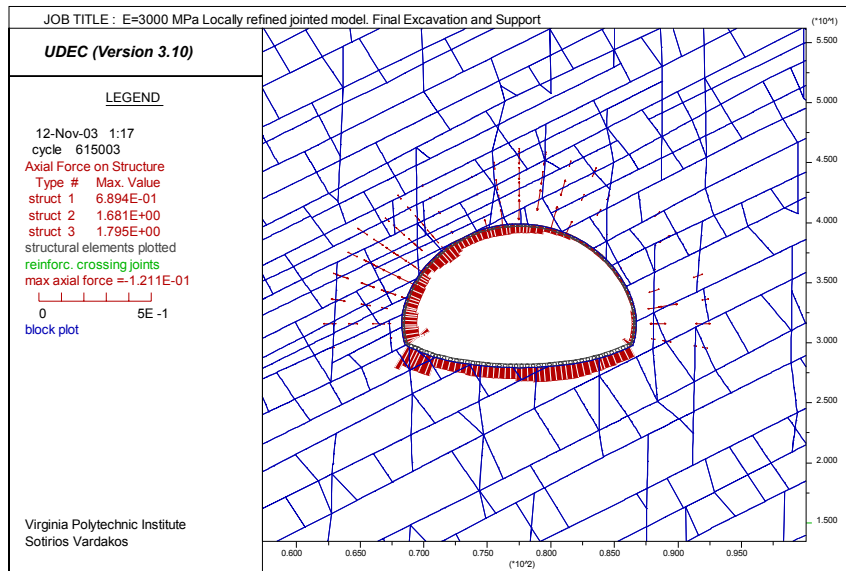


Figure 8.30: Axial loads in primary lining and rock bolts at the end of construction.

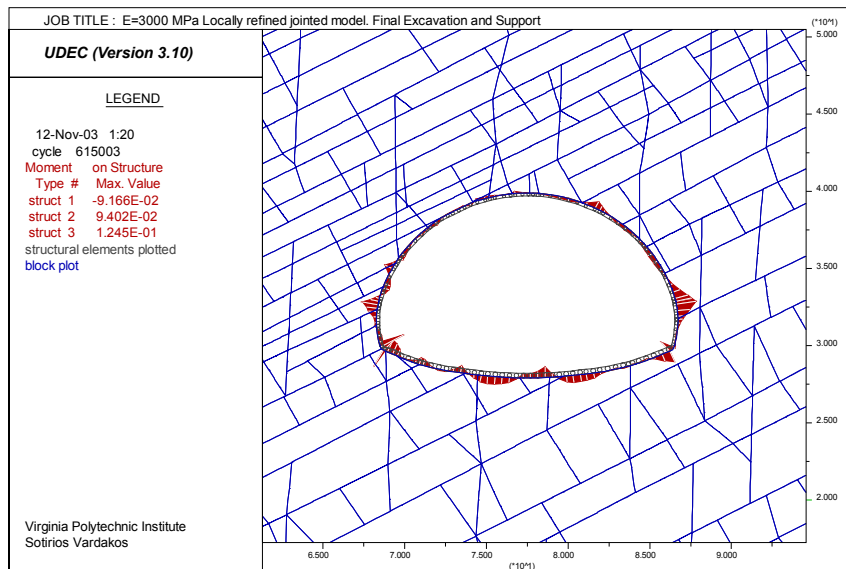


Figure 8.31: Moment distribution on primary lining and invert at the end of construction.

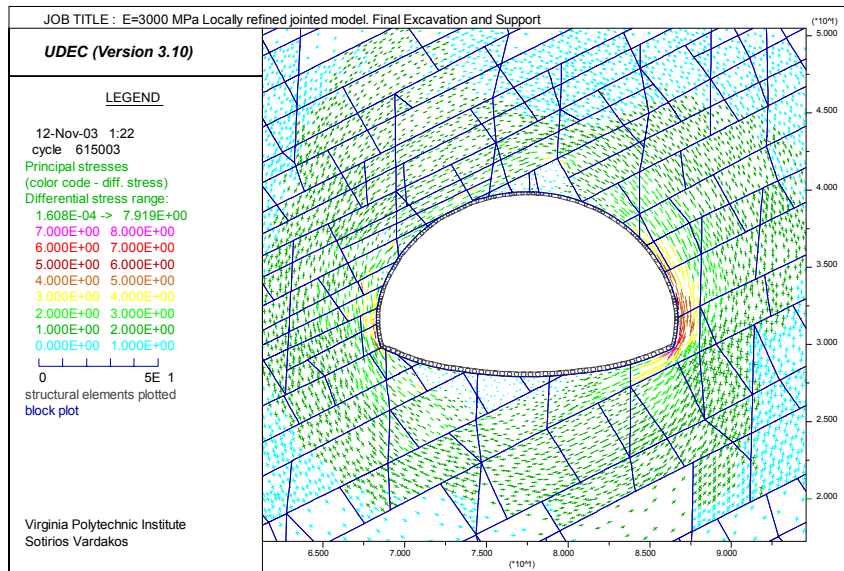


Figure 8.32: Deviator stresses around tunnel at the end of ground-support equilibrium.

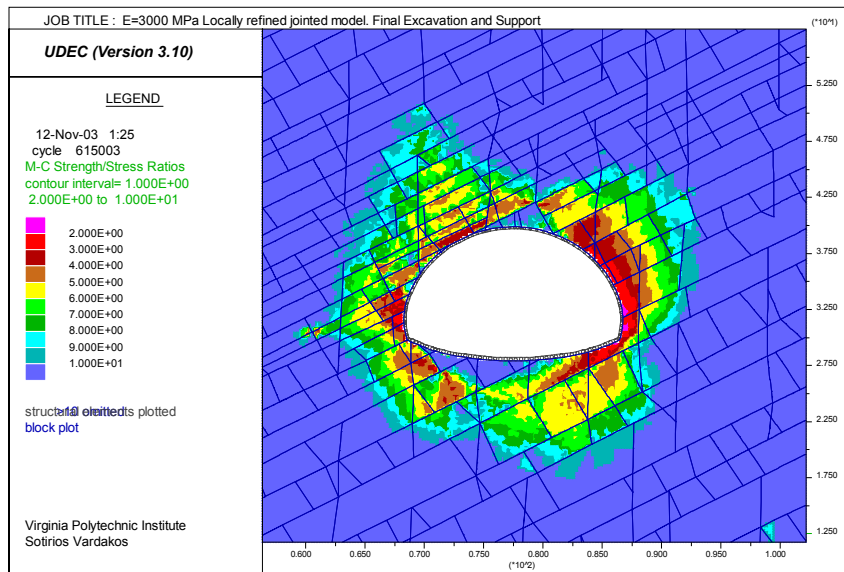


Figure 8.33: Shaded contours of strength/stress ratio around tunnel after final support and equilibrium. Only local failure should be expected at the elephant foot level of the tunnel.

## CHAPTER 9 : Summary and conclusions

In this project a series of analyses were performed to investigate results from the use of a two dimensional distinct element code (UDEC ver.3.1) and the correlation of predicted results with measured magnitudes of deformations and loads from the Shimizu tunnel No.3, part of the Tomei II expressway in Japan. The twin tunnels in the project had a length of about 1.1 km each and were sequentially excavated by the “TBM Pilot and enlargement method.” From the initial geotechnical investigations and reports as well as from previously performed numerical investigations, great discrepancies existed as far as some of the elastic properties of the rock mass were concerned.

In order to investigate and appreciate the general behavior of the unusually large span geometry, extending about 18.0 m laterally a series of parametric numerical analyses were conducted. Initially the numerical code UDEC was used to analyze full continuum models with no support installed. Parametric analyses were performed to examine the effects of :

- The Elastic modulus  $E_m$  of the rock mass.
- The in situ  $K_o$  ratio.
- The model boundary conditions.

From the initial parametric analysis it was concluded that the approximate range of probable elastic modulus values for the “Wadajima” sandstone that predominates in the area of interest, should be significantly lower to the predicted values from rock mass classification estimations. This range of low modulus values indicated a quality that was significantly lower than what anticipated by geologic investigations from the 5.0 m diameter pilot tunnel excavated by TBM. However due to the high degree of uniformity in deformations that the continuum models presented the decision was made to implement the numerical code UDEC and discretely model the influence of the predominant discontinuity features of the surrounding rock mass.

A base model initially designed at the Norwegian Geotechnical Institute (Barton & Gutierrez, 1995) was reconstructed using mean values of discontinuity spatial data, available from geotechnical investigations. The Barton-Bandis model was utilized to simulate the behavior of the discontinuities throughout the entire analysis.

The greatest limitation and challenge of the two dimensional plane strain analysis is to simulate a truly three dimensional problem such as a tunneling operation. The principle of characteristic curves (Fenner & Pacher, 1964) and the controlled relaxation method (Panet, 1986) was used. The quantitative expression of the method is more appropriate for more uniform tunneling problems and is usually applied in two dimensional continuum based finite element or finite difference codes. For this case it would be a challenge to construct “tailor made” characteristic curves without sacrificing the advantage of a discontinuous rock mass.

Due to the multi-parametric character of the problem a series of parametric analysis was performed to examine the influence of different parameters in the characteristic curves.

These parameters included:

- Relative position of the tunnel to the most affecting discontinuity feature (sandstone bedding).
- The parameter  $JRC_o$ .
- The parameter  $JCS_o$ .
- The parameter  $\phi_r$ .

Results of the analysis revealed that there is not significant variation in the convergence curves for the first three parameters. The simultaneous change in the initial discontinuity aperture value along with the  $JRC_o$  and  $JCS_o$  parameters tends to counteract the changes due to the change in the shear strength parameters alone. Assuming an initial global block elastic modulus of  $E=5000$  MPa, statistical change in the residual friction angle tends to influence more the convergence curves as the reduction of the friction angle by one standard deviation of its mean value causes an increment of maximum deformation at the unsupported pilot tunnel of about 4% and an increment of 21.4 % at the top heading crown convergence at 90% of relaxation.



Increase of the residual friction values for the two major discontinuity sets causes reduction of the pilot tunnel roof deformation by 8% and a reduction of the top heading deformation by 9.8% at 90% of stress relaxation.

After establishing the sensitivity of the convergence curves on the Barton-Bandis model parameters, a complete ground-support interaction analysis was initially performed in UDEC along with the convergence-confinement method, yielding to results in disagreement to the measured ones.

Further analyses were made on different types of models, involving reduction in the elastic properties but also involving local refinements in the fracture network. From the analysis it was concluded that refinement in the 280 dipping sandstone bedding, resulted in much closer results to the measured displacements. The measurements indicated a great degree of anisotropy in the rock mass and the subsequent trial analyses in UDEC were based on this behavior.

Finally a distinct element model was constructed, incorporating close refinements in the bedding spacing but also a reduction in the global elastic modulus was made and a value of  $E=3000$  MPa was chosen. For this model a relatively good agreement resulted between the predicted displacements and the measured results. Back analysis can be considered to be successful since it was able to capture the non-symmetric deformation due to inherent anisotropy in the rock.

The analysis showed that two general guidelines should be followed and executed with extreme caution when using the distinct element method:

1. Analysis must incorporate well chosen relaxation factor to account for three dimensional effects in a plane strain model. Even though the general assumptions of the method include some limitations (i.e., circular or near circular excavations, isotropic rock mass and isotropic stress conditions) the method can be applied in such cases with caution. The major limitation of the controlled relaxation analysis is that in order to construct the convergence curves, the same relaxation factor is

assumed for the model. This fact may not necessarily be true especially for a tunnel section geometry deviating from the circular model.

2. The distinct element modeling will result most of the times at rock block failures inside the excavated space. If these local failures are not extended, i.e., do not result in great geometry changes in an unsupported tunnel analysis, then they do not affect the general redistribution of stresses and the natural arching of the model. Furthermore their existence or not is a matter of statistical analysis and could also be treated in conjunction with an approach such as the Keyblock Theory (Goodman & Shi, 1984), unless specific geological data exist to manifest their locations and existence. For a stress redistribution analysis involving simultaneously the convergence–confinement method, local failures should be avoided so that better convergence curves can be obtained for locations at the boundary of the excavated region, by controlled relaxation. Therefore in this analysis what is most important is the stress-deformation response of the tunnel and not the local, structurally controlled failure modes.

The proposed method can be beneficial for cases where plane strain simulations of ground-support interaction analysis are needed to verify the support requirements in a timely manner. More advanced three dimensional numerical codes, which are able to simulate discontinuous masses are certainly an excellent design tool in underground engineering and can be more advantageous in cases where the tunnel heading may not be sub-parallel to the strike of the joint sets. However, increased technological requirements for this method, promote the two dimensional distinct element simulations coupled with the convergence-confinement method, for back analysis purposes.

From the above analysis it was concluded that the true rock mass quality should be quite lower than what had been interpreted before the tunnel excavation. As was shown in chapters 3 and 6 initial estimations of the average rock mass modulus showed a range of 5.0 – 9.0 GPa with the upper bound value mainly corresponding to harder sandstone in the central sector of the tunnel. Reasons for which this reduction had to be made can be the following:

- Rock mass classification performed from the TBM pilot tunnel includes the danger of overestimating the quality of the rock due to the highly regular excavation section and the minimal disturbance that these machines usually cause to the host rock.
- The initially estimated rock mass either by the pilot tunnel or by borehole logging or even from geophysical data interpretation, can be downgraded as the enlargement sections of the tunnel are excavated by drill and blast.
- Finally it is always possible that the location of certain unfavorable ground- geologic conditions (highly weathered regions, clay bearing zones e.t.c) may not always be known for the vicinity of the tunnel before the main excavation takes place.

For all the above reasons, the importance of driving the tunnel by frequent monitoring and good interpretation of results should be employed especially in cases of poor quality rock masses. This type of “Observational method” (i.e., NATM) even though imposes a further economic addition to a project budget estimate, if applied correctly by the contractors can lead to a safe work in long term and lower budget overruns usually experienced in most tunnel projects.

## REFERENCES:

1. Bandis, S., Lumsden, A.C., Barton, N., "Experimental studies of scale effects on the shear behaviour of rock joints," Norwegian Geotechnical Institute, Publication No.:162, Oslo, Norway, 1986, pp. 1-21.
2. Barla, G., "Tunnelling under squeezing rock conditions," Department of structural and geotechnical engineering, Politecnico di Torino, 2001.
3. Barton, N., "Some new Q-value correlations to assist in site characterization and tunnel design," International journal of rock mechanics and mining sciences, Pergamon Press, Vol: 39, 2002, pp.185-216.
4. Barton, N., Bandis, S., Bakhtar, K., "Strength, deformation and conductivity coupling of rock joints," Norwegian Geotechnical Institute, Publication No.:162, Oslo, Norway, 1986, pp. 1-20.
5. Barton, N., Chrysanthakis, P., "Shimizu Tunnel No.3 – Tomei II Highway Project. Preliminary NMT modeling using UDEC-BB, UDEC-S(fr) and 3DEC, with M=1 GPa and M=2 GPa deformation moduli," Norwegian Geotechnical Institute Report No: 951024-3/1, Oslo, Norway, 1996, pp. 1-34.
6. Barton, N., Grimstad, E., "Rock mass conditions dictate choice between NMT and NATM," Tunnels and Tunnelling, Issue: October 1994.
7. Barton, N., Grimstad, E., "The Q system following twenty years of application in NMT support selection," Österreichische Gesellschaft für Geomechanik, Felsbau 12, Nr. 6, Austria, 1994, pp.428-436.
8. Barton, N., Grimstad, E., "Updating of the Q system for NMT," Proceedings of the International Symposium on sprayed concrete-Modern use of wet mix sprayed concrete for underground support, Fagernes, Oslo, Norway, 1993.
9. Barton, N., Grimstad, E., Aas, G., Opsahl, O.A., Bakken, A., Pedersen, L., Johansen, E.D., "Norwegian Method of Tunnelling," World Tunnelling and subsurface exploration, Vol: June 1992, Mining Journal Ltd., London, United Kingdom, 1992.
10. Barton, N., Grimstad, E., Aas, G., Opsahl, O.A., Bakken, A., Pedersen, L., Johansen, E.D., "Norwegian Method of Tunnelling," World Tunnelling and

- subsurface exploration, Issue: August 1992, Mining Journal Ltd., London, United Kingdom, 1992.
11. Barton, N., Gutierrez, M., Løset, F., “Shimizu Tunnel No.3 – Tomei II Highway Project. Application of Q system, UDEC-BB and NMT principles to Shimizu Tunnel No.3 design – Phase I,” Norwegian Geotechnical Institute Report No: 951024-1, Oslo, Norway, 1995, pp. 1-56.
  12. Bieniawski, Z.T., “Engineering rock mass classifications”, John Wiley and Sons, Pennsylvania, USA, 1989, pp.29-95.
  13. Craig, R., “JTA reflects high level of activity,” World Tunnelling, Issue: August, 2002, Mining Journal Ltd., London, United Kingdom, 2002.
  14. Craig, R., “Okabe Tunnel on Japan’s largest motorway project,” World Tunnelling, Issue: November, 2000, Mining Journal Ltd., London, United Kingdom, 2000.
  15. Deffayet, M., Robert, A., “Dimensionnement et réalisation d’un tunnel à partir de mesures de convergence,” Tunnels et Micro-tunnels en terrain meuble – Du chantier à la théorie. Actes du colloque organisé à Paris, 7-10 February, 1989, Presses de l’école Nationale des Ponts et chaussées, Paris, France, 1989, pp.316-324.
  16. Einstein, H.H., Schwarz, C.W., Steiner, W., Baligh, M.M., Levitt., R.E, “Improved design for tunnel supports, Final Report” Report No. DOT/RSPA/DPB-50/79/10 for the U.S Department of Transportation, Department of Civil Engineering, Massachusetts Institute of Technology, Cambridge, Massachusetts, 1980, pp. 20-56,252-282.
  17. Golser, H., Schubert, W., “Numerical simulation in tunnelling,” Edited by Beer, G., Springer, Vienna, Austria, 2003, pp. 427-473.
  18. Goodman, R.E., “Introduction to Rock mechanics,” Second Edition, Berkeley, California, USA, John Wiley and Sons, 1989, pp. 257-270.
  19. Hoek, E., Carranza Torres, C., Corkum, B., “Hoek-Brown failure criterion – 2002 Edition,” 5th North American Rock Mechanics Symposium and 17th Tunneling Association of Canada Conference: NARMS-TAC, 2002, pp. 267-271.
  20. Hoek, E., Kaiser, P.K., Bawden, W.F., “Support of underground excavations in hard rock,” Balkema, Rotterdam, The Netherlands, 2000, pp.27-45, 48-54, 84-97, 152-161.

21. Institute of Civil Engineers, "ICE Design and practice guide: Sprayed concrete linings (NATM) for tunnels in soft ground," British ICE, Thomas Telford, London, United Kingdom, 1996, pp.6-13, 53-76.
22. Ishihara, Y., "Japanese tunneling and rock engineering," Norwegian Trade Council, Tokyo, Japan, 2002, pp.11-18, 29-32.
23. Itasca Consulting Group., "Universal Distinct Element Code (UDEC) User's guide," Minneapolis, Minnesota, USA, 2000.
24. Itasca Consulting Group., "Universal Distinct Element Code (UDEC) Verification problems and example applications," Minneapolis, Minnesota, USA, 2000.
25. Itasca Consulting Group., "Universal Distinct Element Code (UDEC) Theory and backround," Minneapolis, Minnesota, USA, 2000.
26. Itasca Consulting Group., "Universal Distinct Element Code (UDEC) Command reference," Minneapolis, Minnesota, USA, 2000.
27. Itasca Consulting Group., "Universal Distinct Element Code (UDEC) Fish in UDEC," Minneapolis, Minnesota, USA, 2000.
28. Itasca Consulting Group., "Universal Distinct Element Code (UDEC) Special features," Minneapolis, Minnesota, USA, 2000.
29. Japan Highway Public Corporation, "Second Tomei Highway: Analysis of tunnel loads for Shimizu tunnel No.3 and results of three dimensional FEM analysis," Vol: Expremental research phase, in Japanese, JHPC Tunneling division, Japan, 1998.
30. Japan Nuclear Cycle Development Institute., "DH12: Project to establish the scientific and technical basis for HLW disposal in Japan, Supporting report No.:2 Repository design and engineering technology," Ibaraki, Japan, 1999, pp. A.3.
31. Japan Society of Engineering Geology, "Rock mass classification in Japan," Engineering geology special issue, JSEG, Japan, 1992, pp.8-12.
32. Kavvadas, M., "Notes on design of underground works," course notes in Greek, National Technical University of Athens, Athens, Greece, 2000, pp 3.1-3.9, 4.1-4.15, 5.1-5.28.
33. Kovari, K., Lunardi, P., "On the observational method in tunnelling," ETH, Zurich, Switzerland, 2000.

34. Kulhawy, F.H., "Finite Element modeling criteria for underground openings in rock," *International Journal of Rock mechanics and Mining Sciences*, Vol: 11, Pergamon Press, United Kingdom, pp.465-472.
35. Lunardi, P., "The design and construction of tunnels using the approach based on the analysis of controlled deformation in rocks and soils," *Tunnels and Tunnelling International*, Issue: May, 2000, pp. 3-30.
36. Mahtab, M.A., Grasso, P., "Geomechanics principles in the design of tunnels and caverns in rocks," *Series for developments in geotechnical engineering No.:72*, Elsevier, Turin, Italy, 1992, pp.1-2, 11-14, 27-51, 52-87, 124-133.
37. Marinos, P., Hoek, E., "GSI: A geologically friendly tool for rock mass strength estimation," *Proceedings, GeoEng 2000*, Melbourne, Australia, 2000.
38. Martin, C.D., Kaiser, P.K., McReath, D.R., "Hoek-Brown parameters for predicting the depth of brittle failure around tunnels," *Canadian Geotechnical Journal*, Vol: 36, Toronto, Canada, 1999, pp. 136-151.
39. Miura, K., "Shimizu tunnel No.3 on New Tomei Meishin Expressway," *Challenges and changes: Tunnelling activities in Japan 1998*, Annual revised edition of the Japan Tunnelling Association, Tokyo, Japan, 1998, pp.13-14.
40. Müller, L., "The reason for unsuccessful applications of the New Austrian Tunnelling Method," *Proceedings of the International Tunnel Symposium*, edited by Kitamura, I., from the Japan Tunnelling Association., Pergamon Press, Tokyo, Japan, 1978, pp.67-72.
41. Nasri, V., Guimbal, F., Andre, D., Wone, M., "Verification of numerical analysis with monitoring data for the Magenta station of Paris Subway EOLE," *Proceedings of the Rapid Excavation and Tunneling Conference 2003*, Society for Mining, Metallurgy, and Exploration Inc., Littleton, Colorado, 2003, pp.894-904.
42. Nihon Doro Kodan - Japan Highway Public Corporation, "Annual Report, 2002," Tokyo, Japan, 2002, pp.7-15.
43. Norwegian Trade Council, "Shotcrete Technologies: The Norwegian Method of Tunnelling," Publishing Department NTC, Oslo, Norway, 1994.

44. Palmstrøm, A., "RMI a rock mass characterization system for rock engineering purposes," Dissertation for the degree Doctor Scientarum, Department of Geology, University of Oslo, Oslo, Norway, 1995, pp.6.4-6.36.
45. Panet, M., "Le calcul des tunnels par la méthode convergence-confinement," Presses de l'Ecole Nationale des Ponts et Chaussées, Paris, France, 1995.
46. Panet, M., "Recommendations on the Convergence-Confinement Method," Association Française des Travaux en Souterrain (AFTES), Online publication available in English at: <http://www.aftes.asso.fr/>, Paris, France, 2001, pp.1-10.
47. Romero, V., "NATM in soft ground: a contradiction of terms?," World Tunnelling, Issue: September, 2000, Mining Journal Ltd., London, United Kingdom, 2000.
48. Sauer, G., "Further Insights into the NATM: When an invention is something new: from practice to theory in tunnelling," 23<sup>rd</sup> Sir Julius Wernher Memorial Lecture, Online publication from Dr. Sauer Company available at [www.dr-sauer.com](http://www.dr-sauer.com), Salzburg, Austria, 2002.
49. Sauer, G., "In situ measurements," Online publication from Dr. Sauer Company available at: [www.dr-sauer.com](http://www.dr-sauer.com), Salzburg, Austria, 2002.
50. Sauer, G., "Instrumentation and its implications. DART section NC-1B, City Place Station, Dallas TX," Online publication from Dr. Sauer Company available at: [www.dr-sauer.com](http://www.dr-sauer.com), Salzburg, Austria, 2002.
51. Sauer, G., "Light at the end of the tunnel. The New Austrian Tunelling Method is beginning to carve out an excellent world-wide reputation," Online publication from Dr. Sauer Company available at: [www.dr-sauer.com](http://www.dr-sauer.com), Salzburg, Austria, 2002.
52. Schubert, W., "Grundlagen der NATM - Neue Österreichische Tunnelbauweise", in German, Publication No: 220.001, Institut für Felsmechanik und Tunnelbau, Technische Universität Graz, Graz, Austria, 1997, pp. 5-9, 31-43, 53-58.
53. Schwarz, C.W., Einstein, H.H., "Improved Design of tunnel supports: Volume 1- Simplified analysis for ground – structure interaction in tunneling," Report No. UMTA-MA-06-0100-80-4 for U.S Department of Transportation, Department of Civil Engineering, Massachusetts Institute of Technology, Cambridge, Massachusetts, 1980, pp. 90-104,143-165.



54. Sofianos, A.I., "Stabilization of underground openings," course notes in Greek, Department of Mining Engineering and Metallurgy, National Technical University of Athens, Athens, Greece, 2000, pp. A2.1-A2.5, D2.1-D2.2, D3.1-D3.5, D4.1-D4.18.
55. Sofianos, A.I., "Tunnel Excavation Techniques," course notes in Greek, Department of Mining Engineering and Metallurgy, National Technical University of Athens, Athens, Greece, 2000, pp.1.1-1.10, 5.1-5.15.
56. St. Marie, J., "Tunnelling: Mechanics and hazards," Online article available at: [www.umich.edu/~gs265/tunnel.htm](http://www.umich.edu/~gs265/tunnel.htm), University of Michigan, Michigan, USA.
57. Stine, J.K., Rosen, H., "Going underground, Tunneling past, present and future," American Public Works Association, Kansas City, Missouri, USA, 1998, pp. 68-70,86-88,90-97.
58. Swoboda, G., "Finite Element analysis of the New Austrian tunneling method," Third International Conference on Numerical Methods in Geomechanics, Aachen, Germany, 1979, pp.581-586.
59. Tsoutrelis, C., "Rock Mechanics - Part 1, Principle theories and experimental methods," Department of Mining Engineering and Metallurgy, National Technical University of Athens, Athens, Greece, 1985, pp.168-181.
60. United States Army Corps of Engineers, "Engineering and design: Tunnels and shafts in rock," Department of the Army, EM 1110-2-2901, Washington, D.C, USA, 1997, pp. 5.1-5.30.
61. Wanninger, R., "New Austrian tunnelling method and finite elements," Third International Conference on Numerical Methods in Geomechanics, Aachen, Germany, 1979, pp.587-597.

## APPENDIX

## A.1 Main input file in UDEC

\*-----Input File Eblock=3000 MPa, refined jointed model-----

ro 0.01

set edge 0.75

bl 0,0 0,90 155,90 155,0

jreg 0,0 0,90 155,90 155,0

jset 28, 2 15,2 0, 0 3,1

jset 88, 4 12,5 3, 2 6,3

jset 120, 5 6,2 3, 1 3,1

save geol.sav

set edge 0.1

\*additional cracks

cr 77.702 38.628 77.595 41.72

cr 78.45 38.628 77.809 41.88

cr 92.371 31.78 91.99 34.803

cr 87.194 40 86.85 42.895

cr 60.35 30.384 75.38 38.603

cr 79.85 40.71 90.662 46.427

cr 62.487 28.149 82.5 39.06

cr 62.55 35 86.19 47.35

cr 58.93 35.907 89.49 52.15

cr 60.609 40.115 85.87 53.46

cr 67.216 32.554 67.54 28.675

cr 67.734 38.99 67.475 42.679

cr 70.15 38.65 69.9 42.07

cr 65.8 36 75.39 40.8

cr 62.75 44.84 103.39 66.35

cr 43.54 31.21 61.597 40.844

cr 44.46 28.38 59.7 36.36

cr 37.165 31.52 63.4 45.17

cr 43.74 21.445 60.72 30.589

```

cr 45.47 40.31 110.549 74.72
cr 87.197 48.349 112.97 61.7
cr 111.9 62.4 115.07 64.07
cr 89.581 45.849 134.13 69.59
cr 25.25 15.73 63.14 35.3
cr 55.85 27.1 72.845 36
save geo2.sav
*call geometry.txt
*geometry.txt
set edge 0.05
*CREATE TUNNEL EXCAVATION PERIMETER
arc 77.5 30.46 86.37 33.688 140 40
arc 80.735 31.6 86.408 29.646 39 10
arc 79.75 42.3 81.726 28.238 20 10
arc 77.5 52.9 73.15 28.279 20 10
arc 75.25 42.3 68.583 29.762 20 10
arc 74.265 31.6 68.626 33.65 39 10
tun 77.5 36.42 2.5 25
crack 67.6,32.8 87.3,32.8

jdel
save geo.sav

rest geo.sav
* intact rock - Wss – Mohr-Coulomb plastic behavior
* E Wss=3000 MPa
prop mat=1 k=2.5e3 g=1.15e3 dens=2.5e-3 coh=2 fr=38
*
* inside the tunnel
prop mat=2 k=2.5e3 g=1.15e3 dens=2.5e-3 coh=2 fr=38
* inside the TBM

```

```

prop mat=3 k=2.5e3 g=1.15e3 dens=2.5e-3 coh=2 fr=38
* bedding joints J1
prop jmat=1 jrco=3 jcso=30 phir=25 lo=0.1 ln=0.5 &
    sigmac=50 aper=.14 JKS=31e3 JKN=2.7e4
* cross joints J2
prop jmat=2 jrco=7 jcso=40 phir=30 lo=0.1 ln=0.5 &
    sigmac=50 aper=.33 JKS=20e3 JKN=2.7e4
* glued joints (tunnel periphery)
prop jmat=5 jcoh=1e12 jfric=0 jten=1e12 jks=120e3 jkn=120e3
*Optional stiff joints
prop jmat=6 jrco=3 jcso=30 phir=27 lo=0.1 ln=0.5 &
    sigmac=50 aper=.1 JKS=1e4 JKN=4e6
prop jmat=7 jrco=7 jcso=40 phir=30 lo=0.1 ln=0.5 &
    sigmac=50 aper=.33 JKS=20e4 JKN=5e6

*-----Generate Finite Difference Mesh-----
gen edge 3.0 range 0 30 0 90
gen edge 3.0 range 130 155 0 90
gen edge 3.0 range 30 130 0 20
gen edge 3.0 range 30 130 50 90
gen edge 1.0 range 30 130 20 50
*-----
*-----Apply Global Mohr Coulomb Intact Block Const. Model-----
*-----Apply Global Barton Bandis Joint Model-----
change cons=3 mat=1 jcons=7 jmat=2
*-----Assign materials to joints and blocks-----
*call chblk.dat
*chblk.dat
ch    bl    571344    cons=3 mat=2
ch    bl    586556    cons=3 mat=2
ch    bl    586978    cons=3 mat=2

```

ch	bl	587340	cons=3 mat=2
ch	bl	571958	cons=3 mat=2
ch	bl	142873	cons=3 mat=2
ch	bl	376619	cons=3 mat=2
ch	bl	572360	cons=3 mat=2
ch	bl	377001	cons=3 mat=2
ch	bl	572902	cons=3 mat=2
ch	bl	565380	cons=3 mat=2
ch	bl	382329	cons=3 mat=2
ch	bl	573708	cons=3 mat=2
ch	bl	574122	cons=3 mat=2
ch	bl	593154	cons=3 mat=2
ch	bl	569168	cons=3 mat=2
ch	bl	517652	cons=3 mat=2
ch	bl	518154	cons=3 mat=2
ch	bl	592486	cons=3 mat=2
ch	bl	592868	cons=3 mat=2
ch	bl	568554	cons=3 mat=2
ch	bl	595122	cons=3 mat=2
ch	bl	567486	cons=3 mat=2
ch	bl	567948	cons=3 mat=2
ch	bl	369539	cons=3 mat=2
ch	bl	595694	cons=3 mat=2
ch	bl	566932	cons=3 mat=2
ch	bl	594490	cons=3 mat=2
ch	bl	593822	cons=3 mat=2
ch	bl	594836	cons=3 mat=2
ch	bl	593440	cons=3 mat=2
ch	bl	594204	cons=3 mat=2
ch	bl	595884	cons=3 mat=2
ch	bl	583662	cons=3 mat=2

ch	bl	586270	cons=3 mat=2
ch	bl	584412	cons=3 mat=2
ch	bl	135563	cons=3 mat=2
ch	bl	584894	cons=3 mat=2
ch	bl	595408	cons=3 mat=2
ch	bl	135181	cons=3 mat=2
ch	bl	582022	cons=3 mat=2
ch	bl	581464	cons=3 mat=2
ch	bl	581178	cons=3 mat=2
ch	bl	362669	cons=3 mat=2
ch	bl	369157	cons=3 mat=2
ch	bl	136577	cons=3 mat=2
ch	bl	376137	cons=3 mat=2
ch	bl	381361	cons=3 mat=2
ch	bl	582756	cons=3 mat=2
ch	bl	575112	cons=3 mat=2
ch	bl	363051	cons=3 mat=2
ch	bl	129949	cons=3 mat=2
ch	bl	369661	cons=3 mat=2
ch	bl	579738	cons=3 mat=2
ch	bl	579376	cons=3 mat=2
ch	bl	578566	cons=3 mat=2
ch	bl	578220	cons=3 mat=2
ch	bl	576414	cons=3 mat=2
ch	bl	580200	cons=3 mat=2
ch	bl	587814	cons=3 mat=3
ch	bl	588664	cons=3 mat=3
ch	bl	585752	cons=3 mat=3
ch	bl	589122	cons=3 mat=3
ch	bl	592144	cons=3 mat=3
ch	bl	589624	cons=3 mat=3

ch bl 591734 cons=3 mat=3  
ch bl 591272 cons=3 mat=3  
ch bl 590514 cons=3 mat=3

\* bedding plane J1

change angle 18, 38 jcons=7 jmat=1

\*-----Joint Modifications-----

\*Glue artificial tunnel geometry joints

change int 1,2 jcons=2 jmat=5

change int 2,3 jcons=2 jmat=5

change int 4,2 jcons=2 jmat=5

change angle -1,1 jcons=2 jmat=5

\*-----Optional joint Modifications-----

\*Glue unbalanced wedges or modify joints empirically-----

change contact 135705 jcons=2 jmat=5

change contact 586460 jcons=2 jmat=5

change jmat=6 range region 62.7,37.7 62.52,47.78 80.483,59 80.29,47.02 &  
angle 26,31

change contact 136827 jmat=6

change contact 1371211 jmat=6

change contact 1690801 jmat=6

change contact 444320 jmat=6

change contact 438374 jmat=6

change contact 1690145 jmat=6

change contact 438326 jmat=6

change contact 444368 jmat=6

change contact 1690901 jmat=6

change contact 1024453 jmat=6

change contact 370055 jmat=6

change contact 363558 jmat=7



change contact 1157741 jmat=7  
change contact 1371279 jmat=7  
change contact 515398 jmat=7  
change contact 515446 jmat=7  
change contact 1371141 jmat=7  
change contact 1400479 jmat=7  
change contact 1371347 jmat=7  
change contact 136875 jmat=7  
change contact 19914 jcons=2 jmat=5  
change contact 1403285 jcons=2 jmat=5  
change contact 1403185 jcons=2 jmat=5  
change contact 19578 jcons=2 jmat=5  
change contact 1414265 jcons=2 jmat=5  
change contact 1413389 jcons=2 jmat=5  
change contact 1414119 jcons=2 jmat=5  
change contact 124471 jcons=2 jmat=5  
change contact 344150 jcons=2 jmat=5  
change contact 1414695 jcons=2 jmat=5  
change contact 1413535 jcons=2 jmat=5  
change contact 1414595 jcons=2 jmat=5  
change contact 344187 jcons=2 jmat=5  
change contact 131431 jcons=2 jmat=5  
change contact 1387227 jcons=2 jmat=5  
change contact 1387089 jcons=2 jmat=5  
change contact 1387295 jcons=2 jmat=5  
change contact 131298 jcons=2 jmat=5  
change contact 356908 jcons=2 jmat=5  
change contact 1165863 jcons=2 jmat=5  
change contact 1164887 jcons=2 jmat=5  
change contact 1165763 jcons=2 jmat=5  
change contact 131335 jcons=2 jmat=5

change contact 512939 jcons=2 jmat=5  
change contact 1166055 jcons=2 jmat=5  
change contact 1164987 jcons=2 jmat=5  
change contact 1166155 jcons=2 jmat=5  
change contact 512976 jcons=2 jmat=5  
change contact 124434 jcons=2 jmat=5  
change contact 356775 jcons=2 jmat=5  
change contact 1388467 jcons=2 jmat=5  
change contact 1697863 jcons=2 jmat=5  
change contact 594941 jcons=2 jmat=5  
change contact 567752 jcons=2 jmat=5  
change contact 1388397 jcons=2 jmat=5  
change contact 593964 jcons=2 jmat=5  
change contact 356690 jcons=2 jmat=5  
change contact 1388397 jcons=2 jmat=5  
change contact 593964 jcons=2 jmat=5  
change contact 131621 jcons=2 jmat=5  
change contact 148455 jcons=2 jmat=5  
change contact 1163083 jcons=2 jmat=5  
change contact 567054 jcons=2 jmat=5  
change contact 1162875 jcons=2 jmat=5  
change contact 1163151 jcons=2 jmat=5  
change contact 24954 jcons=2 jmat=5  
change jcons=2 jmat=5 range 69.93 70.89 37.06 37.615  
change jcons=2 jmat=5 range 87.771 88.23 36.24 37.8  
change jcons=2 jmat=5 range 90 90.73 37.705 38.807  
change jcons=2 jmat=5 range 83.86 84.54 38.85 40.6  
change jcons=2 jmat=5 range 86.847 87.211 40.65 42.048  
change jcons=2 jmat=5 range 83.235 83.727 39.36 39.98  
change jcons=2 jmat=5 range 87.42 87.77 36.94 37.54  
change jcons=2 jmat=5 range 84.361 84.386 38.059 38.44

```
change jcons=2 jmat=5 range 84.369 85.269 36.664 38.459
change contact 567704 jcons=7 jmat=2
change contact 356557 jcons=7 jmat=2
```

```
*
```

```
damp auto
mscale off
set jcondf 7
set jmatdf 2
```

```
*
```

```
save mat.sav
*call consko83b.txt
```

```
*Model consolidation: consko83b.txt
```

```
rest mat.sav
```

```
*Boundary conditions
```

```
bo -.1 155.1 89.9 90.1 str 0 0 -0.575
bo -.1 .1 -.1 90.1 str -2.35 0 -2.83 ygrad 0.02 0 0.025
bo 154.9 155.1 -.1 90.1 str -2.35 0 -2.83 ygrad 0.02 0 0.025
bo -.1 155.1 -.1 .1 yvel 0
bo 75.0 77.0 -.1 .1 xvel 0 yvel 0
insitu -.1 155.1 -.1 90.1 str -2.35 0 -2.83 ygrad 0.02 0 0.025
insitu -.1 155.1 -.1 90.1 szz -2.35 zgrad 0 0.02
set grav 0.0,-10.
```

```
*History points around tunnel
```

```
hist ydis 77.8 39.417
hist sxx 77.88 39.188
hist syy 77.88 39.188
```

hist xdis 74.859 36.8

hist sxx 74.64 36.657

hist syy 74.64 36.657

hist xdis 80.35 36.76

hist sxx 80.114 36.749

hist syy 80.114 36.749

hist ydis 77.26 40.24

hist sxx 77.44 40.14

hist syy 77.44 40.14

hist ydis 70.748 37.617

hist sxx 70.71 37.438

hist syy 70.71 37.438

hist ydis 84.278 37.606

hist sxx 84.17 37.481

hist syy 84.17 37.481

hist xdis 68.171 33.488

hist sxx 68.171 33.488

hist syy 68.171 33.488

hist xdis 86.518 34.368

hist sxx 86.518 34.368

hist syy 86.518 34.368

hist ydis 77.946 27.634

hist sxx 77.946 27.634

hist syy 77.946 27.634

\*additional history point

\*roof

hist ydis 77.687 42.065

hist sxx 77.687 42.065

hist syy 77.687 42.065

hist ydis 77.63 43.46

hist sxx 77.608 43.143

hist syy 77.608 43.143

hist ydis 77.452 44.975

hist sxx 77.452 44.975

hist syy 77.452 44.975

hist ydis 78.246 46

hist sxx 78.246 46

hist syy 78.246 46

\*right roof

hist ydis 85.576 38.659

hist sxx 85.767 38.554

hist syy 85.767 38.554

hist ydis 85 39.7

hist sxx 85 39.7

hist syy 85 39.7

hist ydis 83.732 41.669

hist sxx 83.732 41.669

hist syy 83.732 41.669

\*left roof

hist ydis 70.464 38

hist sxx 70.532 37.772

hist syy 70.532 37.772

hist ydis 70.947 39.028

hist sxx 70.947 39.028

hist syy 70.947 39.028

hist ydis 70.731 41.815

hist sxx 70.731 41.815

hist syy 70.731 41.815

hist ydis 70.173 38.199

hist sxx 69.96 38.23

hist syy 69.96 38.23

hist ydis 68.958 39.187

hist sxx 68.837 39.217

hist syy 68.837 39.217

hist ydisp 78.79 40.22

hist unbal

\*Line plot locations

set pline 77.5 0 77.5 90 80

set pline 0 36.4 155 36.4 150

set pline 0 32.8 155 32.8 150

\*Optional mass scaling

\*mscale on

cyc 100000

save cons.sav

\*call excav1full.txt

\*excav1full.txt

\*Pilot tunnel excavation - complete relaxation

rest cons.sav

jhist on 0.1

reset disp

reset time

reset rota

reset hist

\* history points around tunnel

\*

hist ydis 77.8 39.417

hist sxx 77.88 39.188

hist syy 77.88 39.188

hist xdis 74.859 36.8

hist sxx 74.64 36.657

hist syy 74.64 36.657

hist xdis 80.35 36.76

hist sxx 80.114 36.749

hist syy 80.114 36.749

hist ydis 77.26 40.24

hist sxx 77.44 40.14

hist syy 77.44 40.14

hist ydis 70.748 37.617

hist sxx 70.71 37.438

hist syy 70.71 37.438

hist ydis 84.278 37.606

hist sxx 84.17 37.481

hist syy 84.17 37.481

hist xdis 68.171 33.488

hist sxx 68.171 33.488

hist syy 68.171 33.488

hist xdis 86.518 34.368

hist sxx 86.518 34.368

hist syy 86.518 34.368

hist ydis 77.946 27.634

hist sxx 77.946 27.634

hist syy 77.946 27.634

\*additional history points

\*roof

hist ydis 77.687 42.065

hist sxx 77.687 42.065

hist syy 77.687 42.065

hist ydis 77.63 43.46

hist sxx 77.608 43.143

hist syy 77.608 43.143

hist ydis 77.452 44.975



hist sxx 77.452 44.975

hist syy 77.452 44.975

hist ydis 78.246 46

hist sxx 78.246 46

hist syy 78.246 46

\*right roof

hist ydis 85.576 38.659

hist sxx 85.767 38.554

hist syy 85.767 38.554

hist ydis 85 39.7

hist sxx 85 39.7

hist syy 85 39.7

hist ydis 83.732 41.669

hist sxx 83.732 41.669

hist syy 83.732 41.669

\*left roof

hist ydis 70.464 38

hist sxx 70.532 37.772

hist syy 70.532 37.772

hist ydis 70.947 39.028

hist sxx 70.947 39.028

hist syy 70.947 39.028

hist ydis 70.731 41.815

hist sxx 70.731 41.815

hist syy 70.731 41.815

hist ydis 70.173 38.199

hist sxx 69.96 38.23

hist syy 69.96 38.23

hist ydis 68.958 39.187

hist sxx 68.837 39.217

hist syy 68.837 39.217

hist ydisp 78.79 40.22

hist unbal

\* 1st stage: TBM Pilot

del bl 587814

del bl 588664

del bl 585752

del bl 589122

del bl 592144

del bl 589624

del bl 591734

del bl 591272

del bl 590514

cycle 100000

save excav1full.sav

\*call excav2full.txt

\*excav2full.txt

rest excav1full.sav

\* 2nd stage: Top Heading

del	bl	571344
del	bl	586556
del	bl	586978
del	bl	587340
del	bl	571958
del	bl	142873
del	bl	376619
del	bl	572360
del	bl	377001
del	bl	572902
del	bl	565380
del	bl	382329
del	bl	573708
del	bl	574122
del	bl	593154
del	bl	569168
del	bl	517652
del	bl	518154
del	bl	592486
del	bl	592868
del	bl	568554
del	bl	595122
del	bl	567486
del	bl	567948
del	bl	369539
del	bl	595694
del	bl	566932
del	bl	594490

del bl 593822  
del bl 594836  
del bl 593440  
del bl 594204  
del bl 595884

\*mscale off

\*-----

\*1 Short Relaxation lamda=0.5

\*2 Rock Bolt Installation

\*3 Additional relaxation to lamda=0.65

\*3 Application of Steel Sets H-200

\*4 Application of SFR t=20 cm

\*Final Cycling

\*-----

\*Line plot locations for extensometers & measuring anchors

set	pline	86.052	34.459	96.669	40.052	40
set	pline	83.827	37.608	91.360	46.948	40
set	pline	77.800	39.900	77.800	51.900	40
set	pline	71.173	37.608	63.640	46.948	40
set	pline	68.948	34.459	58.331	40.052	40

cycle 1000

save excav2f1.sav

cycle 1000

save excav2f2.sav

cycle 1000

save excav2f3.sav

cycle 1000

save excav2f4.sav

cycle 1000

save excav2f5.sav  
cycle 1000  
save excav2f6.sav  
cycle 1000  
save excav2f7.sav  
cycle 1000  
save excav2f8.sav  
cycle 1000  
save excav2f9.sav  
cycle 1000  
save excav2f10.sav  
cycle 10000  
save excav2f11.sav  
cycle 10000  
save excav2f12.sav  
cycle 10000  
save excav2f13.sav  
cycle 10000  
save excav2f14.sav  
cycle 50000  
save excav2f15.sav  
save excav2full.sav

\*call rein2.dat

\*rein2.dat

rest excav2f5.sav

\*Install Top Heading Support

\* bolt tunnel

\* 22mm Diameter grouted rock bolts/S500 Steel

```
prop mat=9 ras=1957.412 rrs=131.347 rl=0.044 &  
rua=0.1467 rush=0.10267 rrf=1 rse=1 raex=1
```

```
reinf 9 78.778 39.813 79.590 45.758  
reinf 9 77.500 39.900 77.500 45.900  
reinf 9 76.222 39.813 75.410 45.758  
reinf 9 71.573 37.808 67.807 42.478  
reinf 9 74.968 39.554 73.359 45.334  
reinf 9 86.371 33.689 92.009 35.741  
reinf 9 85.852 34.859 91.161 37.656  
reinf 9 85.180 35.949 90.061 39.438  
reinf 9 84.366 36.938 88.731 41.056  
reinf 9 83.427 37.808 87.193 42.478  
reinf 9 82.378 38.542 85.478 43.679  
reinf 9 81.239 39.128 83.615 44.637  
reinf 9 80.032 39.554 81.641 45.334  
reinf 9 73.761 39.128 71.385 44.637  
reinf 9 72.622 38.542 69.522 43.679  
reinf 9 70.634 36.938 66.269 41.056  
reinf 9 69.820 35.949 64.939 39.438  
reinf 9 69.148 34.859 63.839 37.656  
reinf 9 68.629 33.689 62.991 35.741
```

```
save rein2a.sav  
cycle 2000
```

\*Installation of Composite Element: Steel H200 sections and Shotcrete

```
prop mat=14 if_kn 1e5 if_ks 1e3 if_coh=2 if_friction=30
```

```
struct generate fang = -2.7 &
```

```
mat = 13 &
npoint = 150 &
theta = 185.3 &
thickness = 0.2 &
xc = 77.5 &
yc = 33.3 &
```

```
property mat = 13 if_cohesion = 1
property mat = 13 if_friction = 50
property mat = 13 if_kn = 1.00E+05
property mat = 13 if_ks = 2.00E+04
property mat = 13 if_tensile = 1
property mat = 13 st_density = 0.0079
property mat = 13 st_prat = 0.2
property mat = 13 st_ycomp = 200
property mat = 13 st_yield = 370
property mat = 13 st_ymod = 200000
```

```
struct change area = 0.0266 &
inertia = 0.0001113 &
shape = 0.7433
```

```
cycle 20000
```

```
*-----Optional modifications-----
```

```
set ovtol 0.01
```

```
cycle 3
```

```
*-----
```

```
cycle 80000
```

```
save rein2final.sav
```

```
*call excav3.txt
```

\*excav3.txt

\* 3rd stage: Bench excavation in one stage

rest rein2final.sav

del	bl	583662
del	bl	586270
del	bl	584412
del	bl	135563
del	bl	584894
del	bl	595408
del	bl	135181
del	bl	582022
del	bl	581464
del	bl	581178
del	bl	362669
del	bl	369157
del	bl	136577
del	bl	376137
del	bl	381361
del	bl	582756
del	bl	575112
del	bl	363051
del	bl	129949
del	bl	369661
del	bl	579738
del	bl	579376
del	bl	578566
del	bl	578220
del	bl	576414
del	bl	580200



\*-----Optional modifications in beam interface-----

prop mat=15 if\_kn=1e8

struct change jmat 15 range 74.15 75.58 39.26 39.73

\*-----

cycle 1000

save excav3f1.sav

cycle 1000

save excav3f2.sav

cycle 1000

save excav3f3.sav

cycle 1000

save excav3f4.sav

cycle 1000

save excav3f5.sav

cycle 1000

save excav3f6.sav

cycle 1000

save excav3f7.sav

cycle 1000

save excav3f8.sav

cycle 1000

save excav3f9.sav

cycle 1000

save excav3f10.sav

cycle 10000

save excav3f11.sav

cycle 10000

save excav3f12.sav

cycle 10000

save excav3f13.sav

cycle 10000

```

save excav3f14.sav
cycle 50000
save excav3f15.sav
save excav3full.sav
*
rest excav3f5.sav
*
*bolt walls of tunnel
reinf  9      86.644 30.558 92.553 29.516
reinf  9      86.735 31.600 92.735 31.600
reinf  9      86.644 32.642 92.553 33.684

reinf  9      68.629 33.689 62.991 35.741
reinf  9      68.356 30.558 62.447 29.516
reinf  9      68.265 31.600 62.265 31.600
reinf  9      68.356 32.642 62.447 33.684

cyc 3000
save rein3a.sav
*Installation of Composite Element: Steel IPB 200 and Shotcrete
struct generate          fang  =    174.4 &
                        mat   =    13 &
                        npoint =    150 &
                        theta  =    190.95 &
                        thickness = 0.2 &
                        xc     =    77.5 &
                        yc     =    32 &
                        connect
save stru1.sav
struct change          area =    0.0266 &

```

```

                                inertia =    0.0001113    &
                                shape  =    0.7433    &
                                range 68.244 68.75 29.67 32.91

save stru2.sav
struct change    area  =    0.0266    &
                                inertia =    0.0001113    &
                                shape  =    0.7433    &
                                range 86.22 86.77 29.67 32.91

save stru3.sav
property    mat  =    16    if_cohesion  =    1
property    mat  =    16    if_friction  =    50
property    mat  =    16    if_kn    =    200000
property    mat  =    16    if_ks    =    2.0e4
property    mat  =    16    if_tensile  =    1
property    mat  =    16    st_density  =    0.0025
property    mat  =    16    st_prat    =    0.2
property    mat  =    16    st_ycomp   =    30
property    mat  =    16    st_yield   =    3.15
property    mat  =    16    st_ymod    =    21875
property    mat  =    16    st_yresid  =    2

struct change mat 16 range 68.59 86.4 27.77 29.768
struct change    area  =    0.3    &
                                inertia =    0.00225    &
                                shape  =    0.833    &
                                thick = 0.3    &
                                range 68.59 86.4 27.77 29.768

cycle 100000
save rein3final1.sav
cycle 100000

```

```
save rein3final2.sav  
cycle 100000  
save rein3final.sav  
ret
```

## A.2 Controlled relaxation analysis input files

### A.2.1 Relaxation subroutine for pilot tunnel (After Itasca, 2000)

; fish function to:

; 1. retrieve reaction forces from boundary corner data,

; 2. change boundary type to force boundary

; 3. gradually reduce the reaction force

;

;

def zonk

; mark gridpoints that are on interior boundary

; and set to force boundary

;

ib=block\_head ; start of block list

loop while ib #0 ; loop through all blocks

igp=b\_gp(ib) ; start of gridpoint list for block ib

loop while igp # 0 ; loop through all gridpoints

ibou=gp\_bou(igp) ; index of boundary corner associated with gridpoint

if(ibou) < 0 then ; if address is negative then it is interior

ibou2=abs(ibou)

if (imem(ibou2+2)) = 4 then

imem(ibou2+2)= 1 ; force boundary

imem(ibou2+3)= 1 ; force boundary

gp\_extra(igp) = 1.0

endif

else

gp\_extra(igp) = 0.0

endif

igp=gp\_next(igp) ; next gridpoint

endloop

ib= b\_next(ib) ; next block in list

endloop

end

def reduce

ib=block\_head ; start of block list

loop while ib #0 ; loop through all blocks

igp=b\_gp(ib) ; start of gridpoint list for block ib

loop while igp # 0 ; loop through all gridpoints

ibou=gp\_bou(igp) ; index of boundary corner associated with gridpoint

if(ibou) < 0 then ; if address is negative then it is interior

ibou2=abs(ibou)

if gp\_extra(igp) > 0.0 then

forcex=fmem(ibou2+4) ; get current total x-force

forcey=fmem(ibou2+5) ; get current total y-force

fmem(ibou2+4)= forcex \* red\_factor ;reduce reaction force

fmem(ibou2+5)= forcey \* red\_factor ;reduce reaction force

endif

endif

igp=gp\_next(igp) ; next gridpoint

endloop

ib= b\_next(ib) ; next block in list

endloop

end

def relax1

old\_factor = 1.0

new\_factor = .9

red\_factor = new\_factor/old\_factor

reduce

command

cycle 20000

save relax1a.sav

```

endcommand
old_factor = new_factor
new_factor = new_factor - .1
red_factor = new_factor/old_factor
reduce
command
  cycle 20000
  save relax1b.sav
endcommand
old_factor = new_factor
new_factor = new_factor - .1
red_factor = new_factor/old_factor
reduce
command
  cycle 20000
  save relax1c.sav
endcommand
old_factor = new_factor
new_factor = new_factor - .1
red_factor = new_factor/old_factor
reduce
command
  cycle 20000
  save relax1d.sav
endcommand
old_factor = new_factor
new_factor = new_factor - .1
red_factor = new_factor/old_factor
reduce
command
  cycle 20000

```

```

    save relax1e.sav
endcommand
old_factor = new_factor
new_factor = new_factor - .1
red_factor = new_factor/old_factor
reduce
command
    cycle 20000
    save relax1f.sav
endcommand
old_factor = new_factor
new_factor = new_factor - .1
red_factor = new_factor/old_factor
reduce
command
    cycle 20000
    save relax1g.sav
endcommand
old_factor = new_factor
new_factor = new_factor - .1
red_factor = new_factor/old_factor
reduce
command
    cycle 20000
    save relax1h.sav
endcommand
old_factor = new_factor
new_factor = new_factor - .1
red_factor = new_factor/old_factor
reduce
command

```



```
cycle 20000
save relax1i.sav
endcommand
old_factor = new_factor
new_factor = new_factor - .1
red_factor = new_factor/old_factor
reduce
command
cycle 20000
save relax1j.sav
endcommand
end
```

## A.2.2 Relaxation subroutine for top heading

```
;
; fish function to:
; 1. retrieve reaction forces from boundary corner data
; 2. change boundary type to force boundary
; 3. gradually reduce the reaction force
;
;
def relax2a
  old_factor = 1.0
  new_factor = .9
  red_factor = new_factor/old_factor
  reduce
  command
    cycle 20000
    save relax2a1.sav
  endcommand
  old_factor = new_factor
  new_factor = new_factor - .1
  red_factor = new_factor/old_factor
  reduce
  command
    cycle 20000
    save relax2a2.sav
  endcommand
  old_factor = new_factor
  new_factor = new_factor - .1
  red_factor = new_factor/old_factor
  reduce
  command
    cycle 20000
```

```
save relax2a3.sav
endcommand
old_factor = new_factor
new_factor = new_factor - .1
red_factor = new_factor/old_factor
reduce
command
cycle 20000
save relax2a4.sav
endcommand
old_factor = new_factor
new_factor = new_factor - .1
red_factor = new_factor/old_factor
reduce
command
cycle 20000
save relax2a5.sav
endcommand
old_factor = new_factor
new_factor = new_factor - .1
red_factor = new_factor/old_factor
reduce
command
cycle 20000
save relax2a6.sav
endcommand
old_factor = new_factor
new_factor = new_factor - .1
red_factor = new_factor/old_factor
reduce
command
```

```
cycle 20000
save relax2a7.sav
endcommand
old_factor = new_factor
new_factor = new_factor - .1
red_factor = new_factor/old_factor
reduce
command
cycle 20000
save relax2a8.sav
endcommand
old_factor = new_factor
new_factor = new_factor - .1
red_factor = new_factor/old_factor
reduce
command
cycle 20000
save relax2a9.sav
endcommand
old_factor = new_factor
new_factor = new_factor - .1
red_factor = new_factor/old_factor
reduce
command
cycle 20000
save relax2a10.sav
endcommand

end
```

### A.3 Complete input file for controlled relaxation

\*Controlled relaxation analysis for TBM pilot

rest cons.sav

jhist on 0.1

reset disp

reset time

reset rota

reset hist

call zonk1.fis

\* 1st stage: TBM Pilot

\*

del bl 587814

del bl 588664

del bl 585752

del bl 589122

del bl 592144

del bl 589624

del bl 591734

del bl 591272

del bl 590514

\*Fix excavation boundary gridpoints

\*Cycle once to get reactions

boundary interior xvel=0 yvel=0 range domain 591057

cycle 1

\* history locations around tunnel

\*

hist ydis 77.8 39.417

hist sxx 77.88 39.188

hist syy 77.88 39.188

hist xdis 74.859 36.8

hist sxx 74.64 36.657

hist syy 74.64 36.657

hist xdis 80.35 36.76

hist sxx 80.114 36.749

hist syy 80.114 36.749

hist ydis 77.26 40.24

hist sxx 77.44 40.14

hist syy 77.44 40.14

hist ydis 70.748 37.617

hist sxx 70.71 37.438

hist syy 70.71 37.438

hist ydis 84.278 37.606

hist sxx 84.17 37.481

hist syy 84.17 37.481

hist xdis 68.171 33.488

hist sxx 68.171 33.488

hist syy 68.171 33.488

hist xdis 86.518 34.368

hist sxx 86.518 34.368

hist syy 86.518 34.368

hist ydis 77.946 27.634  
hist sxx 77.946 27.634  
hist syy 77.946 27.634

\*additional history point

\*roof

hist ydis 77.687 42.065  
hist sxx 77.687 42.065  
hist syy 77.687 42.065

hist ydis 77.63 43.46  
hist sxx 77.608 43.143  
hist syy 77.608 43.143

hist ydis 77.452 44.975  
hist sxx 77.452 44.975  
hist syy 77.452 44.975

hist ydis 78.246 46  
hist sxx 78.246 46  
hist syy 78.246 46

\*right roof

hist ydis 85.576 38.659  
hist sxx 85.767 38.554  
hist syy 85.767 38.554

hist ydis 85 39.7  
hist sxx 85 39.7  
hist syy 85 39.7

hist ydis 83.732 41.669

hist sxx 83.732 41.669

hist syy 83.732 41.669

\*left roof

hist ydis 70.464 38

hist sxx 70.532 37.772

hist syy 70.532 37.772

hist ydis 70.947 39.028

hist sxx 70.947 39.028

hist syy 70.947 39.028

hist ydis 70.731 41.815

hist sxx 70.731 41.815

hist syy 70.731 41.815

hist ydis 70.173 38.199

hist sxx 69.96 38.23

hist syy 69.96 38.23

hist ydis 68.958 39.187

hist sxx 68.837 39.217

hist syy 68.837 39.217

hist ydisp 78.79 40.22

hist unbal

hist ncyc 100



```
hist typ 1
mscale on
zonk
relax1
save excav1.sav
*call excav2.dat
```

```
*Controlled relaxation analysis for Top Heading
```

```
rest excav1.sav
```

```
*
```

```
call zonk2a.fis
```

```
* 2nd stage: Top Heading
```

```
del bl 571344
```

```
del bl 586556
```

```
del bl 586978
```

```
del bl 587340
```

```
del bl 571958
```

```
del bl 142873
```

```
del bl 376619
```

```
del bl 572360
```

```
del bl 377001
```

```
del bl 572902
```

```
del bl 565380
```

```
del bl 382329
```

```
del bl 573708
```

```
del bl 574122
```

```
del bl 593154
```

```
del bl 569168
```

```
del bl 517652
```

```
del bl 518154
```

```
del bl 592486
```

```
del    bl    592868
del    bl    568554
del    bl    595122
del    bl    567486
del    bl    567948
del    bl    369539
del    bl    595694
del    bl    566932
del    bl    594490
del    bl    593822
del    bl    594836
del    bl    593440
del    bl    594204
del    bl    595884
```

```
*Fix excavation boundary gridpoints
```

```
*Cycle once to get reactions
```

```
boundary interior xvel=0 yvel=0 range domain 575299
```

```
cycle 1
```

```
*mscale on
```

```
zonk
```

```
relax2a
```

```
save excav2.sav
```

```
ret
```

## VITA

Sotirios Vardakos was born in Athens, Greece in November 21<sup>st</sup>, 1978 and he is the only child of Dr. Spyridon Vardakos and Helen Vardakou. He grew in a traditional classic environment of downtown Athens close to the Ancient monument of the Parthenon in the area of the Acropolis. Even though the family background was mainly inclined towards studies in Social and Political sciences as also towards Financial studies, he soon showed interest towards applied physics and mechanics. He was accepted at the First Experimental High School of Athens where he attended six years of education.

The aspiration to become a geotechnical engineer and his interest in underground engineering, came during his undergraduate studies at the Department of Mining Engineering and Metallurgy, at the National Technical University of Athens where he was accepted in 1997. During these years he had the chance to gain training by Mining Engineering industries, to gain experience from the tunneling practices but significant experience was also gained during his involvement in private geotechnical engineering consulting. After the five year education he graduated first in his class in 2002 with highest academic distinction and a Silver Dean's Award for Academic Excellence. He was also honored with a U.S governmental scholarship by the Fulbright Foundation, to study in United States of America. He was accepted at Virginia Polytechnic Institute and State University where he studied towards his Master of Science Degree.

Under the supervision of Dr. Marte Gutierrez, Sotirios Vardakos worked on research regarding numerical analysis for tunneling applications by the use of the distinct element method and it was concluded that the present research in execution and verification of numerical simulations, would be an academically challenging project.